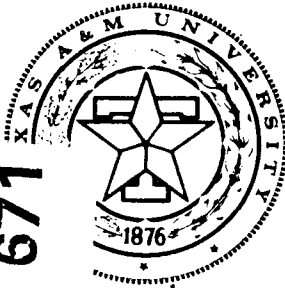


(2)

CENTER for MECHANICS of COMPOSITES

Texas A&M University
College Station, Texas



AD-A226 671

**EXPERIMENTAL AND THEORETICAL
DETERMINATION OF THE
THERMOMECHANICAL RESPONSE
OF INELASTIC STRUCTURAL MATERIALS
TO HIGH ENERGY THERMAL INPUTS**

FINAL TECHNICAL REPORT

submitted by

D.H. Allen
Aerospace Engineering Department

and

M.S. Pilant
Mathematics Department

Texas A&M University
College Station, TX 77843

to the

Air Force Office of Scientific Research
Office of Aerospace Research
Bolling AFB
Washington, DC 20332

DTIC
SEP 25 1990
S
D C

CMC 5485-90-1

Contract No. F49620-85-K-0016
July 1990

DIS
App

REPORT DOCUMENTATION PAGE				Form Approved OMB No. 0704-0188	
1a. REPORT SECURITY CLASSIFICATION unclassified			1b. RESTRICTIVE MARKINGS		
2a. SECURITY CLASSIFICATION AUTHORITY			3. DISTRIBUTION / AVAILABILITY OF REPORT unlimited		
2b. DECLASSIFICATION / DOWNGRADING SCHEDULE					
4. PERFORMING ORGANIZATION REPORT NUMBER(S) CMC 5485-90-1			5. MONITORING ORGANIZATION REPORT NUMBER(S) AFOSR-TR- 90 0922		
6a. NAME OF PERFORMING ORGANIZATION Aerospace Engineering Dept.		6b. OFFICE SYMBOL (If applicable)	7a. NAME OF MONITORING ORGANIZATION Air Force Office of Scientific Research		
6c. ADDRESS (City, State, and ZIP Code) Texas A & M University College Station, Tx. 77843			7b. ADDRESS (City, State, and ZIP Code) Bolling AFB Washington, DC 20332		
8a. NAME OF FUNDING / SPONSORING ORGANIZATION Air Force Office of Scientific		8b. OFFICE SYMBOL (If applicable) NA	9. PROCUREMENT INSTRUMENT IDENTIFICATION NUMBER F49620-86-K-0016		
8c. ADDRESS (City, State, and ZIP Code) Bolling AFB Washington, DC 20332			10. SOURCE OF FUNDING NUMBERS		
			PROGRAM ELEMENT NO. 611024	PROJECT NO. 2302	TASK NO. B1
11. TITLE (Include Security Classification) Experimental and Theoretical Determination of the Thermomechanical Response of Inelastic Structural Materials to High Energy Thermal Inputs-Second Annual Report (W)					
12. PERSONAL AUTHOR(S) D.H. Allen and M.S. Pilant					
13a. TYPE OF REPORT Final		13b. TIME COVERED FROM July 86 TO Dec. 89		14. DATE OF REPORT (Year, Month, Day) July 1990	
15. PAGE COUNT					
16. SUPPLEMENTARY NOTATION					
17. COSATI CODES			18. SUBJECT TERMS (Continue on reverse if necessary and identify by block number)		
FIELD	GROUP	SUB-GROUP	laser heating ' Constitutive properties		
			viscoplasticity. heat transfer		
			finite element methods. thermomechanics. (TS)		
19. ABSTRACT (Continue on reverse if necessary and identify by block number)					
<p>The general objective of this research is to improve on existing theoretical models for predicting the response of inelastic aerospace structural components subjected to hostile thermal environments with emphasis on transient temperature conditions, radiation boundary conditions, extremely rapid heating rates, and possible phase change of the materials involved. For materials subjected to the conditions under study herein it is necessary to perform extremely complex experiments in order to determine the precise form of the theoretical constitutive equations. Finally, it is necessary to implement the resulting equations to boundary value problem solving algorithms in order to model the response of structural components with stress, strain, and temperature gradient fields.</p>					
20. DISTRIBUTION / AVAILABILITY OF ABSTRACT <input checked="" type="checkbox"/> UNCLASSIFIED/UNLIMITED <input type="checkbox"/> SAME AS RPT. <input checked="" type="checkbox"/> DTIC USERS			21. ABSTRACT SECURITY CLASSIFICATION unclassified		
22a. NAME OF RESPONSIBLE INDIVIDUAL Lt. Col. George Haritos			22b. TELEPHONE (Include Area Code) (202) 767-0463		22c. OFFICE SYMBOL AFOSR/NA

**EXPERIMENTAL AND THEORETICAL DETERMINATION
OF THE THERMOMECHANICAL RESPONSE
OF INELASTIC STRUCTURAL MATERIALS
TO HIGH ENERGY THERMAL INPUTS**

FINAL TECHNICAL REPORT

submitted by

D.H. Allen
Aerospace Engineering Department

and

M.S. Pilant
Mathematics Department

Texas A&M University
College Station, TX 77843

to the

Air Force Office of Scientific Research
Office of Aerospace Research
Bolling AFB
Washington, DC 20332



Accession For	
NTIS	CPAS
DTIC	TAM
Unannounced	
Just to hand	
By	
Distribution	
Availability Codes	
Dist	Admin. or Special
A-1	

CMC 5485-90-1

Contract No. F49620-86-K-0016
July 1990

TABLE OF CONTENTS

	<u>Page</u>
1. INTRODUCTION	1
1.1 Summary	1
1.2 Statement of Work	1
2. RESEARCH COMPLETED	2
2.1 Summary of Completed Research	2
2.2 Theoretical Developments	2
2.2.1 One-Way Coupled Model	2
2.2.2 Two-Way Coupled Model	9
2.2.3 Damage Dependent Constitutive Model for Metal Matrix Composites	19
2.2.4 Effective Elastic Properties of Randomly Oriented Fiber Composites Due to Forming	25
2.3 Experimental Programs	38
2.3.1 Constitutive Testing	38
2.3.2 Plate Testing	48
2.4 Conclusions	63
2.5 References	65
3. PUBLICATION LIST	68
4. RESEARCH ASSIGNMENTS	70
5. INTERACTIONS	71
5.1 Presentations	71
5.2 Awards and Achievements	71
5.3 Other	72
6. GRADUATE STUDENT ACTIVITIES	73
6.1 Theses Completed	73
6.2 Thesis Abstracts	73

7. APPENDIX - INTERIM TECHNICAL REPORTS

- 7.1 Analysis of Coupling and Rate Effects in Viscoplastic Plates Subjected to Rapid Heating**
- 7.2 A Model for Predicting the Effective Elastic Properties of Randomly Oriented Fiber Composites Subjected to Hot Pressing, Extrusion, and Rolling**
- 7.3 A Self-Consistent Thermoviscoplastic Constitutive Model for Short Fiber Composites**
- 7.4 Application of Current Unified Viscoplastic Constitutive Models to Hastelloy X at Elevated Temperatures**
- 7.5 A Review of the Theory of Thermomechanical Coupling in Inelastic Solids**
- 7.6 Nonlinear Constitutive Behavior of Metals**
- 7.7 Laser/Structure Interaction - A Comparison of Theory to Experiment**

INTRODUCTION

1.1 Summary

This report details results of research performed under AFOSR contract no. F49620-86-K-0016. The contract was initiated on June 1, 1986 and expired on December 31, 1989.

Aerospace vehicles are often subjected to hostile thermal environments capable of adversely affecting their life. Examples are: 1) space structures subjected to solar radiation or other external heating sources, as well as onboard heating; 2) structural components subjected to laser heating; and 3) aerodynamic vehicles in hypersonic flight. The structural materials utilized in these applications may be metallic superalloys, metal matrix composites, or even ceramic composites. All of these materials undergo substantial material inelasticity at elevated temperatures. In order to accurately predict the thermomechanical response of structural components composed of these materials, it is imperative to develop accurate constitutive models capable of accounting for material nonlinearity in the presence of cyclic load and transient temperature conditions. These models must be capable of accurately accounting for temperature and history dependent constitutive properties, as well as two-way thermomechanical coupling via modified heat conduction equations which are material specific. In addition, these media may undergo extremely rapid heating rates due to the presence of large external heat sources. Although models are currently available for some of these materials at elevated temperature, little has been done to extend these theories to transient temperature conditions such as those encountered in the three examples cited above.

The general objective of this research is to improve on existing theoretical models for predicting the response of inelastic aerospace structural components subjected to hostile thermal environments with emphasis on transient temperature conditions, radiation boundary conditions, extremely rapid heating rates, and possible phase change of the materials involved. For materials subjected to the conditions under study herein it is necessary to perform extremely complex experiments in order to determine the precise form of the theoretical constitutive equations. Finally, it is necessary to implement the resulting equations to boundary value problem solving algorithms in order to model the response of structural components with stress, strain, and temperature gradient fields.

1.2 Statement of Work

Experimental and theoretical research were performed to characterize the response of structural components subjected to transient temperature conditions resulting in inelastic material behavior. The research was performed in the following stages:

- 1) theoretical development of thermodynamic constraints on inelastic materials under transient temperature conditions;

- 2) development of modified heat conduction equations to account for two-way thermomechanical coupling in these inelastic materials;
- 3) experimentation to determine further constraints on inelastic materials under transient temperature conditions;
- 4) development of multi-dimensional theoretical algorithms for predicting response of the inelastic structural components described above; and
- 5) experimentation to verify the theoretical algorithms described in item 4).

Items 1) through 4) above were performed entirely on the main campus at Texas A&M University. Item 5) was performed both at the Air Force Wright Aeronautics Laboratory at Wright Patterson Air Force Base and Texas A&M University. Details of this research will be described further below.

RESEARCH COMPLETED

2.1 Summary of Completed Research

The results of the three year program are as summarized below:

- 1) a one-way coupled model was developed for the thermoviscoplastic plate subjected to rapid laser heating (see references 1 and 2);
- 2) thermodynamic constraints were developed for the thermoviscoplastic medium studied herein (see reference 2);
- 3) a two-way coupled model was also developed for the thermoviscoplastic plate subjected to rapid laser heating (see Appendix 7.1);
- 4) a thermoviscoplastic constitutive model was developed for short fiber composites (see Appendix 7.2);
- 5) a model for determining the effects of certain forming processes on short fiber composites was constructed (see Appendix 7.3);
- 6) constitutive testing and model development were performed to determine the thermoviscoplastic constitutive behavior of Hastelloy X (see Appendix 7.4); and
- 7) structural tests were performed on Hastelloy X plates in the LHMEI laboratory at WPAFB (see reference 2).

Items 1,2 and 7 above have been previously documented in the first and second annual reports [1,2]. Items 3 through 6 are detailed in the Appendix of this report. These items are summarized in the following sections.

2.2 Theoretical Developments

Theoretical results obtained during the course of the contract are discussed below.

2.2.1 One-Way Coupled Model

A solution algorithm has been developed by the authors for modeling the transient response of a thin metallic plate with viscoplastic constitution subjected to rapid external heating. The model assumes one-way coupling in the sense that the heat transfer solution is assumed to be independent of deformations, whereas the mechanical response depends on the temperature field. In addition to radiation boundary conditions and material inelasticity, geometric nonlinearity has been included. A nonlinear incremental formulation for an anisotropic plate has been developed using variational methods and finite element discretization. The algorithm utilizes constitutive models for viscoplastic media previously proposed by Bodner and Partom [3] and Walker [4]. The model results are briefly reviewed in this section. Further details can be found in references 1 and 2.

The solution algorithm is constructed in two stages: the thermal analysis and the structural analysis. The general flowchart is shown in Fig. 1. On a given time step, the thermal loads are evaluated. Then the temperature field is solved by the finite element method. Together with the inelastic strain increment evaluated from the previous time step, the thermal strain results in an unbalanced load with which the deformation is approximated. Iteration will bring the solution to equilibrium for a given time step. Due to the induced high in-plane stresses, it is necessary to update the effective stiffness matrix in the iterative procedure.

To demonstrate the use of this model, an isotropic circular plate with fixed plate boundary and radius $r=10$ in is selected. The material used is B1900+Hf, which is a nickel-based superalloy commonly used in hot gas turbines. The plate is subjected to an instantaneous constant heat input applied axisymmetrically about the center of the plate with radius 0.5 in. The thermal boundary conditions are radiation type with reference temperature $T_R=0^\circ\text{F}$. The finite element mesh diagrams for the thermal and structural analyses are shown in Fig. 2.

Figure 3 shows the history of plate center deflection for cases with and without geometric nonlinearity. Considering the in-plane stresses, the transverse deflection is significantly decreased, which demonstrates the importance of including geometric nonlinearity in this model. Figures 4 through 8 are the results for cases which include geometric effects and the viscoplasticity models. Figure 4 shows the deflection history of the plate center. When the

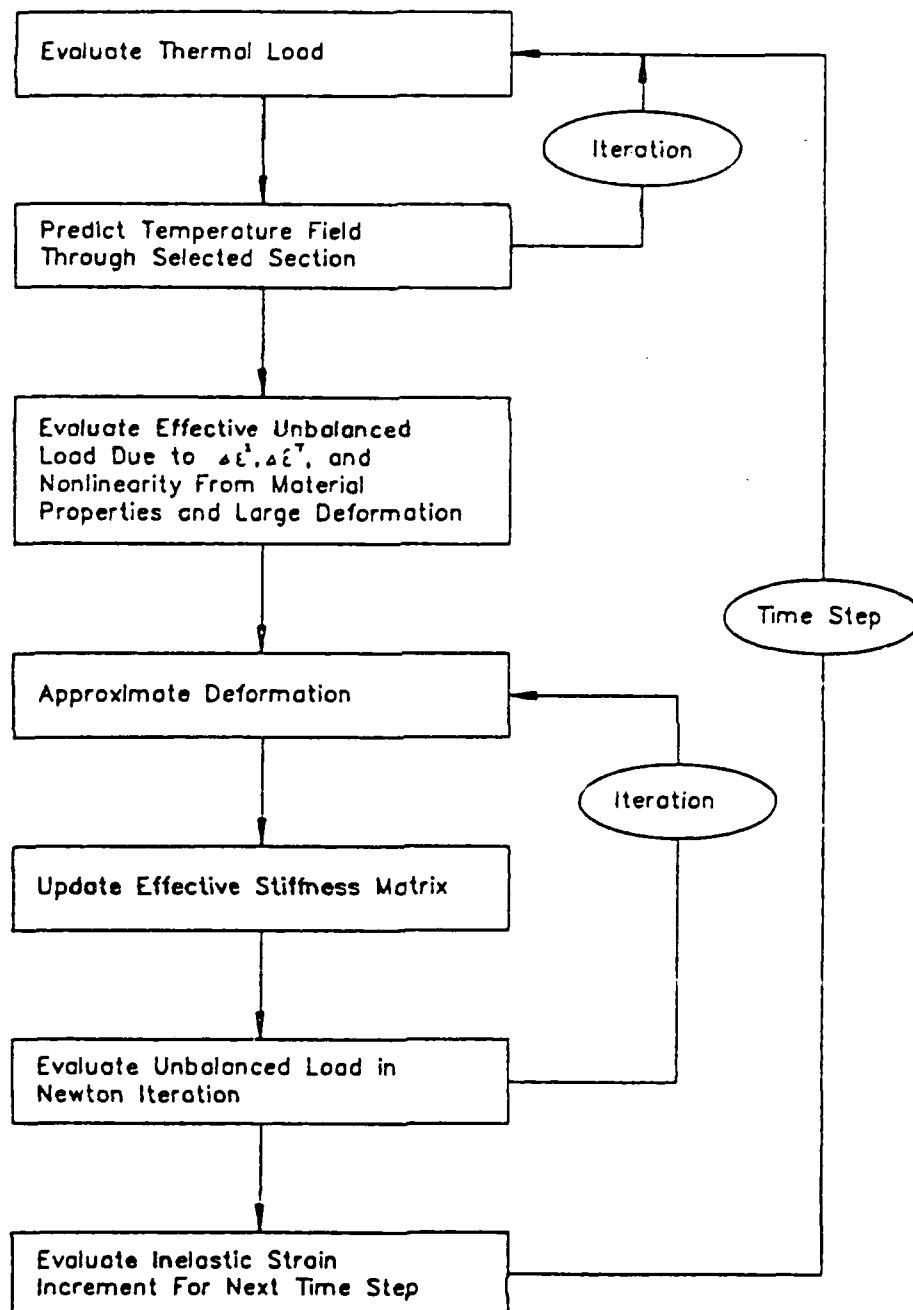


Fig.1 Flowchart of Solution Algorithm

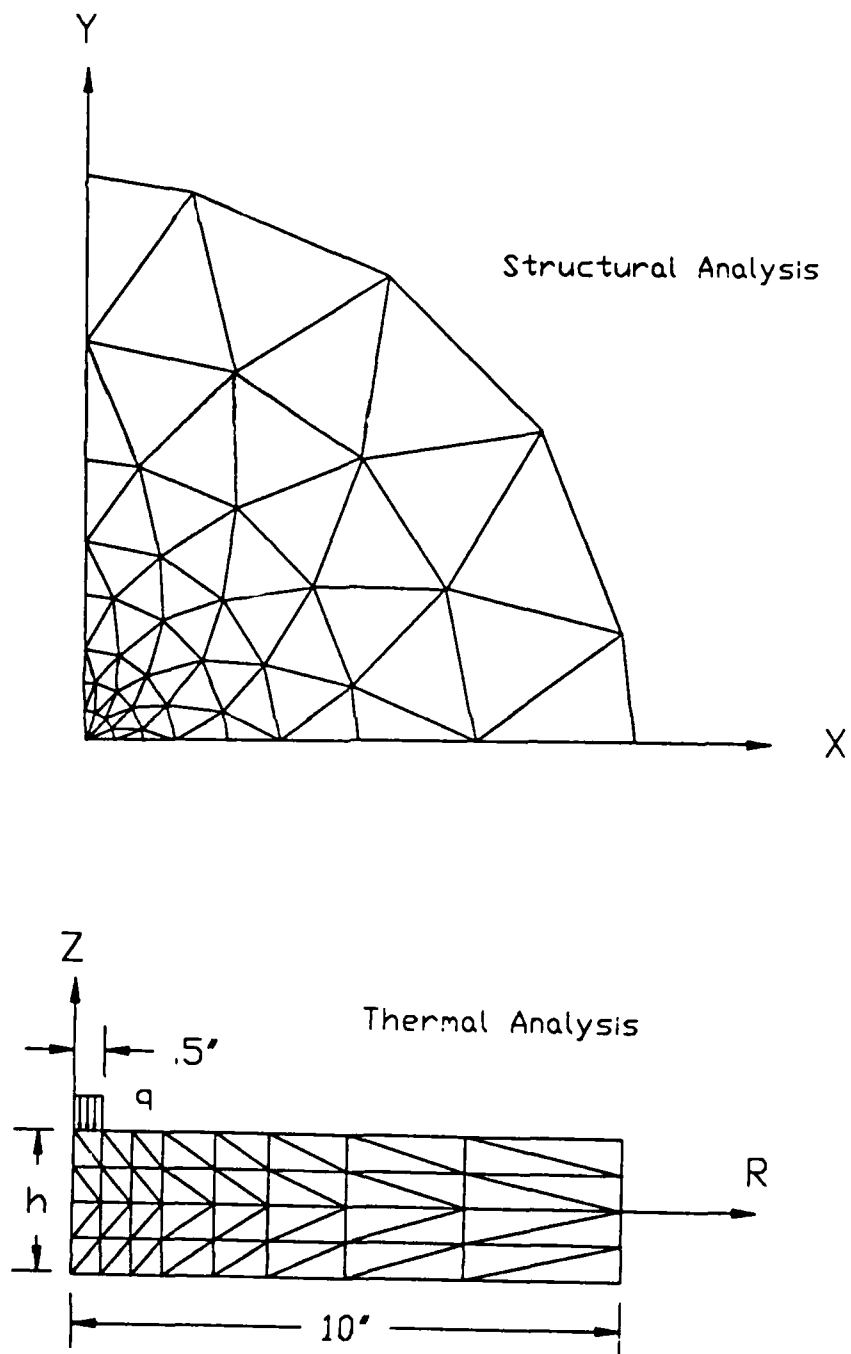


Fig.2 Mesh Diagram of Thermal & Structural Analysis.

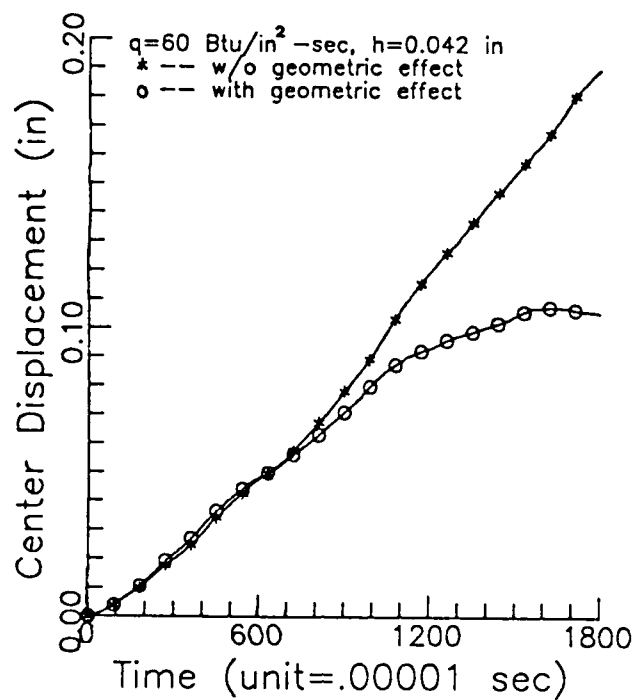


Fig.3 Center Displacement History.

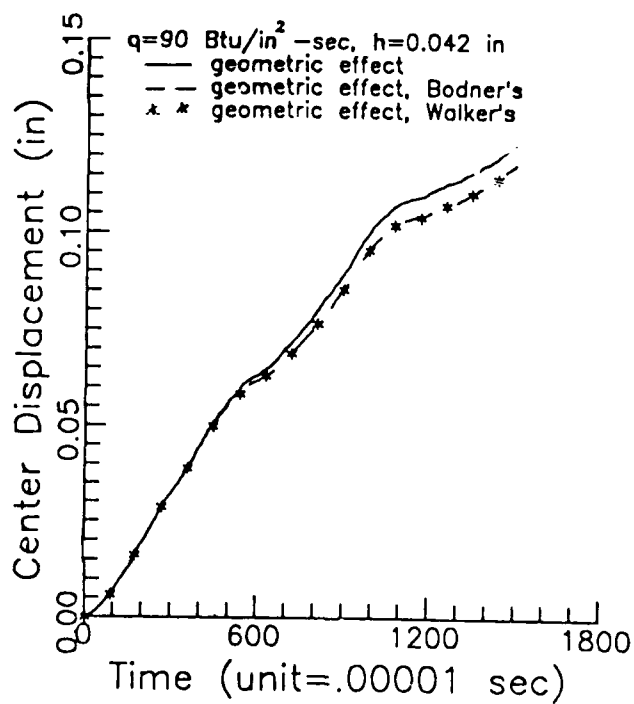


Fig.4 Center Displacement History.

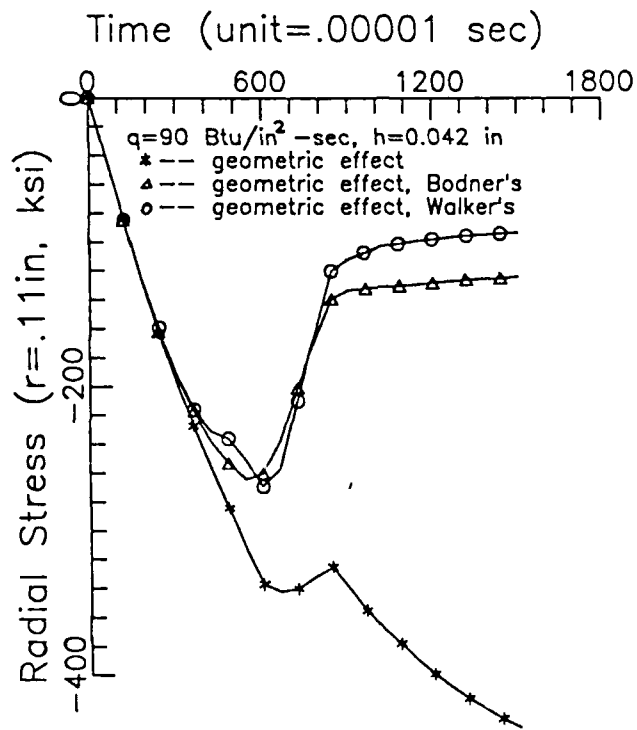


Fig.5 Radial Stress History at $r=0.11 \text{ in}$.

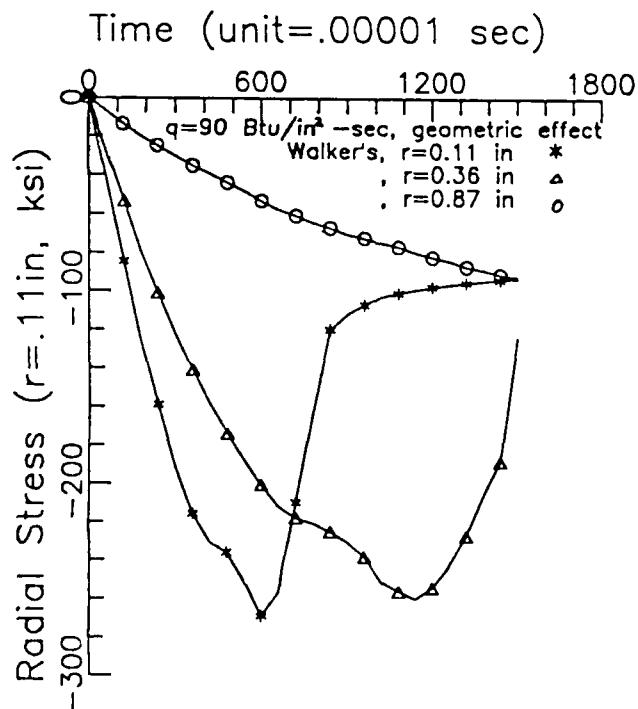


Fig.6 Radial Stress History at Various Positions.

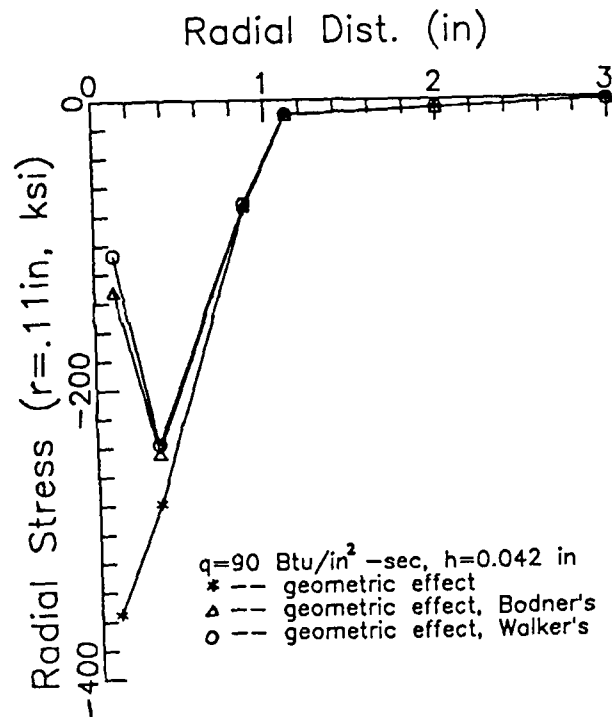


Fig.7 Radial Stress Distribution at time=0.01 sec.

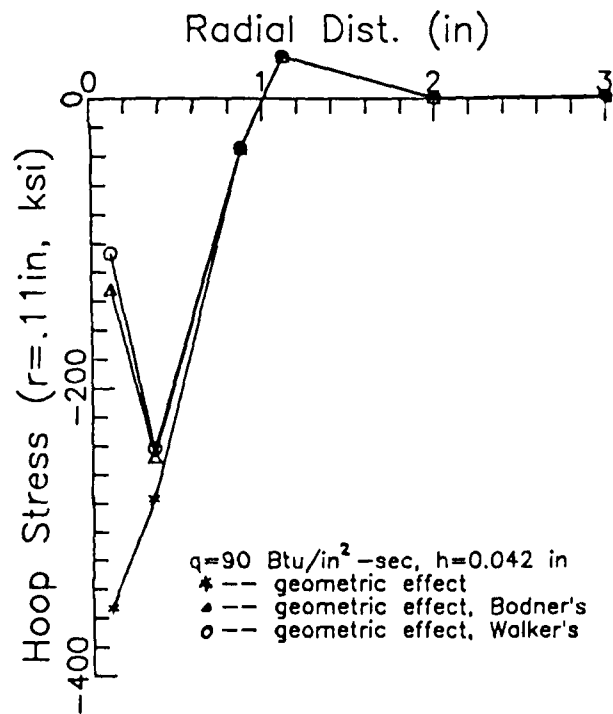


Fig.8 Hoop Stress Distribution at time=0.01 sec.

inelastic material response is considered, the deflection of the plate upper surface is reduced. Figure 5 shows the stress history at $r=0.11$ in of the plate upper surface. The stress is significantly reduced by the accumulated inelastic strain. Figure 6 shows the radial stress history predicted by Walker's model at various positions of the plate upper surface. Figures 7 and 8 show the radial stress and hoop stress distribution at time $t=0.01$ sec. Figure 9 shows the in-plane deformation and Fig. 10 shows the accumulated inelastic strain at time $t=0.01$ sec. Walker's model tends to accumulate more inelastic response than Bodner and Partom's, which in turn predicts lower stresses.

Figures 11 through 13 show the results for plates with varying thickness and identical external heating. Figure 11 shows the radial stress at $r=0.11$ in of the plate upper surface for various plate thicknesses. Figure 13 shows the accumulated inelastic strain at time $t=0.01$ sec for varying plate thickness. Figures 14 through 16 show the results for a plate with fixed thickness and various external heating rates. Figure 14 shows that with greater external heating, larger deflection is predicted. Figure 15 shows the stress history at $r=0.11$ in. Higher compressive peak stress is induced and more inelastic strain is accumulated with greater external heating. Figure 16 shows the stress distribution at time $t=0.01$ sec for different external heating rates. Further details about the one-way coupled model can be found in references 1 and 2.

2.2.2 Two-Way Coupled Model

Whereas the one-way coupled model assumes that the strains do not affect the temperature, the two-way coupled model assumes that this effect cannot be neglected. As shown in Appendix 7.5, the resulting heat conduction equation for an isotropic thermoviscoplastic medium is given by:

$$kT_{,ii} = \rho C_p \dot{T} + \rho \dot{r} + (3\lambda + 2\mu)\beta T_0 \dot{\epsilon}_{kk} - \eta \sigma_{ij} \dot{\epsilon}_{ij}^I \quad (1)$$

where the last term is due to inelastic coupling, and the term before it accounts for elastic coupling. These coupling terms introduce significant complexity into any solution procedure, since the heat transfer solution can no longer be solved a priori and substituted into the mechanical field equations. This procedure used herein was to first reduce the equations to the case of an axisymmetric continuum (not a plate), so that the governing equations are two-dimensional as described in Appendix 7.1. The governing equations were cast in a weak variational form and discretized using the finite element method. Solutions were obtained using four node quads. The computer code is available from the authors on request.

Several examples were solved for a circular plate similar to that studied in the previous section. The material was assumed to obey the Bodner-Partom viscoplasticity model [3]. As noted in the appendix, both mesh and time step were optimized to obtain converged results. All results were obtained for a plate of 10 cm radius with a laser spot of 2 cm radius centered at the plate center. The laser input was 2.5×10^4 Btu/m², with a duration of 0.02 sec. Results have been plotted for the in-plane and out-of-plane displacement components at the center of the plate

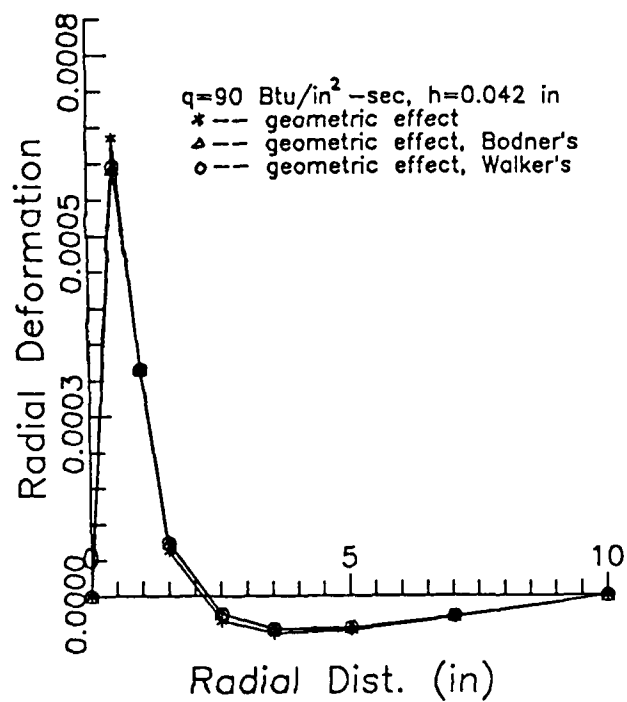


Fig.9 In-plane Deformation at time=0.01 sec.

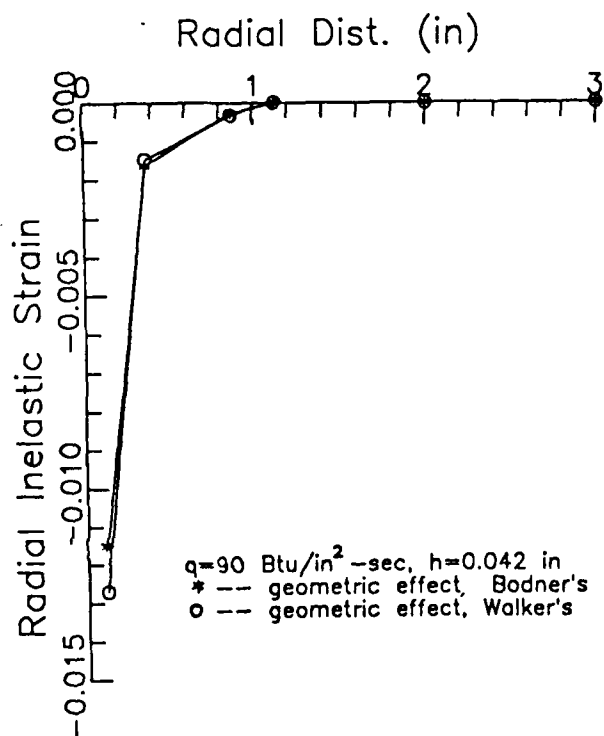


Fig.10 Radial Inelastic Strain Distribution at time=0.01 sec.

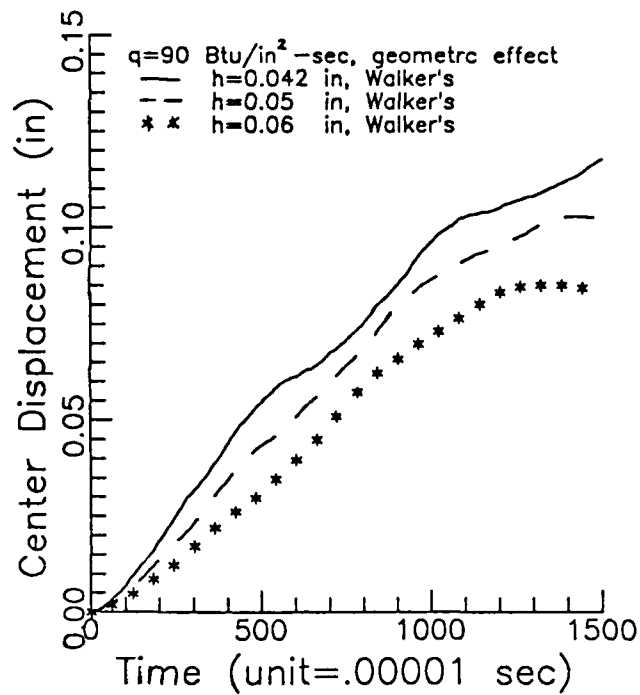


Fig.11 Center Displacement History.

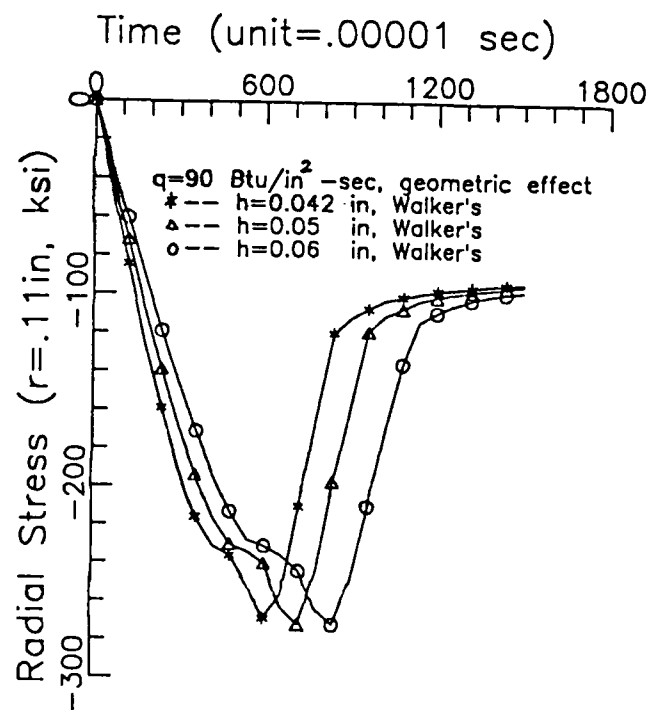


Fig.12 Radial Stress History at r=0.11 in.

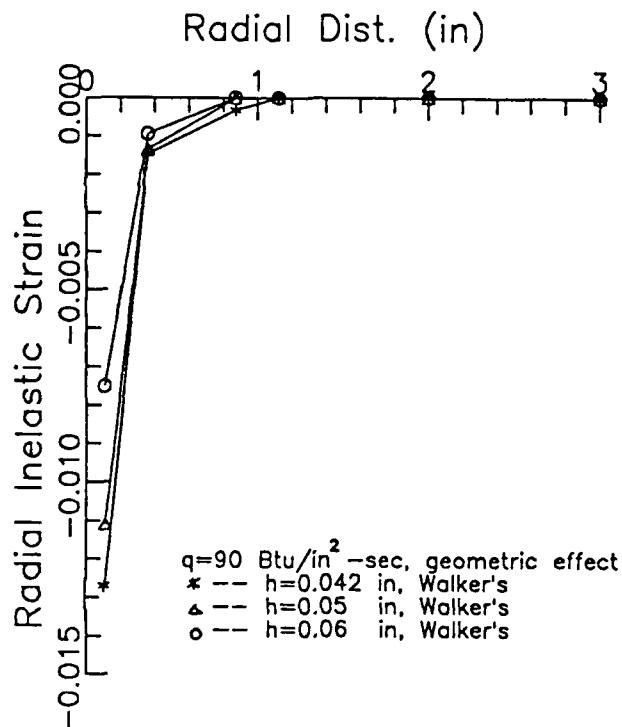


Fig.13 Radial Inelastic Strain Distribution at time=0.01 sec.

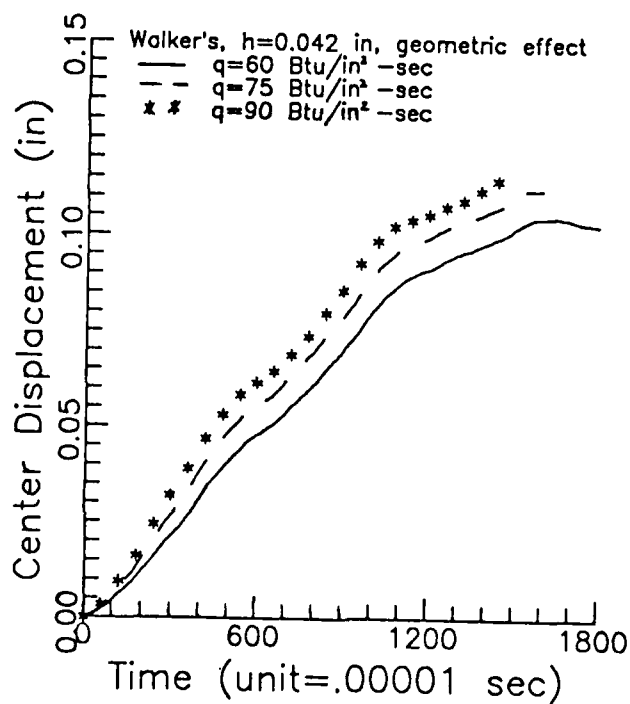


Fig.14 Center Displacement History.

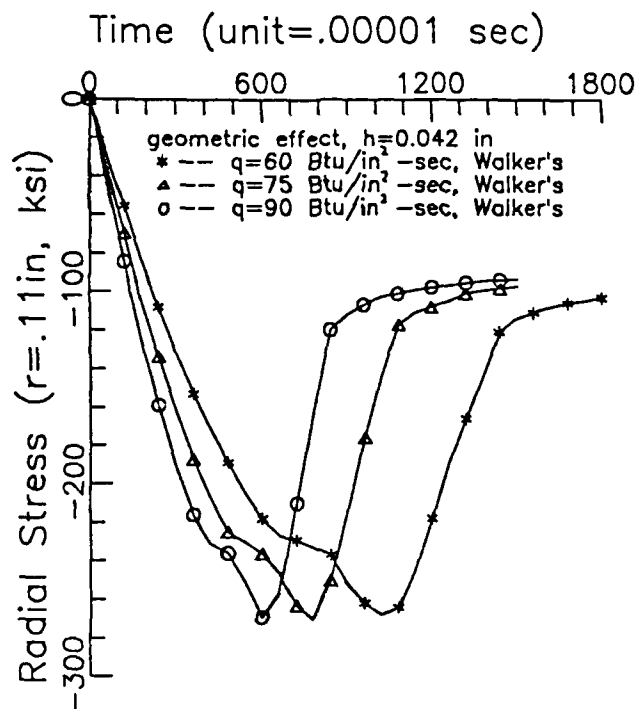


Fig.15 Radial Stress History at $r=0.11$ in.

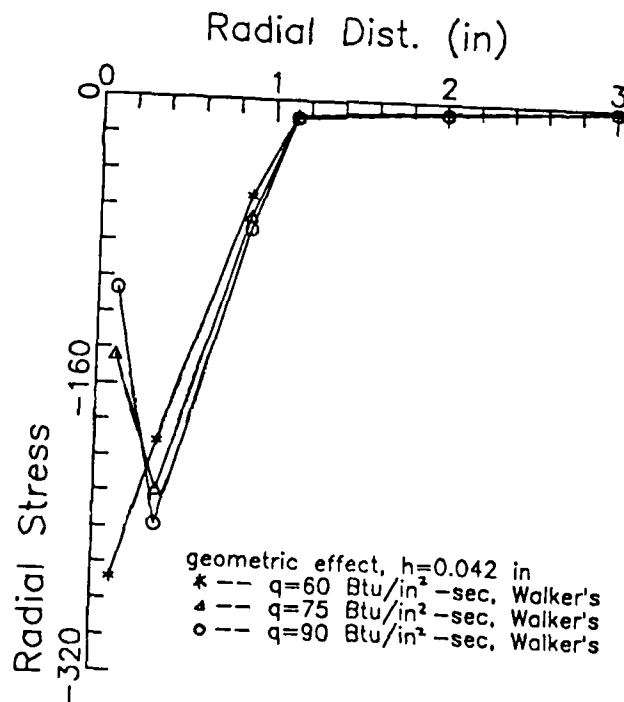


Fig.16 Radial Stress Distribution at time=0.01 sec.

as functions of time. The first result shows the results obtained assuming one-way coupling and thermoelastic material behavior (see Fig. 17). Note that the in-plane component oscillates at about 140 Hz, while the out-of-plane component responds much more slowly.

Fig. 18 compares one-way coupled predictions for the in-plane displacement at the plate center both with and without viscoplasticity included. Note that the inclusion of inelasticity causes effective damping which decreases the amplitude of vibration. Of course, the result is very similar to that obtained in the previous section, as should be expected.

In order to test the effect of the assumption that the heat input is instantaneous, the input was changed to a linear ramp over the first 20 msec, then constant for 80 msec, and then abruptly turned off. as shown in Fig. 19, the results are quite different from the instantaneous results, with the in-plane displacement oscillating at a much slower frequency until the heat source is turned off. Thereafter, a higher frequency response is observed, similar to the results for the instantaneous input solutions. Note that the residual oscillations are centered about a non-zero (compressive) mean, indicating the presence of a residual viscoplastic deformation.

The final result is for the case where full two-way coupling is assumed. As shown in Fig. 20, the results for the one-way and two-way analyses coupled analysis are almost indistinguishable. We attempted without success to induce more substantial differences by sweeping over the input variables. In all cases the differences were insignificant. At this point in time we feel that this is due to the fact that the viscoplastic response is restricted to a very small zone near the plate center and is essentially nonoscillatory in nature. It is our belief that significant two-way coupling could only be introduced by oscillating the heat input, thus producing oscillatory inelastic deformations which would result in more substantial hysteresis.

The following is a summary of the results which we have observed after solving the three-dimensional, axisymmetric, fully coupled, thermoviscoplastic equations for a laser heated thin plate.

1. If the heat impulse is of sufficiently short duration, and very localized near the center of the plate, the fundamental response is that of an elastic plate under a point load. This is true under both stress-free and clamped boundary conditions.
2. If the heat impulse is ramped, a slow oscillation about a deformed state (which would be given by constant thermal input) is observed. After the heat source is turned off, a complicated return to a permanently deformed state is observed.
3. The inclusion of inelastic effects in the momentum equations accounts for about a 5-10% change in out-of-plane displacements.
4. The inclusion of inelastic two-way coupling affects the out-of-plane displacements very little (less than 2% observed change).

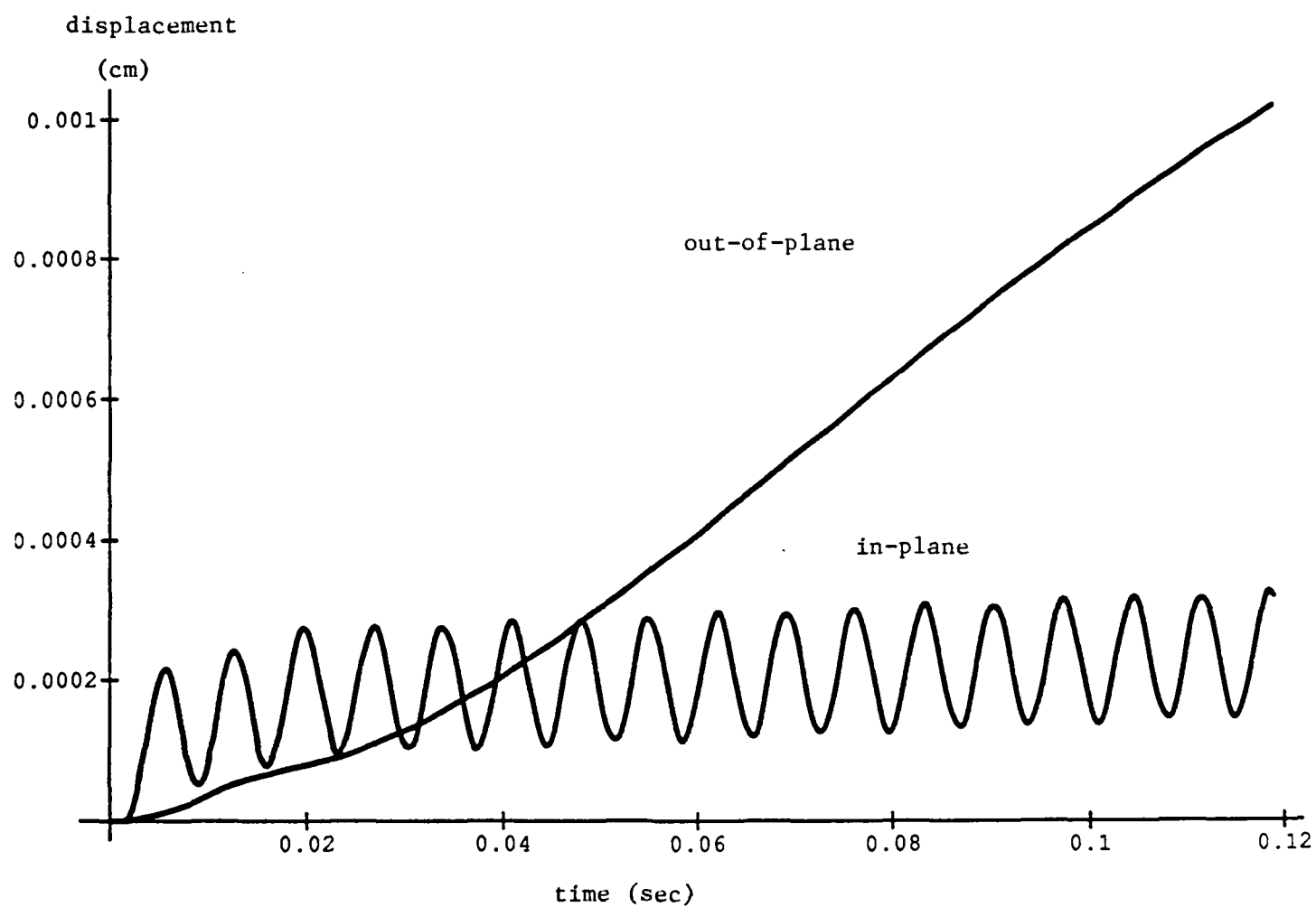


Fig. 17 Predicted Displacements at the Plate Center
Assuming One-Way Coupling and Thermoelastic
Material Behavior

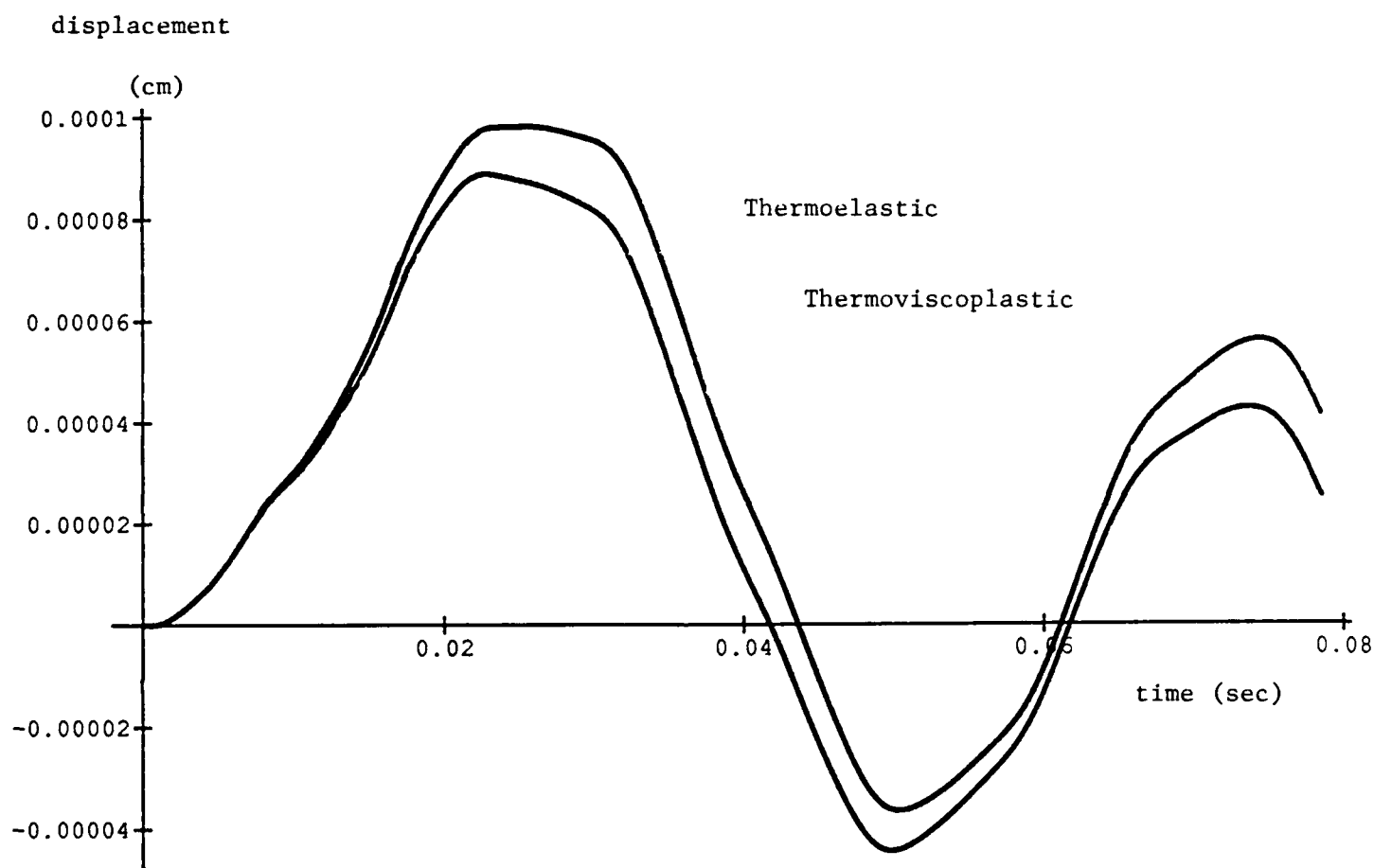


Fig. 18 Comparison of Thermoelastic and Thermoviscoplastic Predictions for In-Plane Displacement Component at the Plate Center

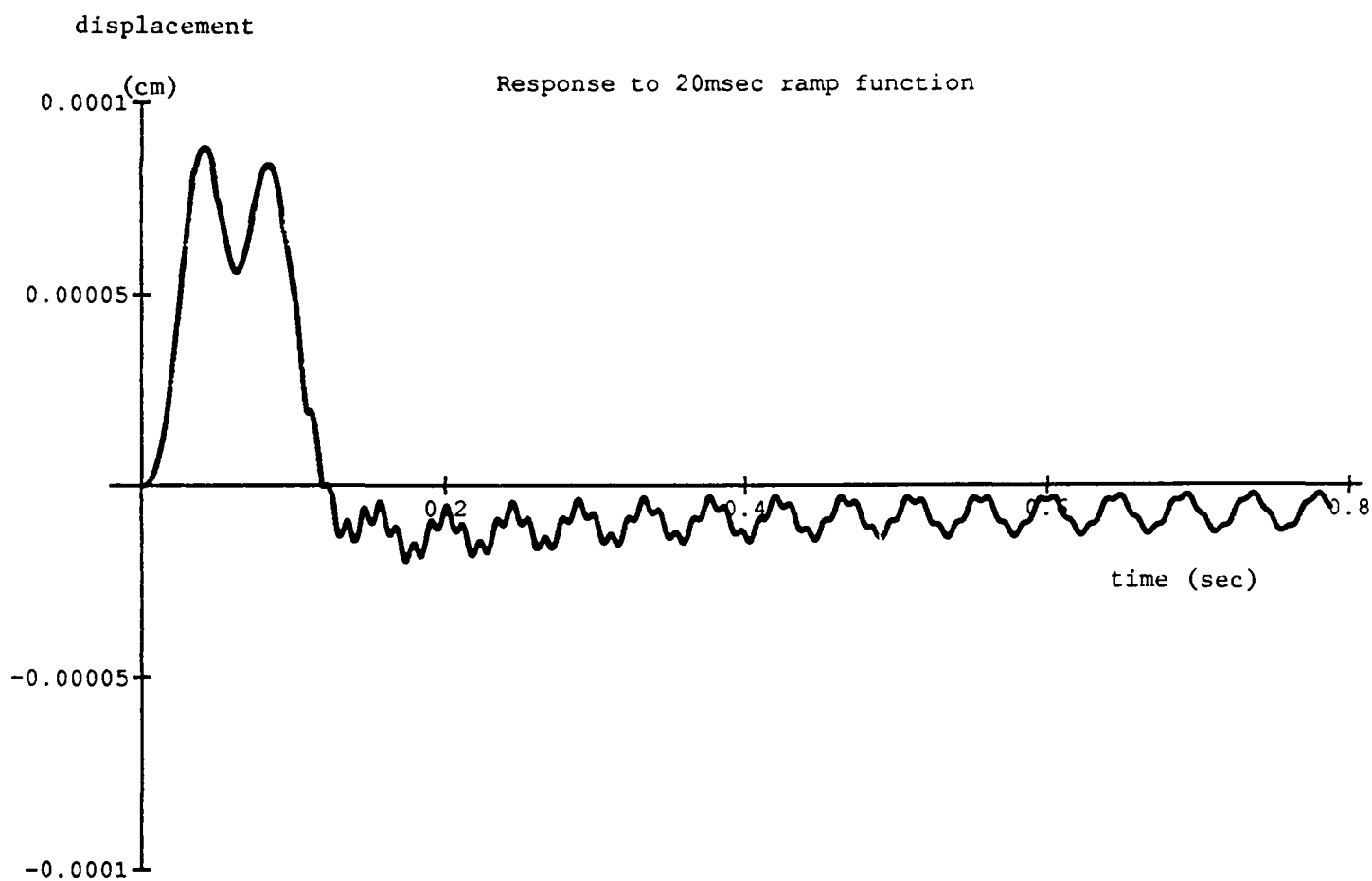


Fig. 19 In-Plane Displacement at the Plate Center
for a Ramp Heat Input

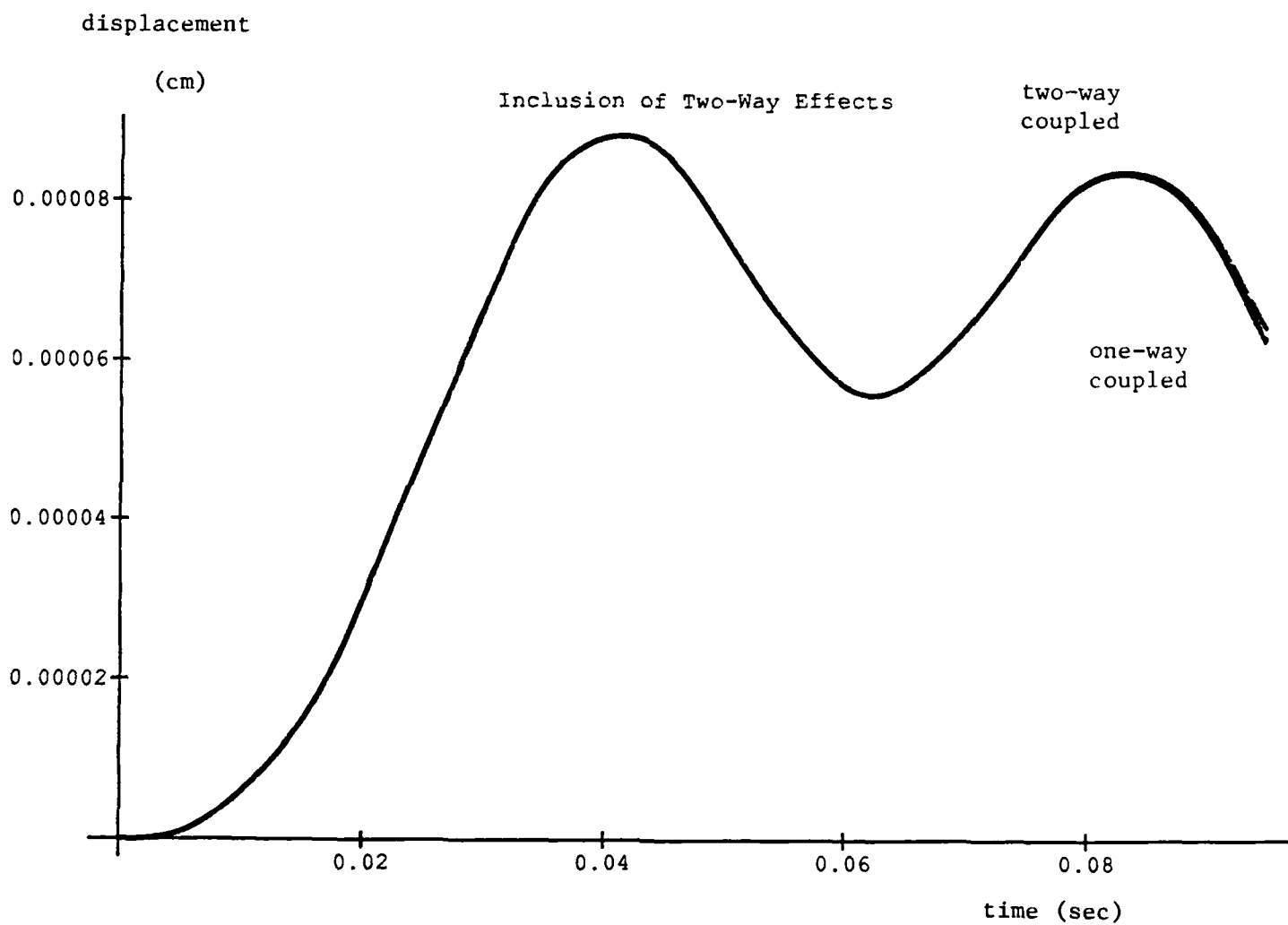


Fig. 20 Comparison of One-Way Coupled and Two-Way Coupled Results for In-Plane Displacement at Plate Center

5. Relatively large grids may be used away from the boundary thermal input. The time step limitation is primarily due to the rapid thermal heating characteristic time.
6. The following appears to be the approximate ranking of effects in the boundary heated, no external loading, axisymmetric plate problem:
 - a) Boundary heating, temperature response can approach 100 degrees Kelvin/sec or more. The induced thermal stresses and strains.
 - b) Inelastic corrections to the deformations, and the resultant change in stress.
 - c) Two-way thermoelastic coupling.
 - d) Two-way thermoinelastic coupling. This effect is extremely localized.

Further details about this portion of the research can be found in Appendix 7.1.

2.2.3 Damage Dependent Constitutive Model for Metal Matrix Composites

The thermoviscoplastic model developed in the previous sections was intended also for use with short fiber metal matrix composites. Therefore, it was necessary to develop a composite constitutive model which accounts for inelasticity in the matrix. This was accomplished by applying the equivalent inclusion method in conjunction with the Mori-Tanaka method, as described in detail in Appendix 7.3. The inclusion was assumed to be linear elastic, and the matrix was assumed to be viscoplastic, according to Miller's model [5].

In order to extend Benveniste's [6] reinterpretation of the elastic version of the Mori-Tanaka [7] method to viscoplasticity, we relate a history of the two phase self-consistent scheme. The use of the self-consistent method to predict the "effective", or overall composite stiffness of elastic-plastic matrices reinforced with elastic inhomogeneities has evolved along two paths - the "equivalent inclusion method" and the "direct approach." For comprehensive reviews, see Mura [8] and Hashin [9], respectively. As originally formulated by Eshelby [10] for dilute concentrations of inhomogeneities, the equivalent inclusion method makes use of the following "equivalency condition."

$$C_{ijkl}^i (\epsilon_{kl}^o + \epsilon_{kl} + \epsilon_{kl}^p) = C_{ijkl}^m (\epsilon_{kl}^m + \epsilon_{kl}^o + \epsilon_{kl}^p - \epsilon_{kl}^*) \quad (2)$$

The reader should note that in the above equation and in the remainder of the paper superscripts denote a qualitative description of the associated variables, whereas subscripts represent tensorial components. Thus, in (2) C_{ijkl}^i and C_{ijkl}^m denote the elastic stiffness of the inhomogeneity

and matrix, respectively, ϵ_{kl}^o is the far-field strain, ϵ_{kl} is the strain in the inhomogeneity, ϵ_{kl}^p is the matrix plastic strain, and ϵ_{kl}^* is the "equivalent transformation strain," or "eigenstrain." Eshelby's principal result was that uniform strain fields are produced in an ellipsoidal inhomogeneity embedded in an infinite matrix under uniform strain ϵ_{kl}^o and uniform plastic strain ϵ_{kl}^p . The method was subsequently extended by Mori and Tanaka [7] by including a "back stress" analysis which accounts for the mutual interaction between inhomogeneities. Composite elastic and plastic hardening moduli were obtained from energy principles. The Mori-Tanaka back stress analysis has, in turn, been extended by Taya and Chou [11] to include two types of inhomogeneities.

As pointed out by Hill [12] in his self-consistent analysis of polycrystalline plasticity, the matrix instantaneous stiffness rather than the elastic stiffness, should be used in the solution of the "auxiliary problem" of a single grain embedded in an elastic-plastic matrix. Following this recommendation, Tandon and Weng [13] corrected the Mori-Tanaka method by replacing the elastic stiffness C_{ijkl}^m in equation (2) with the instantaneous stiffness L_{ijkl}^m and removing the plastic strain ϵ_{kl}^p from the equation. The resulting equivalency condition in the incremental form is

$$C_{ijkl}^i (d\epsilon_{kl}^o + d\tilde{\epsilon}_{kl} + d\epsilon_{kl}) = L_{ijkl}^m (d\epsilon_{kl}^o + d\tilde{\epsilon}_{kl} + d\epsilon_{kl} - d\epsilon_{kl}^*) \quad (3)$$

where $d\tilde{\epsilon}_{kl}$ is the increment of the Mori-Tanaka "back strain." We note that the Mori-Tanaka formulation for an elastic matrix is recovered if the instantaneous stiffness L_{ijkl}^m is replaced by the elastic stiffness C_{ijkl}^m .

Following Hill [14], we write the "direct approach" to the composite elastic stiffness C_{ijkl} as

$$C_{ijkl} = C_{ijkl}^m + c \langle (C_{ijmn}^i - C_{ijmn}^m) A_{mnkl} \rangle \quad (4)$$

where c is the reinforcement volume fraction and the brackets denote the orientation average. The composite elastic stiffness can be obtained following the determination of the orientation dependent "strain concentration factor", A_{ijkl} , which gives the average inhomogeneity strain in terms of the uniform composite strain. The determination of A_{ijkl} is the essential difficulty in the micromechanics method. For dilute concentrations of inhomogeneities, the tensor

$A_{ijkl}^{dil} = T_{ijkl}$ can be obtained from Eshelby [10] as

$$T_{ijkl} = [I_{ijkl} + S_{ijmn}(C_{mnop}^m)^{-1}(C_{opkl}^i - C_{opkl}^m)]^{-1} \quad (5)$$

where S_{ijmn} is the Eshelby tensor, and I_{ijkl} is the identity tensor. For a non-dilute concentration of inhomogeneities, the strain concentration tensor should be derived in a manner which takes into account the particle interaction. Hill [15] obtained such a concentration tensor in his "direct approach" to the self-consistent scheme for two-phase composites.

The Eshelby tensor is a function of the particle aspect ratios and the instantaneous matrix stiffness. Mura [8] has given single integral equations for the Eshelby tensor corresponding to the case of a transversely isotropic matrix with its crystalline directions coincident with the principal directions of a spheroidal inhomogeneity of any aspect ratio. For the case of a generally orthotropic matrix containing spherical inhomogeneities, Morris [16] has given double integrals for the Eshelby tensor.

In order to use Mura's integrals for the Eshelby tensor, the inhomogeneities are assumed to be aligned in the x_3 axis. This condition is not overly restrictive, as it allows for the application of hydrostatic pressure and combined tension/torsion, and triaxial stress states in which $\dot{\sigma}_{11} = \dot{\sigma}_{22}$, $\dot{\sigma}_{33} \neq 0$.

Recently, Benveniste [6] made the remarkable observation that the non-dilute strain concentration tensor could be obtained from a reexamination of the elastic Mori-Tanaka method in terms of equations (4) and (5). Benveniste et al. [6] subsequently extended the analysis to predict the effective elastic stiffness of composites with two types of inhomogeneities. Recall from equation (3) that the elastic-plastic form of the Mori-Tanaka method is obtained by replacing the matrix elastic stiffness with the instantaneous stiffness. Therefore, the elastic-

plastic form of the Benveniste et al. [6] method can be written in terms of instantaneous stiffness L_{ijkl}^m

Under an applied uniform strain rate $\dot{\epsilon}_{ij}^0$, the composite instantaneous tangent stiffness L_{ijkl} is given as

$$L_{ijkl} = [\sum_r c^r L_{ijmn}^r T_{mnop}^r] [\sum_r c^r T_{opkl}^r]^{-1} \quad (6)$$

where $r = 1$ denotes the first particle type,
 $r = 2$ denotes the second particle type, and
 $r = m$ denotes the matrix phase.

The average phase strain rates are given by

$$\dot{\epsilon}_{ij}^r = A_{ijkl}^r \dot{\epsilon}_{kl}^0 \quad r=1,2,\dots,m \quad (7)$$

or

$$\dot{\epsilon}_{ij}^r = T_{ijkl}^r \dot{\epsilon}_{kl}^m \quad r=1,2 \quad (8)$$

where the matrix strain rate is written in terms of the applied strain rate $\dot{\epsilon}_{ij}^0$ as

$$\dot{\epsilon}_{ij}^m = [\sum_r c^r T_{ijkl}^r]^{-1} \dot{\epsilon}_{kl}^0 \quad r = 1,2,\dots,m \quad (9)$$

The dilute strain concentration tensors T_{ijkl}^r are given in the form

$$T_{ijkl}^r = [I_{ijkl} + S_{ijmn}^r (L_{mnop}^m)^{-1} (L_{opst}^r - L_{opst}^m)]^{-1}, \quad r=1,2 \quad (10)$$

$$T_{ijkl}^m = I_{ijkl} \quad (11)$$

where the fourth-order unit tensor is defined by

$$I_{ijkl} = \frac{1}{2}(\delta_{ik}\delta_{jl} + \delta_{il}\delta_{jk}) \quad (12)$$

Similarly, under an applied traction giving rise to a uniform stress rate $\dot{\sigma}_{ij}^o$ the composite instantaneous compliance $M_{ijkl} (=L_{ijkl}^{-1})$ is given as

$$M_{ijkl} = [\sum_r c^r M_{ijmn}^r W_{mnop}^r] [\sum_r c^r W_{opkl}^r]^{-1}, \quad r=1,2,\dots,m \quad (13)$$

with

$$\dot{\sigma}_{ij}^r = B_{ijkl}^r \dot{\sigma}_{kl}^o, \quad r=1,2,\dots,m \quad (14)$$

or

$$\dot{\sigma}_{ij}^r = W_{ijkl}^r \dot{\sigma}_{kl}^m, \quad r=1,2 \quad (15)$$

where the matrix stress rate is written in terms of the applied stress rate $\dot{\sigma}_{ij}^o$ as

$$\dot{\sigma}_{ij}^m = [\sum_r c^r W_{ijkl}^r]^{-1} \dot{\sigma}_{kl}^o, \quad r=1,2,\dots,m \quad (16)$$

The dilute stress concentration tensors are

$$W_{ijkl}^r = L_{ijmn}^r T_{mnop}^r M_{opkl}^m, \quad r=1,2,m \quad (17)$$

Substitution of equations (9) into (14) results in

$$W_{ijkl}^m = I_{ijkl} \quad (18)$$

For a given composite stress rate $\dot{\sigma}_{ij}^o$ the composite total strain rate $\dot{\epsilon}_{ij}^o$ follows from the composite compliance M_{ijkl} , equation (13). The micromechanics leading to M_{ijkl} is

based on the fact that the composite total strain rate is equal to the volume average of the phase total strain rates. As pointed out by Hill [17] the elastic and inelastic components of the composite total strain rate are not direct averages of their microscopic counterparts when the composite stress rate, $\dot{\sigma}_{ij}^o$ maintains inelastic flow in an elastically heterogeneous medium.

The composite inelastic strain is typically obtained from an elastic unloading. Because the unified equations do not allow for regions of purely elastic deformation we will consider only imaginary "instantaneous" elastic unloading. In other words, we assume that during the infinitesimal period of unloading static recovery has insufficient time to induce inelastic flow. With this assumption, we associate with each real state an imaginary elastic state of zero applied stress. The composite inelastic strain rate is then given by

$$\dot{\epsilon}_{ij}^{oI} = [M_{ijkl} - (C_{ijkl})^{-1}] \dot{\sigma}_{kl}^o \quad (19)$$

However, the composite inelastic strain rate may be obtained without calculation the composite compliance. Suquet [18] has given the composite inelastic strain as the volume average of the product of the phase stress concentration factors and the phase inelastic strains. When inelastic flow occurs only in the matrix the result is simply

$$\dot{\epsilon}_{ij}^{oI} = c^m B_{ijkl}^m \dot{\epsilon}_{kl}^{mI} \quad (20)$$

The proof follows from the decomposition of strain and the equivalence of micro and macro virtual power, also known as Hill's Macrohomogeneity Equality.

The model accounts only for the particle volume fraction and not the individual particle sizes. We make the implicit assumption that the individual particles "see" a statistically homogeneous polycrystalline matrix. SiC whiskers of 1-2 μm diameter, however, are embedded within single grains. Walker and Jordan [19] have developed unified constitutive equations for single crystals. The inversion of a single crystal equation to the total strain form may be of limited utility, however, due to the presence of multiple corners on a single crystal SCISR. Fortunately, continuous fibers of 150 μm diameter may be at least one order of magnitude larger than the surrounding grains [Kim et al. [20]. But the Mori-Tanaka method may have limited applicability to typical continuous fiber reinforced metal matrix composites, which are often no more than eight plies thick. In this case, the fiber diameter is of the same order of magnitude as the composite thickness. The rigorous form of the micromechanics may not then reduce to the simple common form (see, for instance, Mori and Tanaka [7].

The model presented herein provides the mechanical equation of state for the composite and the growth law for the composite inelastic strain. The damage state is treated as known. The Mori-Tanaka method has been used [Taya [21]] to obtain the strain energy release rates for cracks in elastic composites. The concept of strain energy release rate is of limited

utility for bodies beyond general yield. Also, proportional macro-loading may result in non-proportional micro-loading. The J integral is therefore not useful for calculating microcrack strain energy release rates.

Although the model has not yet been utilized to predict stress-strain behavior, it has been utilized to predict initial yielding, as shown in Fig. 21. Further details about the model can be found in Appendix 7.3.

2.2.4 Effective Elastic Properties of Randomly Oriented Fiber Composites Due to Forming

One of the proposed tasks in the research program was to develop constitutive equations for metal matrix composites which could be used in the laser heating experiment. Although our ultimate intent was to produce a thermoviscoplastic constitutive model, we discovered that the initial elastic properties of chopped fiber composites were affected by the forming process. Therefore, we developed a model for predicting the initial elastic properties of the composite. The procedure utilizes the equivalent inclusion method, as described in detail in Appendix 7.2.

To see how this is accomplished, consider a single representative volume element of a composite material reinforced by continuous or discontinuous fibers, as illustrated in Figs. 22-a and 22-b, respectively.

It is clear that the above volume elements are transversely isotropic, thus five independent elastic moduli should be determined theoretically or experimentally for both cases. Since it is very cumbersome to solve an exact boundary value problem associated with the double cylinder model shown in Fig. 22, the authors utilize the equivalent inclusion method proposed by Taya, et al. [11,22]. For a continuous fiber composite, a number of theoretical solution schemes have been investigated for determining the five independent elastic moduli of the transversely isotropic volume element [23-26]. When the fiber length is very large compared to the fiber diameter, these solution schemes may be applied to a composite even with discontinuous fibers.

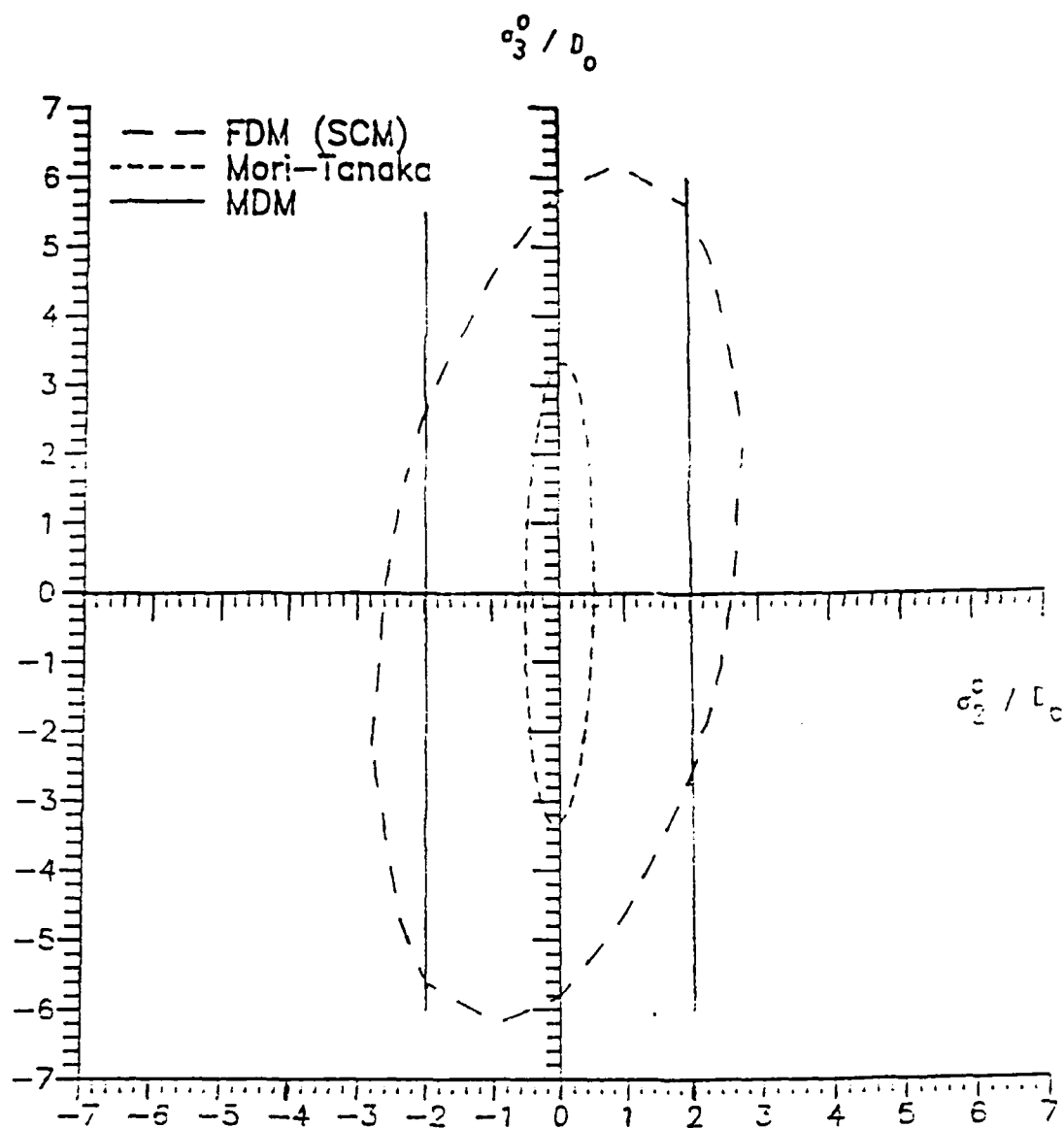


Fig. 21 Initial Yield Surfaces for 50% B/A1, Plane Stress

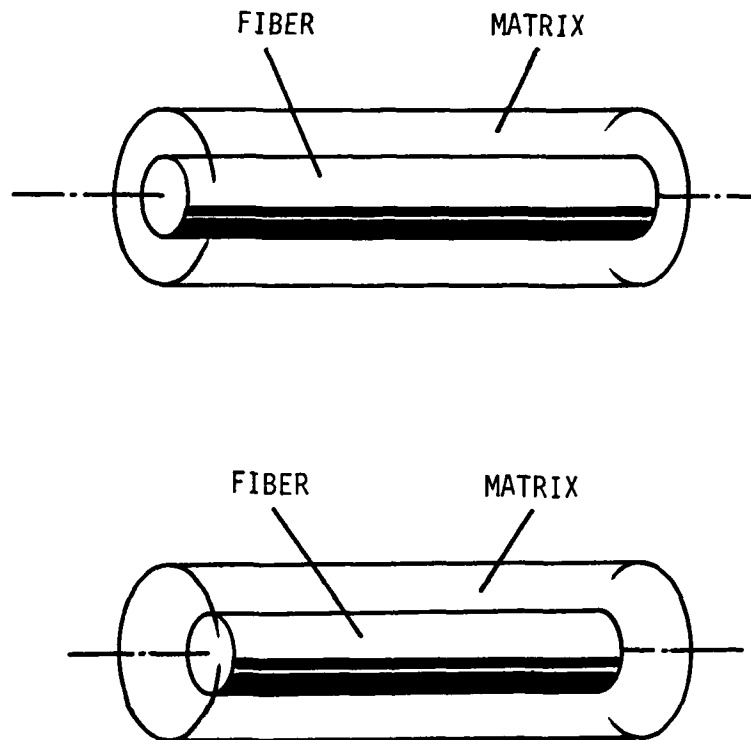


Fig. 22 Representative Volume Elements

(a) Continuous Fiber Element

(b) Discontinuous Fiber Element

For convenience, the composite elastic moduli of the volume element are assumed to be known. In matrix form, they can be written as

$$\begin{Bmatrix} \sigma_{11} \\ \sigma_{22} \\ \sigma_{33} \\ \sigma_{23} \\ \sigma_{31} \\ \sigma_{12} \end{Bmatrix} = \begin{bmatrix} C_{11} & C_{12} & C_{12} & 0 & 0 & 0 \\ C_{12} & C_{22} & C_{23} & 0 & 0 & 0 \\ C_{12} & C_{23} & C_{22} & 0 & 0 & 0 \\ 0 & 0 & 0 & (C_{22}-C_{23}) & 0 & 0 \\ 0 & 0 & 0 & 0 & 2C_{66} & 0 \\ 0 & 0 & 0 & 0 & 0 & 2C_{66} \end{bmatrix} \begin{Bmatrix} e_{11} \\ e_{22} \\ e_{33} \\ e_{23} \\ e_{31} \\ e_{12} \end{Bmatrix} \quad (21)$$

If a composite is initially isotropic, the reinforcing fibers do not have a preferred orientation. The probability density distribution for fiber orientation may be represented by a sphere in the three dimensional case. In the case where the fibers are distributed randomly in a single plane, the sphere degenerates to a circle. The degree of randomness of the volume element can be mathematically formulated for an initially isotropic short fiber composite after certain types of permanent deformation, such as hot pressing, extrusion, or rolling. When the composite is subjected to hot pressing or extrusion, the material becomes transversely isotropic. For example, a cube becomes a square plate or a cylinder becomes a circular disc, and vice versa. For an arbitrary thickness change and diameter change due to hot pressing and extrusion, respectively, an initially isotropic composite becomes transversely isotropic as illustrated in Fig. 23a and 23b. Alternatively, a forming process such as rolling causes orthotropic reorientation of fibers, in which one of the dimensional changes is negligibly small, as shown in Fig. 23c.

The present approach requires three assumptions:

1. Although the fibers after each of the material forming processes mentioned above may not be evenly distributed within the subdomain illustrated in Fig. 24, the fiber distribution density is assumed to be spatially homogeneous for mathematical simplicity.
2. The material forming processes mentioned herein are possible only through the plastic deformation of the matrix material. Plastic strain may not be spatially homogeneous in the matrix material due to stress concentrations near the reinforcing fibers. Also, it is well known that even an isotropic homogeneous material becomes transversely isotropic or orthotropic after the subject forming processes. This plasticity effect is neglected in the present study.
3. The material forming processes mentioned above may cause defects, such as broken fibers, fiber matrix debonding, etc. Furthermore, microvoids cannot be completely removed from the composite. The present study assumes a defect-free composite.

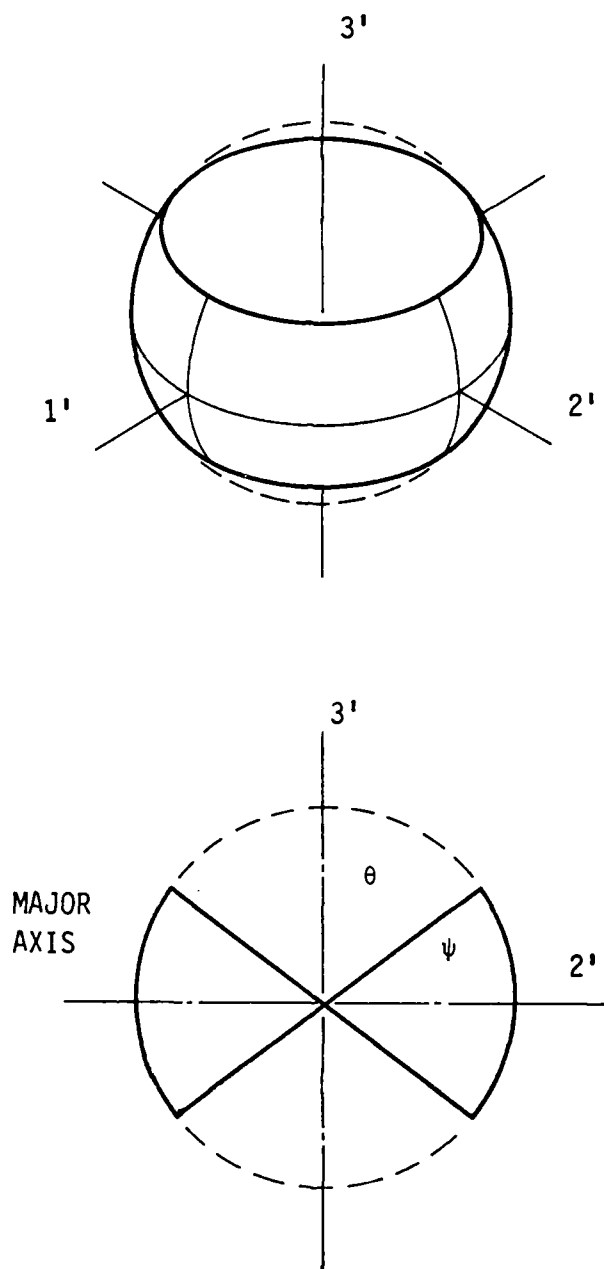


Fig. 23a Fiber Reorientation Due to Hot Pressing

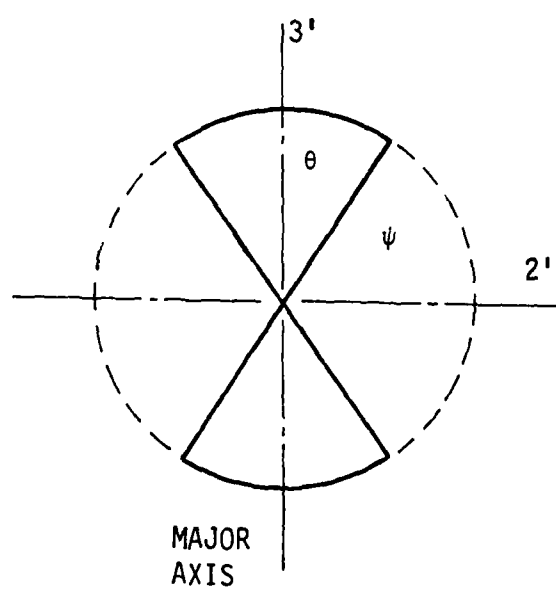
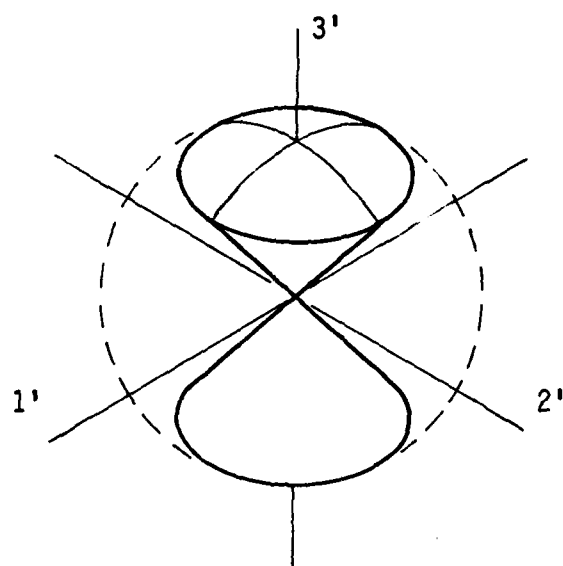


Fig. 23b Fiber Reorientation Due to Extrusion

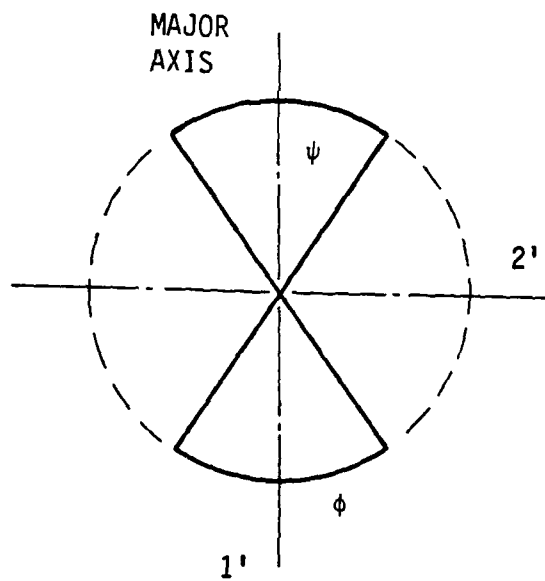
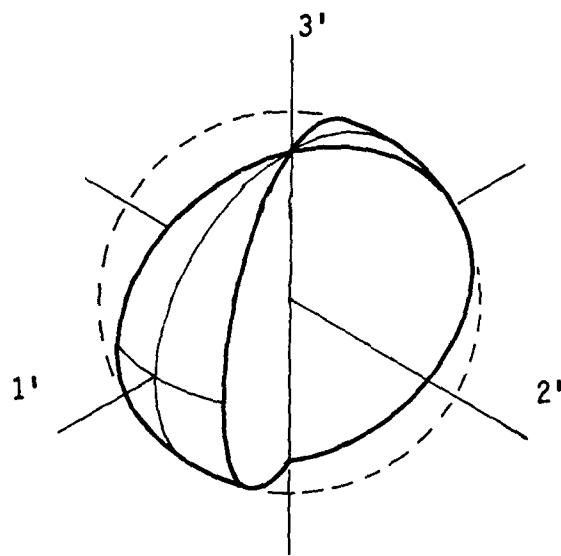


Fig. 23c Fiber Reorientation Due to Rolling

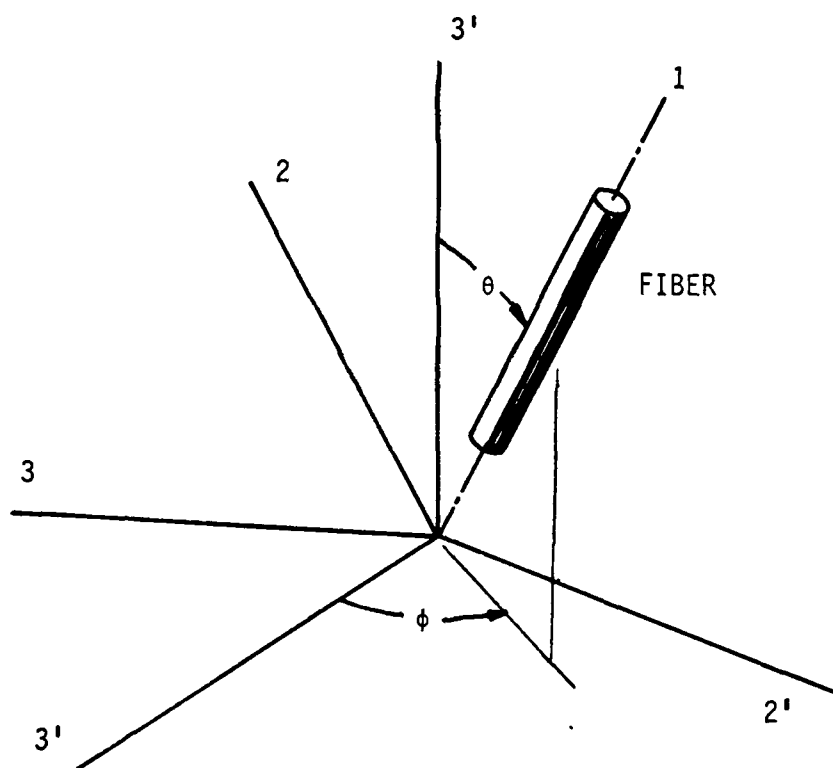


Fig. 24 Description of Fiber Orientation

The composite stiffnesses after reorientation of each volume element due to hot pressing depend on the ratio of virgin material thickness to formed thickness. From Fig. 23-a,

$$\sin \psi = \frac{t_a}{t_b} = \xi \quad (22)$$

Thus, the stiffness components after hot pressing are given by

$$\overline{C}_{ijkl} = \frac{1}{2\pi \sin \psi} \int_0^\pi \int_{\pi/2 - \psi}^{\pi/2 + \psi} C'_{ijkl} \sin \theta \, d\theta \, d\phi \quad (23)$$

where

$$C'_{ijkl} = a_{ip} a_{jq} a_{kr} a_{ls} C_{pqrs} \quad (24)$$

As shown in Fig. 24, the direction cosines, a_{ij} , can be defined as

$$a_{ij} = \begin{bmatrix} \sin \theta \cos \phi & -\cos \theta \cos \phi & \sin \phi \\ \sin \theta \sin \phi & -\cos \theta \sin \phi & -\cos \phi \\ \cos \theta & \sin \theta & 0 \end{bmatrix} \quad (25)$$

Substituting (24) and (25) into (23) gives the five independent elastic constants after hot pressing in terms of the thickness ratio and the elastic constants of a perfectly aligned fiber composite. These are described in Appendix 7.2.

As mentioned earlier, the five independent elastic constants for a perfectly aligned fiber composite must be known prior to the forming process. The shape of reinforcing short fibers or whiskers has been frequently assumed by a number of researchers [11,22] to be a prolate spheroid. This approach is known as the equivalent inclusion method from which all elastic constants of a composite reinforced by aligned inclusions can be estimated either analytically or numerically.

From the present study, the effective elastic constants for aligned continuous or discontinuous fiber composites can be predicted. The effective transverse Young's modulus is compared with the experimental data in Fig. 25.

In Fig. 26 the effective elastic constants for a composite with aligned discontinuous fibers are illustrated for glass fibers in polystyrene. The elastic constants are then utilized as input data for determining the effective Young's modulus of the same composite with randomly

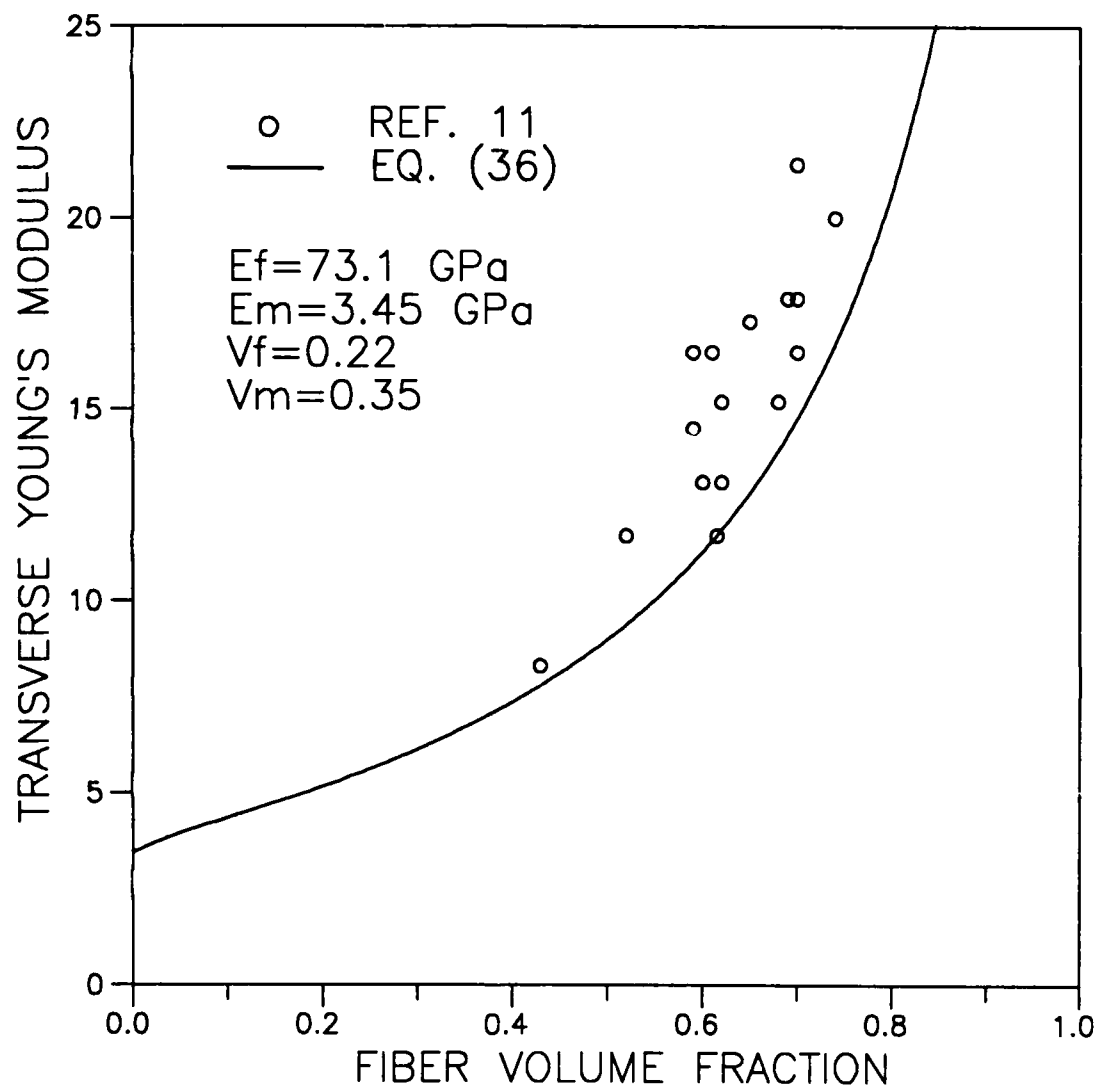


Fig. 25 Transverse Young's Modulus for a Continuous Fiber Composite

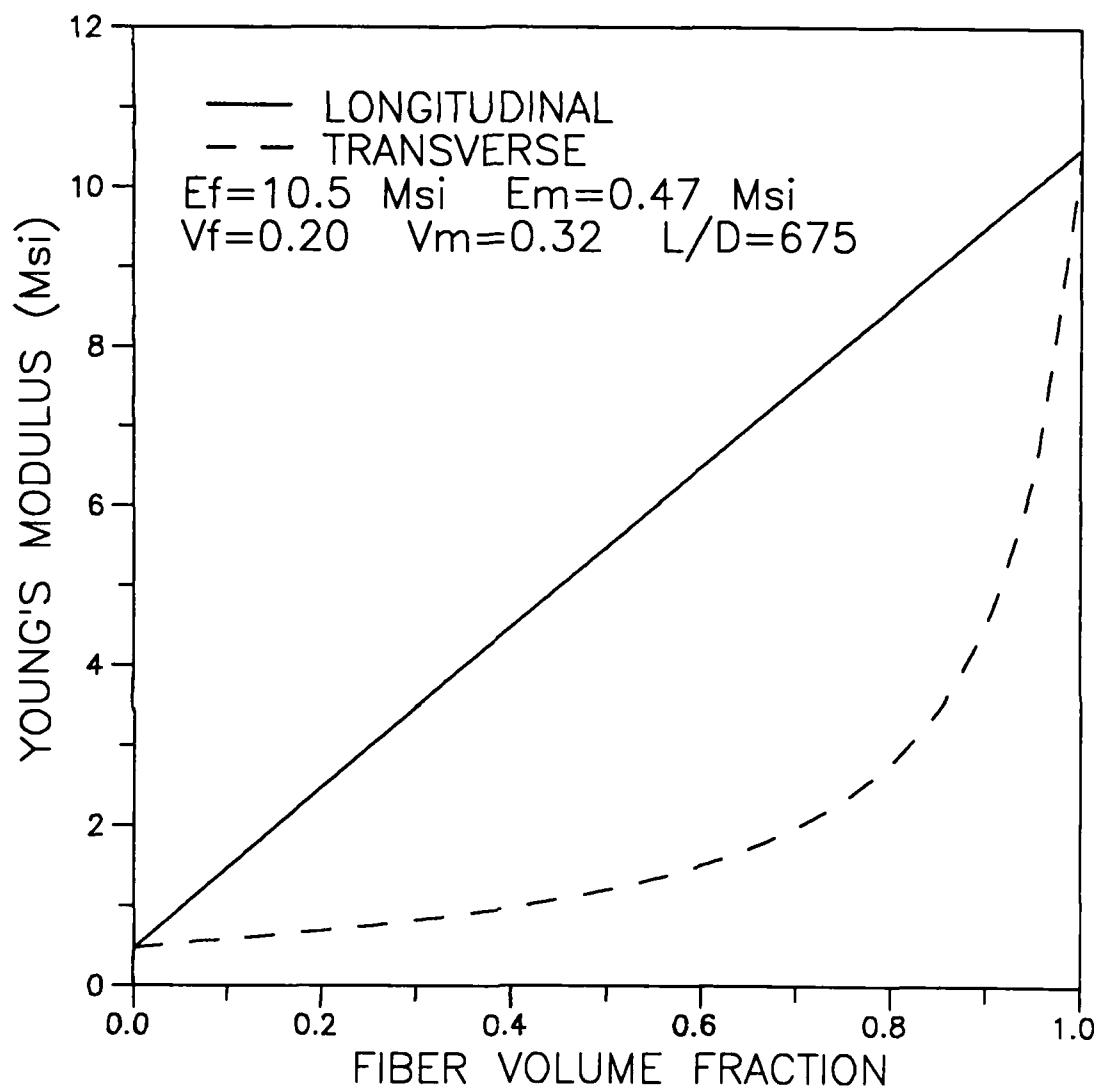


Fig. 26a Young's Modulus for a Perfectly Aligned Fiber Composite

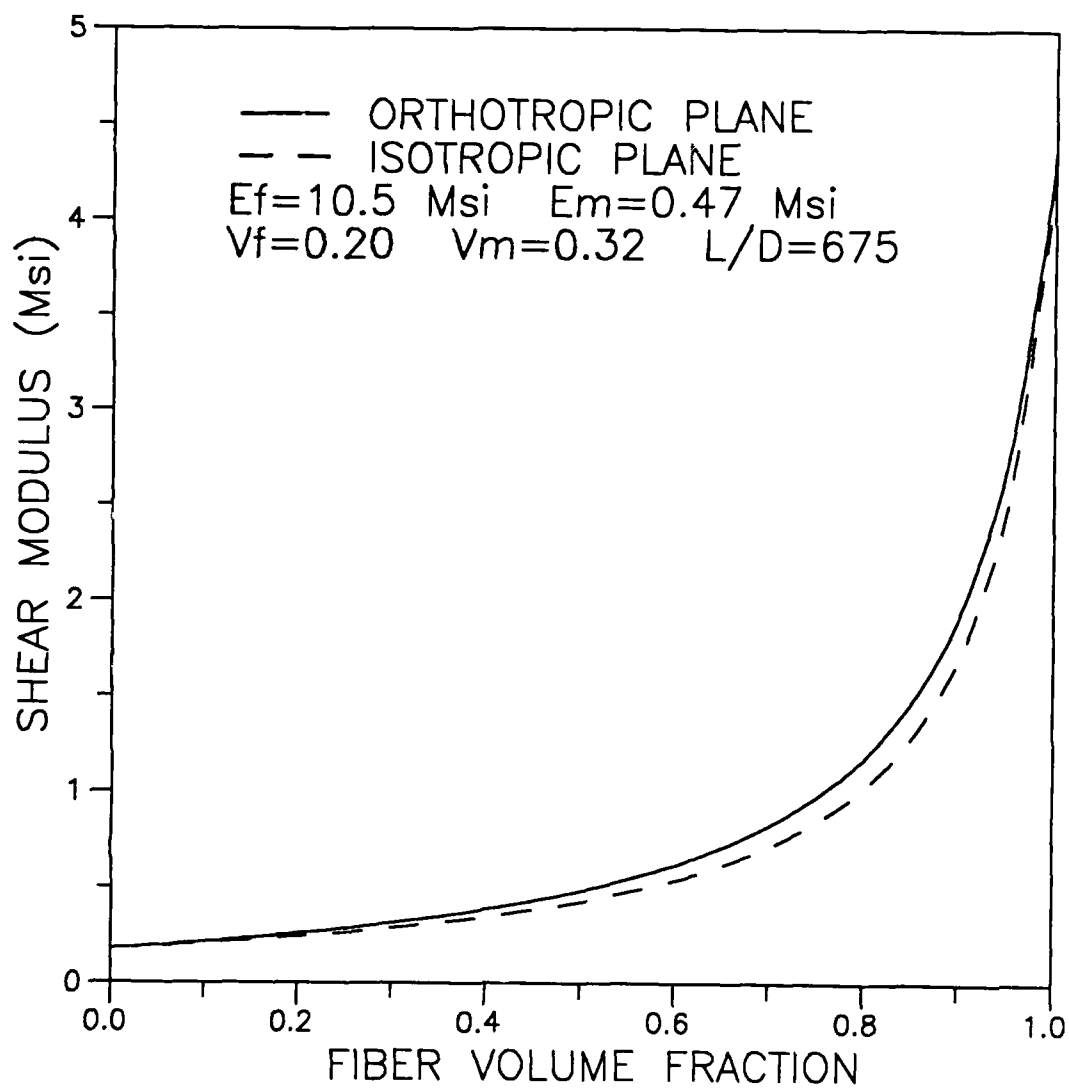


Fig. 26b Shear Modulus for a Perfectly Aligned Fiber Composite

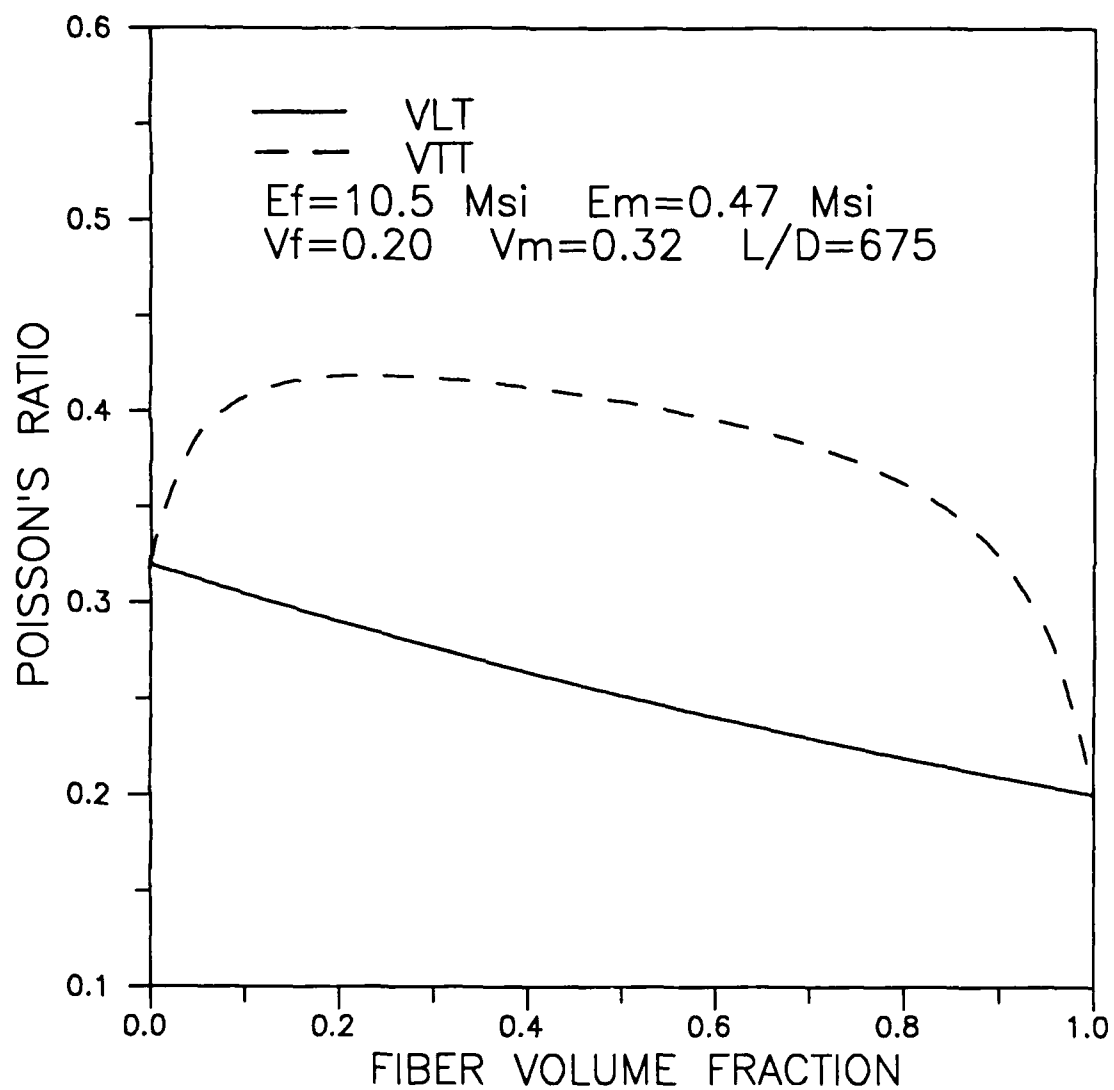


Fig. 26c Poisson's Ratio for a Perfectly Aligned Fiber Composite

oriented fibers in a two dimensional domain. Fig. 27 shows the comparison between the present study and the experimental result of Lee [27].

The variations of the effective Young's modulus in the major axis are illustrated in Fig. 28 for an ideal short fiber composite subjected to each of the three material forming processes discussed earlier. Consider an extreme case in which the thickness ratio is zero. In such a case the fibers after hot pressing or rolling become planar. The material properties after hot pressing become transversely isotropic, while those after rolling remain orthotropic. When the material is subjected to an extrusion in which the diameter ratio approaches zero, the material properties for a perfectly aligned fiber composite are retrieved, as shown in Fig. 28.

From the present study, an engineering tool is proposed for theoretical evaluation of the elastic properties for a composite with perfectly aligned short fibers.

2.3 Experimental Programs

The experimental research was performed in two distinct areas: constitutive testing; and plate response to external heating. The constitutive experiments involved uniaxial testing of coupons at elevated temperature. The results of these tests were utilized to characterize the material constants for current uniaxial thermoviscoplastic constitutive models.

The second experimental area, the testing of plates under external heating was necessary to verify the theoretical models developed herein. These two experimental efforts are discussed in greater detail in the following two subsections.

2.3.1 Constitutive Testing

As a part of the research program it was necessary to produce a thermoviscoplastic constitutive model applicable to Hastelloy X, the material used in the plate experiments. Toward this end, the constitutive theories chosen for this investigation were those of Bodner [3] and Walker [4]. Selection was based upon several considerations, namely: 1) these models have been scrutinized very carefully in the literature and are now considered to be in a mature form; 2) these models have been previously used to model the behavior of Hastelloy X; 3) parameter evaluation schemes are more readily available for obtaining "initial" estimates to the material constants; and 4) continued development of these models requires a thorough understanding of their full potential, as well as their limitations. These models are reviewed in detail in Appendix 7.4.

The construction of these models required that a series of complex experiments be performed for temperatures of 1100 and 1700°F using four different mechanical testing modes. These include monotonic tension, fully reversed cyclic, stress drop, and complex history experiments.

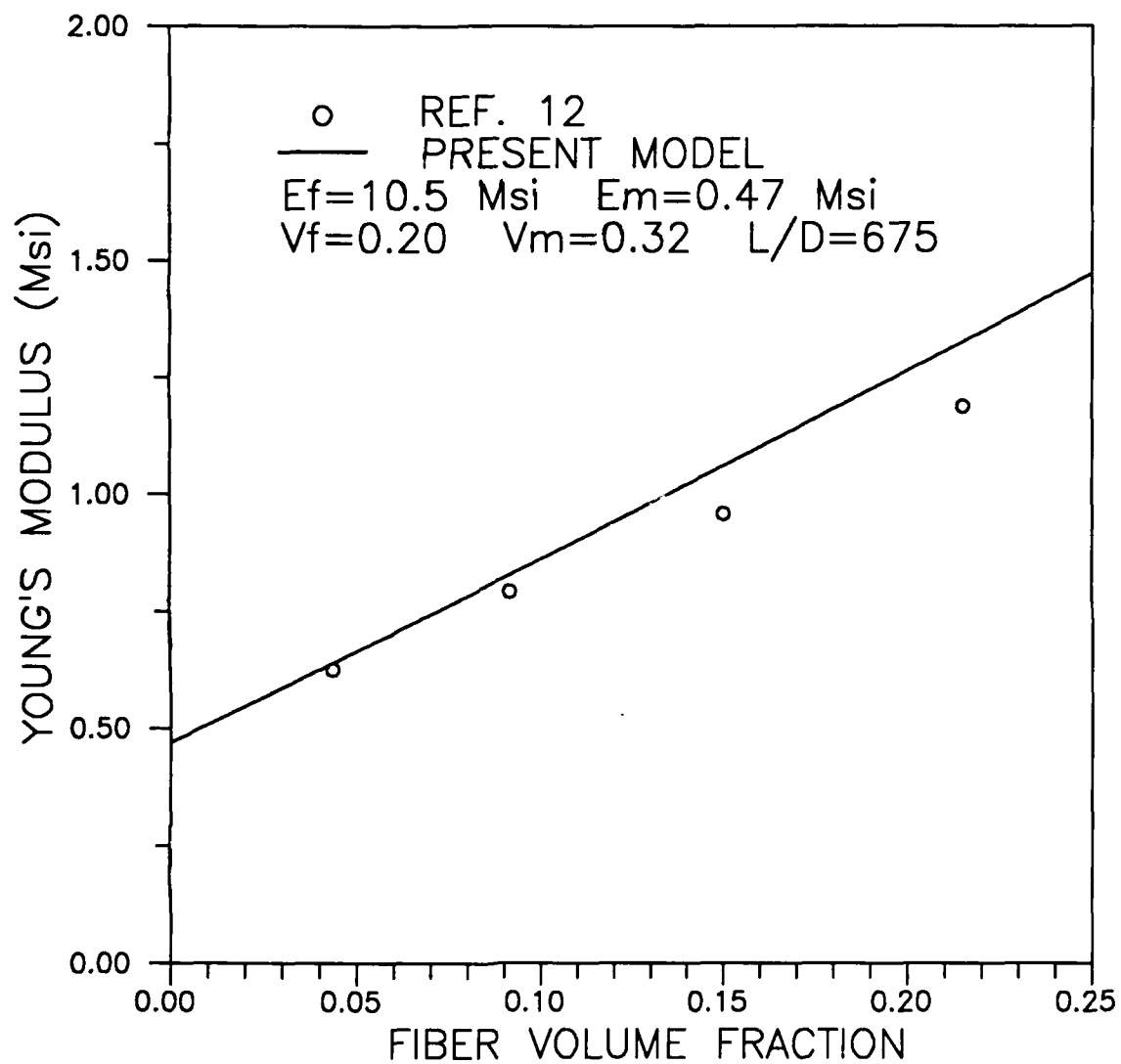


Fig. 27 Effective Young's Modulus for a Composite with Two-Dimensional Random Fibers

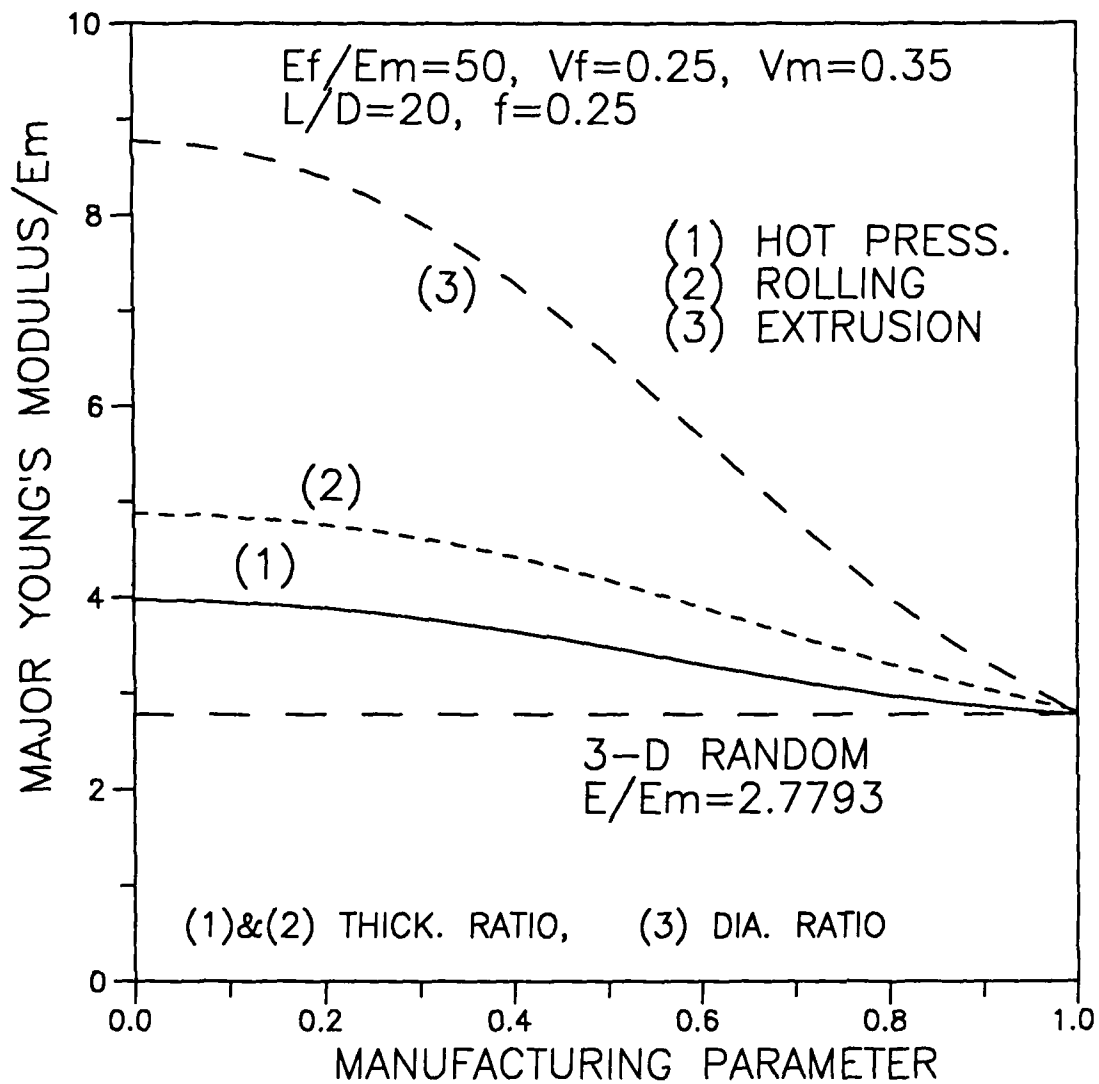


Fig. 28 Effective Major Young's Modulus

All of the tests performed during this program were carried out in the Solid Mechanics Laboratory of the Aerospace Engineering Department at Texas A&M University using an MTS 880 servo-hydraulic closed-loop testing machine. The load frame was configured with a closed-loop heating chamber, water-cooled hydraulic grips, and externally mounted load cell, and axial extensometer, and a mini-computer for controlling testing operations. The heating chamber had a maximum operating range of 1800°F and was of the three zone, resistive heating, clam shell type design. Temperature feedback for each longitudinal set of heating coils was provided by 24/28 gauge K-type bead welded thermocouple wire. The temperature at the center of each zone was monitored by its own process and power controller and enabled the user to establish and maintain a spatially uniform temperature profile (within ASTM specifications for a short term test) along the gauge length of the specimen. A set of Fiberfrax insulating plugs placed on the top and bottom access ports of the furnace and grips which extended into the hot zone were used to reduce and/or minimize the effect of convective and conductive heat losses, respectively.

A high temperature specimen grip system was utilized for this series of experiments and, as stated above, extended into the main body of the furnace. The grips were designed to accept threaded specimens through the use of an inside/outside threaded adapter. Backlash in the specimen/adapter assembly was removed via a hydraulically operated piston which could be loaded to a specified amount. Grip alignment was performed prior to and during testing (failure of one of the specimen adapters necessitated a realignment during the course of the experimental program). This included a check of both concentricity and angularity of the load train with respect to the actuator rod movement. The alignment procedure yielded a total indicated run-out of 0.0008" at an angle of 0.22°, as measured by a digital dial indicator accurate to 0.00005". However, since the adapter assembly contained a number of threaded components, it was not reasonable to expect any degree of repeatability of these measured quantities, however; they are stated for the sake of completeness. It should also be noted that there was no explicit measurement of specimen bending strains to ensure compliance with ASTM specifications.

The primary measured data of interest included load, displacement, and temperature. The load data were obtained via a 10 KIP load cell mounted in the load train. Displacement data were measured using a one inch gauge length, air cooled, axial extensometer. The extensometer was mounted outside the furnace and used a set of conical tipped quartz extender rods to make contact with the specimen. Signal conditioning for both of these transducers was part of the MTS 880 load frame system and possessed a multiple range select feature which provided maximum data resolution. Load and displacement data were measured using a 12 bit A/D system which had a ± 5 mV resolution and was an integral part of the controlling and measuring computer system. Temperature data were obtained using three 24/28 gauge K type thermocouples equally spaced along the gauge length of the specimen. The thermocouples were connected to a multi-channel digital thermometer which was not an integral part of the A/D measuring system. Therefore, temperature data were not automatically recorded on a regular basis, as were the load and displacement measurements. Instead, temperature values at the beginning of a test were entered by hand into the data acquisition program and simply monitored thereafter. The thermocouples were attached to the specimen using the self-supporting method. This method of attachment provided sufficient thermal contact with the material to yield

accurate temperature measurements and did not flaw the specimen (which in general can result in premature failure), as is common with welding thermocouples to the surface.

The Hastelloy X material used to fabricate the specimens was purchased in bar stock form from Atek Metals Center of Houston, Texas. This was a solution strengthened material conforming to ASM specification number 5754H. The design of the specimen was that of a standard, constant gauge section, low cycle fatigue geometry having a nominal one inch gauge length and quarter inch diameter circular cross-section. The specimens were fabricated to meet ASTM E606-77T specifications except for the surface finish and post machining heat treatment. A 32μ finish was used instead of the typical 8μ for cost considerations. In addition, the specimens were used in an "as received" condition with no additional heat treatment to remove microstructural damage resulting from the machining process.

A total of 27 tests were conducted in fulfillment of this isothermal constitutive test program. Two cyclic tests were carried out at 1200 and 1600°F, respectively, and served as a basis of comparison to previously obtained data and for uniaxial constitutive code verification. Specific details of the remaining 25 experiments are as follows. Monotonic tension and fully reversed cyclic tests were performed at 1100 and 1700°F, using a variety of strain rates, ranging from 1×10^{-5} to $3 \times 10^{-3} \text{ sec}^{-1}$, under strain controlled conditions. Strain amplitudes for the tension and cyclic test were 4.0% and 0.8%, respectively. However, the strain amplitude of 0.8% was subsequently reduced to 0.4% during the course of 1100°F experiments because specimen buckling became a problem. This was apparently the result of a material instability at the selected temperature and strain rate.

The fully reversed cyclic experiments were carried out until a saturated condition was achieved. For the purpose of this test program, cyclic saturation was defined as a change in stress amplitude of less than 100 psi from one cycle to the next. The stress drop tests, used to measure values of back stress, were performed by inserting a hold time on the unloading branch of a fully reversed saturated hysteresis loop, and monitoring the creep response. When positive creep was observed, the hold stress was greater than the back stress and vice versa, when negative creep was seen. Since it is very difficult to obtain the exact hold stress which results in no creep, the general procedure was to bracket the positive and negative creep responses and use a linear regression scheme to estimate the values of the back stress. Additional stress drops were made on a specimen after it had been recycled to saturated condition.

Finally, two experiments, one each at 1100°F and 1700°F, were performed in order to verify the predictive capabilities of the constitutive models considered herein. These complex history tests included mechanical effects such as strain rate jumps, relaxation, cyclic behavior, and strain holds. A complete summary of the entire test matrix can be found in Table 1. The material parameters resulting from these experiments are listed in Tables 2 and 3.

Figures 29 and 30 demonstrate the predictive capabilities of the models compared to complex history tests performed on Hastelloy X at 1700°F. Experimental results were compared to Bodner's model at 1700°F, as shown in Fig. 29. This figure shows that Bodner's model

Table 1. Test Matrix.

Test	Specimen	Temp. (F)	Strain Rate (sec ⁻¹)	Strain Amp. (%)	Type of Test
4	4	1100	1.1921E-05	2.5	Monotonic Tension
5	5	1100	1.1921E-05	0.8	Cyclic
6	6	1700	1.1921E-05	0.8	Cyclic
7	7	1700	1.2207E-04	0.8	Cyclic
8	8	1700	1.1903E-03	0.8	Cyclic
9	9	1700	5.0362E-04	0.8	Stress Hold
10 *	10			0.6	Monotonic Tension
11	11	1700	1.1903E-03	4.0	Monotonic Tension
12	12	1700	3.8148E-03	0.8	Cyclic
13 *	13	1100	3.8148E-03	0.8	Cyclic
14	14	1100	1.2207E-04	0.8	Cyclic
15 *	15	1100	1.1903E-03	0.8	Cyclic
16	16	1100	1.1903E-03	4.0	Monotonic Tension
17	17				
18 *	18	1100	1.1903E-03	0.8	Cyclic
19	19				
20	20				
21	21	1100	5.3047E-05	0.8	Stress Hold
22 *	22 *	1100	5.0362E-04	0.8	Cyclic
23	23	1100	5.0355E-04	0.6	Stress Hold
24	24	1100	1.1902E-03	0.4	Stress Hold
25	25				
26	26				
27 @	27	1100		0.6	Complex History
28 @	28	1700		0.6	Complex History

Table 2. Material Parameters for Bodner's
Model at 1100°F and 1700°F.

Parameter	1100°F	1700°F
A_1, sec^{-1}	0.6500E-04	0.6500E-04
A_2, sec^{-1}	0.6500E-04	0.6500E-04
D_0, sec^{-1}	0.1000E+05	0.1000E+05
E, psi	0.2394E-08	0.1900D+08
r_1	0.9800E-00	0.9800E-00
r_2	0.9800E-00	0.9800E-00
m_1, psi^{-1}	0.5500E-03	0.5500E-03
m_2, psi^{-1}	0.1100E-01	0.1100E-02
m_3, psi^{-1}	0.3477E-04	0.3477E-03
n	0.1000E+01	0.7000E-00
Z_0, psi	0.1000E+06	0.2500E+06
Z_1, psi	0.2900E+06	0.2200E+06
Z_2, psi	0.1000E+06	0.2500E+06
Z_3, psi	0.1300E+06	0.8200E+05

Table 3. Material Parameters for Walker's Model at 1100°F and 1700°F.

Parameter	1100°F	1700°F
L_1 , psi	0.8580E+05	0.1080E+06
D_2 , psi	0.0000E-00	0.0000E-00
E , psi	0.2394E+08	0.1900E+08
n_1 , psi	0.0000E-00	0.0000E-00
n_2 , psi	0.4200E+07	0.2500E+06
n_3	0.0000E-00	0.0000E-00
n_4	0.0000E-00	0.0000E-00
n_5	0.0000E-00	0.0000E-00
n_6 , psi ^(1-m) sec ⁻¹	0.0000E-00	0.0000E-00
n_7 , sec	0.0000E-00	0.0000E-00
n	0.1420E+02	0.5000E+01
m	0.1160E+01	0.1160E+01
B_0 , psi	-0.2000E+04	-0.1000E+04

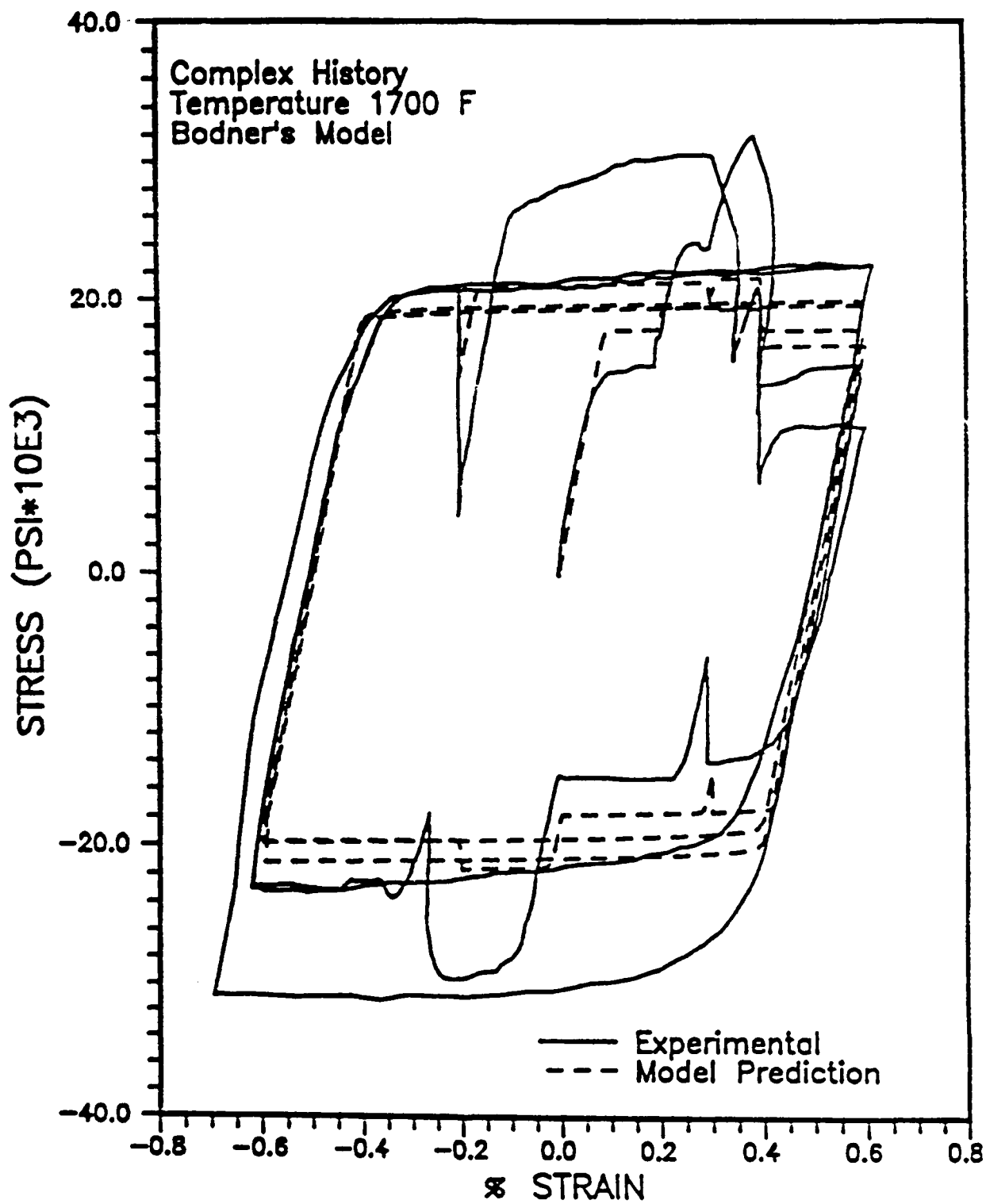


Fig. 29. Comparison of Bodner's Model to Experimental data at 1700°F for a Complex Strain Input History.

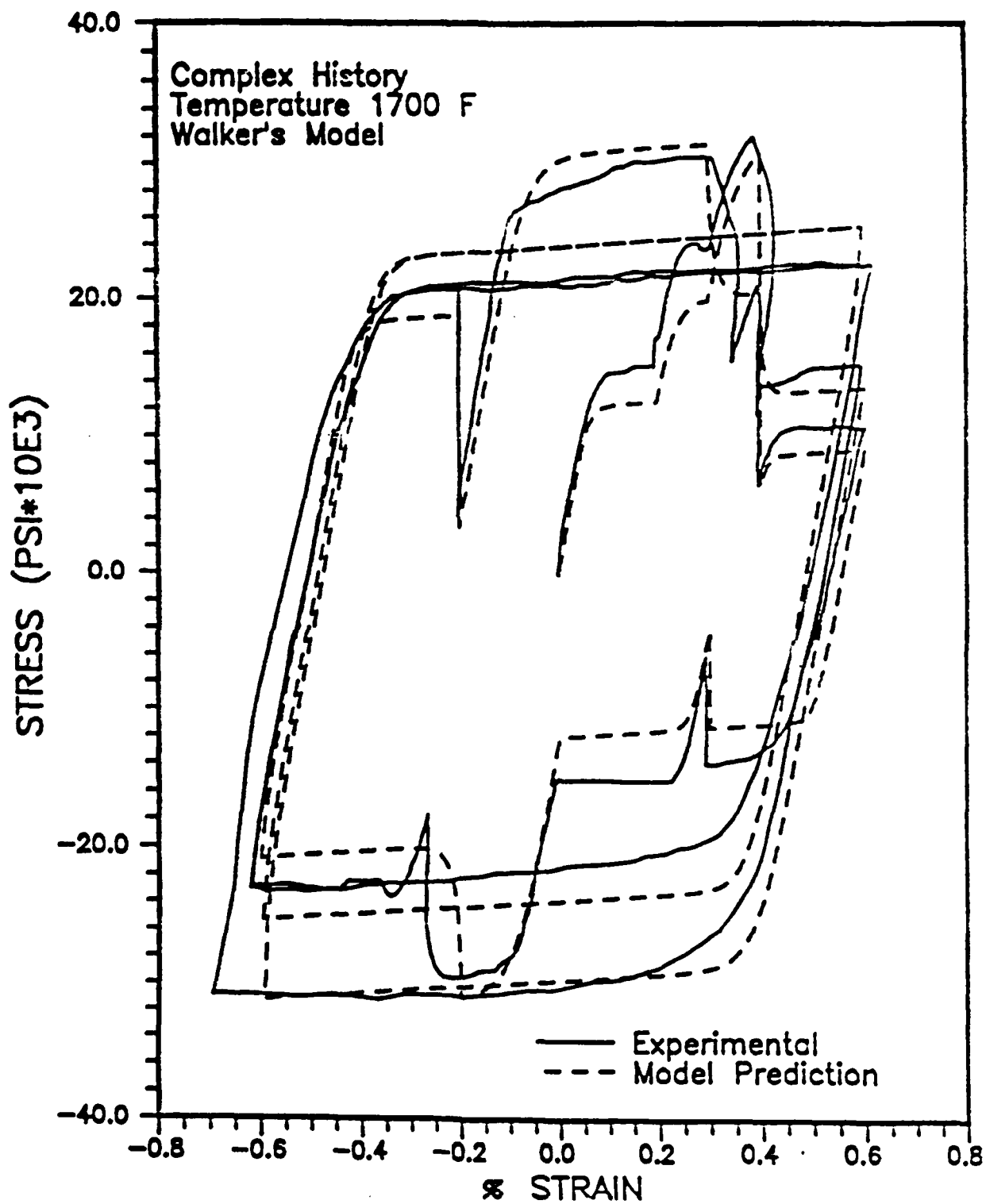


Fig. 30. Comparison of Walker's Model to Experimental data at 1700°F for a Complex Strain Input History.

predicts an extremely "oversquare" response. This response is not in keeping with the observations made previously in this study, where Bodner's theory accurately represented the general shape of the stress-strain curve. Also, this model demonstrates insensitivity to relaxation and strain rate jumps. This response is contrary to information given by Bodner, where it is stated that use of the plastic strain rate as the measure of hardening enables the model to better predict strain rate jump behavior. This inconsistency is possibly due to the fact that the hardening terms in the evolution equations saturate too quickly.

Figure 30 presents a comparison of Walker's theory to measured values at 1700°F. Walker's model predicts the overall response accurately, including general shape, strain jumps, and relaxation. This outcome is congruent with previous results.

Further results for this phase of the research can be found in Appendix 7.4.

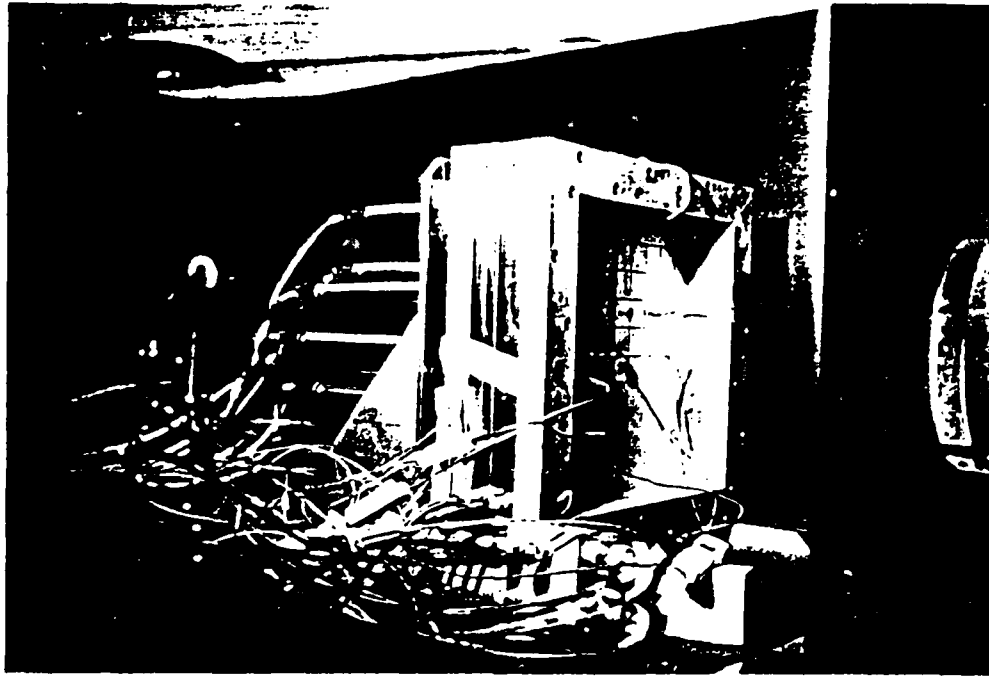
2.3.2 Plate Testing

An experimental program was developed to investigate the transient response of a viscoplastic plate subjected to rapid heat input. Of particular interest was the measurement of the displacement and temperature fields for a rectangular plate specimen undergoing rapid laser heating. The experimental program was performed at the Air Force Wright Aeronautics Laboratories using the LHMEI I (Laser-Hardened Materials Evaluation Laboratory) facility.

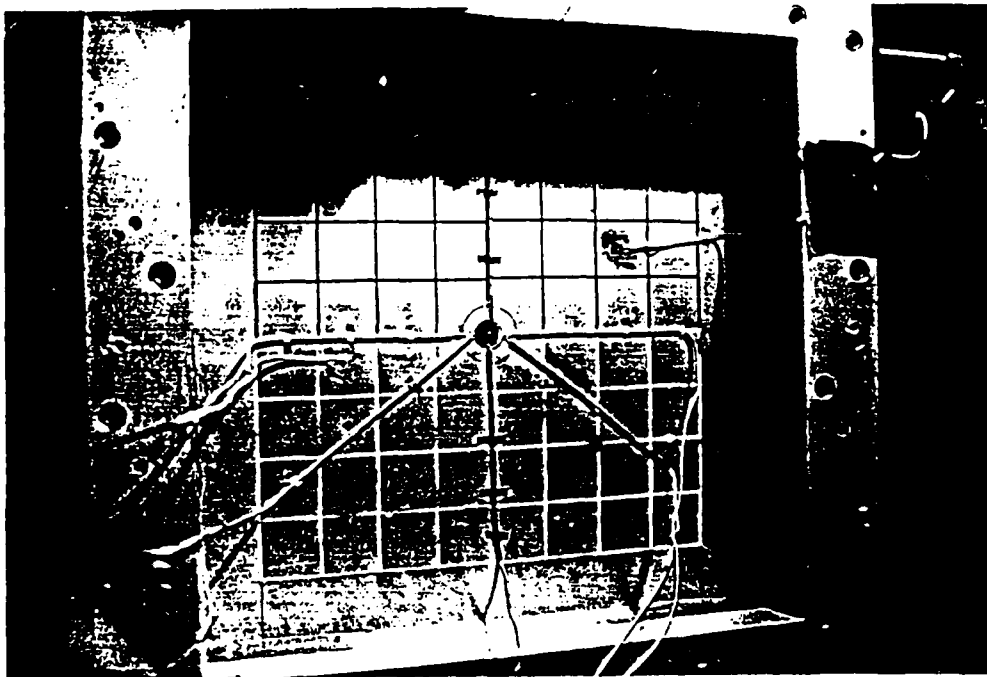
A specimen support fixture was designed to impose clamp-like boundary conditions along each edge of a rectangular plate specimen. The super-structure of the fixture was fabricated from 6061-T6 aluminum to support the specimen in the vertical position, as shown in Figs. 31a and 31b. An insert made of 304 stainless steel served both as a support stiffener and water jacket. The total water cooling system provided a uniform and constant plate boundary temperature using tap water. Thermocouples were attached to each half of the insert at the mid-position, approximately 0.5 in away from the specimen, to record any temperature variations.

Hastelloy X material was obtained in plate form from ATEK Metals Center, Inc., Cincinnati, Ohio. Three 27 x 40 in plates with designated heat numbers 2600-7-4649, 040161, and 260-7-4630, corresponding to nominal plate thicknesses of 1/16 in, 1/8 in, and 1/4 in, respectively, were used to fabricate a total of 18 specimens (6 of each thickness). The material was received in an annealed condition specified by ASTM 5536 and used without further heat treatment. No micrographic studies were performed to investigate the variations in grain structure or size that existed between the different heats.

An integrated instrumentation package was used to simultaneously measure the displacement and temperature fields in a plate specimen undergoing laser irradiation. The primary instrumentation included: 1) LVDT's (Linear Variable Differential Transformers) for measuring displacement; 2) thermocouples for measuring temperature; 3) a radiant pyrometer for measuring surface brightness temperature; and 4) strain gages for measuring the plate vibration frequency. A 12 bit, high speed data system (called the PCM) was used to convert



a) Support Structure Side View



b) Support Structure Front View

Fig. 31 Plate Specimen Support Fixture

the analog output of these transducers and thermocouples to an equivalent binary form at an approximate rate of 1.2 KHz. Once converted, the data were stored on magnetic tape for subsequent conversion to engineering units and any other post-processing. Described below is a more detailed discussion on the implementation of the various pieces of instrumentation.

A total of 11 Schaevitz DC-operated LVDT's (model number GCD-121) were used to sense the out-of-plane displacements resulting from the laser deposition. The outputs of the LVDT's were scaled via the data system, to detect displacements as small as 0.0001 in, at a published maximum frequency response of 15 Hz. The LVDT's were arranged in a symmetric pattern around the heat zone (see Fig. 32) and were rigidly mounted to a support system which was positioned directly behind the specimen, as shown in Fig.'s 33a and 33b. In addition, 2 LVDT's were used to monitor relative movement between the LVDT support system and plate fixture.

Measurement of the in-plane temperature field, through-thickness temperature gradients, and non-contact plate surface temperatures, were made using 21 K-type 30 gage thermocouples. As shown in Fig.'s 34 and 35, the thermocouples were concentrated in a 1 in diameter circle around the heat zone and were arranged in a symmetric pattern for measuring the in-plane temperature field. The through-thickness temperature gradients were measured using thermocouples positioned at the same coordinate locations, but mounted on the front and back of the specimen. All thermocouples were intrinsically mounted to the specimen via a welding operation with the exception of 4 thermocouples. All thermocouples mounted on the front surface of the plate (the heat side) were Inconel 600 heated to withstand the extreme temperatures, whereas the thermocouples mounted on the back side of the specimen were insulated using high temperature glass braid. The thermocouples were connected to the data system via a 150°F reference oven, which for this test was left open to room temperature. For thermocouple input the data system was scaled to record voltage changes on the order of 0.03 mV, which corresponds to a measured temperature resolution of approximately 1.4°F. Thus, taking into account the NBS wire error specification and the above resolution, a maximum temperature uncertainty between 5.36°F and 18.5°F can be expected.

A Thermogage Corporation germanium radiation pyrometer (model number 8000-1) was used to obtain relative measurements of the plate surface brightness temperature. The pyrometer is a high speed transducer, having a peak spectral response at a wavelength of 1.5 μm and an effective temperature range between 900°F and 5400°F within a target area of approximately 0.0491 in². The pyrometer was aligned to record temperatures within the laser irradiated spot diameter in conjunction with a thermocouple. The output of the pyrometer was fed into the data system for use later in developing an appropriate transfer function for the slower responding thermocouples.

A Micro-Measurements CEA-13-12SUN-350, 350 Ω strain gage was used to measure the dynamic response of the specimen resulting from the rapid heating. The strain gage was parallel with the edge of the plate specimen approximately 2.5 in off center. Since vibration frequencies

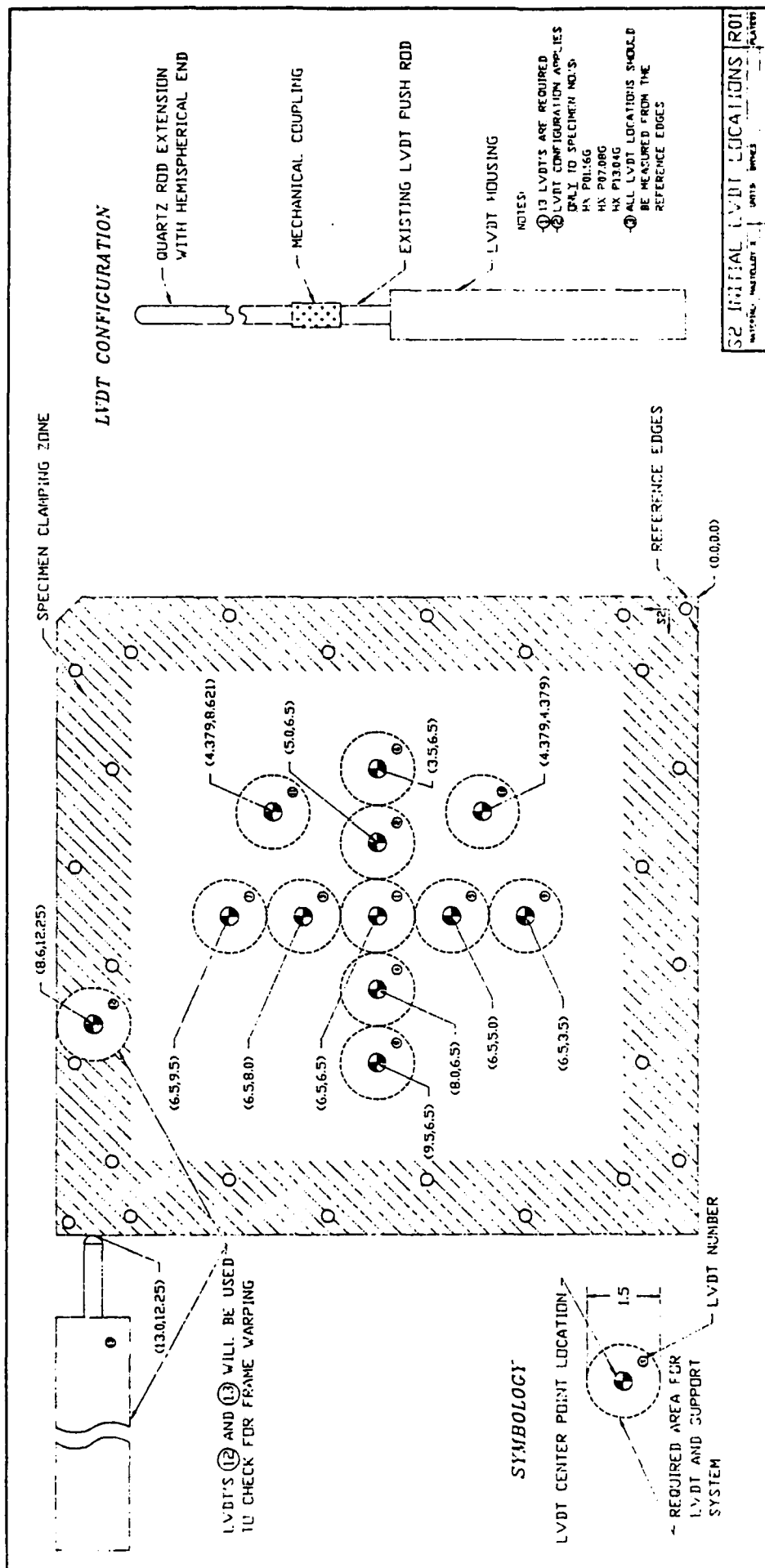
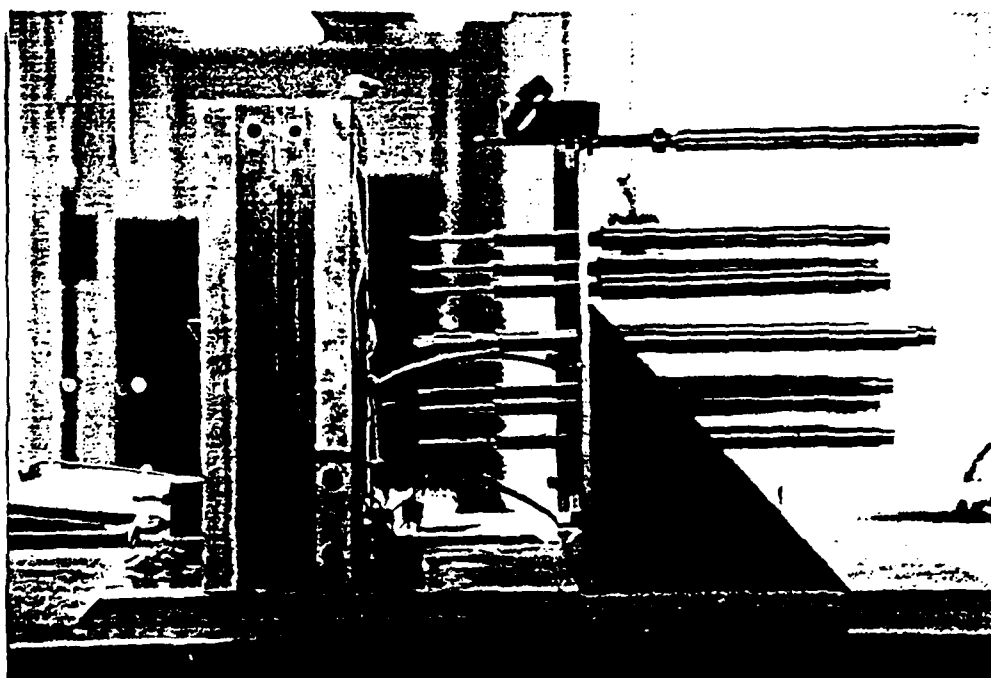


Fig. 32 LVDT Contact Locations on Specimen



a) LVDT Support - Top View



b) LVDT Support - Side View

Fig. 33 LVDT Support Stand Positioned Behind the Specimen

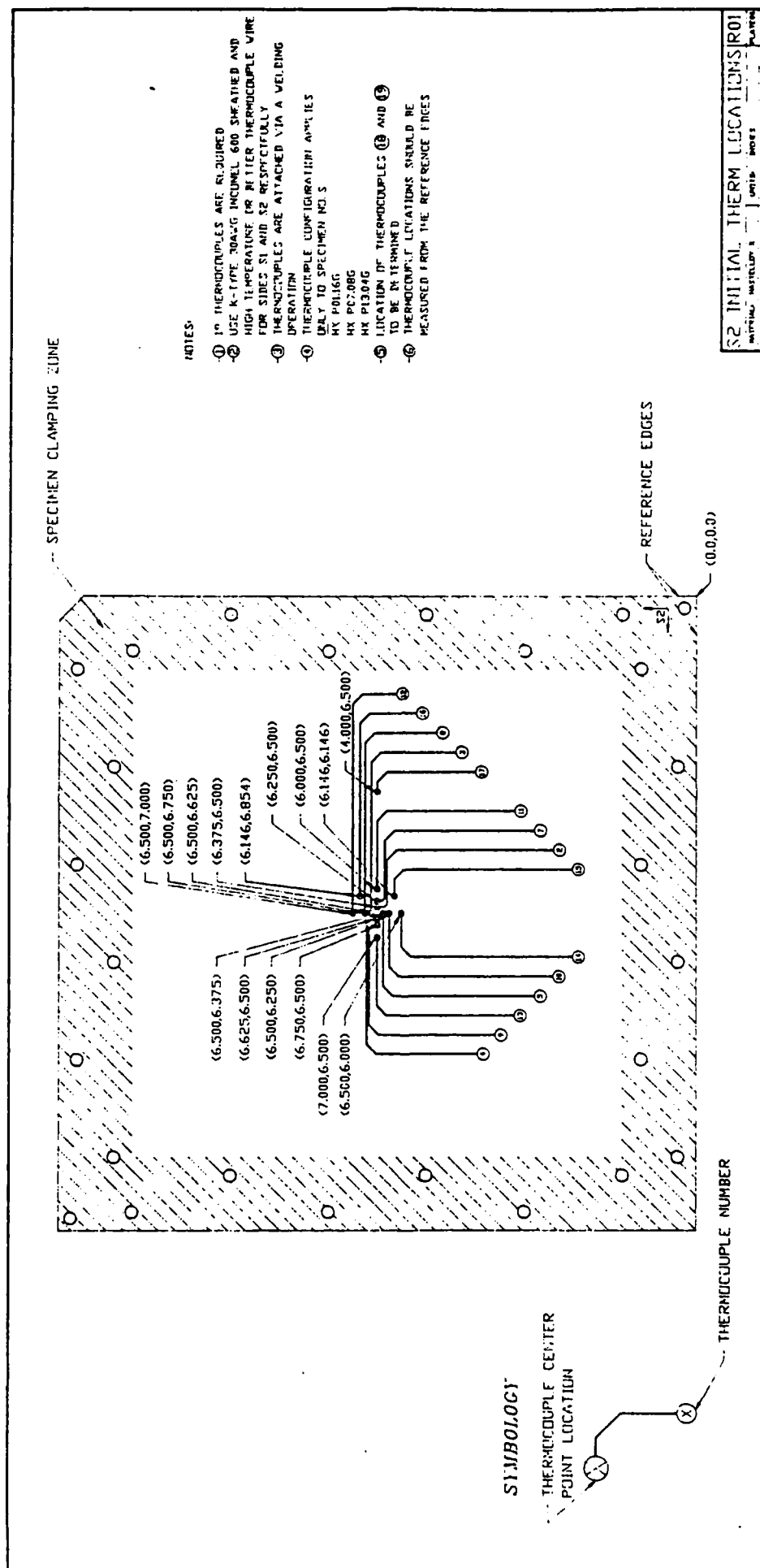


Fig. 34 Thermocouple Locations on the LVDT Side of the Specimen

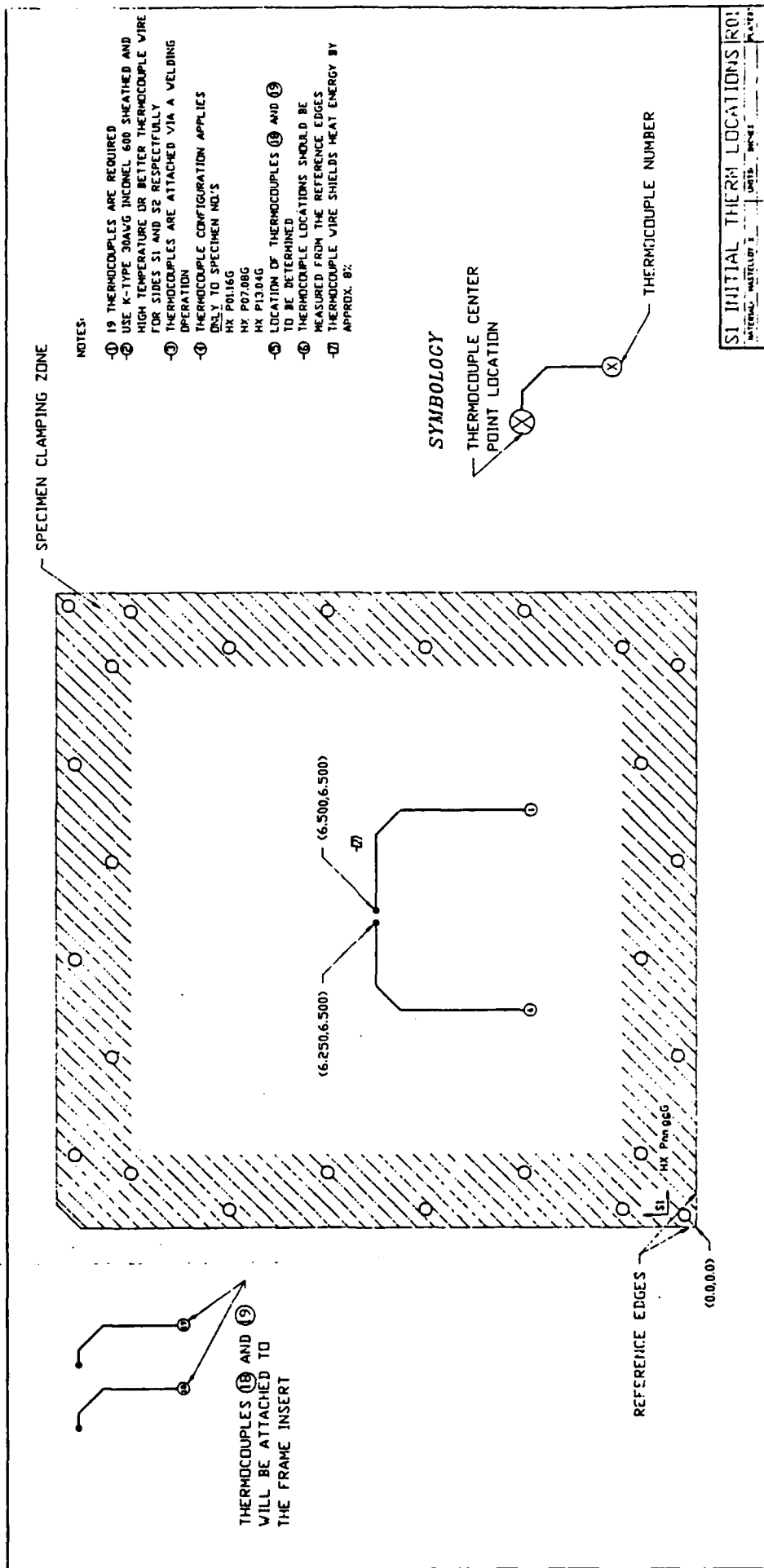


Fig. 35 Thermocouple Locations on the Laser Irradiated Side of the Specimen

and not strain magnitudes were of interest, the output of the strain gage was displayed on a Visicorder strip chart recorder.

The experiments were performed at the Air Force Wright Aeronautics Laboratory in the LHMEI I facility, which is managed and operated by ACUREX Corporation. A schematic of the facility and pertinent equipment is shown in Fig. 36. ACUREX personnel were responsible for the overall test procedures which included: 1) safety considerations; 2) calibration of the laser and other support equipment provided by ACUREX; 3) the laser operating characteristics; 4) the laser fire sequence; and 5) sufficient photographic documentation to reproduce the test setup.

The plate specimens were irradiated using a high energy electric discharge 15 KW continuous-wave carbon dioxide laser operating at a wavelength of $10.6\text{ }\mu\text{m}$ with a flat-top beam profile. The exact beam profile, which includes both width and density, was determined by ablation of square plexiglass specimens, as shown in Fig. 37. By measuring the plexiglass burn patterns, both the laser target area and beam uniformity in the radial direction can be found (see Fig. 's 38a and 38b for a typical example). For this experiment, the laser contact spot was found to be ellipsoidal, having major and minor axis lengths equal to 0.5235 in and 0.5276 in, respectively (this is a result of the beam striking the specimen at a 10° incidence angle in order to prevent energy feed back through the laser z-pattern).

The test apparatus was positioned in the laser facility test cell, as shown in Fig. 39. Additional items used during the experiments, but not previously discussed are: 1) a nitrogen flood box which was used to prevent oxidation of the specimen surface while it was being heated; and 2) video and high speed (500 frames/sec) cameras for documentation of the plate response during laser deposition.

A total of 4 laser/structure interaction experiments were conducted. All 4 tests utilized the same 1/16 in thick plate specimen (number HX PO116G) with input heat flux and exposer time serving as test variables. The primary objectives of the first three tests were to measure the displacement and temperature fields. Therefore, laser power levels and exposer times, as shown in Table 4, were adjusted to bring the specimen temperature to just below the melting point. Figures 40 and 41 show typical output of the LVDT's and thermocouples during laser irradiation.

The last experiment run on the specimen was a burn through test. The objective of this test was to find an upper bound on the laser power settings and exposure time for this material. Only temperature data was taken in order to preclude damaging any of the LVDT's when burn through occurred. The results of this experiment are best shown in Fig. 42.

In summary, a list of the major problems encountered during the tests is as follows: 1) energizing and/or firing the laser adversely affected the measured data, both with noise and voltage shifts; 2) there was no explicit indication of when the laser power was on and off the target area; 3) the nitrogen flood box did not provide an inert environment and made

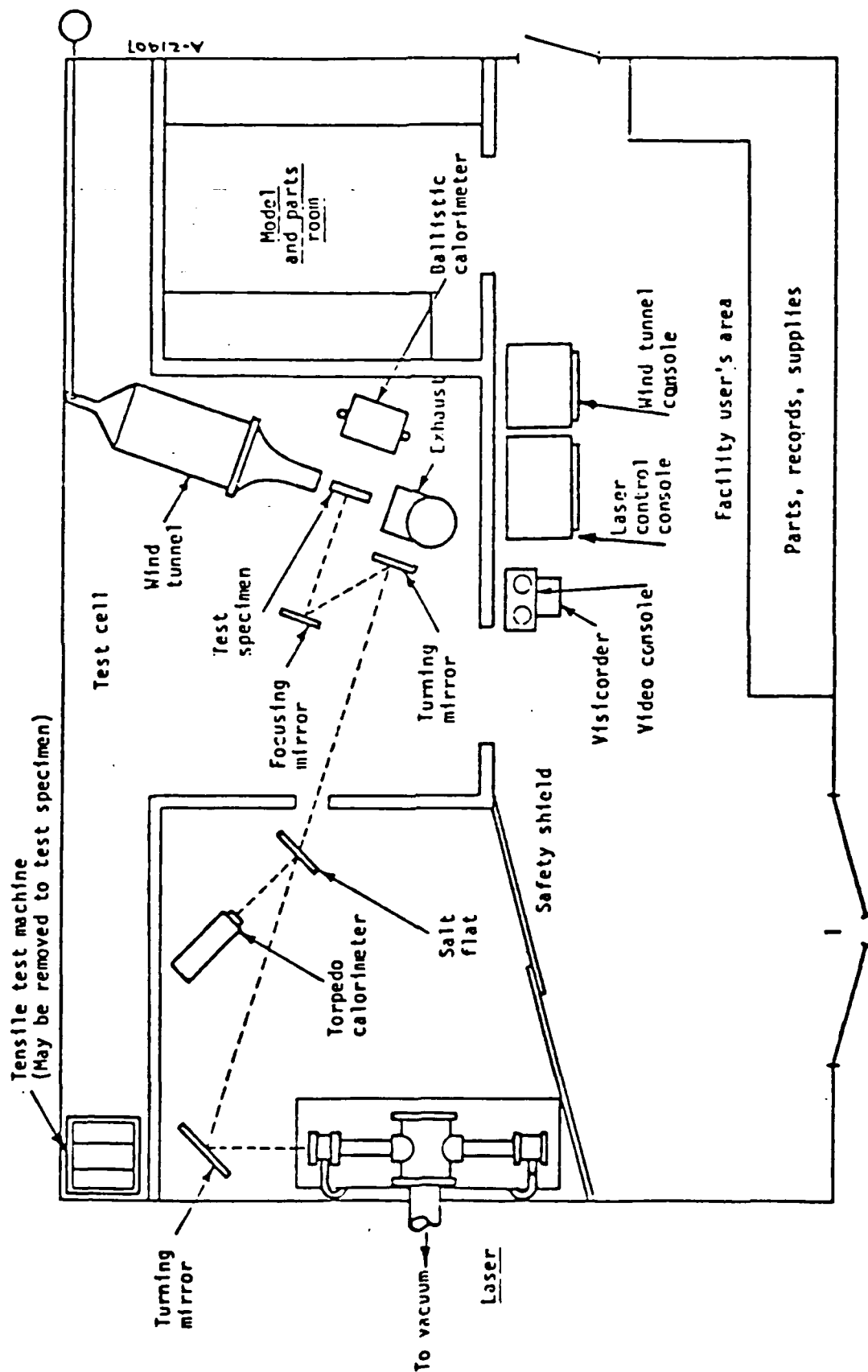


Fig. 36 A Schematic of the LHMEL I Facility at the Air Force Wright Aeronautics Laboratory

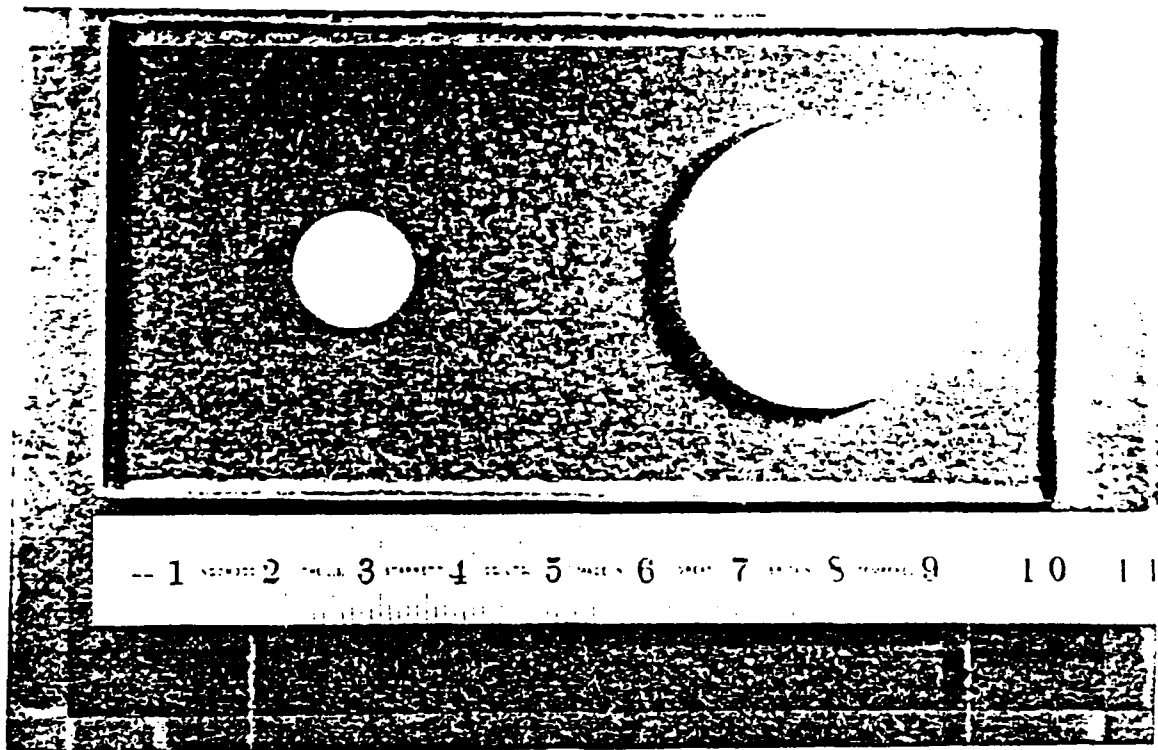


a) Before Ablation

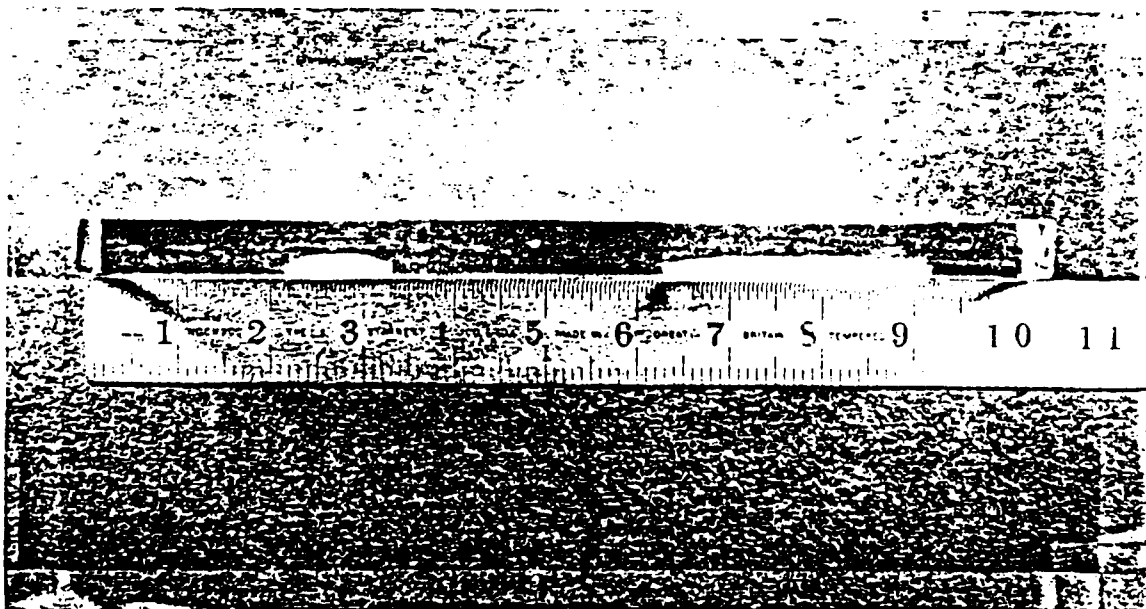


b) After Ablation

Fig. 37 Plexiglass Specimens Used to Check the Laser Beam Width and Density



a) Front View Showing Laser Beam Width



b) Side View Showing Laser Beam Density Distribution

Fig. 38 Typical Plexiglass Burn Patterns

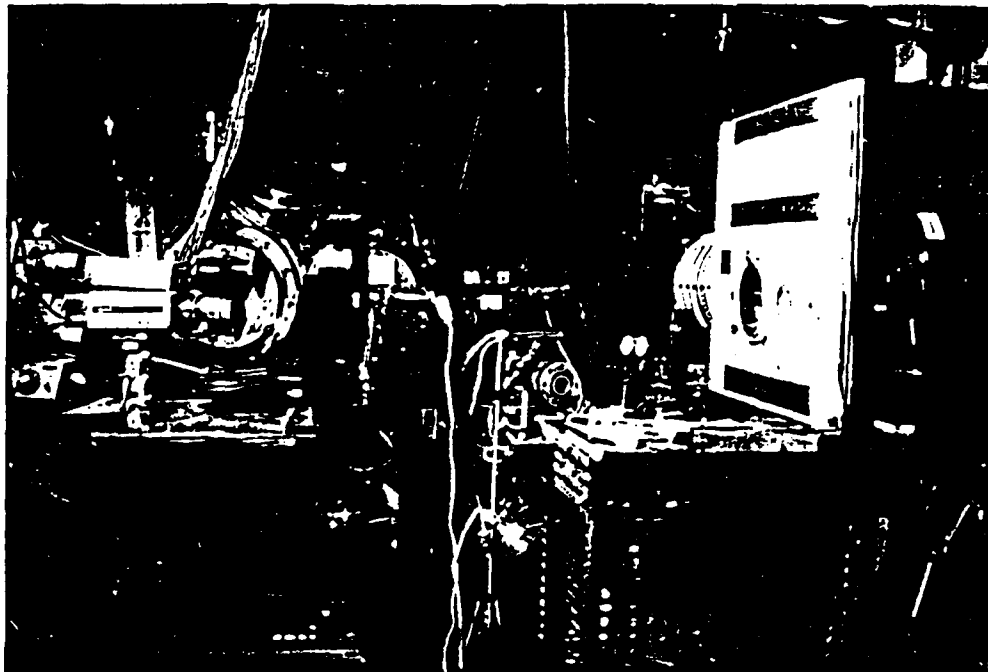


Fig. 39 Test Apparatus Positioned in the Laser Facility
Test Cell

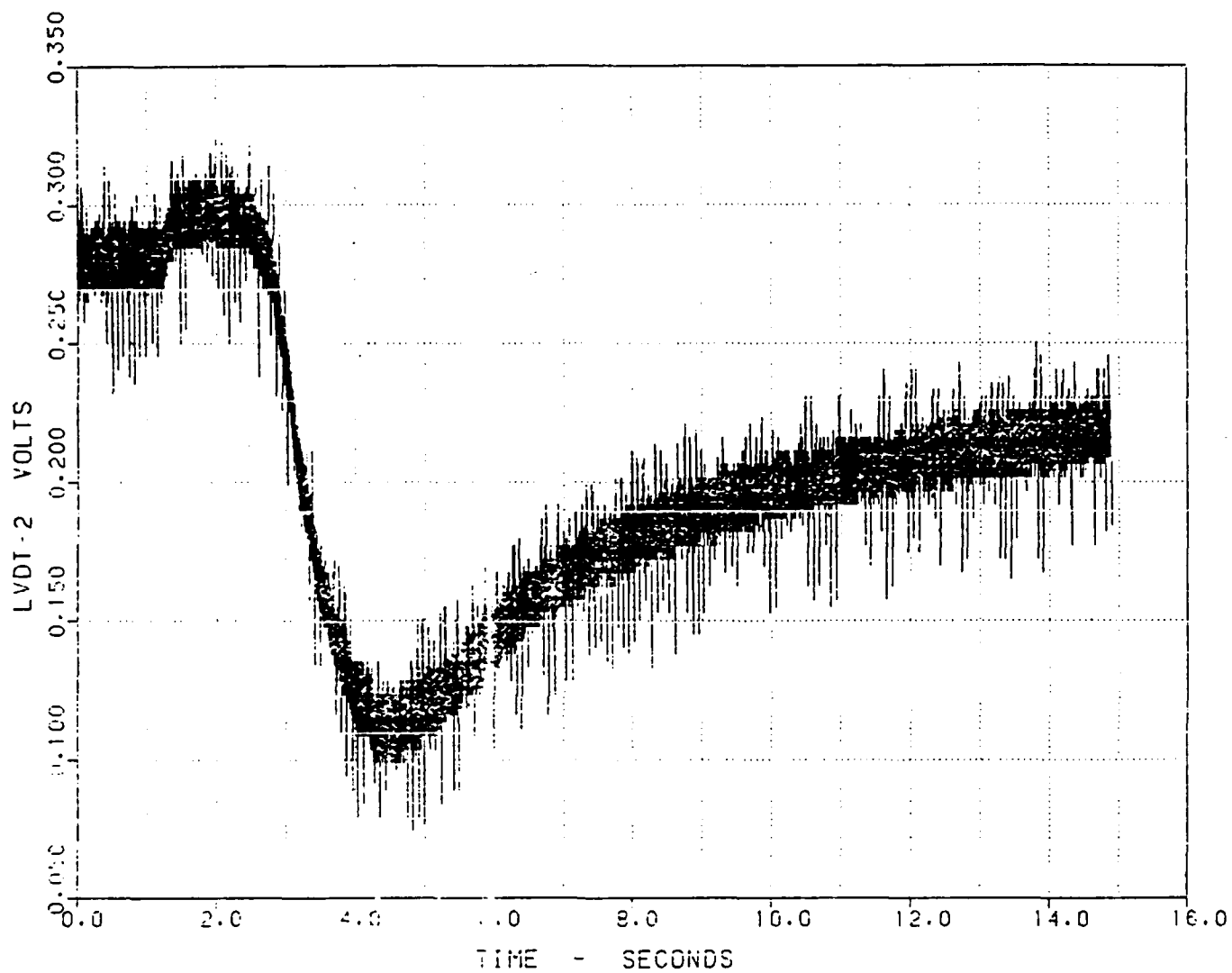


Fig. 40 Typical LVDT Output for a 2 KW/cm² 3 Second Duration Test

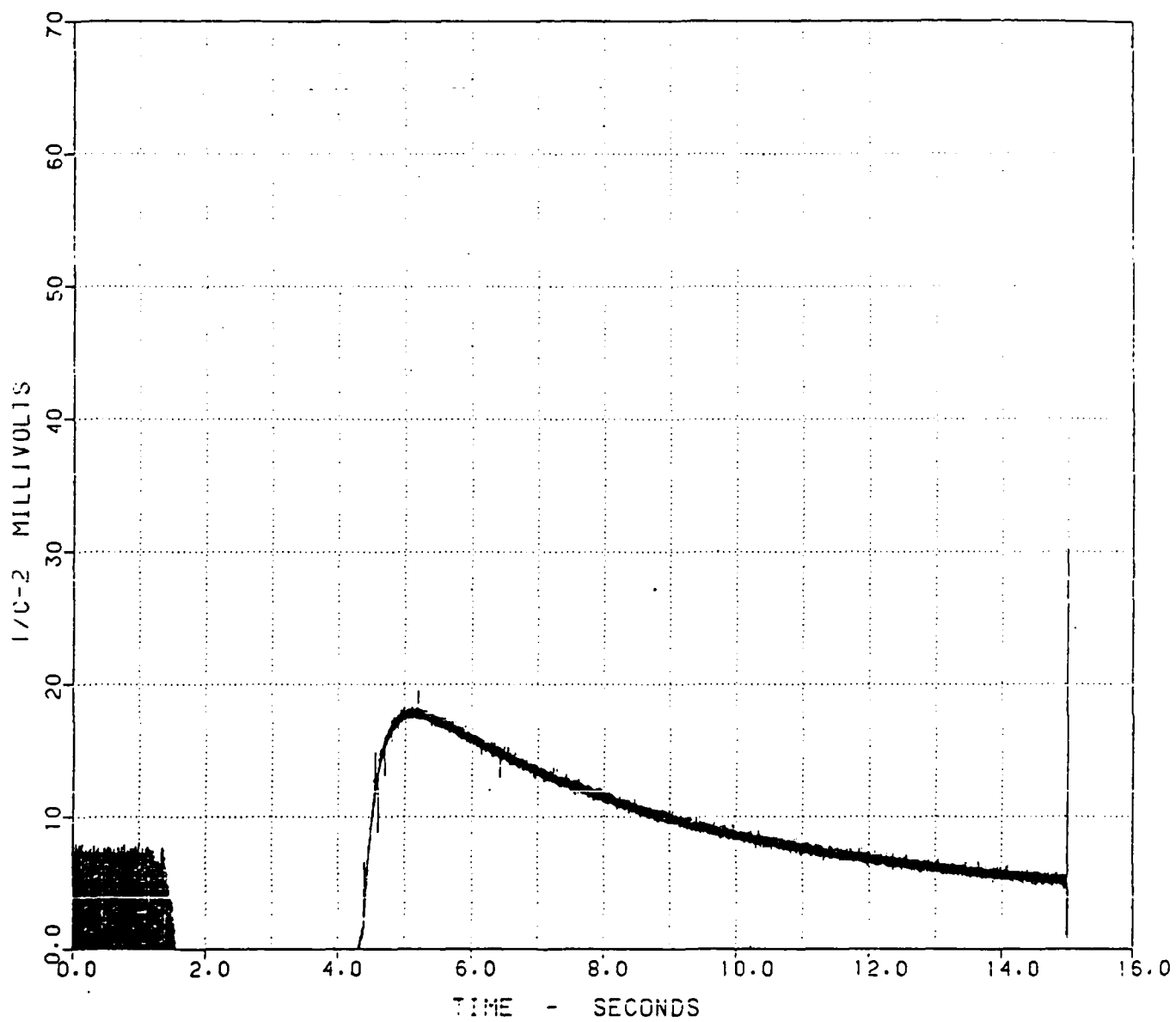


Fig. 41 Typical Thermocouple Output for a 2 KW/cm² 3 Second Duration Test

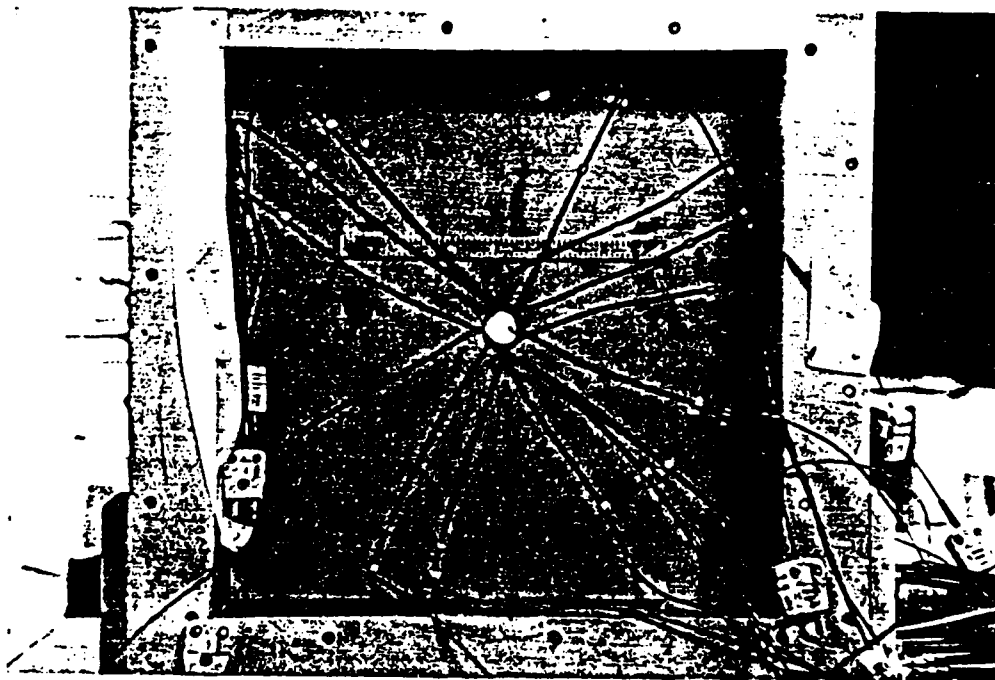
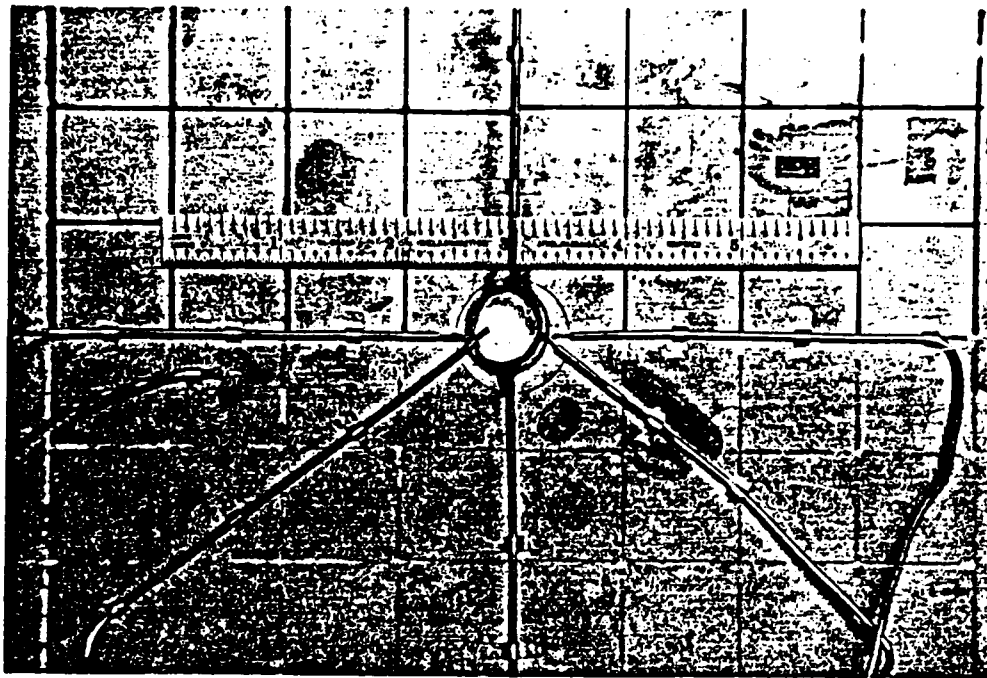


Fig. 42 Results of Burn Through Test on a 1/16 in Plate Specimen
Using 5 KW/cm² of Laser Power for Approximately 1.2 Seconds

photographic documentation difficult; 4) the thermocouple reference junction needed to be below room temperature; 5) a constant aperture setting on the video and high speed cameras made photographic interpretation difficult at the specimen heated up; 6) the pyrometer data was inappropriately scaled; and 7) there was apparent movement of the LVDT support stand during laser deposition.

It appears that the PCM malfunctioned during the experiments. It is believed that significant background noise at 60 Hz was picked up by the apparatus, thus invalidating the experimental results. Due to logistical problems, it was not possible to perform further experiments to study this problem.

Table 4. Laser Parameters for the Specified Tests

Test	Shot Number	Incident Energy (KW- sec)	Beam Area (cm ²)	Heat Flux(KW/cm ²)	Shot Duration
1	49540	1.4	1.4	1	5.0
2	49541	2.8	1.4	2	3.0
3	49546	4.2	1.4	3	1.0
4	49550	7.0	1.4	5	1.2-1.6

Further details about the experimental program on plates can be found in reference 2 and Appendix 7.7.

2.4 Conclusions

We have synopsised herein the results obtained during the course of AFOSR contract no. F49620-86-K-0016. Below are a few of the major conclusions formed as a result of this research effort:

- 1) analytic results suggest that high energy laser heating can induce dynamic response in plate-like structural components;
- 2) where heating is of sufficient intensity, it is possible to induce significant viscoplastic deformations in plates, and this inelastic response produces significantly different behavior from elastic results;
- 3) laser heating of thin plates can produce significant geometric nonlinearity;

- 4) two-way thermomechanical coupling in laser heated plates does not appear to be significant because the inelastic strains do not oscillate substantially;
- 5) elastic properties in plates composed of short fiber metal matrix composites appear to be strongly affected by the forming process - a model has been proposed herein to account for this effect;
- 6) the thermoviscoplastic constitution of short fiber metal matrix composites is highly complicated - a thermoviscoplastic model has been proposed herein which utilizes the equivalent inclusion method;
- 7) in order to model the thermoviscoplastic deformations that occur in a laser heated metallic plate, it is necessary to develop sophisticated constitutive equations; these equations require that a series of complicated experiments be performed - this has been done herein for two candidate models; and
- 8) laser heating experiments on plates are extremely complex - although some initial experiments were performed as a part of this research, more experiments are needed before concise statements can be made about the accuracy of the models developed under this contract.

2.5 References

1. Allen, D.H. and Pilant, M.S., "Experimental and Theoretical Determination of the Thermomechanical Response of Inelastic Structural Materials to High Energy Thermal Inputs - First Annual Technical Report," MM 5485-87-7, Texas A&M University Mechanics and Materials Center, July, 1987.
2. Allen, D.H. and Pilant, M.S., "Experimental and Theoretical Determination of the Thermomechanical Response of Inelastic Structural Materials to High Energy Thermal Inputs - Second Annual Technical Report," MM 5485-88-5, Texas A&M University Mechanics and Materials Center, July, 1988.
3. Bodner, S.R. and Partom, Y., "Constitutive Equations for Elastic Viscoplastic Strain-Hardening Materials," Journal of Applied Mechanics, Vol. 42, No. 2, pp. 385-389, 1975.
4. Walker, K.P., "Representation of Hastelloy-X Behavior at Elevated Temperature with a Functional Theory of Viscoplasticity," ASME J. Eng. Mat. & Tech., 1982.
5. Miller, A.K., "A Unified Phenomenological Model for Monotonic, Cyclic and Creep Deformation of Strongly Work-Hardening Materials," Ph.D. Dissertation, Stanford University, May, 1975.
6. Benveniste, Y., Dvorak, G.J., and Chen, T., "Stress Fields in Composites with Coated Inclusions," Mechanics of Materials, vol. 6, 1987, pp. 147-157.
7. Mori, T., and Tanaka, K., "Average Stress in Matrix and Average Elastic Energy of Materials with Misfitting Inclusions," Acta Metallurgica, vol. 21, 1973, pp. 571-574.
8. Mura, T., Micromechanics of Defects in Solids, Martinus Nijhoff, 1982.
9. Hashin, Z., "Analysis of Composite Materials," Journal of Applied Mechanics, vol. 50, 1983, pp. 481-505.
10. Eshelby, J.D., "The Determination of the Elastic Field of the Ellipsoidal Inclusion, and Related Problems," Proceedings of the Royal Society, London vol. A241, 1957, pp. 376-396.
11. Taya, M., and Chou, T.-W., "On Two Kinds of Ellipsoidal Inhomogeneities in an Infinite Elastic Body: An Application to a Hybrid Composite," International Journal of Solids and Structures, vol. 17, 1981, pp. 553-563.
12. Hill, R., "Continuum Micro-Mechanics of Elastoplastic Polycrystals," Journal of the Mechanics and Physics of Solids, vol. 13, 1965, pp. 89-101.

13. Tandon, G.P., and Weng, G.J., "A Theory of Particle-Reinforced Plasticity," Journal of Applied Mechanics, vol. 55, 1988, pp. 136-135.
14. Hill, R., "Elastic Properties of Reinforced Solids: Some Theoretical Principles," Journal of Mechanics and Physics of Solids, Vol. 11, 1963, pp. 357-372.
15. Hill, R., "A Self-Consistent Mechanics of Composite Materials," Journal of the Mechanics and Physics of Solids, vol. 13, 1965, pp. 213-222.
16. Morris, P.R., "Elastic Constants of Polycrystals," International Journal of Engineering Science, vol. 8, 1970, pp. 49-61.
17. Hill, R., "The Essential Structure of Constitutive Laws for Metal Composites and Polycrystals," Journal of the Mechanics and Physics of Solids, vol. 15, 1967, pp. 79-95.
18. Suquet, P.M., "Local and Global Aspects in the Mathematical Theory of Plasticity," in Plasticity Today, A. Sawczuk, ed., Elsevier, 1985, pp. 279-310.
19. Walker, K.P., and Jordan, E.M., "Biaxial Constitutive Modelling and Testing of a Single Crystal Superalloy at Elevated Temperatures," in Biaxial and Multiaxial Fatigue, M.W. Brown, ed., Mechanical Engineering Publications, Ltd., London, 1989, pp. 145-170.
20. Kim, Y.S., Verrilli, M.J., and Gabb, T.P., "Characterization of Failure Processes in Tungsten Copper Composites Under Fatigue Loading Conditions," NASA Technical Memorandum 102371, 1989.
21. Taya, M., "On Stiffness and Strength of an Aligned Short-Fiber Reinforced Composite Containing Penny-Shaped Cracks in the Matrix," Journal of Composite Materials, vol. 15, 1981, pp. 198-210.
22. Taya, M. and Mura, T., "On Stiffness and Strength of an Aligned Short-Fiber Reinforced Composite Containing Fiber-End Cracks Under Uniaxial Applied Stress," Journal of Applied Mechanics, June 1981, vol. 48, pp. 361-367.
23. Hashin, Z. and Rosen, B.W., "The Elastic Moduli of Fiber-Reinforced Materials," Journal of Applied Mechanics, 1964, pp. 223-231.
24. Chou, T.W., Nomura, S., and Taya, M., "A Self-Consistent Approach to the Elastic Stiffness of Short-Fiber Composites," Journal of Composite Materials, Vol. 14, 1980, pp. 178-188.
25. Halpin, J.C. and Pagano, N.J., "The Laminate Approximation for Randomly Oriented Fibrous Composites," Journal of Composite Materials, Vol. 3, 1969, pp. 720-724.

26. Christensen, R.M. and Waals, F.M., "Effective Stiffness of Randomly Oriented Fibrous Composites," Journal of Composite Materials, Vol. 6, 1972, pp. 518-532.
27. Lee, L.H., "Strength-Composition Relationships of Random Short Glass Fiber-Thermoplastic Composites," Polymer Engineering and Science, Vol.9, No. 3, 1969, pp. 213-224.

PUBLICATION LIST

1. Chang, H.T. and Allen, D.H., "A Finite Element Analysis of a Viscoplastic Plate Subjected to Rapid Heating," Mechanics of Structures and Machines An International Journal, Vol. 17, No. 1, pp. 1-21, 1989 (see reference 1).
2. Chang, H.T. and Allen, D.H., "Analysis of a Viscoplastic Plate Subjected to Rapid External Heating," Finite Elements in Analysis and Design, Vol. 5, pp. 167-179, 1989 (see reference 2).
3. Allen, D.H., "A Review of the Theory of Thermomechanical Coupling in Inelastic Solids," Applied Mechanics Reviews, ASME, 1990 (to appear-see Appendix 7.5).
4. Allen, D.H. and Harris, C.E., "Nonlinear Constitutive Behavior of Metals," NASA Special Technical Publication, 1990 (to appear-see Appendix 7.6).
5. Imbrie, P.K. and Allen, D.H., "Laser/Structure Interaction - A Comparison of Theory to Experiment," Proceedings AIAA Aerospace Sciences Meeting, Reno, 1989 (see Appendix 7.7).
6. Lee, J.W. and Allen, D.H., "A Model for Predicting the Effective Elastic Properties of Randomly Oriented Fiber Composites Subjected to Hot Pressing, Extrusion, and Rolling," Proceedings 30th AIAA/ASME/ASCE/AHS/ASC Structures, Structural Dynamics, and Materials Conference, Mobile, Part II, pp. 820-825, 1989 (see Appendix 7.2).
7. Boyd, J.G., "A Self-Consistent Thermoviscoplastic Constitutive Model for Short-Fiber Composites," to appear in Proc. Symposium on Microcracking Induced Damage in Composites, ASME Winter Annual Meeting, 1990 (see Appendix 7.3).
8. McCrea, L.D., Imbrie, P.K., and Allen, D.H., "Application of Current Unified Viscoplastic Constitutive Models to Hastelloy X at Elevated Temperatures," submitted to the Journal of Engineering Materials Technology, 1990 (see Appendix 7.4).
9. Chang, H.T. and Allen, D.H., "Analysis of Viscoplastic Plates Subjected to Rapid External Heating," Proc. 29th AIAA/ASME/ASCE/AHS Structures, Structural Dynamics and Materials Conference, Part III, pp. 1640-1647, 1988 (see reference 1).
10. Pilant, M.S., Analysis of Coupling and Rate Effects in Viscoplastic Plates Subjected to Rapid Heating," Texas A&M University Center for Mechanics of Composites, 1990 (see Appendix 7.1).

11. Bryan, S.K., Allen, D.H., and Pilant, M.S., "Development of Hyperbolic Heat Conduction Equations for Solids," Texas A&M University Mechanics and Materials Center, 1987 (see reference 1).

RESEARCH ASSIGNMENTS

4.1 Faculty Assignments

1. Dr. D.H. Allen (Co-principal Investigator) - overall project coordination; development of coupled field equations; development of transient temperature constitutive equations; experimental programs; one-way coupled finite element models.
2. Dr. M.S. Pilant (Co-principal Investigator) - development of coupled field equations; two-way coupled finite element models.
3. Mr. P.K. Imbrie (Lecturer and Ph.D. Candidate) - coordinator for experimental programs; transient temperature constitutive models.

4.2 Additional Staff

1. Mrs. C. Terry (Secretary) - secretarial support.
2. Mr. H.T. Chang (Ph.D. Research Assistant) - one-way coupled finite element model (completed degree June, 1988).
3. Capt. S.K. Bryan (Ph.D. Candidate) - development of coupled field equations (completed degree June, 1988).
4. Ms. L.D. McCrea (M.S. Research Assistant) - experimental constitutive equations (completed degree June, 1990).
5. Mr. G. Geong (Ph.D. Candidate) - two-way coupled finite element model.

INTERACTIONS

5.1 Presentations (since second annual report)

1. Allen, D.H., "Modelling Nonlinear Response of Metallic Media at Elevated Temperatures," NASA Langley Research Center, April, 1988.
2. Allen, D.H., "Analysis of Viscoplastic Plates Subjected to Laser Heating," Lawrence Livermore National Labs, February, 1989.
3. Allen, D.H., "Damage Mechanics in Laminated Composites," Florida State University, June, 1989.
4. Allen, D.H., "Mechanics of Damage in Metal Matrix Composites," University of Virginia, February, 1990.
5. Allen, D.H., "Thermal Effects in Inelastic Solids," M.I.T., February, 1990.
6. Allen, D.H., "A Review of the Theory of Thermomechanical Coupling in Inelastic Solids," University of Virginia, February 1990.
7. Allen, D.H., "Analysis and Experiment of Rapidly Heated Viscoplastic Plates," Sixth Forum on Large Space Structures, Atlanta, 1988.
8. Allen, D.H., Imbrie, P.K. Chang, H.T., and Jeong, G.S., "Analysis and Experiment of Rapidly Heated Viscoplastic Plates," ASME Winter Annual Meeting, Chicago, 1988.
9. Allen, D.H. and Lee, J.W., "The Effective Thermoelastic Properties of Whisker-Reinforced Composites as Functions of Material Forming Parameters," ASME Winter Annual of Material Forming Parameters" ASME Winter Annual Meeting, San Francisco, 1989.

5.2 Awards and Achievements

1. Dr. Allen has been named Director of the newly created Center for Mechanics of Composites at Texas A&M University.
2. Dr. Allen received the Texas A&M University Association of Former Students Award for Distinguished Research Achievement in 1989.
3. Dr. Allen received the Halliburton Award for Distinguished Research in 1988.
4. Dr. Allen was promoted to full professor in 1988.

5. Dr. Pilant was tenured and promoted to associate professor in 1989.

5.3 Other

1. Dr. Allen served as Associate Editor of the Journal of Spacecraft and Rockets from 1984 to 1990.
2. Dr. Allen taught three shortcourses on thermoviscoplasticity through the AIAA Professional Educational Program in 1988, 1989, and 1990.

GRADUATE STUDENT ACTIVITIES

6.1 Theses Completed

1. H.T. Chang, "Analysis of Viscoplastic Plates Subjected to Rapid Heat Inputs," Ph.D., 1988.
2. L.D. McCrea, "Application of Current Unified Viscoplastic Constitutive Models to Hastelloy X at Elevated Temperatures," M.S., 1990.
3. G. Jeong, "Modelling of Two-Way Coupling in Rapidly Heated Thermoviscoplastic Plates," Ph.D., 1990 (to appear in December).
4. P.K. Imbrie, "Experimental Testing of Viscoplastic Metals During Thermal Transients," Ph.D., 1990 (to appear in December).

6.2 Thesis Abstracts

ABSTRACT

A Finite Element Model for Predicting Nonlinear Thermomechanical
Response of Plate Structures to Rapid External Heating. (August 1988)

Huang-Tsang Chang, B.S., National Taiwan University;

M.S., Oklahoma State University

Chairman of Advisory Committee: David H. Allen

The objective of this dissertation is to develop a solution algorithm capable of predicting transient thermal/structural response of viscoplastic metallic thin plates exposed to hostile thermal loads. In the second chapter of this dissertation, the author will describe the general background of the problem being considered in this research. By assuming one-way coupled thermal/structural response, a solution approach is then outlined in the following chapter. In chapter four, a finite element formulation is utilized to construct the solution algorithm. The developed code is verified with several simple cases in chapter five. In chapter six example problems are given to demonstrate the full capabilities of the model. Finally, suggestions to improve the current model are given and conclusions are drawn from this research in chapter seven.

ABSTRACT

APPLICATION OF CURRENT UNIFIED VISCOPLASTIC
CONSTITUTIVE MODELS TO HASTELLOY X AT
ELEVATED TEMPERATURES. (August 1990)

Lisa Diane McCrea, B.S., Texas A&M University;

M.S., Texas A&M University

Chair of Advisory Committee: Dr. David H. Allen

The unified viscoplastic constitutive theories of Bodner-Partom and Walker were investigated to determine their predictive capabilities using experimentally obtained data on Hastelloy X, at 1100 and 1700°F, as the basis of comparison. Material parameters for these models were obtained using an iterative style approach, which does not require the constants to be explicitly evaluated, as is traditionally done. Instead, the nonlinear form of the constitutive equations are numerically integrated using physical insight, as well as knowledge of the parameters, until acceptable values are obtained.

Comparisons to experimental data revealed that the constitutive theories are not able to simultaneously model the initial and fully saturated condition of a material which has undergone a considerable amount of cyclic hardening. In addition, a power law based strain rate equation is shown to model this material system best overall.

The iterative method for determining the material constants is shown to be a viable alternative, proving to be much simpler and less time consuming than previously developed procedures.

APPENDIX
INTERIM TECHNICAL REPORTS

Appendix 7.1

**Analysis of Coupling and Rate Effects
in Viscoplastic Plates
Subjected to Rapid Heating**

**Analysis of Coupling and Rate Effects
in Viscoplastic Plates
Subjected to Rapid Heating**

by

M.S. Pilant
Mathematics and Aerospace Engineering Departments
Texas A&M University
College Station, TX 77843

**Analysis of Coupling and Rate Effects
in Viscoplastic Plates
Subjected to Rapid Heating**

by

M.S. Pilant
Mathematics and Aerospace Engineering Departments
Texas A&M University
College Station, TX 77843

ABSTRACT

In this paper the governing equations of motion are constructed for a three dimensional domain which is composed of a thermoviscoplastic material subjected to both thermal and mechanical loading. The resulting thermodynamic and mechanical field equations are two-way coupled in the sense that the deformations are temperature dependent and vice versa. The field equations are cast into a well-posed boundary value problem, and a weak variational form is constructed. This form is then discretized using the finite element method.

Example problems are solved for a circular plate subjected to rapid external heating simulating a laser input. It is found that inertial effects cannot be neglected, since the plate undergoes vibrational response. However, the two-way coupling appears to be a second order effect.

Formulation of 3-D, axi-symmetric equations of motion

0. Introduction

In this report, we derive the governing equations for a three dimensional plate, either freely supported or clamped (with no external loads), subjected to boundary heating by a laser focused on the center of the plate. No geometric nonlinearities are included, but two-way coupling between thermal and mechanical forces are allowed, as is the generation of heat by inelastic deformations.

In the first section, we derive the governing equations. In the second section, we derive the weak formulation of the system of partial differential equations. In the third section, we derive the Galerkin finite element method (FEM) for this problem. In section 4, we define various coefficients and forces for the problem.

1. Governing equations

We consider a radially symmetric three dimensional plate. We examine two different boundary conditions – freely supported with no external loads and clamped, with no external loads. The momentum equations are

$$\rho \frac{\partial^2 u}{\partial t^2} - \left[\frac{\partial}{\partial r} \sigma_{rr} + \frac{1}{r} \sigma_{rr} - \frac{1}{r} \sigma_{\theta\theta} + \frac{\partial}{\partial z} \sigma_{rz} \right] = 0, \quad (1.1)$$

$$\rho \frac{\partial^2 w}{\partial t^2} - \left[\frac{\partial}{\partial r} \sigma_{rz} + \frac{1}{r} \sigma_{rz} + \frac{\partial}{\partial z} \sigma_{zz} \right] = 0, \quad (1.2)$$

With thermo-elastic and inelastic coupling terms, the thermal equations are [1]

$$\rho c_v \frac{\partial T}{\partial t} - k \nabla^2 T + \alpha \dot{\epsilon}_{ii} T = \sigma_{ii} \dot{\epsilon}_{ii}^I, \quad (1.3)$$

and the constitutive relations are given by the simplified Bodner-Partom constitutive model [2]

$$\dot{\epsilon}_{ij}^I = \sqrt{2} D_0 \frac{\sigma_{ij}}{|\sigma_{ij}|} \exp\left(-\frac{2^{n-1}}{3^n} \left|\frac{\alpha_2}{|\sigma_{ij}|}\right|^{2n}\right), \quad (1.4)$$

$$\dot{\alpha}_2 = m(Z_1 - \alpha_2) \sigma_{ij} \dot{\epsilon}_{ij}^I - A_1 Z_1 \left(\frac{\alpha_2 - Z_I}{Z_1}\right)^r,$$

where ϵ_{ij}^I are the components of the inelastic strain, and α_2 is the drag stress. We have defined $\bar{\sigma}_{ij} = \frac{1}{3}(\sum \sigma_{ii})\delta_{ij}$ and $|\sigma_{ij}| = \sqrt{\sum (\sigma_{ij} - \bar{\sigma}_{ij})^2}$.

The dependent variables are u — the radial displacement, w — the vertical displacement, T — the temperature, and $\epsilon_{ij}^I, \alpha_2$ — the internal state variables.

The stress-strain relations are given by

$$\sigma_{rr} = (\lambda + 2\mu)\epsilon_{rr} + \lambda(\epsilon_{\theta\theta} + \epsilon_{zz})$$

$$\sigma_{\theta\theta} = (\lambda + 2\mu)\epsilon_{\theta\theta} + \lambda(\epsilon_{rr} + \epsilon_{zz})$$

$$\sigma_{zz} = (\lambda + 2\mu)\epsilon_{zz} + \lambda(\epsilon_{rr} + \epsilon_{\theta\theta})$$

$$\sigma_{rz} = 2\mu\epsilon_{rz}$$

and the strains are related to the dependent variables by

$$\epsilon_{rr} = \frac{\partial u}{\partial r} - \epsilon_{rr}^I - \alpha(T - T_R)$$

$$\epsilon_{\theta\theta} = \frac{1}{r}u - \epsilon_{\theta\theta}^I - \alpha(T - T_R)$$

$$\epsilon_{zz} = \frac{\partial w}{\partial z} - \epsilon_{zz}^I - \alpha(T - T_R)$$

$$\epsilon_{rz} = \frac{1}{2}\left(\frac{\partial u}{\partial z} + \frac{\partial w}{\partial r}\right) - \epsilon_{rz}^I - \alpha(T - T_R)$$

We have assumed a thermal stress tensor α which is isotropic.

The above equations are the fully coupled, axi-symmetric equations describing the thermo-mechanically induced motion of a circular plate subject to boundary heating at the center of the plate.

In the next section, we derive the weak formulation of equations (1.1)-(1.4).

2. Weak formulation

Multiplying equation (1.1) by a test function ϕ and integrating by parts, we obtain

$$\frac{\partial^2}{\partial t^2} \int \int \phi \rho u r dr dz + \int \int \left[\frac{\partial \phi}{\partial r} r \sigma_{rr} + \frac{\partial \phi}{\partial z} r \sigma_{rz} + \phi \sigma_{\theta\theta} \right] dr dz = \int \phi r \sigma_{ri} n_i ds = 0 \quad (2.1)$$

Substituting for σ in the above equation, we have

$$\begin{aligned} & \frac{\partial^2}{\partial t^2} \int \int \phi \rho u r dr dz + \int \int \frac{\partial \phi}{\partial r} r (\lambda + 2\mu) \frac{\partial u}{\partial r} dr dz + \int \int \frac{\partial \phi}{\partial r} r \lambda \left(\frac{u}{r} + \frac{\partial w}{\partial z} \right) dr dz \\ & + \int \int \frac{\partial \phi}{\partial z} r \mu \left(\frac{\partial u}{\partial z} + \frac{\partial w}{\partial r} \right) dr dz + \int \int \left[\phi (\lambda + 2\mu) \frac{u}{r} + \phi \lambda \frac{\partial u}{\partial r} + \phi \lambda \frac{\partial w}{\partial z} \right] dr dz = \\ & \int \int \frac{\partial \phi}{\partial r} r [2\mu \epsilon_{rr}^I + (3\lambda + 2\mu) \alpha (T - T_R)] dr dz + \int \int \phi [2\mu \epsilon_{\theta\theta}^I + (3\lambda + 2\mu) \alpha (T - T_R)] dr dz + \\ & \int \int \frac{\partial \phi}{\partial z} r [2\mu \epsilon_{rz}^I + 2\mu \alpha (T - T_R)] dr dz \end{aligned} \quad (2.2)$$

where we have used the fact that $\dot{\epsilon}_{ii}^I = 0$ and consequently $\epsilon_{ii}^I = 0$, since we are starting from the elastic regime. Note that the right hand side of (2.2) is driven by two competing effects – the temperature difference $T - T_R$ and the inelastic terms ϵ_{ij}^I .

From equation (1.2) we obtain

$$\frac{\partial^2}{\partial t^2} \int \int \phi \rho w r dr dz + \int \int \left[\frac{\partial \phi}{\partial r} r \sigma_{rz} + \frac{\partial \phi}{\partial z} r \sigma_{zz} \right] dr dz = \int \phi r \sigma_{zi} n_i ds = 0 \quad (2.3)$$

Substituting for σ in the above equation, we have

$$\begin{aligned} & \frac{\partial^2}{\partial t^2} \int \int \phi \rho w r dr dz + \int \int \frac{\partial \phi}{\partial r} r \mu \left(\frac{\partial u}{\partial z} + \frac{\partial w}{\partial r} \right) dr dz \\ & + \int \int \frac{\partial \phi}{\partial z} r (\lambda + 2\mu) \frac{\partial w}{\partial z} dr dz + \int \int \frac{\partial \phi}{\partial z} r \lambda \left(\frac{\partial u}{\partial r} + \frac{u}{r} \right) dr dz = \\ & \int \int \frac{\partial \phi}{\partial r} r 2\mu [\epsilon_{rz}^I + \alpha (T - T_R)] dr dz + \int \int \frac{\partial \phi}{\partial z} r [2\mu \epsilon_{zz}^I + (3\lambda + 2\mu) \alpha (T - T_R)] dr dz \end{aligned} \quad (2.4)$$

Again, note that the right hand side of (2.4) is driven by two competing effects – the temperature difference $T - T_R$ and the inelastic terms ϵ_{ij}^I .

Integrating (1.3) against a test function ϕ we get

$$\frac{\partial}{\partial t} \int \int \phi \rho c_v T r dr dz + \int \int k r \left[\frac{\partial \phi}{\partial r} \frac{\partial T}{\partial r} + \frac{\partial \phi}{\partial z} \frac{\partial T}{\partial z} \right] dr dz = \quad (2.5)$$

$$\int \phi Q ds + \int \int \phi \sigma_{ii} \dot{\epsilon}_{ii}^I r dr dz - \int \int \phi \alpha \dot{\sigma}_{ii} T r dr dz$$

where the normal flux $Q = k \frac{\partial T}{\partial n}$ is given by the Boltzmann Law

$$Q = Q_{in} + \sigma_s \epsilon (T^4 - T_\infty^4) \quad (2.6)$$

where Q_{in} is the thermal input (on the boundary), σ_s is the Boltzmann constant, and ϵ is the emissivity of the surface. The heat equation (2.5) is driven by the boundary heat input Q (which appears as a forcing term), the inelastic heating, and the thermo-elastic coupling term.

The FEM equations for u are fairly singular when $r = 0$. Since the radial displacement must vanish at $r = 0$ for an intact plate, we define a new variable U by $u \equiv rU$. In terms of the variables U , w and T we have

$$\begin{aligned} & \frac{\partial^2}{\partial t^2} \int \int \phi \rho U r^2 dr dz + \int \int \frac{\partial \phi}{\partial r} r (\lambda + 2\mu) (U + r \frac{\partial U}{\partial r}) dr dz + \int \int \frac{\partial \phi}{\partial r} r \lambda (U + \frac{\partial w}{\partial z}) dr dz \quad (2.2') \\ & + \int \int \frac{\partial \phi}{\partial z} r \mu (r \frac{\partial U}{\partial z} + \frac{\partial w}{\partial r}) dr dz + \int \int [\phi (\lambda + 2\mu) U + \phi \lambda (U + \frac{\partial U}{\partial r}) + \phi \lambda \frac{\partial w}{\partial z}] dr dz = \\ & \int \int \frac{\partial \phi}{\partial r} r [2\mu \epsilon_{rr}^I + (3\lambda + 2\mu) \alpha (T - T_R)] dr dz + \int \int \phi [2\mu \epsilon_{\theta\theta}^I + (3\lambda + 2\mu) \alpha (T - T_R)] dr dz + \\ & \int \int \frac{\partial \phi}{\partial z} r [2\mu \epsilon_{rz}^I + 2\mu \alpha (T - T_R)] dr dz \end{aligned}$$

and

$$\begin{aligned} & \frac{\partial^2}{\partial t^2} \int \int \phi \rho w r dr dz + \int \int \frac{\partial \phi}{\partial r} r \mu (r \frac{\partial U}{\partial z} + \frac{\partial w}{\partial r}) dr dz \quad (2.4') \\ & + \int \int \frac{\partial \phi}{\partial z} r (\lambda + 2\mu) \frac{\partial w}{\partial z} dr dz + \int \int \frac{\partial \phi}{\partial z} r \lambda (r \frac{\partial U}{\partial r} + 2U) dr dz = \\ & \int \int \frac{\partial \phi}{\partial r} r 2\mu [\epsilon_{rz}^I + \alpha (T - T_R)] dr dz + \int \int \frac{\partial \phi}{\partial z} r [2\mu \epsilon_{zz}^I + (3\lambda + 2\mu) \alpha (T - T_R)] dr dz \end{aligned}$$

and (2.5).

In terms of U , these equations no longer have a singularity at $r = 0$.

3. FEM formulation

To solve equations (2.2'), (2.4'), and (2.5), we approximate the unknowns by

$$U = \sum_{i=0}^{i=N} U_i(t) \phi_i(r, z), \quad (3.1)$$

$$w = \sum_{i=0}^{i=N} w_i(t) \phi_i(r, z), \quad (3.2)$$

and

$$T = \sum_{i=0}^{i=N} T_i(t) \phi_i(r, z) \quad (3.3)$$

This leads to the set of ordinary differential equations of the form

$$\begin{aligned} \mathbf{A}^{(1)} U'' + \mathbf{C}^{(1)} U &= \mathbf{F}^{(1)} - \mathbf{B}^{(1)} w \\ \mathbf{A}^{(2)} w'' + \mathbf{C}^{(2)} w &= \mathbf{F}^{(2)} - \mathbf{B}^{(2)} U \\ \mathbf{B}^{(3)} T' + \mathbf{C}^{(3)} T &= \mathbf{F}^{(3)} \end{aligned} \quad (3.4)$$

where the matrices are given by:

$$\mathbf{A}_{ij}^{(1)} = \int \int \phi_i \rho r^2 \phi_j dr dz$$

$$\mathbf{A}_{ij}^{(2)} = \int \int \phi_i \rho r \phi_j dr dz$$

$$\mathbf{B}_{ij}^{(1)} = \int \int \frac{\partial \phi_i}{\partial z} \mu r \frac{\partial \phi_j}{\partial r} dr dz + \int \int \frac{\partial \phi_i}{\partial r} \lambda r \frac{\partial \phi_j}{\partial z} dr dz + \int \int \phi_i \lambda \frac{\partial \phi_j}{\partial z} dr dz$$

$$\mathbf{B}_{ij}^{(2)} = \int \int \frac{\partial \phi_i}{\partial r} \mu r^2 \frac{\partial \phi_j}{\partial z} dr dz + \int \int \frac{\partial \phi_i}{\partial z} \lambda r^2 \frac{\partial \phi_j}{\partial r} dr dz + \int \int \frac{\partial \phi_i}{\partial z} 2 \lambda r \phi_j dr dz$$

$$\mathbf{B}_{ij}^{(3)} = \int \int \phi_i \rho c_v r \phi_j dr dz$$

$$\mathbf{C}_{ij}^{(1)} = \int \int \frac{\partial \phi_i}{\partial r} (\lambda + 2\mu) r^2 \frac{\partial \phi_j}{\partial r} dr dz + \int \int \frac{\partial \phi_i}{\partial r} (\lambda + 2\mu) r \phi_j dr dz + \int \int \frac{\partial \phi_i}{\partial z} \mu r^2 \frac{\partial \phi_j}{\partial z} dr dz$$

$$+ \iint \phi_i \lambda r \frac{\partial \phi_j}{\partial r} dr dz + \iint \frac{\partial \phi_i}{\partial r} \lambda r \phi_j dr dz + \iint \phi_i (2\lambda + 2\mu) \phi_j dr dz$$

$$C_{ij}^{(2)} = \iint \frac{\partial \phi_i}{\partial r} \mu r \frac{\partial \phi_j}{\partial r} dr dz + \iint \frac{\partial \phi_i}{\partial z} (\lambda + 2\mu) r \frac{\partial \phi_j}{\partial z} dr dz$$

$$C_{ij}^{(3)} = \iint \left[\frac{\partial \phi_i}{\partial r} k r \frac{\partial \phi_j}{\partial r} + \frac{\partial \phi_i}{\partial z} k r \frac{\partial \phi_j}{\partial z} \right] dr dz$$

and the forcing functions by:

$$\begin{aligned} F_i^{(1)} &= \iint \frac{\partial \phi_i}{\partial r} [2\mu \epsilon_{rr}^I + (3\lambda + 2\mu)\alpha(T - T_R)] r dr dz + \\ &\iint \frac{\partial \phi_i}{\partial z} [2\mu \epsilon_{rz}^I + 2\mu\alpha(T - T_R)] r dr dz + \iint \phi_i [2\mu \epsilon_{\theta\theta}^I + (3\lambda + 2\mu)\alpha(T - T_R)] dr dz \\ F_i^{(2)} &= \iint \frac{\partial \phi_i}{\partial r} 2\mu [\epsilon_{rz}^I + \alpha(T - T_R)] r dr dz + \iint \frac{\partial \phi_i}{\partial z} [2\mu \epsilon_{zz}^I + (3\lambda + 2\mu)\alpha(T - T_R)] r dr dz \\ \text{and} \\ F_i^{(3)} &= \iint \phi_i Q ds + \iint \phi_i \sigma_{jj} \dot{\epsilon}_{jj}^I r dr dz - \iint \phi_i k \dot{\sigma}_{jj} T r dr dz \end{aligned}$$

We note, for future reference, that if ρ , c_v , λ , μ , are constant in time, and independent of the temperature T , then the system of differential equations (3.1) have constant coefficients. This makes the solution by numerical integration very efficient, and allows one to investigate the relative importance of various terms in the equations without excessive computation.

If the coefficients change rapidly with temperature, the various stiffness matrices must be recomputed (and re-factored) at every time step, which is very time consuming. If the coefficients change more slowly, one must still periodically recompute and re-factor the matrix coefficients.

The first integral in $F_i^{(3)}$ is the contribution from the external heating on the boundary, the second integral is the contribution from the heating due to inelastic deformation, and the final integral contains the contribution due to elastic deformation.

If the second and third term are included, we call the model *two-way coupled*, otherwise it is *one-way coupled*. In the one-way coupled model, the temperature can be computed independently of the mechanical deformations of the material. We also note that the second contribution is always positive, that is inelastic deformation always yields heat.

In equation (1.3), we have

$$\alpha \dot{\sigma}_{ii} T = \alpha (3\lambda + 2\mu) \left[\frac{\partial u}{\partial r} + \frac{\dot{u}}{r} + \frac{\partial w}{\partial z} - 3\alpha \dot{T} \right] T$$

Therefore the coefficient of the $\frac{\partial T}{\partial t}$ term is

$$\rho c_v - 3\alpha^2(3\lambda + 2\mu)T.$$

If this quantity is negative, then (1.3) is no longer a well posed parabolic equation. This quantity is continuously monitored in the numerical computations.

4. Definitions of coefficients (for Computer Program)

In order to compute the integrals systematically, we define the following coefficients:

$$\begin{array}{lll} c_1 = \rho r & c_2 = \rho c_v r & c_3 = (\lambda + 2\mu)r \\ c_4 = \lambda r & c_5 = \mu r & c_6 = (\lambda + 2\mu) \\ c_7 = \lambda & c_8 = \mu & c_9 = kr \\ c_{10} = 1.0 & c_{11} = \rho r^2 & c_{12} = (\lambda + 2\mu)r^2 \\ c_{13} = \mu r^2 & c_{14} = \lambda r^2 & c_{15} = \alpha(3\lambda + 2\mu)Tr \\ c_{16} = \alpha(3\lambda + 2\mu)Tr^2 & c_{17} = \alpha 3(3\lambda + 2\mu)Tr. \end{array}$$

The flags icoeff are defined by:

$$\begin{array}{l} \text{icoeff} = 1 \text{ for expressions of the form } \iint \phi_i F \phi_j, \\ \text{icoeff} = 2 \text{ for expressions of the form } \iint \phi_i F \frac{\partial \phi_j}{\partial r}, \\ \text{icoeff} = 3 \text{ for expressions of the form } \iint \phi_i F \frac{\partial \phi_j}{\partial z}, \\ \text{icoeff} = 4 \text{ for expressions of the form } \iint \frac{\partial \phi_i}{\partial r} F \frac{\partial \phi_j}{\partial r}, \\ \text{icoeff} = 5 \text{ for expressions of the form } \iint \frac{\partial \phi_i}{\partial r} F \frac{\partial \phi_j}{\partial z}, \\ \text{icoeff} = 6 \text{ for expressions of the form } \iint \frac{\partial \phi_i}{\partial z} F \frac{\partial \phi_j}{\partial r}, \\ \text{icoeff} = 7 \text{ for expressions of the form } \iint \frac{\partial \phi_i}{\partial z} F \frac{\partial \phi_j}{\partial z}, \\ \text{icoeff} = 8 \text{ for expressions of the form } \iint \frac{\partial \phi_i}{\partial r} F \phi_j, \\ \text{icoeff} = 9 \text{ for expressions of the form } \iint \frac{\partial \phi_i}{\partial z} F \phi_j. \end{array}$$

The physical paramers for the material under consideration are

$$k_{\text{therm}} = 4.133 \times 10^{-3} \frac{\text{kg cal}}{\text{m sec } ^\circ \text{K}}$$

$$\lambda = 1.15 \times 10^7 \text{ MPa}$$

$$\mu = 4.9 \times 10^6 \text{ MPa}$$

$$\alpha = 8.64 \times 10^{-6} \frac{\text{cm}}{\text{cm } ^\circ \text{K}}$$

$$\rho = 8.221 \times 10^3 \frac{\text{kg}}{\text{m}^3}$$

$$c_v = 0.1 \frac{\text{cal}}{^\circ \text{K}}$$

$$\epsilon = 1.0,$$

$$\text{tmpref} = 493.0, \text{ and}$$

$$\text{steff} = 3.3 \times 10^{-15}.$$

The constitutive paramaters are given representatively by

$$n = 1$$

$$Z_1 = 2.03 \times 10^3 \text{ MPa}$$

$$A_1 = 6.5 \text{ sec}^{-1}$$

$$Z_I = Z_2 = 1.2 \times 10^3 \text{ MPa}$$

$$r = 0.98.$$

5. System of Equations

The formulation in sections 2 and 3 is sufficient to compute the displacements accurately; however, computing the stresses and strains (which involve gradients of the displacements) near the origin where $r = 0$ is a delicate procedure. As an alternative method, we could write the system in terms of the nine dependent variables $\{u, \frac{\partial u}{\partial r}, \frac{\partial u}{\partial z}, w, \frac{\partial w}{\partial r}, \frac{\partial w}{\partial z}, T, \frac{\partial T}{\partial r}, \frac{\partial T}{\partial z}\}$.

With $u_1 = \frac{u}{r} = U$, $u_2 = \frac{\partial U}{\partial r}$, $u_3 = \frac{\partial U}{\partial z}$, $w_1 = w$, $w_2 = \frac{\partial w}{\partial r}$, $w_3 = \frac{\partial w}{\partial z}$, $T_1 = T$, $T_2 = \frac{\partial T}{\partial r}$, $T_3 = \frac{\partial T}{\partial z}$, the system of equations can be written as:

$$\frac{\partial^2}{\partial t^2} \int \int \phi \rho r^2 u_1 dr dz + \int \int \left[\frac{\partial \phi}{\partial r} r (2\lambda + 2\mu) + \phi (2\lambda + 2\mu) \right] u_1 dr dz = \quad (5.1)$$

$$- \int \int \frac{\partial \phi}{\partial r} r^2 (\lambda + 2\mu) u_2 dr dz - \int \int \phi \lambda r u_2 dr dz - \int \int \frac{\partial \phi}{\partial z} r^2 \mu u_3 dr dz$$

$$- \int \int \frac{\partial \phi}{\partial z} r \mu w_2 dr dz - \int \int \left[\frac{\partial \phi}{\partial r} r \lambda + \phi \lambda \right] w_3 dr dz$$

$$+ \int \int \left[(3\lambda + 2\mu) \alpha \left(\phi + r \frac{\partial \phi}{\partial r} \right) + 2\mu \alpha r \frac{\partial \phi}{\partial z} \right] (T_1 - T_R) dr dz$$

$$+ \int \int \left[\frac{\partial \phi}{\partial r} 2\mu r \epsilon_{rr}^I \frac{\partial \phi}{\partial z} 2\mu r \epsilon_{rz}^I + \phi 2\mu \epsilon_{\theta\theta}^I \right] dr dz$$

$$\int \int \phi u_2 dr dz = \int \int \phi \frac{\partial}{\partial r} u_1 dr dz \quad (5.2)$$

$$\int \int \phi u_3 dr dz = \int \int \phi \frac{\partial}{\partial z} u_1 dr dz \quad (5.3)$$

$$\frac{\partial^2}{\partial t^2} \int \int \phi \rho r w_1 dr dz = - \int \int \frac{\partial \phi}{\partial z} 2r \lambda u_1 dr dz - \int \int \frac{\partial \phi}{\partial z} r^2 \lambda u_2 dr dz \quad (5.4)$$

$$\begin{aligned}
& - \int \int \frac{\partial \phi}{\partial r} r^2 \mu u_3 dr dz - \int \int \frac{\partial \phi}{\partial r} r \mu w_2 dr dz - \int \int \frac{\partial \phi}{\partial z} r (\lambda + 2\mu) w_3 dr dz \\
& + \int \int \left[\frac{\partial \phi}{\partial z} (3\lambda + 2\mu) \alpha r + \frac{\partial \phi}{\partial r} 2\mu \alpha r \right] (T_1 - T_R) dr dz \\
& + \int \int \left[\frac{\partial \phi}{\partial r} 2\mu r \epsilon_{rz}^I + \phi 2\mu r \epsilon_{zz}^I \right] dr dz \\
& \int \int \phi w_2 dr dz = \int \int \phi \frac{\partial}{\partial r} w_1 dr dz \tag{5.5}
\end{aligned}$$

$$\int \int \phi w_3 dr dz = \int \int \phi \frac{\partial}{\partial z} w_1 dr dz \tag{5.6}$$

$$\frac{\partial}{\partial t} \int \int \phi \rho c_v r T_1 dr dz = - \int \int \frac{\partial \phi}{\partial r} k r T_2 dr dz - \int \int \frac{\partial \phi}{\partial z} k r T_3 dr dz \tag{5.7}$$

$$\begin{aligned}
& + \int \phi Q ds + \int \int \phi \sigma_{jj} \dot{\epsilon}_{jj}^I dr dz - \int \int \phi \alpha \dot{\sigma}_{jj} T_1 r dr dz = \\
& - \int \int \frac{\partial \phi}{\partial r} k r T_2 dr dz - \int \int \frac{\partial \phi}{\partial z} k r T_3 dr dz + \int \phi Q ds
\end{aligned}$$

$$\begin{aligned}
& + \int \int \phi \sigma_{jj} \dot{\epsilon}_{jj}^I dr dz - \int \int \phi r \alpha (3\lambda + 2\mu) T_1 [2\dot{u}_1 + r\dot{u}_2 + \dot{w}_3 - 3\alpha \dot{T}_1] dr dz \\
& \int \int \phi T_2 dr dz = \int \int \phi \frac{\partial}{\partial r} T_1 dr dz \tag{5.8}
\end{aligned}$$

$$\int \int \phi T_3 dr dz = \int \int \phi \frac{\partial}{\partial z} T_1 dr dz \tag{5.9}$$

This leads to a 9×9 system of ordinary equations

$$A_1 u_1'' + A_2 u_1 = -M_1 u_2 - M_2 u_3 - M_3 w_2 - M_4 w_3 + M_5 (T_1 - T_R)$$

$$A_3 u_2 = M_6 u_1 + A_3 u_1$$

$$A_3 u_3 = M_7 u_1$$

$$A_4 w_1'' = -M_8 u_1 - M_9 u_2 - M_{10} u_3 - M_{11} w_2 - M_{12} w_3 + M_{13} (T_1 - T_R)$$

$$A_3 w_2 = M_{19} w_1$$

$$A_3 w_3 = M_{20} w_1$$

$$A_5 T_1' = -M_{14} T_2 - M_{15} T_3 + Q - 2M_{16} \dot{u}_1 - M_{17} \dot{u}_2 - M_{16} \dot{w}_3 + M_{18} \dot{T}_1$$

$$A_3 T_2 = M_{19} T_1$$

$$A_3 T_3 = M_{20} T_1$$

where

$$A_1 = \int \int \phi_i \rho r^2 \phi_j dr dz$$

$$A_2 = \int \int \frac{\partial \phi_i}{\partial r} r (2\lambda + 2\mu) \phi_j dr dz + \int \int \phi_i (2\lambda + 2\mu) \phi_j dr dz$$

$$A_3 = \int \int \phi_i \phi_j dr dz$$

$$A_4 = \int \int \phi_i \rho r \phi_j dr dz$$

$$A_5 = \int \int \phi_i \rho c_v r \phi_j dr dz$$

$$M_1 = \int \int \frac{\partial \phi_i}{\partial r} r^2 (\lambda + 2\mu) \phi_j dr dz + \int \int \phi_i \lambda r \phi_j dr dz$$

$$M_2 = \int \int \frac{\partial \phi_i}{\partial z} r^2 \mu \phi_j dr dz$$

$$M_3 = \int \int \frac{\partial \phi_i}{\partial z} r \mu \phi_j dr dz$$

$$M_4 = \int \int \frac{\partial \phi_i}{\partial r} r \lambda \phi_j dr dz + \int \int \phi_i \lambda \phi_j dr dz$$

$$M_5 = \int \int \phi_i (3\lambda + 2\mu) \alpha \phi_j dr dz + \int \int \frac{\partial \phi_i}{\partial r} (3\lambda + 2\mu) \alpha r \phi_j dr dz + \int \int \frac{\partial \phi_i}{\partial z} 2\mu \alpha r \phi_j dr dz$$

$$M_6 = \int \int \phi_i r \frac{\partial \phi_j}{\partial r} dr dz$$

$$M_7 = \int \int \phi_i r \frac{\partial \phi_j}{\partial z} dr dz$$

$$M_8 = \int \int \frac{\partial \phi_i}{\partial z} 2r \lambda \phi_j dr dz$$

$$M_9 = \int \int \frac{\partial \phi_i}{\partial z} r^2 \lambda \phi_j dr dz$$

$$M_{10} = \int \int \frac{\partial \phi_i}{\partial r} r^2 \mu \phi_j dr dz$$

$$M_{11} = \int \int \frac{\partial \phi_i}{\partial r} r \mu \phi_j dr dz$$

$$\begin{aligned}
M_{12} &= \int \int \frac{\partial \phi_i}{\partial z} r (\lambda + 2\mu) \phi_j dr dz \\
M_{13} &= \int \int \frac{\partial \phi_i}{\partial z} (3\lambda + 2\mu) \alpha r \phi_j dr dz + \int \int \frac{\partial \phi_i}{\partial r} 2\mu \alpha r \phi_j dr dz \\
M_{14} &= \int \int \frac{\partial \phi_i}{\partial r} k r \phi_j dr dz \\
M_{15} &= \int \int \frac{\partial \phi_i}{\partial z} k r \phi_j dr dz \\
M_{16} &= \int \int \phi_i (3\lambda + 2\mu) r \alpha T_1 \phi_j dr dz \\
M_{17} &= \int \int \phi_i (3\lambda + 2\mu) r^2 \alpha T_1 \phi_j dr dz \\
M_{18} &= \int \int \phi_i (3\lambda + 2\mu) 3\alpha^2 T_1 \phi_j dr dz \\
M_{19} &= \int \int \phi_i \frac{\partial \phi_j}{\partial r} dr dz \\
M_{20} &= \int \int \phi_i \frac{\partial \phi_j}{\partial z} dr dz \\
M_{21} &= \int \int \frac{\partial \phi_i}{\partial r} k r \frac{\partial \phi_j}{\partial r} dr dz \\
M_{22} &= \int \int \frac{\partial \phi_i}{\partial z} k r \frac{\partial \phi_j}{\partial z} dr dz
\end{aligned}$$

This was in fact coded up, but did not give satisfactory results.

6. Alternate First Order System of Equations

With the substitutions $u_1 = U = u/r$, $u_2 = \frac{\partial}{\partial t} u_1/r$, $u_3 = \frac{\partial}{\partial r} u_1$, $u_4 = \frac{\partial}{\partial z} u_1$, $u_5 = w$, $u_6 = \frac{\partial w}{\partial t}$, $u_7 = \frac{\partial w}{\partial r}$, $u_8 = \frac{\partial w}{\partial z}$, and $u_9 = T$, this leads to a slightly different 9×9 system of ordinary equations.

$$u'_1 = u_2$$

$$A_1 u'_2 = -A_2 u_1 - M_1 u_3 - M_2 u_4 - M_3 u_7 - M_4 u_8 + M_5 (u_9 - T_R)$$

$$A_3 u'_3 = M_{19} u_2$$

$$A_3 u'_4 = M_{20} u_2$$

$$u'_5 = u_6$$

$$A_4 u'_6 = -M_8 u_1 - M_9 u_3 - M_{10} u_4 - M_{11} u_7 - M_{12} u_8 + M_{13} (u_9 - T_R)$$

$$A_3 u'_7 = M_{19} u_5$$

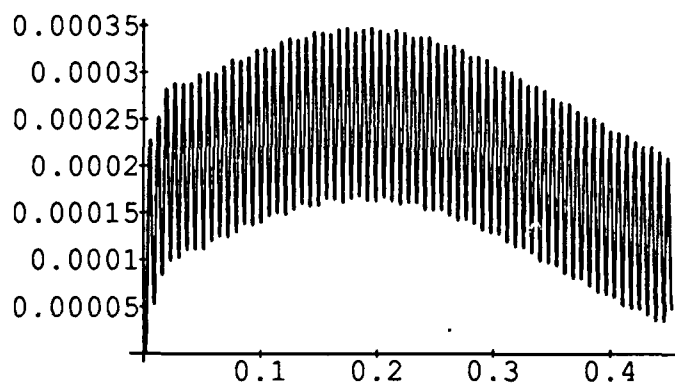
$$A_3 u'_8 = M_{20} u_5$$

$$A_5 u'_9 + M_{21} u_9 + M_{22} u_9 = Q - 2M_{16} \dot{u}_1 - M_{17} \dot{u}_3 - M_{16} \dot{u}_8 + M_{18} \dot{u}_9$$

Although mathematically interesting, we were not able to numerically implement this effectively either.

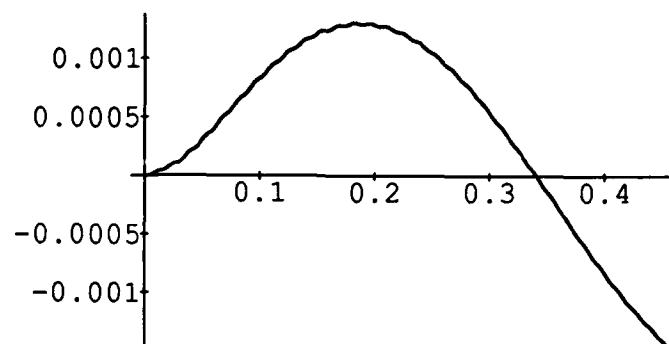
Case I. The laser input was given by a step function, with $Q = Q_{max} = 2.5 \times 10^4$ Btu/m², duration 0.020 sec, and a radius of 2.0 cm. The equations were integrated with $\theta_i = 0.5$, $\Delta t = 0.0001$, N_ITER=4, with condensing and smoothing flags on. No thermo-elastic or inelastic heating effects were included.

The graph below is that of the horizontal deflection $u(r_{max}, z_{max}, t)$, where the horizontal deflection reaches its maximum.

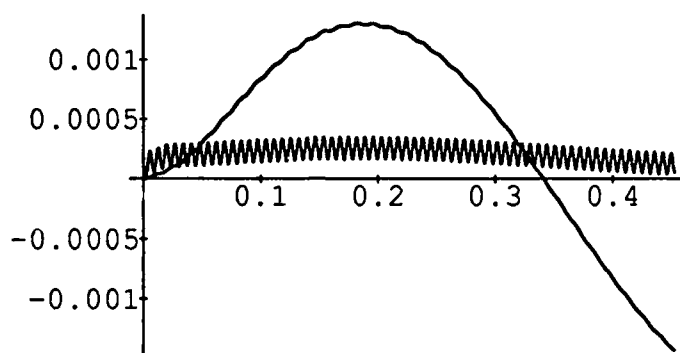


Note that a characteristic frequency of 142.5 cycles/sec is present in the radial direction, whereas a much slow vertical oscillation is induced (see the next figure).

The following is a graph of the vertical deflection $w(0, z_{\max}, t)$ at the point where the laser is impinging.



On the same scale, we have



The r-coordinates are given by

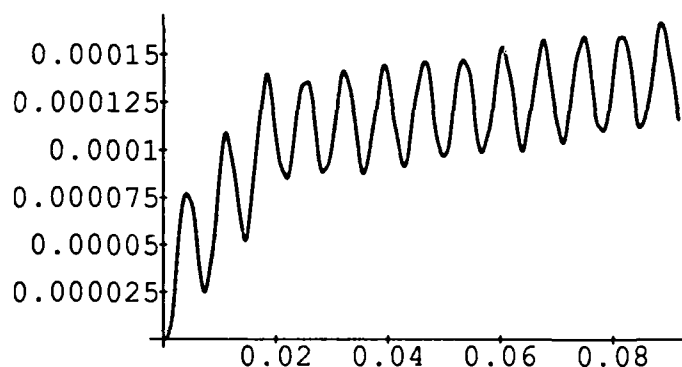
$\{0.00e-2, 0.02e-2, 0.05e-2, 0.10e-2, 0.20e-2, 0.50e-2, 1.00e-2, 2.00e-2, 4.00e-2, 7.00e-2, 10.00e-2\}$

and the z-coordinates by

$\{0.00e-3, 0.20e-3, 0.40e-3, 0.60e-3, 0.70e-3, 0.80e-3, 0.90e-3, 1.00e-3\}$.

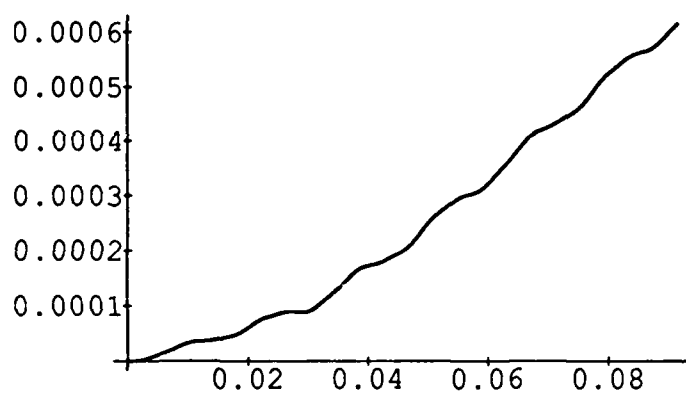
Case II. The laser input was given by a step function, with $Q = Q_{max} = 2.5 \times 10^4$ Btu/m², duration 0.020 sec, and a radius of 2.0 cm. The equations were integrated with $\theta_i = 0.5$, $\Delta t = 0.00002$, N_ITER=4, with condensing and smoothing flags on. No thermo-elastic or inelastic heating effects were included.

The graph below is that of the horizontal deflection $u(r_{max}, z_{max}, t)$, where the horizontal deflection reaches its maximum.

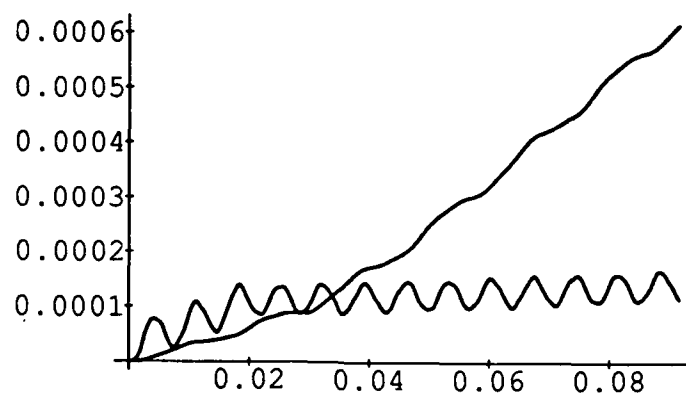


Note that a characteristic frequency of 150 cycles/sec is present in the radial direction, whereas a much slow vertical oscillation is induced (see the next figure).

The following is a graph of the vertical deflection $w(0, z_{\max}, t)$ at the point where the laser is impinging.



On the same scale, we have



The r-coordinates are given by

$\{0.00e-2, 0.02e-2, 0.05e-2, 0.10e-2, 0.20e-2, 0.50e-2, 1.00e-2, 2.00e-2, 4.00e-2, 7.00e-2, 10.00e-2\}$

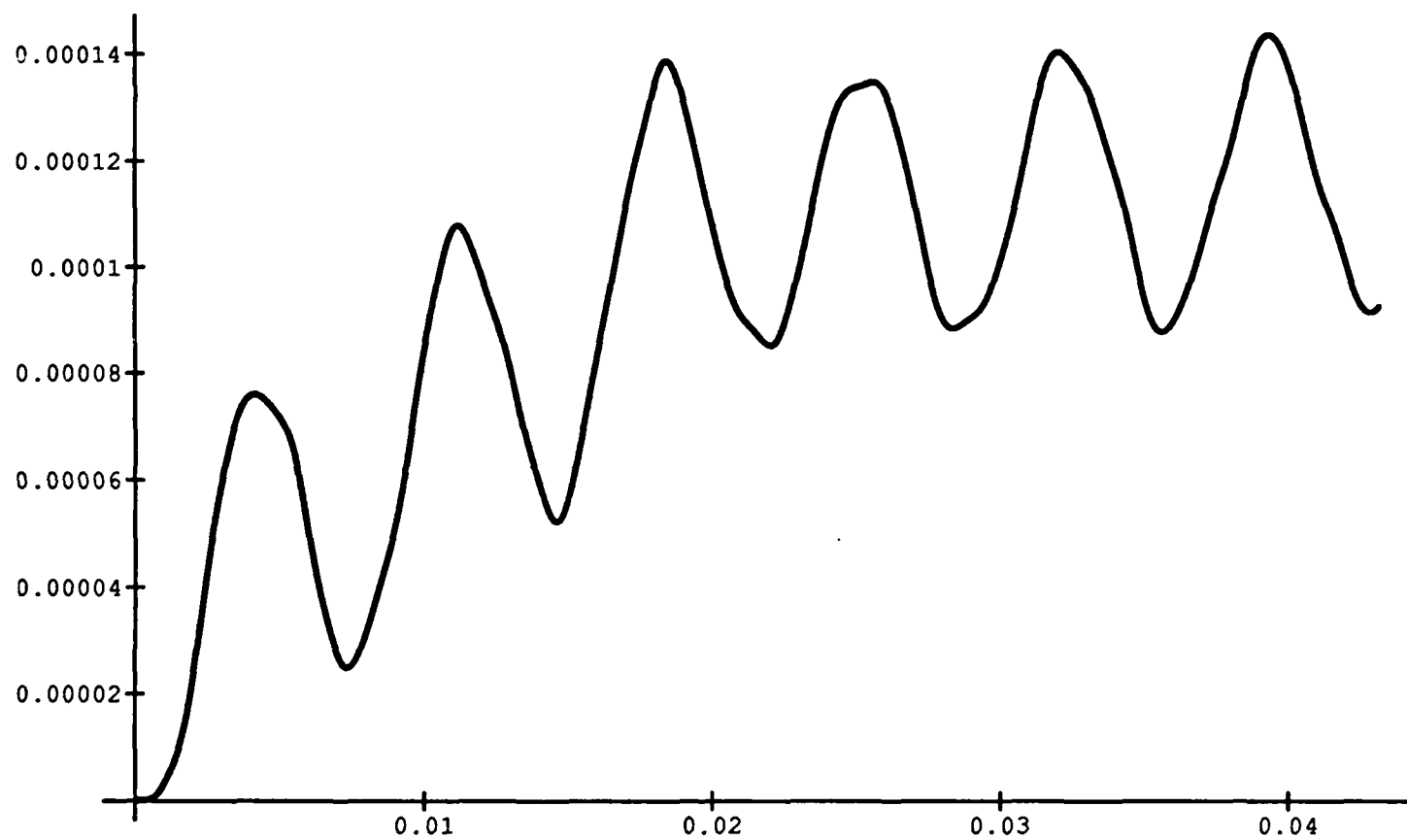
and the z-coordinates by

$\{0.00e-3, 0.20e-3, 0.40e-3, 0.60e-3, 0.70e-3, 0.80e-3, 0.90e-3, 1.00e-3\}$.

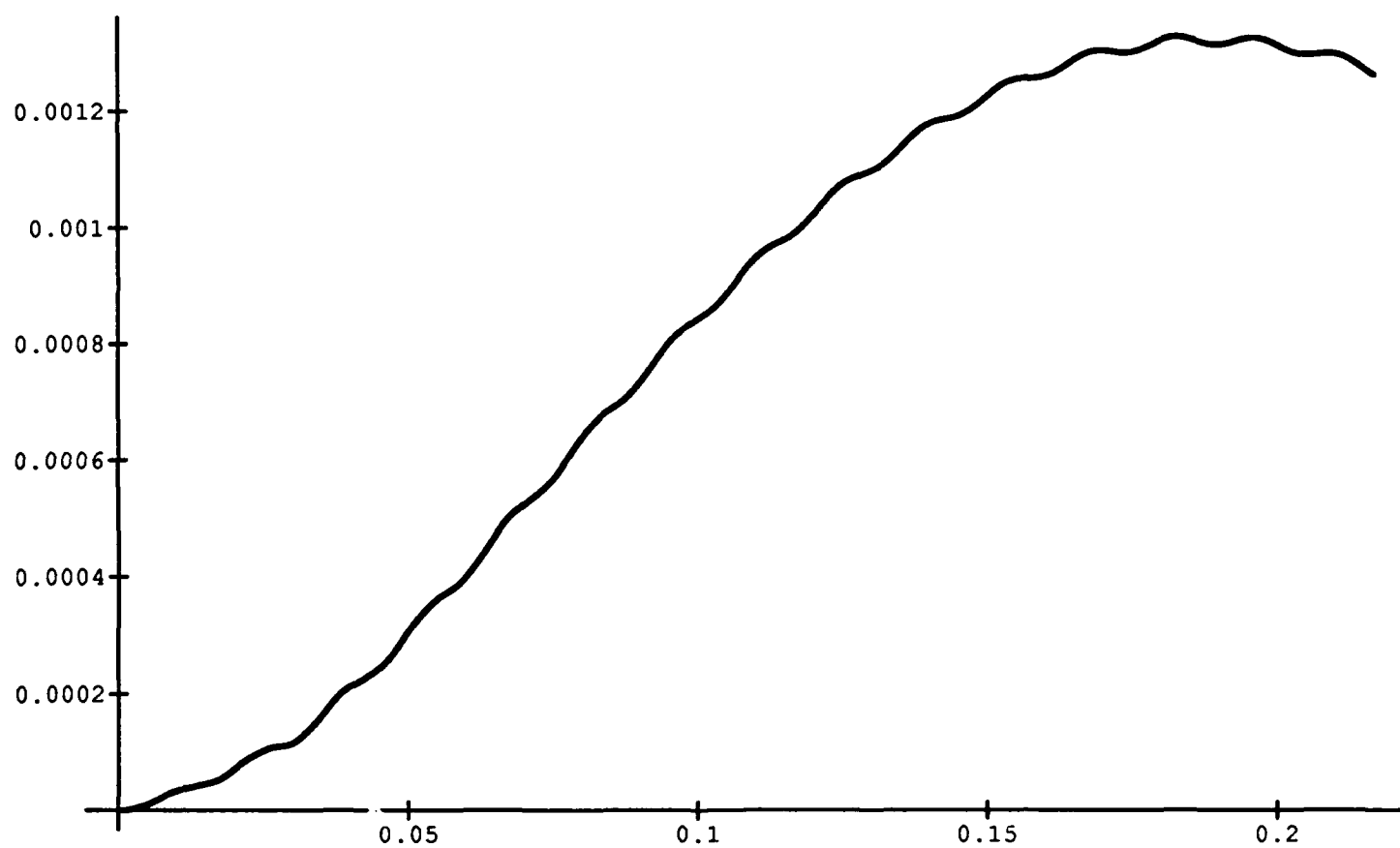
Case III. The laser input was given by a step function, with $Q = Q_{max} = 2.5 \times 10^4$ Btu/m², duration 0.020 sec, and a radius of 2.0 cm. The equations were integrated with $\theta_i = 0.5$, $\Delta t = 0.0001$, N_ITER=4, with condensing and smoothing flags on. No thermo-elastic or inelastic heating effects were included.

The graph below is that of the horizontal deflection $u(r_{max}, z_{max}, t)$, where the horizontal deflection reaches its maximum.

Note that a characteristic frequency of approximately 140 cycles/sec is present in the radial direction. whereas a much slow vertical oscillation is induced (see the next figure).



The following is a graph of the vertical deflection $w(0, z_{\max}, t)$ at the point where the laser is impinging.



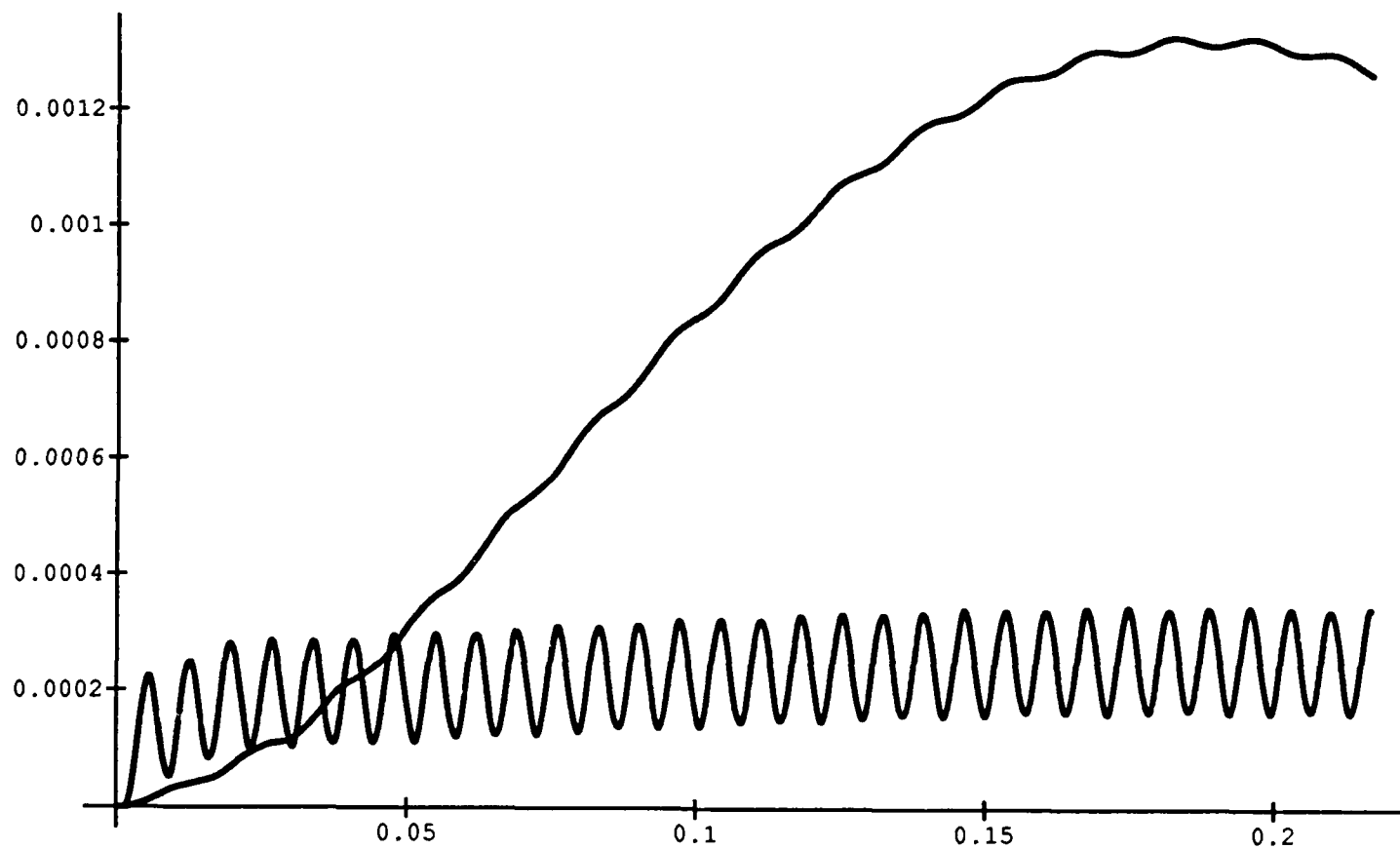
On the same scale, we have

The r-coordinates are given by a finer grid

$\{0.00e-2, 0.01e-2, 0.02e-2, 0.035e-2, 0.05e-2, 0.10e-2, 0.15e-2, 0.20e-2, 0.50e-2, 1.00e-2, 2.00e-2, 4.00e-2, 7.00e-2, 10.00e-2\}$

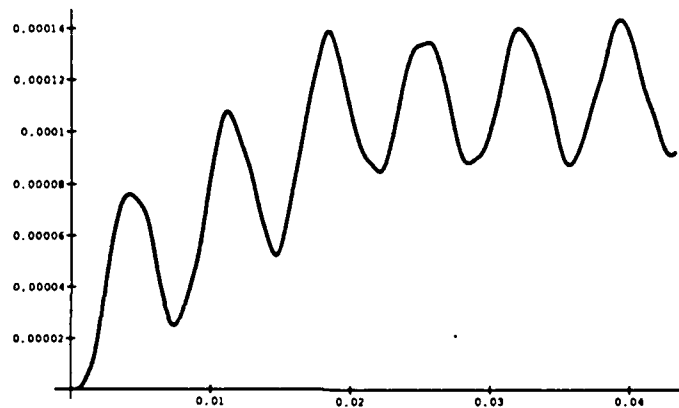
and the z-coordinates by a finer grid

$\{0.00e-3, 0.05e-3, 0.10e-3, 0.20e-3, 0.30e-3, 0.40e-3, 0.60e-3, 0.70e-3, 0.80e-3, 0.90e-3, 1.00e-3\}$.



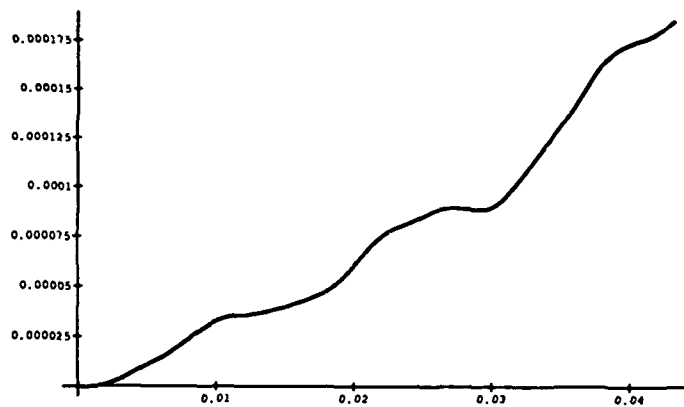
Case IV. The laser input was given by a step function, with $Q = Q_{max} = 2.5 \times 10^4$ Btu/m², duration 0.020 sec, and a radius of 2.0 cm. The equations were integrated with $\theta_i = 0.5$, $\Delta t = 0.00002$, N_ITER=4, with condensing and smoothing flags on. No thermo-elastic or inelastic heating effects were included.

The graph below is that of the horizontal deflection $u(r_{max}, z_{max}, t)$, where the horizontal deflection reaches its maximum.

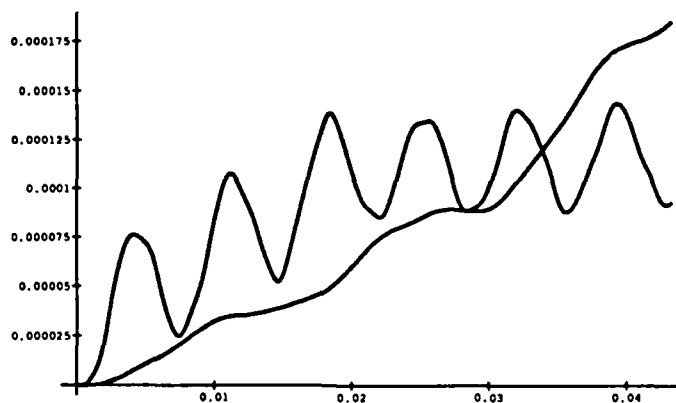


Note that a characteristic frequency of 150 cycles/sec is present in the radial direction, whereas a much slow vertical oscillation is induced (see the next figure).

The following is a graph of the vertical deflection $w(0, z_{\max}, t)$ at the point where the laser is impinging.



On the same scale, we have



The r-coordinates are given by a finer grid

$\{0.00e-2, 0.01e-2, 0.02e-2, 0.035e-2, 0.05e-2, 0.10e-2, 0.15e-2, 0.20e-2, 0.50e-2, 1.00e-2, 2.00e-2, 4.00e-2, 7.00e-2, 10.00e-2\}$

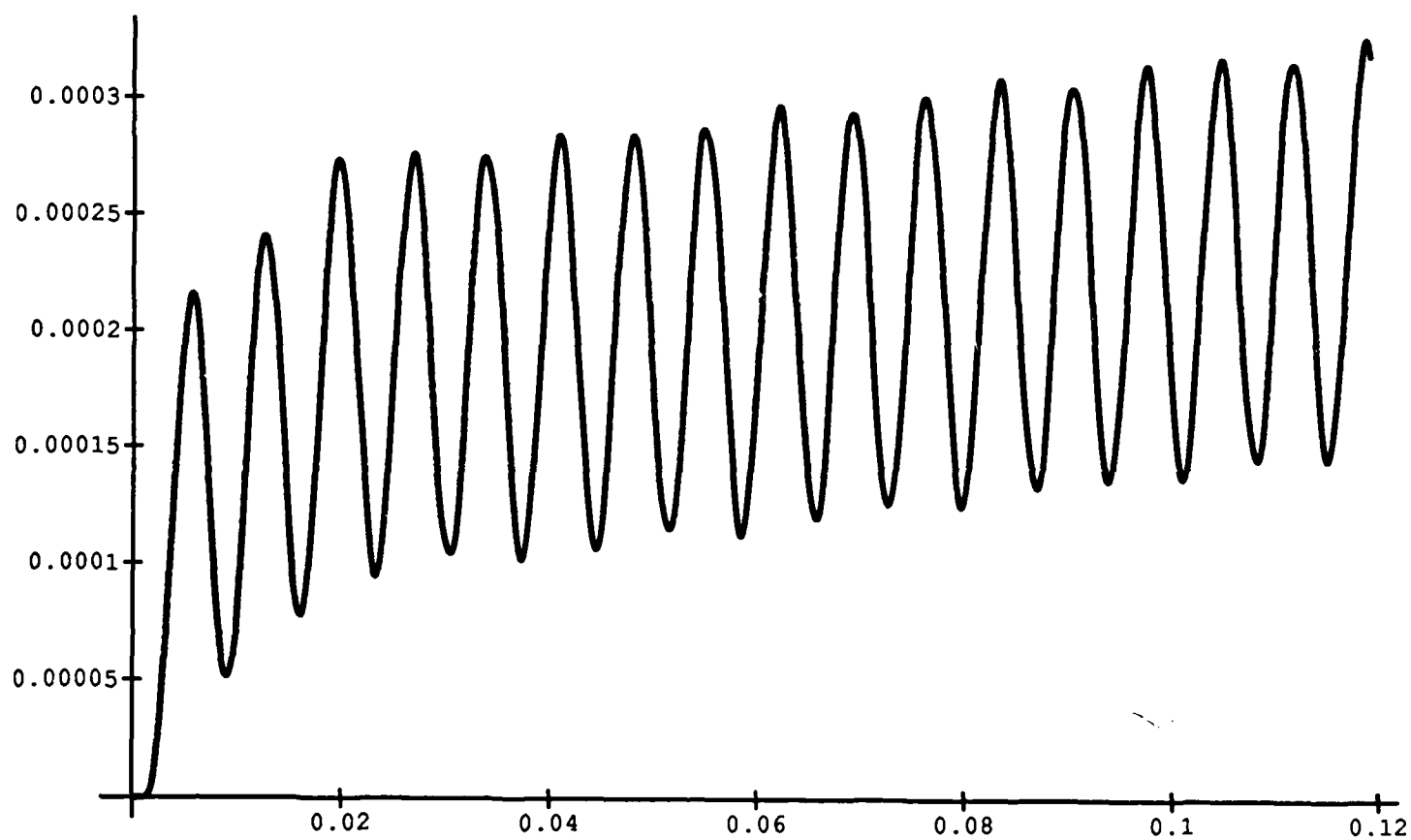
and the z-coordinates by a finer grid

$\{0.00e-3, 0.05e-3, 0.10e-3, 0.20e-3, 0.30e-3, 0.40e-3, 0.60e-3, 0.70e-3, 0.80e-3, 0.90e-3, 1.00e-3\}$.

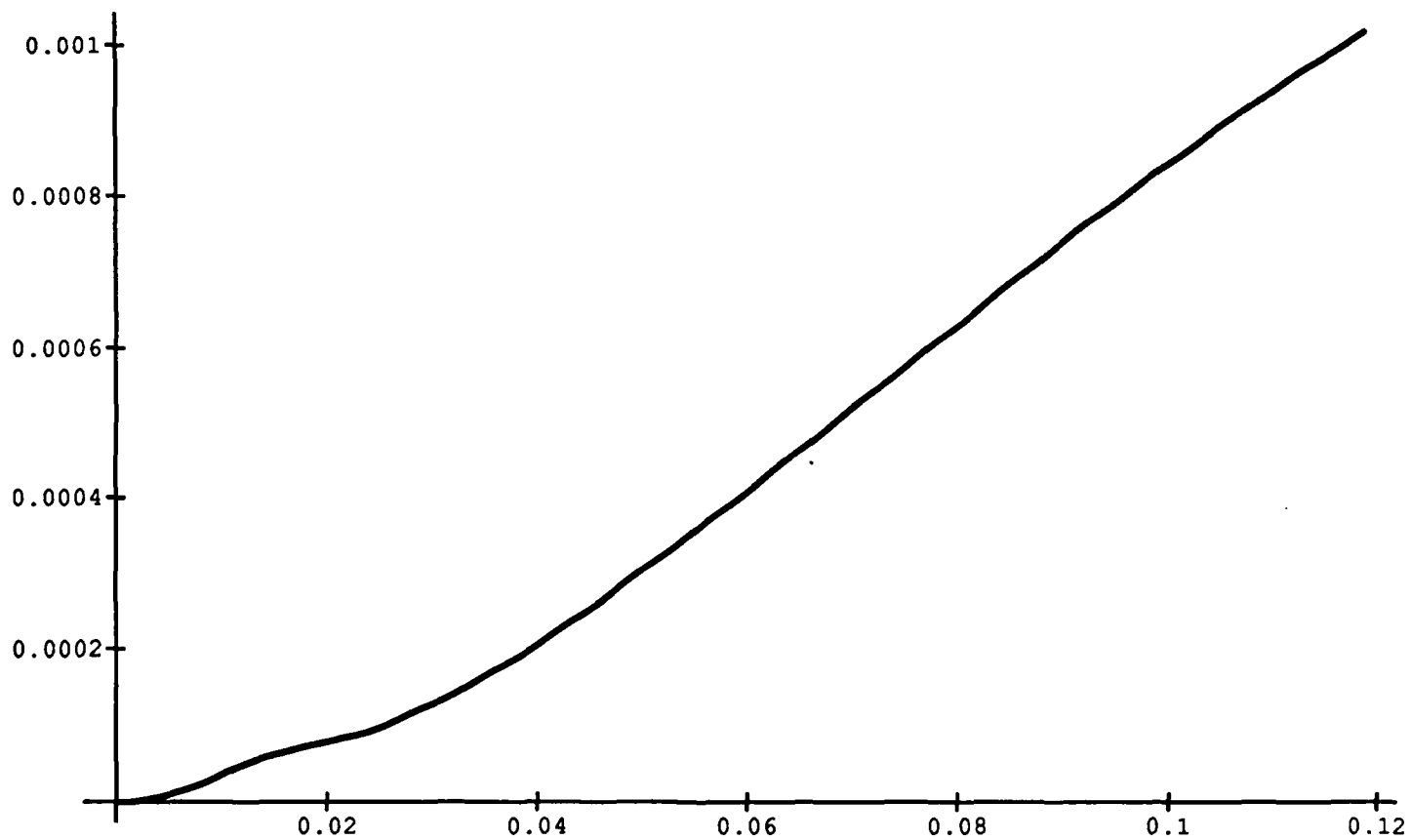
Case V. The laser input was given by a step function, with $Q = Q_{max} = 2.5 \times 10^4$ Btu/m², duration 0.020 sec, and a radius of 2.0 cm. The equations were integrated with $\theta_i = 0.5$, $\Delta t = 0.0001$, N_ITER=4, with condensing and smoothing flags on. No thermo-elastic or inelastic heating effects were included.

The graph below is that of the horizontal deflection $u(r_{max}, z_{max}, t)$, where the horizontal deflection reaches its maximum.

Note that a characteristic frequency of approximately 120-140 cycles/sec is present in the radial direction, whereas a much slow vertical oscillation is induced (see the next figure).



The following is a graph of the vertical deflection $w(0, z_{\max}, t)$ at the point where the laser is impinging.



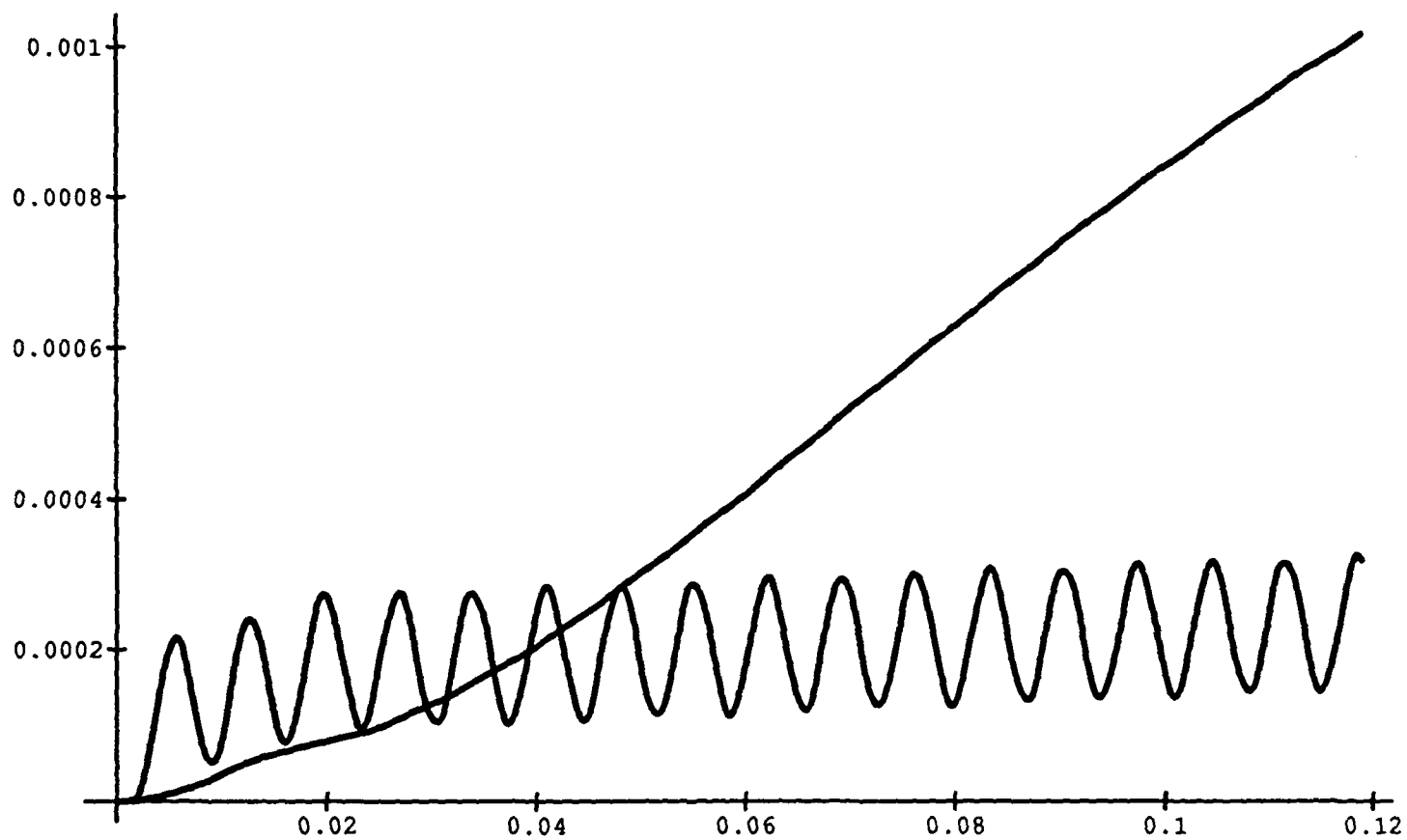
On the same scale, we have

The r-coordinates are given by

$\{0.00e-2, 0.01e-2, 0.02e-2, 0.03e-2, 0.04e-2, 0.06e-2, 0.10e-2, 0.15e-2, 0.20e-2, 0.30e-2, 0.60e-2, 1.00e-2, 2.00e-2, 4.00e-2, 6.00e-2, 8.00e-2, 10.00e-2\}$

and the z-coordinates by

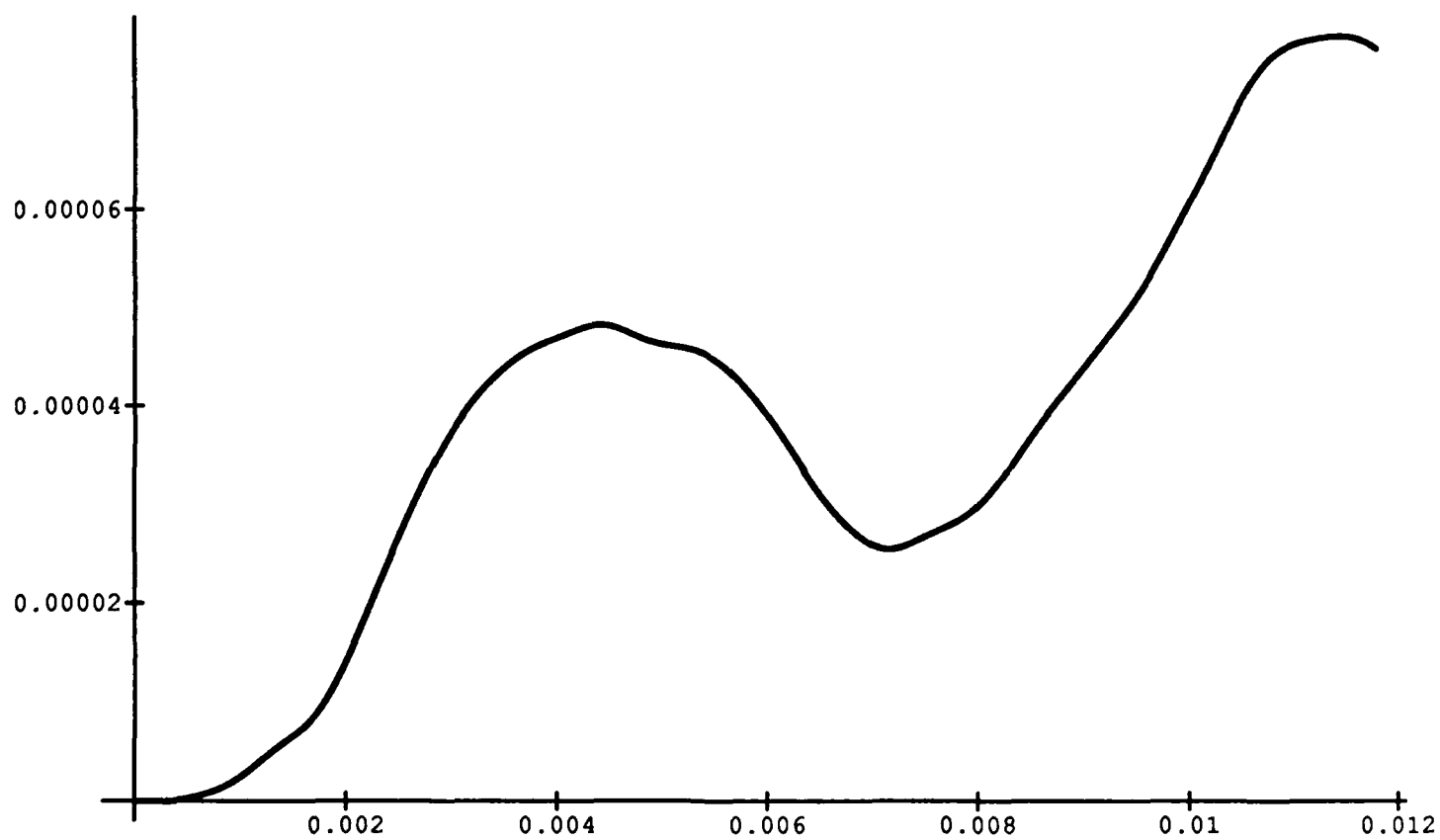
$\{0.00e-3, 0.02e-4, 0.04e-3, 0.07e-3, 0.10e-3, 0.15e-3, 0.20e-3, 0.30e-3, 0.40e-3, 0.60e-3, 0.70e-3, 0.80e-3, 0.90e-3, 1.00e-3, \}$.



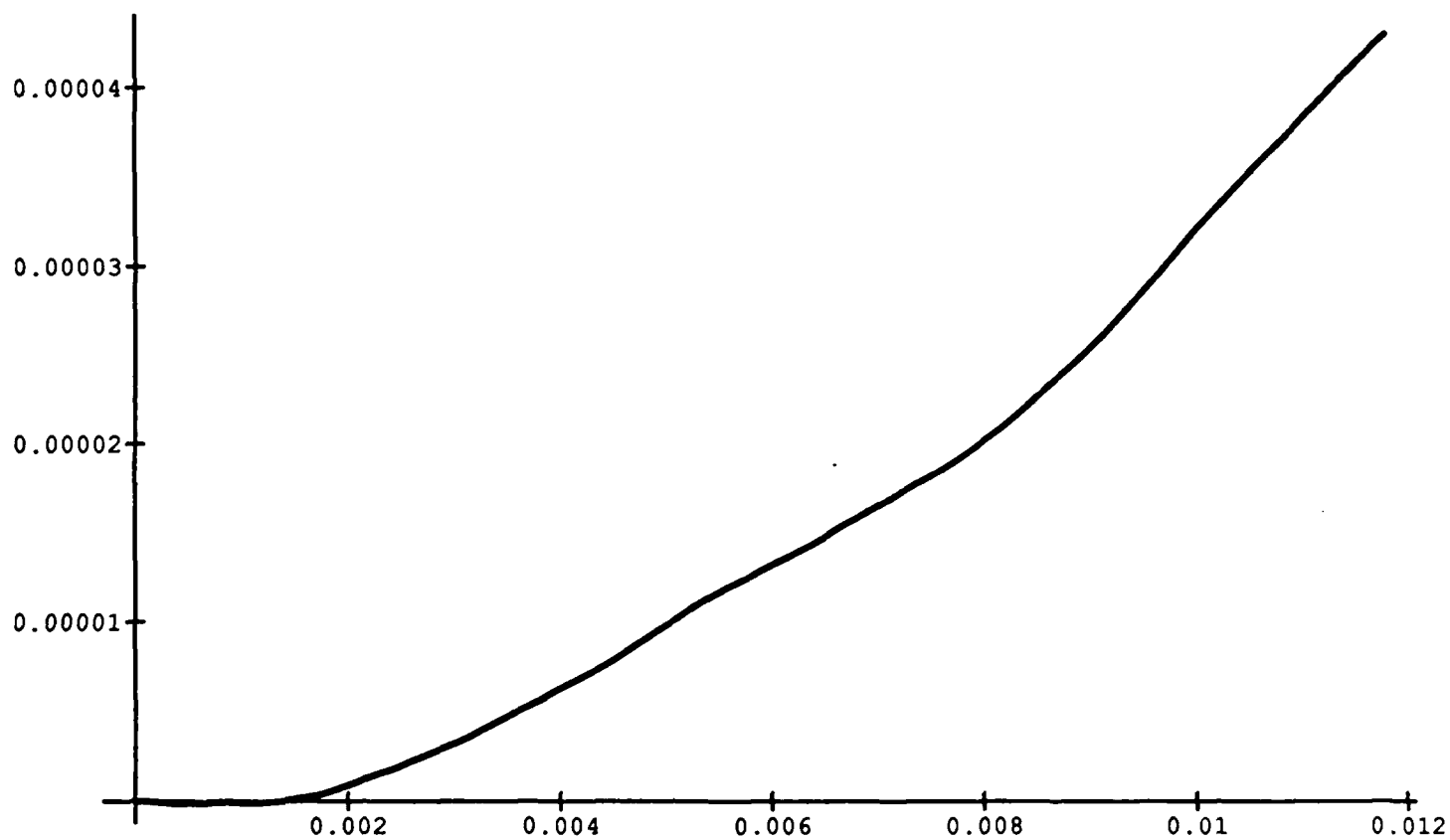
Case VI. The laser input was given by a step function, with $Q = Q_{max} = 2.5 \times 10^4$ Btu/m², duration 0.020 sec, and a radius of 2.0 cm. The equations were integrated with $\theta_i = 0.5$, $\Delta t = 0.00002$, N_ITER=4, with condensing and smoothing flags on. No thermo-elastic or inelastic heating effects were included.

The graph below is that of the horizontal deflection $u(r_{max}, z_{max}, t)$, where the horizontal deflection reaches its maximum.

Note that a characteristic frequency of 150 cycles/sec is present in the radial direction, whereas a much slow vertical oscillation is induced (see the next figure).



The following is a graph of the vertical deflection $w(0, z_{\max}, t)$ at the point where the laser is impinging.



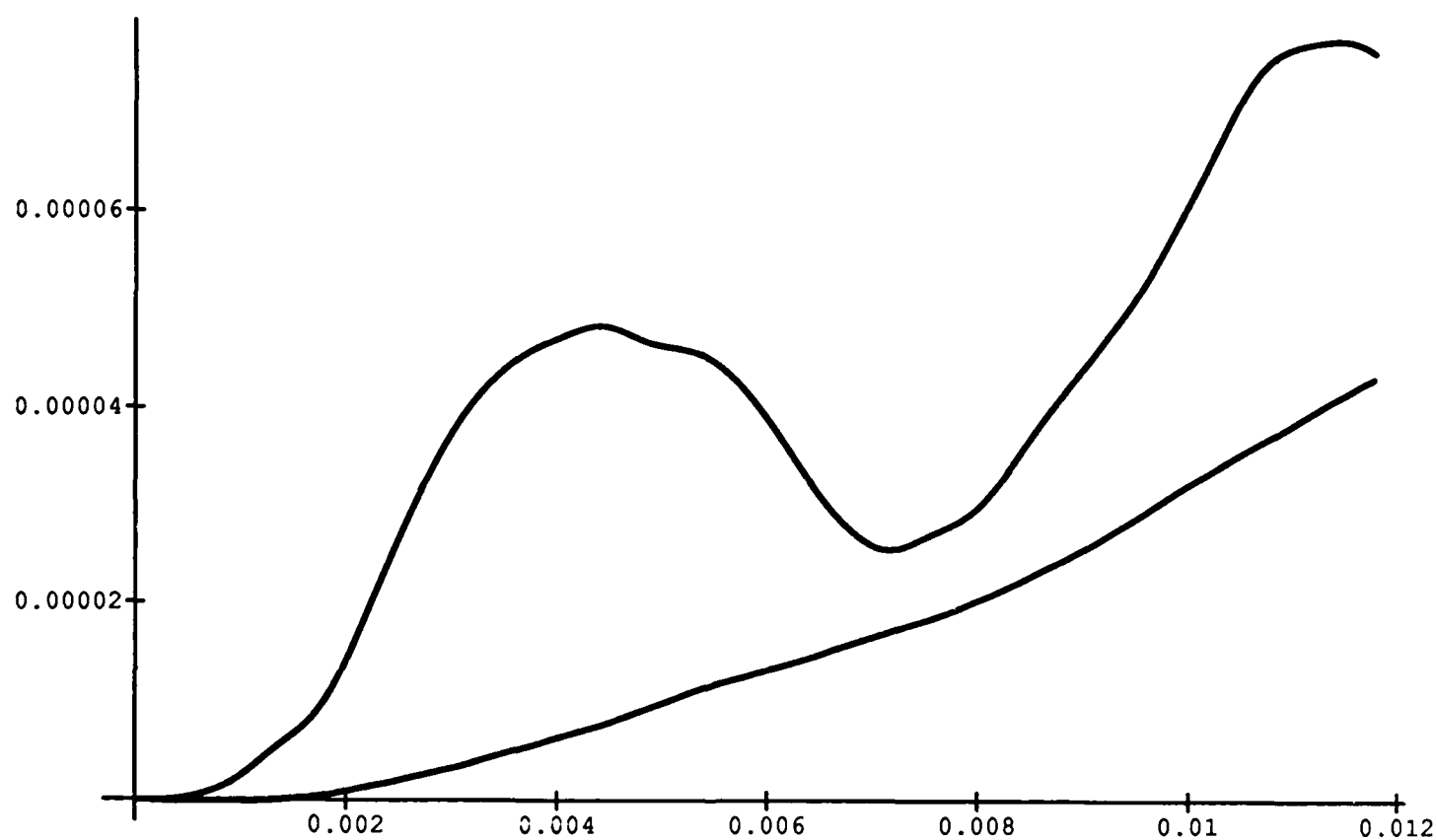
On the same scale, we have

The r-coordinates are given by

$\{0.00e-2, 0.01e-2, 0.02e-2, 0.03e-2, 0.04e-2, 0.06e-2, 0.10e-2, 0.15e-2, 0.20e-2, 0.30e-2, 0.60e-2, 1.00e-2, 2.00e-2, 4.00e-2, 6.00e-2, 8.00e-2, 10.00e-2\}$

and the z-coordinates by

$\{0.00e-3, 0.02e-3, 0.04e-3, 0.07e-3, 0.10e-3, 0.15e-3, 0.20e-3, 0.30e-3, 0.40e-3, 0.60e-3, 0.70e-3, 0.80e-3, 0.90e-3, 1.00e-3, \}$.

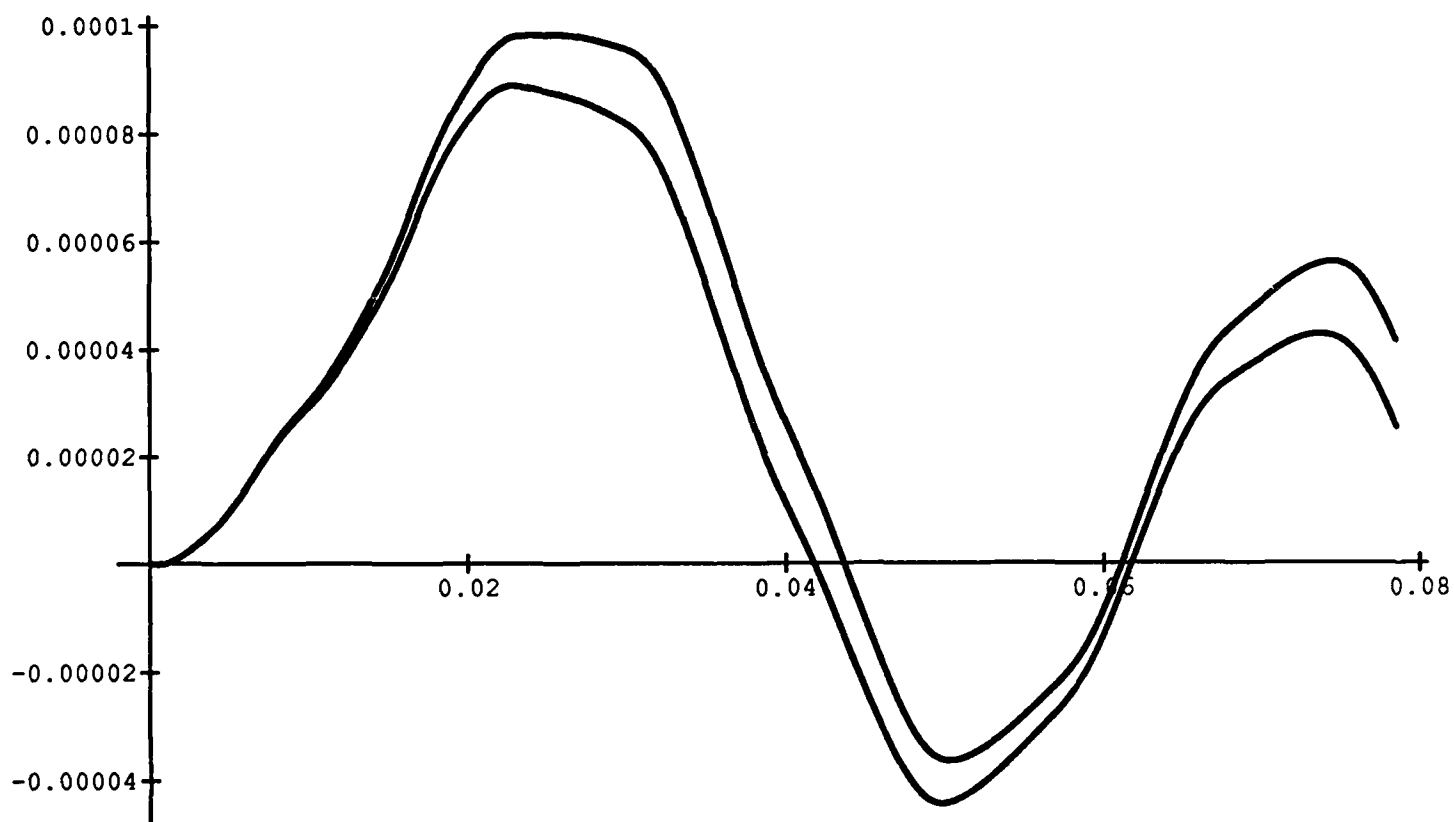


Numerical Simulations

The following numerical simulations were run to test the code's sensitivity to mesh size, time step, one-way versus two-way coupling, elastic and inelastic heating, and various types of heat inputs.

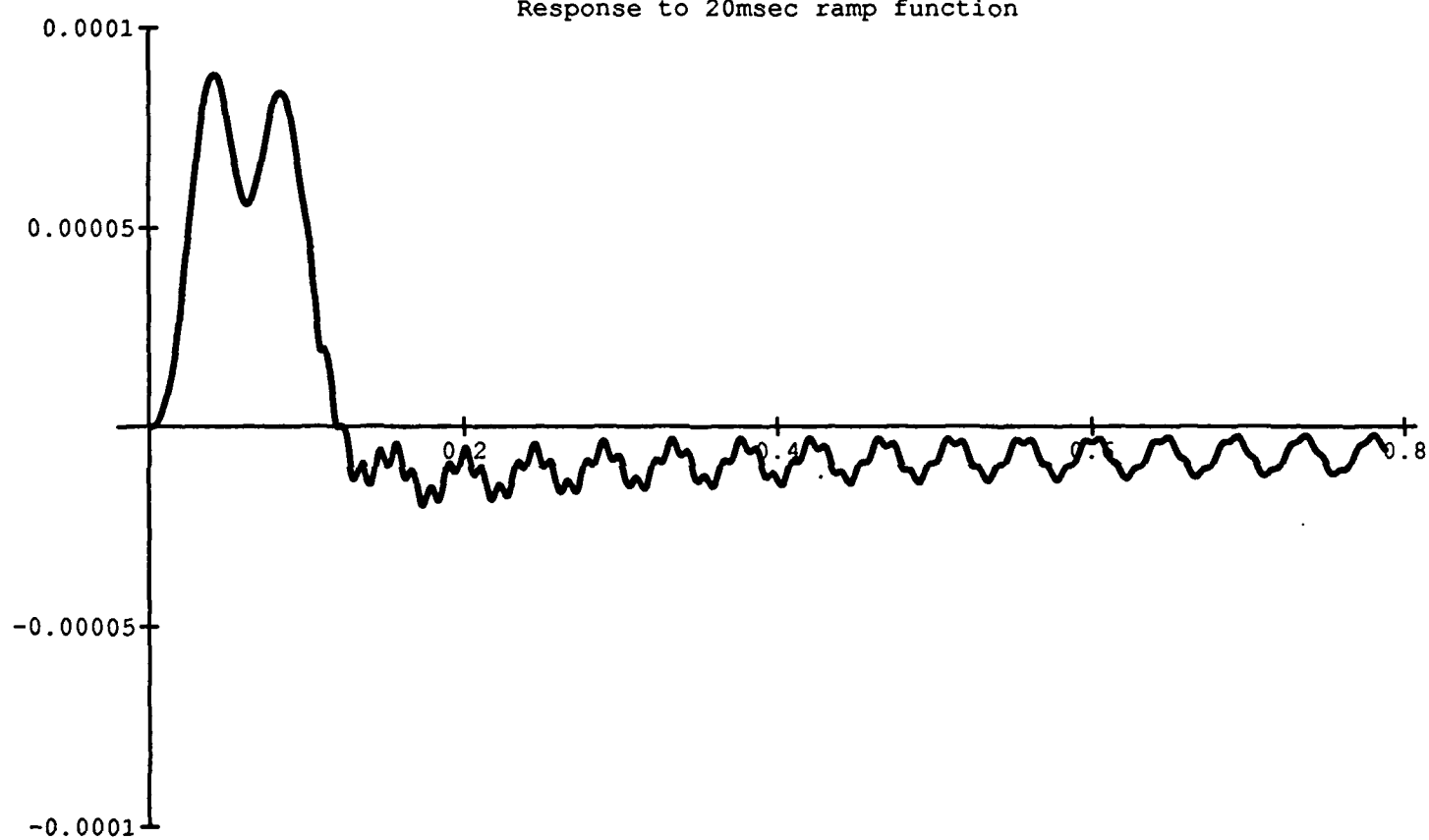
Comparison of Various Effects:

In this section, we analyze the effect of including various terms in the mathematical model. First, if we neglect the inelastic terms in the momentum equations we are solving a pure thermo-elastic model. As an input, we have a step function, magnitude 2.5×10^4 for 20 msec duration. After it stops the plate oscillates with a frequency of about 20 hz. If we include the inelastic terms in the momentum equations, one can see that the out of plane displacement is correspondingly less, due to the damping of the inelastic terms. The region of plasticity is small enough that the behavior is predominantly that of a thermo-elastic plate under an impulsive heat source, with a small amount of damping due to inelasticity.



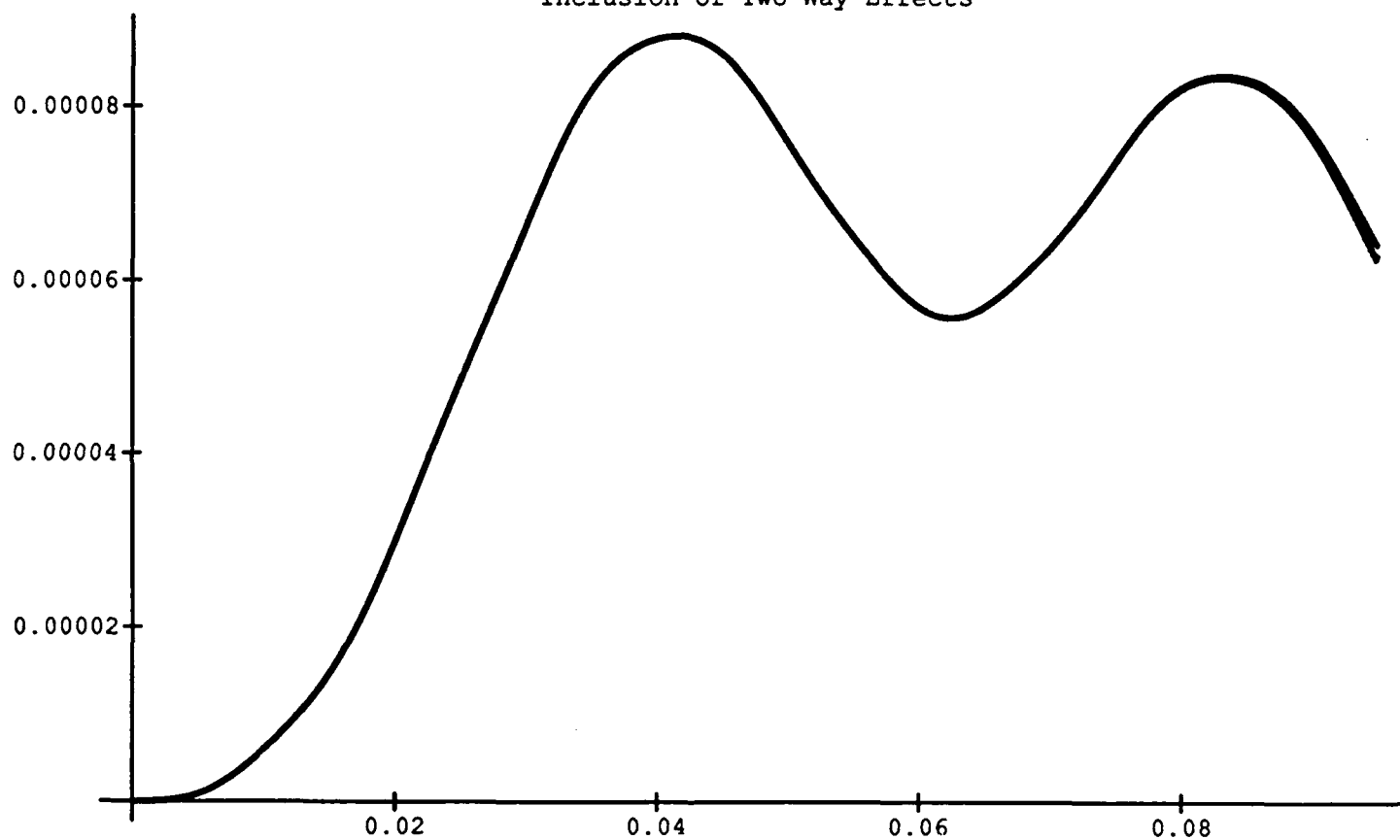
Next, we change the input to correspond to a ramp function which is linear for 20 msec, then constant (2.5×10^4) till 100 msec, and then abruptly turns off. From the graph on the next page, one can see that a slowly varying oscillation is induced about the displacement which arises from a constant temperature source. Turning off the impulsive heating then gives rise to noisy oscillation which is then damped out. Asymptotically, the motion is damped oscillation about a displaced equilibrium state.

Response to 20msec ramp function



Finally, we have incorporated the inelastic terms in the momentum equations, and tested the inclusion of the thermo-elastic and inelastic heating terms in the heat equation. This gives rise to the figure on the next page. The results are virtually indistinguishable. Numerical instability set in at the end of the run, due to small oscillations in the stress levels reaching a certain amplitude. When the inelastic stresses and the thermal stresses are of the same magnitude with the resultant stress, the numerical codes become very sensitive to slight integration errors. This appears to be an intrinsic difficulty with initial value methods for integrating the dynamic plasticity equations.

Inclusion of Two-Way Effects



Summary:

The following is a summary of the results which we have observed after solving the three-dimensional, axi-symmetric, fully coupled, thermo-viscoplastic equations for a laser heated thin plate.

1. If the heat impulse is of sufficiently short duration, and very localized near the center of the plate, the fundamental response is that of an elastic plate under a point load. This is true under both stress-free and clamped boundary conditions.
2. If the heat impulse is ramped, a slow oscillation about a buckled state (which would be given by constant thermal input) is observed. After the heat source is turned off, a complicated return to a permanently deformed state is observed.
3. The inclusion of inelastic effects in the momentum equations accounts for about a 5-10% change in out of plane displacements.
4. The inclusion of inelastic two-way effects affects the out of plane displacements very little (less than 2% observed change).
5. Relatively large grids may be used away from the boundary thermal input. The time step limitations is primarily due to the rapid thermal heating characteristic time.
6. The following appears to be the approximate ranking of effects in the boundary heated, no external loading, axi-symmetric plate problem:
 - a) Boundary heating, temperature response can approach 1000 degrees Kelvin/sec or more. The induced thermal stresses and strains.
 - b) Inelastic corrections to the deformations, and the resultant change in stress.
 - c) Two-way thermo-elastic coupling.
 - d) Two-way thermo-inelastic coupling. This effect is extremely localized.

Conclusions:

The use of a finite element code to solve the initial value problem describing the mechanical response of a thermal-input driven axi-symmetric plate appears to yield reasonable short term response. If the duration of heat input is the characteristic time, then the finite element code could predict reasonable results up to 10 or 20 characteristic time intervals.

The simulator can distinguish between elastic and inelastic effects, as well as one-way versus two-way coupling in the initial stages of nonlinear thermal-mechanical response.

The dominant effect is that of thermo-elastic oscillation under impulsive loading, with secondary (permanent) inelastic deformations and damping, with tertiary thermal input corrections due to two-way elastic and inelastic coupling.

Long time integration of the equations (on the order of 10,000 or more time steps) did not appear reliable with the current code. Even though implicit predictor-corrector and stiff integrators were used throughout, the accumulated error in the stress-strain predictions, and the sensitivity of the constitutive laws to errors in maximum stress, lead to innaccurate asymptotic behavior. Constraining the inelastic behavior to lie on the correct energy surface was difficult to impose with the initial-boundary value finite element model.

Large residual stresses, due to permanent inelastic deformation, also limit the time step-size, even after the plate has ceased to be thermally excited.

Appendix 7.2

A Model for Predicting the Effective Elastic Properties of Randomly Oriented Fiber Composites Subjected to Hot Pressing, Extrusion, and Rolling

A MODEL FOR PREDICTING THE EFFECTIVE ELASTIC PROPERTIES OF RANDOMLY ORIENTED FIBER COMPOSITES SUBJECTED TO HOT PRESSING, EXTRUSION, AND ROLLING

Jong-Won Lee* and David H. Allen**
Aerospace Engineering Department
Texas A&M University, College Station, Texas

Abstract

The present paper develops analytical solutions for predicting the effects of hot pressing, extrusion, and rolling on the elastic properties of composite materials reinforced by either continuous or discontinuous randomly oriented fibers. The bounded orientation of fibers in the matrix material is explicitly expressed in terms of manufacturing parameters. These manufacturing parameters account for hot pressing, extrusion, and rolling of an initially isotropic composite with randomly oriented fibers prior to the above material forming processes. The effective elastic properties after material forming are given as functions of material forming parameters representing dimensional change during manufacturing and the five independent elastic constants for a perfectly aligned fiber composite. Finally, the present model predictions are compared with other theoretical models and experimental data.

Nomenclature

a_{ij}	direction cosines
C_{ijkl}	stiffness tensor for an aligned fiber composite
\bar{C}_{ijkl}	stiffness tensor in the spherical coordinates of an aligned fiber composite
\bar{C}_{ijkl}	stiffness tensor after material forming where $i, j, k, l = 1, 2, 3$
C_{ij}	stiffness tensor in contracted Voigt notation where $i, j = 1, 2, \dots, 6$
D_a	diameter after extrusion
D_b	diameter before extrusion
E	Young's Modulus
F	fiber
f	fiber volume fraction
G	shear modulus
M	matrix
S_{ijkl}	Eshelby's tensor
t_a	thickness after hot pressing or rolling
t_b	thickness before hot pressing or rolling
ϵ_{ij}	strain tensor
$\bar{\epsilon}_{ijkl}$	quasi-stiffness tensor
σ_{ij}	stress tensor
ν	Poisson's ratio

* Research Assistant

** Professor

I. Introduction

A number of models have been proposed for predicting the effective elastic properties of aligned or randomly oriented fiber composites.¹⁻⁸ The equivalent inclusion method utilized by Taya and Chow⁷, and Taya and Mura⁸ provides a straightforward tool for estimating the effective Young's modulus of a composite reinforced by either continuous or discontinuous fibers. Hashin and Rosen's method¹ may be utilized to estimate all elastic properties of aligned fiber composites. The effective elastic properties have been calculated for two or three dimensionally random fiber orientation³⁻⁶ and bounded fiber orientation in a two dimensional domain⁹ utilizing simple integration schemes. However, these models are not directly applicable to a composite experiencing certain types of material forming because forming processes induce oriented fiber distribution.

A systematic procedure has not previously been developed to model an arbitrarily bounded random orientation of fibers caused by material forming. The authors thus propose herein a relatively simple mathematical/graphical model for determining the influence of bounded random orientation of fibers on the effective elastic moduli of continuous/discontinuous fiber reinforced composites.

II. Model Formulation

Consider a single representative volume element of a composite material reinforced by continuous or discontinuous fibers, as illustrated in Figs. 1-a and 1-b, respectively.

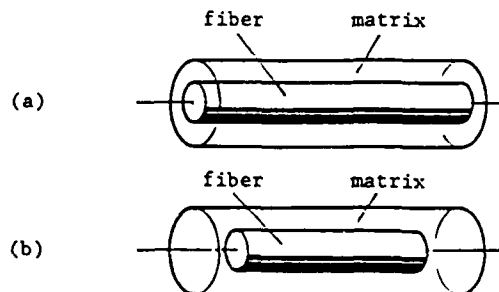


Fig. 1 Representative volume elements

(a) Continuous fiber element

(b) Discontinuous fiber element

It is clear that the above volume elements are transversely isotropic, thus five independent elastic moduli should be determined theoretically or experimentally for both cases. Since it is very cumbersome to solve an exact boundary value problem associated with the double cylinder model shown in Fig. 1-b, the authors utilize the equivalent inclusion method proposed by Taya, et al.^{7,8} For a continuous fiber composite, a number of theoretical solution schemes have been investigated for determining the five independent elastic moduli of the transversely isotropic volume element.^{1,4} When the fiber length is very large compared to the fiber diameter, these solution schemes may be applied to a composite even with discontinuous fibers.

For convenience, the composite elastic moduli of the volume element are assumed to be known. In matrix form, they can be written as

$$\begin{Bmatrix} \sigma_{11} \\ \sigma_{22} \\ \sigma_{33} \\ \sigma_{23} \\ \sigma_{31} \\ \sigma_{12} \end{Bmatrix} = \begin{bmatrix} C_{11} & C_{12} & C_{12} & 0 & 0 & 0 \\ C_{12} & C_{22} & C_{23} & 0 & 0 & 0 \\ C_{12} & C_{23} & C_{22} & 0 & 0 & 0 \\ 0 & 0 & 0 & (C_{22}-C_{23}) & 0 & 0 \\ 0 & 0 & 0 & 0 & 2C_{66} & 0 \\ 0 & 0 & 0 & 0 & 0 & 2C_{66} \end{bmatrix} \begin{Bmatrix} \epsilon_{11} \\ \epsilon_{22} \\ \epsilon_{33} \\ \epsilon_{23} \\ \epsilon_{31} \\ \epsilon_{12} \end{Bmatrix} \quad (1)$$

If a composite is initially isotropic, the reinforcing fibers do not have a preferred orientation. The probability density distribution for fiber orientation may be represented by a sphere in the three dimensional case. In the case where the fibers are distributed randomly in a single plane, the sphere degenerates to a circle. The degree of randomness of the volume element can be mathematically formulated for an initially isotropic short fiber composite after certain types of permanent deformation, such as hot pressing, extrusion, or rolling. When the composite is subjected to hot pressing or extrusion, the material becomes transversely isotropic. For example, a cube becomes a square plate or a cylinder becomes a circular disc, and vice versa. For an arbitrary thickness change and diameter change due to hot pressing and extrusion, respectively, an initially isotropic composite becomes transversely isotropic under a transversely isotropic forming process as illustrated in Figs. 2-a and 2-b. Alternatively, a forming process such as rolling causes orthotropic reorientation of fibers, in which one of the dimensional changes is negligibly small as shown in Fig. 2-c.

The present approach requires three assumptions:

1. Although the fibers after each of the material forming processes mentioned above may not be evenly distributed within the subdomain illustrated in Fig. 2, the fiber distribution density is assumed to be spatially homogeneous for mathematical simplicity.

2. The material forming processes mentioned herein are possible only through the plastic deformation of the matrix material. Plastic strain may not be spatially homogeneous in the matrix material due to stress concentrations near the reinforcing fibers. Also, it is well known that even an isotropic homogeneous material becomes transversely isotropic or orthotropic after the

subject forming processes. This plasticity effect is neglected in the present study.

3. The material forming processes mentioned above may cause defects, such as broken fibers, fiber matrix debonding, etc. Furthermore, microvoids cannot be completely removed from the composite. The present study assumes a defect-free composite.

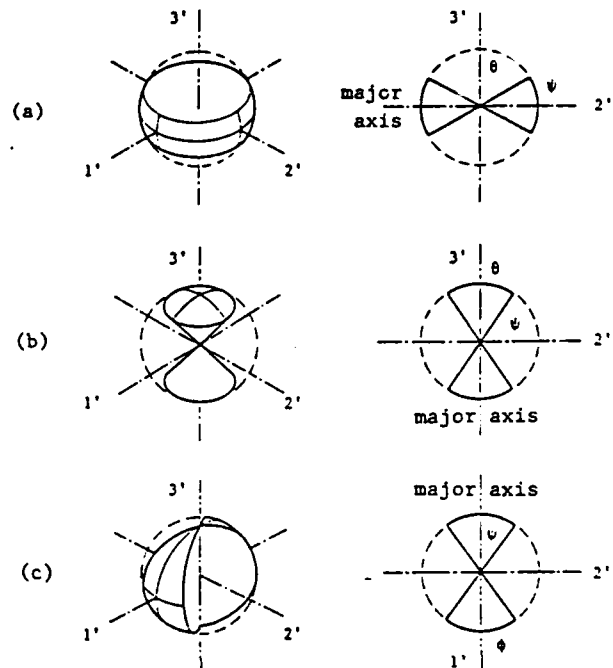


Fig. 2 Fiber reorientation due to forming

- (a) Hot pressing
- (b) Extrusion
- (c) Rolling

II-1. Hot Pressing

The composite stiffnesses after reorientation of each volume element due to hot pressing depend on the ratio of virgin material thickness to formed thickness. From Fig. 2-a,

$$\sin\psi = \frac{t_a}{t_b} = \xi \quad (2)$$

Thus, the stiffness components after hot pressing are given by

$$\bar{C}_{ijkl} = \frac{1}{2\pi \sin\psi} \int_0^\pi \int_{\pi/2-\psi}^{\pi/2+\psi} C_{ijkl} \sin\theta \, d\theta \, d\phi \quad (3)$$

where

$$C_{ijkl} = a_{ip} a_{jq} a_{kr} a_{ls} C_{pqrs} \quad (4)$$

As shown in Fig. 3, the direction cosines, a_{ij} , can be defined as

$$a_{ij} \rightarrow \begin{bmatrix} \sin\theta\cos\phi & -\cos\theta\cos\phi & \sin\phi \\ \sin\theta\sin\phi & -\cos\theta\sin\phi & -\cos\phi \\ \cos\theta & \sin\theta & 0 \end{bmatrix} \quad (5)$$

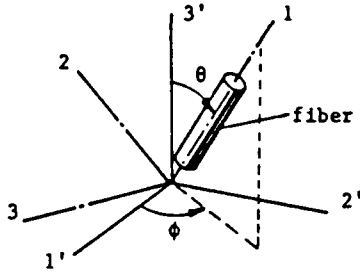


Fig. 3 Direction cosines

Substituting (4) and (5) into (3) gives the five independent elastic constants after hot pressing in terms of the thickness ratio and the elastic constants of a perfectly aligned fiber composite. Thus,

$$\begin{aligned} \bar{C}_{11} &= \bar{C}_{22} \\ &= C_{11}(3/8 - \xi^2/4 + 3\xi^4/40) \\ &\quad + C_{22}(3/8 + \xi^2/12 + 3\xi^4/40) \\ &\quad + C_{12}(1/4 + \xi^2/6 - 3\xi^4/20) \\ &\quad + C_{66}(1/2 + \xi^2/3 - 3\xi^4/10) \end{aligned} \quad (6)$$

$$\begin{aligned} \bar{C}_{33} &= C_{11}\xi^4/5 + C_{22}(1 - 2\xi^2/3 + \xi^4/5) \\ &\quad + (C_{12} + 2C_{66})(2\xi^2/3 - 2\xi^4/5) \end{aligned} \quad (7)$$

$$\begin{aligned} \bar{C}_{12} &= (C_{11} + C_{22} - 4C_{66})(1/8 - \xi^2/12 + \xi^4/40) \\ &\quad + C_{23}\xi^2/3 + C_{12}(3/4 - \xi^2/6 - \xi^4/20) \end{aligned} \quad (8)$$

$$\begin{aligned} \bar{C}_{13} &= \bar{C}_{23} \\ &= (C_{11} + C_{22} - 4C_{66})(\xi^2/6 - \xi^4/10) \\ &\quad + C_{12}(1/2 - \xi^2/6 + \xi^4/5) \\ &\quad + C_{23}(1/2 - \xi^2/6) \end{aligned} \quad (9)$$

$$\begin{aligned} \bar{C}_{44} &= \bar{C}_{55} \\ &= (C_{11} - 2C_{12})(\xi^2/6 - \xi^4/10) \\ &\quad + C_{22}(1/4 + \xi^2/12 - \xi^4/10) \\ &\quad - C_{23}(1/4 - \xi^2/12) \\ &\quad + C_{66}(1/2 - \xi^2/2 + 2\xi^4/5) \end{aligned} \quad (10)$$

$$\bar{C}_{66} = (\bar{C}_{11} - \bar{C}_{12})/2 \quad (11)$$

When the hot pressing ratio, ξ , is zero, the transversely isotropic material properties studied by Berthelot⁹ are recovered as listed below.

$$\begin{aligned} \bar{C}_{11} &= \bar{C}_{22} \\ &= 3(C_{11} + C_{22})/8 + (C_{12} + 2C_{66})/4 \end{aligned} \quad (12)$$

$$\bar{C}_{33} = C_{22} \quad (13)$$

$$\bar{C}_{12} = (C_{11} + C_{22} - 4C_{66})/8 + 3C_{12}/4 \quad (14)$$

$$\bar{C}_{13} = \bar{C}_{23} = (C_{12} + C_{23})/2 \quad (15)$$

$$\bar{C}_{44} = \bar{C}_{55} = (C_{22} - C_{23} + 2C_{66})/4 \quad (16)$$

$$\begin{aligned} \bar{C}_{66} &= (\bar{C}_{11} - \bar{C}_{12})/2 \\ &= (C_{11} + C_{22} - 2C_{12} + 4C_{66})/8 \end{aligned} \quad (17)$$

Christensen⁴ also predicted 3-D isotropic and transversely isotropic material properties of a composite with randomly oriented continuous fibers. By setting changes in dimensions to zero, i. e. $\xi = 1$, the present approach simplifies to the 3-D isotropic material properties predicted by Christensen listed below.

$$\bar{C}_{11} = (3C_{11} + 4C_{12} + 8C_{22} + 8C_{66})/15 \quad (18)$$

$$\bar{C}_{12} = (C_{11} + 8C_{12} + C_{22} - 4C_{66} + 5C_{23})/15 \quad (19)$$

II-2. Extrusion

From Fig. 2-b, the stiffness components after extrusion are given by

$$\bar{C}_{ijkl} = \frac{1}{\pi(1 - \sin\psi)} \int_0^\pi \int_0^{\pi/2 - \psi} C_{ijkl} \sin\theta \, d\theta \, d\phi \quad (20)$$

$$\cos\psi = \frac{D_a}{D_b}, \quad \sin\psi = \xi \quad (21)$$

Thus, the effective elastic properties after extrusion are given by

$$\begin{aligned} \bar{C}_{11} &= \bar{C}_{22} \\ &= C_{11}(8 - 7\xi - 7\xi^2 + 3\xi^3 + 3\xi^4)/40 \\ &\quad + C_{22}(64 + 19\xi + 19\xi^2 + 9\xi^3 + 9\xi^4)/120 \\ &\quad + (C_{12} + 2C_{66})(16 + \xi + \xi^2 - 9\xi^3 - 9\xi^4)/60 \end{aligned} \quad (22)$$

$$\begin{aligned}\bar{C}_{33} = & C_{11}(1+\zeta^2+\zeta^3+\zeta^4)/5 \\ & + C_{22}(1-\zeta)^2(8+9\zeta+3\zeta^2)/15 \\ & + (2C_{12}+4C_{66})(1-\zeta)(2+4\zeta+6\zeta^2+3\zeta^3)/15\end{aligned}\quad (23)$$

$$\begin{aligned}\bar{C}_{12} = & (C_{11}+C_{22}-4C_{66})(8-7\zeta-7\zeta^2+3\zeta^3+3\zeta^4)/120 \\ & - C_{12}(-32+13\zeta+13\zeta^2+3\zeta^3+3\zeta^4)/60 \\ & + C_{23}(1+\zeta^2)/3\end{aligned}\quad (24)$$

$$\begin{aligned}\bar{C}_{13} = & \bar{C}_{23} \\ = & (C_{11}+C_{22}-4C_{66})(2+2\zeta+2\zeta^2-3\zeta^3-3\zeta^4)/30 \\ & + C_{23}(2-\zeta-\zeta^2)/6 \\ & + C_{12}(16+\zeta+\zeta^2+6\zeta^3+6\zeta^4)/30\end{aligned}\quad (25)$$

$$\begin{aligned}\bar{C}_{44} = & \bar{C}_{55} \\ = & (C_{11}-2C_{12})(2+2\zeta+2\zeta^2-3\zeta^3-3\zeta^4)/30 \\ & - C_{23}(2-\zeta-\zeta^2)/12 \\ & + C_{22}(14-\zeta-\zeta^2-6\zeta^3-6\zeta^4)/60 \\ & - C_{66}(-4+\zeta+\zeta^2-4\zeta^3-4\zeta^4)/10\end{aligned}\quad (26)$$

$$\bar{C}_{66} = \bar{C}_{12} = (\bar{C}_{11}+\bar{C}_{12})/2\quad (27)$$

II-3. Rolling

In the case of rolling, the fiber reorientation kinematics are slightly different from the above cases. Since the thickness change is much greater than the width change, the width change may be assumed to be negligible. From Fig. 2-c, the effective stiffness components and thickness ratio after rolling are then given by

$$\bar{C}_{ijkl} = \frac{1}{4\psi} \int_{-\psi}^{\psi} \int_0^{\pi} C_{ijkl} \sin\theta \, d\theta \, d\phi\quad (28)$$

$$\sin\psi = \frac{\tau_a}{\tau_b}\quad (29)$$

The effective elastic properties after rolling then become orthotropic, resulting in nine independent elastic constants given by

$$\begin{aligned}\bar{C}_{11} = & C_{11}(3 \pm 2\sin 2\psi/\psi + \sin 4\psi/4\psi)/15 \\ \bar{C}_{22} = & C_{22}(8 \mp 3\sin 2\psi/\psi + \sin 4\psi/4\psi)/15 \\ & + (2C_{12}+4C_{66})(2 \pm \sin 2\psi/2\psi \\ & - \sin 4\psi/4\psi)/15\end{aligned}\quad (30)$$

$$\bar{C}_{33} = C_{11}/5 + (4C_{12}+8C_{66})/15 + 8C_{22}/15\quad (31)$$

$$\begin{aligned}\bar{C}_{12} = & (C_{11}+C_{22}-4C_{66})(1 - \sin 4\psi/4\psi)/15 \\ & + C_{23}/3 + C_{12}(8 + \sin 4\psi/2\psi)/15\end{aligned}\quad (32)$$

$$\begin{aligned}\bar{C}_{13} = & (C_{11}+C_{22}-4C_{66})(1 \pm \sin 2\psi/2\psi)/15 \\ \bar{C}_{23} = & C_{23}(1 \mp \sin 2\psi/2\psi)/3 \\ & + C_{12}(8 \pm 3\sin 2\psi/2\psi)/15\end{aligned}\quad (33)$$

$$\begin{aligned}\bar{C}_{44} = & (C_{11}-2C_{12})(1 \mp \sin 2\psi/2\psi)/15 \\ \bar{C}_{55} = & C_{23}(1 \pm \sin 2\psi/2\psi)/6 \\ & + C_{22}(7 \pm 3\sin 2\psi/2\psi)/30 \\ & + C_{66}(2 \mp \sin 2\psi/6\psi)/5\end{aligned}\quad (34)$$

$$\begin{aligned}\bar{C}_{66} = & (C_{11}-2C_{12})(1 - \sin 4\psi/4\psi)/15 \\ & - C_{23}/6 + C_{22}(7 - \sin 4\psi/2\psi)/30 \\ & + C_{66}(2 + \sin 4\psi/3\psi)/5\end{aligned}\quad (35)$$

III. Aligned Short Fiber Composite

As mentioned earlier, the five independent elastic constants of a perfectly aligned fiber composite must be known prior to the forming process. The shape of reinforcing short fibers or whiskers has been frequently assumed by a number of researchers^{7,8} to be a prolate spheroid. This approach is known as the equivalent inclusion method from which all elastic constants of a composite reinforced by aligned inclusions can be estimated either analytically or numerically. The effective compliances of an aligned short fiber composite, or those of the representative volume element shown in Fig. 1-b are given by

$$\begin{aligned}C_{ijkl}^{-1} = & C_{ijkl}^{-1} - (f/2)(C_{mnpq}^F - C_{mnpq}^M) \times \\ & (\Xi_{ijmn}^{-1} C_{pqkl}^{-1} + \Xi_{klmn}^{-1} C_{pqij}^{-1})\end{aligned}\quad (36)$$

where

$$\begin{aligned}\Xi_{ijkl} = & (1-f)(C_{ijmn}^F - C_{ijmn}^M)S_{mnkl} \\ & + (1-f)C_{ijkl}^M + fC_{ijkl}^F\end{aligned}\quad (37)$$

and S_{ijkl} is Eshelby's tensor for a prolate spheroid.¹⁰

IV. Results and Discussion

From the present study, the effective elastic constants for aligned continuous or discontinuous fiber composite can be predicted. When the fiber aspect ratio approaches infinity, eq. (36) gives the effective elastic constants for an aligned continuous fiber composite. After the effective elastic constants of aligned fiber composite are calculated by eq. (36), the solutions to the subject material forming processes discussed earlier can be utilized for predicting the material properties after each forming process. The solutions to extreme hot pressing where $t_a/t_b = 0$ can be compared with an experimental result of two dimensional random fiber composite.

The effective transverse Young's modulus calculated from eq. (36) is compared with the experimental data in Tsai and Hahn¹¹, as shown in Fig. 4.

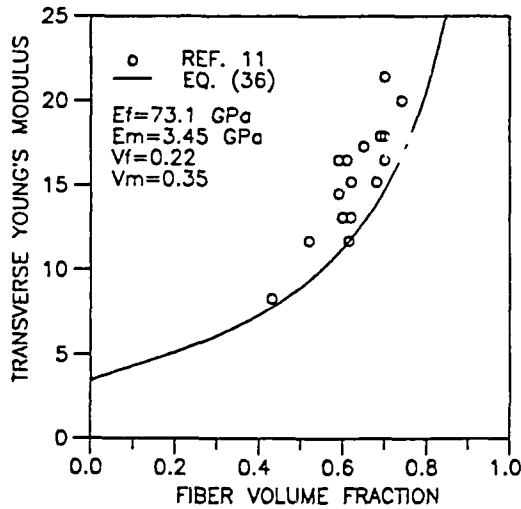


Fig. 4 Transverse Young's modulus of a continuous fiber composite

In Fig. 5, the effective elastic constants for a composite with aligned discontinuous fibers calculated from eq. (36) are illustrated for glass fibers in polystyrene.¹² The elastic constants shown in Fig. 5 are then utilized as input data for determining the effective Young's modulus of the same composite with randomly oriented fibers in a two dimensional domain. Fig. 6 shows the comparison between the present study and the experimental result of Lee.¹²

The variations of the effective Young's modulus in the major axis are illustrated in Fig. 7 for an ideal short fiber composite subjected to each of the three material forming processes discussed earlier. Consider an extreme case in which the thickness ratio is zero. In such a case the fibers after hot pressing or rolling become planar. The material properties after hot pressing become transversely isotropic, while those after rolling remain orthotropic. When the material is subjected to an extrusion in which the diameter ratio approaches zero, the material properties of a perfectly aligned fiber composite are retrieved as shown in Fig. 7.

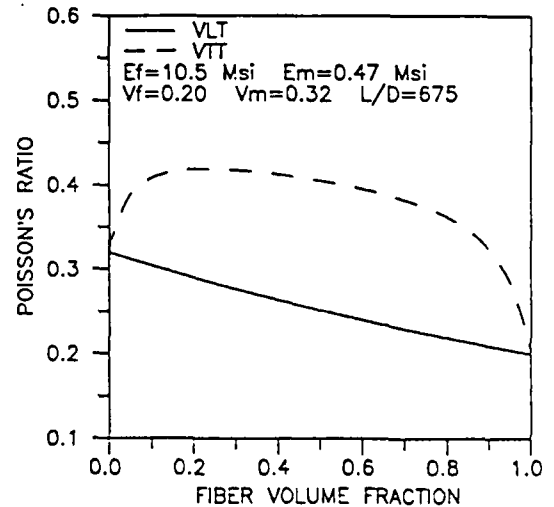
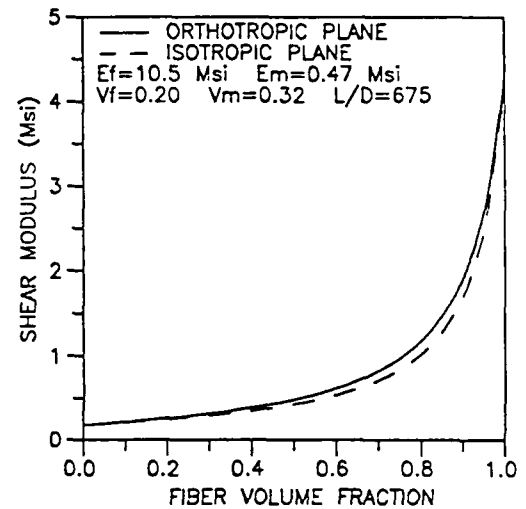
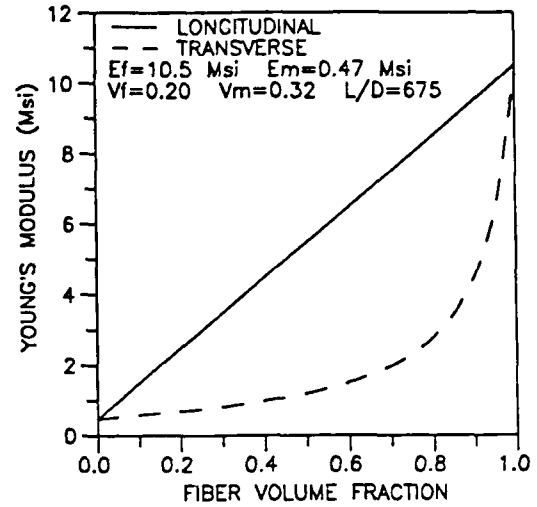


Fig. 5 Elastic constants of a perfectly aligned fiber composite

- (a) Young's moduli
- (b) Shear moduli
- (c) Poisson's ratios

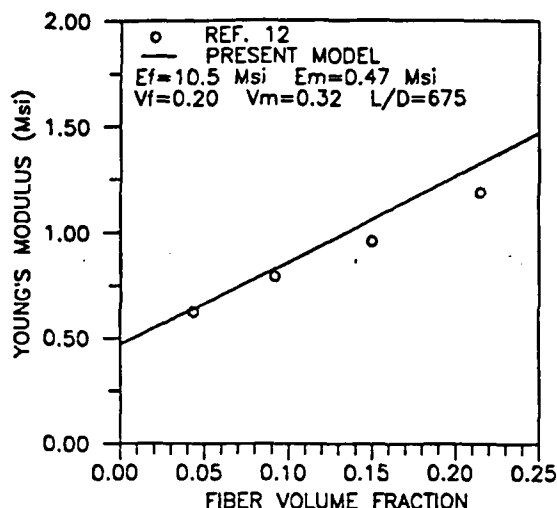


Fig. 6 Effective Young's modulus of a composite with two-dimensional random fibers

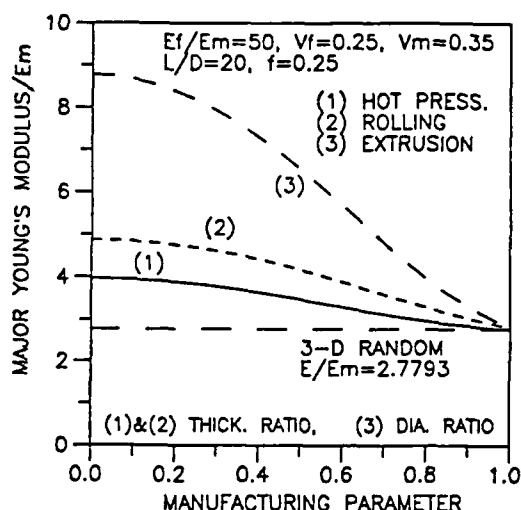


Fig. 7 Effective Major Young's Modulus

V. Concluding Remarks

From the present study, an engineering tool is proposed for theoretical evaluation of the elastic properties of a composite with perfectly aligned short fibers. Since a practical manufacturing scheme for the subject composite has not been developed, all existing analytical models except for those of continuous fiber composites cannot be directly verified by experimental data. Therefore, the authors propose herein an alternative method which minimizes the required effort and number of specimens. If the material elastic properties after a known material forming process are measured, the five elastic properties of the aligned fiber composite can be obtained by inverting the explicit solutions to hot pressing, extrusion or rolling discussed herein. The effective elastic properties of the same composite after different material forming processes then can be predicted using the same expression but with different material forming parameters. Also, the five indepen-

dent elastic constants obtained this way can be used for evaluating all existing empirical and theoretical models.

The present model can be generalized for combined material forming processes, such as transverse rolling after extrusion and transverse rolling after longitudinal rolling. In the former case, the θ rotation occurs prior to the ϕ rotation. Alternatively, the ϕ rotation is followed by another θ rotation in the latter case. Thus, the elastic properties of two final products with the same dimension may be different if the material forming histories are different. In conclusion, the entire material forming history of a composite reinforced by continuous or discontinuous fibers must be known a priori in order to predict the material elastic response.

Acknowledgements

This research was supported by the Texas Advanced Research Program.

References

1. Hashin, Z. and Rosen B. W., "The Elastic Moduli of Fiber-Reinforced Materials," *Journal of Applied Mechanics* BIE, Jun. 1964, pp. 223-231.
2. Chou, T. W., Nomura, S., and Taya, M., "A Self-Consistent Approach to the Elastic Stiffness of Short-Fiber Composites," *Journal of Composite Materials*, Vol. 14, 1980, pp. 178-188.
3. Halpin, J. C. and Pagano, N. J., "The Laminate Approximation for Randomly Oriented Fibrous Composites," *Journal of Composite Materials*, Vol. 3, 1969, pp. 720-724.
4. Christensen, R. M. and Waals F. M., "Effective Stiffness of Randomly Oriented Fibre Composites," *Journal of Composite Materials*, Vol. 6, 1972, pp. 518-532.
5. Chang, D. C., Weng, G. J., "Elastic Moduli of Randomly Oriented, Chopped-Fibre Composites with Filled Resin," *Journal of Materials Science*, Vol. 14, 1979, pp. 2183-2190.
6. Takao, Y., Chou, T. W., and Taya, M., "Effective Longitudinal Young's Modulus of Misoriented Short Fiber Composites," *Journal of Applied Mechanics*, Sep. 1982, Vol. 49, pp. 537-540.
7. Taya, M. and Chow, T. W., "On Two Kinds of Ellipsoidal Inhomogeneities in an Infinite Elastic Body: An Application to a Hybrid Composite," *Int. J. of Solids and Structures*, Vol. 17, 1981, pp. 553-563.
8. Taya, M. and Mura, T., "On Stiffness and Strength of an Aligned Short-Fiber Reinforced Composite Containing Fiber-End Cracks under Uniaxial Applied Stress," *Journal of Applied Mechanics*, June 1981, Vol. 48, pp. 361-367.
9. Berthelot, J. M., "Effect of Fibre Misalignment on the Elastic Properties of Oriented Discontinuous Fibre Composites," *Fiber Science and Technology*, Vol. 17, 1982, pp. 25-39.
10. Mura, T., *Micromechanics of Defects in Solids*, Mechanics of elastic and inelastic solids 3, Martinus Nijhoff Publishers, 1982, pp. 66-71.
11. Tsai, S. W. and Hahn, H. T., *Introduction to Composite Materials*, Technomic Publishing Co., Inc., 1980, pp. 394.
12. Lee, L. H., "Strength-Composition Relationships of Random Short Glass Fiber-Thermoplastics Composites," *Polymer Engineering and Science*, May 1969, Vol. 9, No. 3, pp. 213-224.

Appendix 7.3

A Self-Consistent Thermoviscoplastic Constitutive Model for Short Fiber Composites

**A SELF-CONSISTENT THERMO-VISCOPLASTIC
CONSTITUTIVE MODEL FOR
SHORT FIBER COMPOSITES**

by

J.G. Boyd
D.H. Allen

and

A.L. Highsmith

Aerospace Engineering Department
Texas A&M University
College Station, TX 77843

ABSTRACT

The Benveniste reinterpretation of the elastic version of the Mori-Tanaka method is extended to model the viscoplasticity of composites containing voids and/or microcracks. The matrix unified viscoplasticity equations of Miller are cast in a total strain formulation to yield the instantaneous tangent stiffness for use in the micromechanics model. For steady state creep, the composite strain rate is given in terms of the matrix stress rate. Initial yield surfaces are drawn for SiC/Al composites.

1. INTRODUCTION

Products manufactured by the sintering or not pressing of metal powders are finding increased use due to improvements in fabrication to near-net-shape and control of density. Filters and bearing cages are intentionally manufactured with a high degree of porosity. Conversely, load bearing powder metallurgy products such as superalloy turbine blades and SiC/aluminum aircraft structures require the highest possible densification.

Constitutive equations describing the elevated temperature behavior of reinforced porous metals are needed to enable their efficient production and service. The high temperature behavior of metals is best described by unified viscoplastic constitutive equations [Miller (1987), Walker (1984), and Bodner (1984)]. The unified equations combine plastic and creep strains in a single inelastic strain, and the models do not utilize a yield condition or delineate regions of purely elastic deformation. The constants in these unified equations are obtained from creep, monotonic tension, stress relaxation and cyclic tests. When the composite is modelled from a phenomenological perspective, this test regimen must be repeated for each combination of reinforcement and void morphology and volume fraction. A more efficient approach is to obtain the constants for the neat matrix from a single set of tests. The matrix constitutive equations could then be used in a micromechanics model to predict the overall composite behavior for various combinations of inclusion morphology and volume fraction.

At a representative material point, micromechanical constitutive modelling requires the solution of a localization boundary value problem followed by a homogenization procedure. The phenomenological approach to constitutive modelling is therefore computationally more efficient than the micromechanical approach. As the macroscopic history and rate dependent response of porous composites is not intuitively simple, a micromechanical model may be used to provide insight into the proper form of phenomenological models.

Due to the second phase reinforcement, voids, and microcracks, phenomenological composite constitutive equations should account for pressure dependent anisotropic flow even though the matrix may be inelastically isotropic. A number of phenomenological models have been proposed for metal matrix composites. Dvorak and Rao (1976) developed rate-independent hardening and flow rules for a composite consisting of a non-hardening matrix reinforced with continuous elastic fibers. The predicted plastic dilatation was of the same order of magnitude as the elastic dilatation. Porosity and microcracks were not considered. More recently, Robinson et al. (1987) introduced a con-

based unified viscoplasticity theory for transversely isotropic, fully dense composites. In both of these studies, the inelastic strain rate was obtained from normality to a macroscopic yield function or its rate-dependent analog. For porous metals, however, the inelastic strain rate is not generally normal to the phenomenological yield function. The problem is then complicated by the need to identify both a dissipation function and a yield function. [Nemat-Nasser and Shokooh(1980)].

Micromechanics models have also been developed to predict the inelastic behavior of composites and porous metals. Chu and Hashin (1971) applied the "composite spheres assemblage" model to predict the bulk modulus of strain-hardening metals containing either elastic particles or cavities. The results indicated that plastic macro-dilatation was not significant for elastic particles, but was very significant for porous metals. The Mori-Tanaka (1973) extension of Eshelby's (1957) equivalent inclusion method has been used to model rate-independent plasticity [Arsenault and Taya (1987), Tandon and Weng (1988)] and creep [Zhu and Weng (1989)] of metals reinforced with elastic particles and whiskers. All of these micromechanics methods made use of deformation plasticity theory to model the matrix. A "vanishing fiber diameter" model has been developed by Dvorak and Bahei-El-Din (1982) to predict the mechanical behavior of a kinematic-hardening, rate-independent matrix reinforced with elastic fibers. More recently, Dvorak and Bahei-El-Din (1987) developed a "bimodal" plasticity theory for fibrous composites with non-hardening matrices. The composite response was described in terms of either a fiber-dominated mode or a matrix-dominated mode. Aboudi (1987) has predicted the response of composites consisting of metals, described by unified viscoplasticity equations, containing elastic reinforcement and voids. The method is a simplification of a non-classical, or "continuum with microstructure" type model introduced by Sun et al. (1968) to study wave dispersion in laminates. The model was subsequently extended to model fibrous composites by Achenbach and Sun (1972).

Apparently, no "effective modulus" (defined in the sense of Hashin (1983)) micromechanics theory exists to predict the mechanical response of unified viscoplasticity-type metals containing particulate elastic reinforcement and/or voids and/or microcracks. This shortcoming is in part due to the complicated nature of the composite inelastic deformation. Due to second phase reinforcement, voids and microcracks, metal matrix composites have low ductility. The matrix constitutive equations must therefore account for both elastic and transient viscoplastic deformation. Also, inelastic deformation can alter the symmetry of the matrix stiffness, and macro-proportional loading may result in micro-nonproportional loading. Therefore, the present research has been undertaken to develop a model with the aforementioned capabilities. First, a micromechanics model is developed by extending to viscoplasticity Benveniste's (1987) reinterpretation of the elastic version of the Mori-Tanaka (1973) method. Next, the matrix unified viscoplasticity equations of Miller (1975) are cast in a total strain formulation suitable for use in the micromechanics model. Finally, the composite constitutive equations are presented in the unified form.

Although the presence of the reinforcement may lead to significant material strengthening of the in-situ matrix [Taya and Arsenault (1989)], the present analysis is concerned only with mechanical phase interaction.

II. MODEL FORMULATION

In the present study, the Mori-Tanaka method has been used to develop a mean field micromechanics model of a particulate reinforced metal matrix composite. The model is applicable at high homologous temperatures. The reinforcing particles are assumed to be linear elastic. Nonlinear composite behavior results from the viscoplastic character of the matrix material.

A. Matrix Constitutive Equations

The original unified viscoplasticity theory of Miller (1975) is reproduced in Table 1. Although more recent and more accurate versions of Miller's (1987) model are available, the simple original equations are better suited to elucidate the phase interaction in the composite. The evolution law for the kinematic hardening variable, or "back stress", σ_{ij}^b is similar to the familiar Bailey-Orowan form of strain hardening and static (thermal) recovery (softening). The evolution law for the isotropic hardening variable, or "drag stress", D includes a dynamic recovery term. The back stress and drag stress are coupled in equation (1.4). The back stress is constrained to be purely deviatoric.

Table 1. Summary of the Miller Constitutive Theory

$$\dot{\epsilon}_{ij} = (C_{ijkl})^{-1} \dot{\sigma}_{kl} + \dot{\epsilon}_{ij}^I \quad (1.1)$$

$$\dot{\epsilon}_{ij}^I = \frac{3}{2} \frac{\dot{\bar{\epsilon}}^I}{\sigma - \sigma^b} (\sigma'_{ij} - \sigma_{ij}^b) \quad (1.2)$$

$$\dot{\sigma}_{ij}^b = H_1 \dot{\epsilon}_{ij}^I - \frac{3}{2} H_1 B \theta [\sinh(A_1 \bar{\sigma}^b)]^n \frac{\sigma_{ij}^b}{\bar{\sigma}^b} \quad (1.3)$$

$$\dot{D} = H_2 \dot{\bar{\epsilon}}^I (C_2 + \bar{\sigma}^b - \frac{A_2}{A_1} D^3) - H_2 C_2 B \theta [\sinh(A_2 D^3)]^n \quad (1.4)$$

$$\dot{\bar{\epsilon}}^I = (\frac{2}{3} \dot{\epsilon}_{ij}^I \dot{\epsilon}_{ij}^I)^{1/2} = B \theta \left\{ \sinh\left[\frac{\sigma - \sigma^b}{D}\right]^{1.5} \right\}^n \quad (1.5)$$

$$\bar{\sigma}^b = (\frac{3}{2} \sigma_{ij}^b \sigma_{ij}^b)^{1/2} \quad (1.6)$$

$$\sigma - \sigma^b = [\frac{3}{2} (\sigma'_{ij} - \sigma_{ij}^b)(\sigma'_{ij} - \sigma_{ij}^b)]^{1/2} \quad (1.7)$$

$$\theta = \exp \left\{ \left[- \frac{Q^*}{0.5 RT_m} \right] [\ln(0.5 T_m / T) - 1] \right\} \quad \text{for } T \leq 0.6 T_m \quad (1.8)$$

$$\theta = \exp \left(- \frac{Q^*}{RT} \right) \quad \text{for } T > 0.6 T_m$$

At high homologous temperatures, the inelastic behavior of metals can no longer be described in terms of the yield function of classical plasticity. However, surfaces of constant inelastic strain rate, or SCISRs, formulated in stress space, have been shown experimentally [Blass and Findley (1971)] and analytically [Robinson (1985)] to serve as a viscoplastic analogy to the yield surface of classical plasticity. That is, the SCISR is a flow potential for the inelastic strain rate. The inelastic strain rate in Miller's model can be derived from a combined hardening type potential.

$$F = \frac{1}{2} (\sigma_{ij}^i - \sigma_{ij}^b) (\sigma_{ij}^i - \sigma_{ij}^b) - \frac{1}{3} \bar{\sigma}^2 = 0 \quad (4)$$

Thus, equation (1.2) is analogous to the flow rule of classical plasticity,

$$\dot{\epsilon}_{ij}^I = \dot{\lambda} \frac{\partial F}{\partial \sigma_{ij}} \quad (5)$$

We make the usual assumption that the back stress is initially zero and the initial value D_0 of the drag stress corresponds to the 0.2% offset "yield" stress in a uniaxial test. In classical plasticity, inelastic deformation does not occur until the stress state reaches the initial yield surface. From inspection of the flow rule (1.2) and the equivalent inelastic strain rate (1.5), it is apparent that inelastic deformation begins concurrently with the applied stress. The inelastic strain rate is negligible, however, if the effective stress is small relative to the drag stress. Also, due to static recovery, the inelastic multiplier $\dot{\lambda}$ is not generally equal to zero for tangential, or neutral, loading in the deviatoric plane or parallel to the hydrostatic axis. In fact, inelastic flow will occur unless $\sigma_{ij}^b = \sigma_{ij}^i$. Unlike the yield surface of classical plasticity the SCISR is free to contract as well as expand.

The stress state must lie on the SCISR at all times. By differentiating (4) the consistency condition can be written as

$$\frac{\partial F}{\partial \sigma_{ij}} (\dot{\sigma}_{ij}^i - \dot{\sigma}_{ij}^b) = \frac{2}{3} \dot{D} \quad (6)$$

The kinematic hardening rule (1.3) is similar in form to Prager's rule of kinematic hardening. Indeed, at low temperature and $\dot{\sigma}^b$, recovery is negligible, and Prager's rule of linear kinematic hardening is recovered. Although Prager's rule is physically correct, it is not geometrically correct in all stress subspaces. Fortunately, Prager's rule is geometrically correct for a number of matrix stress subspaces corresponding to technologically relevant composite loads. For the micromechanics analysis, consider the case where the inhomogeneities are aligned along the specimen principal axes, the composite loading is along the principal axes, and no shear tractions are applied. One possible configuration satisfying these constraints is shown in Figure 1. Under these circumstances, the average shear stress in the matrix is zero. Prager's rule is correct in a stress 6-space free of shear. In fact, the specimen axes now coincide with the principal axes of matrix stress, and Prager's rule is correct in the subspace of principal stresses when the principal stress axes are fixed.

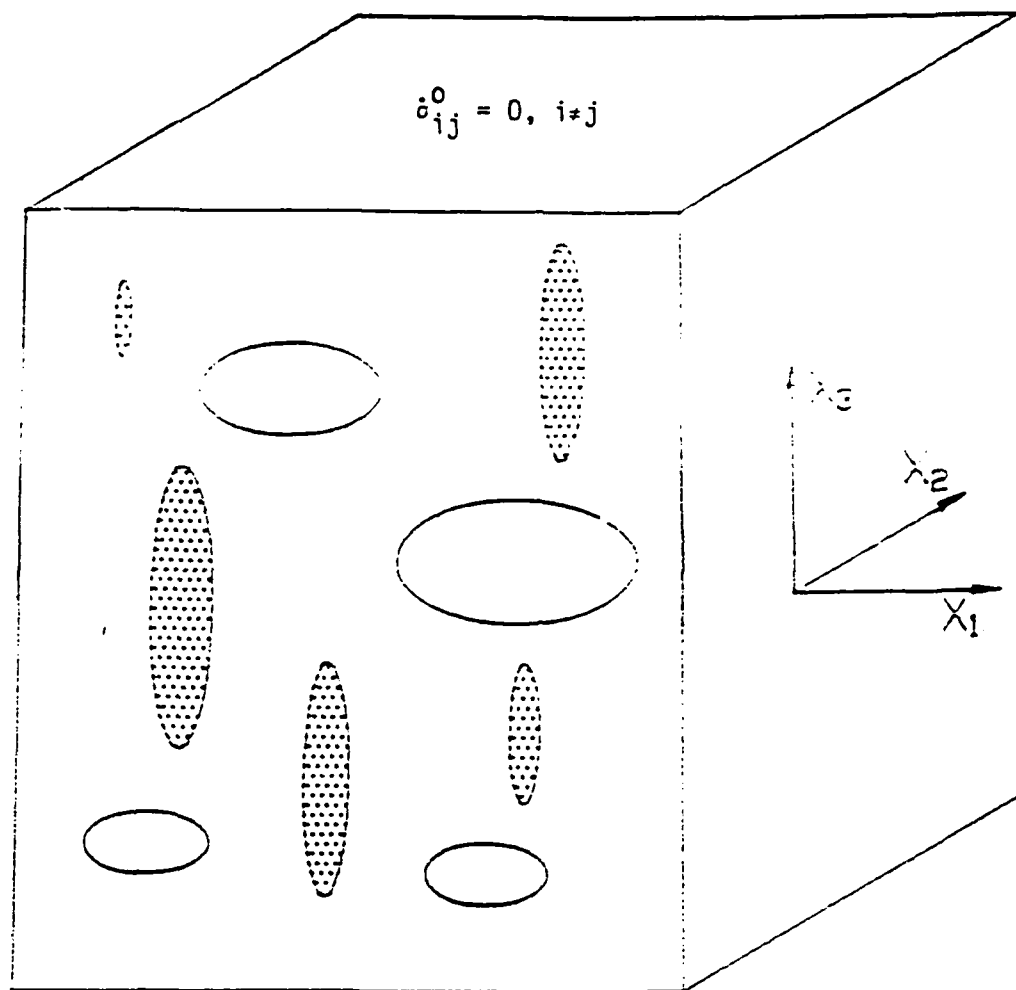


Figure 1. Theoretical model

Equations (3) thru (6) enable the derivation of the instantaneous stiffness corresponding to

$$L_{ijkl} = \frac{\partial \sigma_{ij}}{\partial \epsilon_{kl}} \quad (7)$$

Following the derivation in the Appendix, we obtain

$$L_{ijkl} = C_{ijkl} - \frac{C_{ijkl} \frac{\partial F}{\partial \sigma_{uv}} \frac{\partial F}{\partial \sigma_{mn}} C_{mnop}}{B} \quad (8)$$

where

$$B = \frac{\partial \sigma_{OD}^I}{\partial \epsilon_{st}^I} \frac{\partial \sigma_{OD}^I}{\partial \epsilon_{st}^I} + \frac{\partial F}{\partial \sigma_{mn}} \frac{\partial F}{\partial \sigma_{mn}} + \frac{\partial F}{\partial \sigma_{mn}} C_{mnop} \frac{\partial F}{\partial \sigma_{op}} \quad (9)$$

At small inelastic strain, Miller's model predicts primarily kinematic hardening. Thus, because metal matrix composites have low ductility, we predict predominantly kinematic hardening of the in situ matrix. It is well known that kinematic hardening may induce inelastic anisotropy. In a complete elastic-plastic stiffness such as (8), isotropic hardening induces anisotropy in the instantaneous stiffness. Deformation theory does not usually account for development of anisotropy.

B. Micromechanics

In order to extend Benveniste's (1987) reinterpretation of the elastic version of the Mori-Tanaka (1973) method to viscoplasticity, we relate a history of the two phase self-consistent scheme. The use of the self-consistent method to predict the "effective", or overall composite, stiffness of elastic-plastic matrices reinforced with elastic inhomogeneities has evolved along two paths -- the "equivalent inclusion method" and the "direct approach." For comprehensive reviews, see Mura (1982) and Hashin (1983), respectively. As originally formulated by Eshelby (1957), for dilute concentrations of inhomogeneities, the equivalent inclusion method makes use of an "equivalency condition"

$$C_{ijkl}^i (\epsilon_{kl}^o + \epsilon_l + \epsilon_{kl}^p) = C_{ijkl}^m (\epsilon_{kl}^m + \epsilon_{kl}^o + \epsilon_{kl}^p - \epsilon_{kl}^*) \quad (10)$$

The reader should note that in the above equation and in the remainder of the paper superscripts denote qualitative description of the associated variables, whereas subscripts represent tensorial components. Thus in (10)

C_{ijkl}^i and C_{ijkl}^m denote the elastic stiffness of the inhomogeneity and matrix, respectively, ϵ_{kl}^o is the far-field strain, ϵ_{kl} is the strain in the inhomogeneity, ϵ_{kl}^p is the matrix plastic strain, and ϵ_{kl}^* is the "equivalent transformation strain", or "eigenstrain." Eshelby's principal result was that uniform strain fields are produced in an ellipsoidal

inhomogeneity embedded in an infinite matrix under uniform strain ϵ_{kl}^0 and uniform plastic strain ϵ_{kl}^p . The method was subsequently extended by Mori and Tanaka (1973) by including a "back stress" analysis which accounts for the mutual interaction between inhomogeneities. Composite elastic and plastic hardening moduli were obtained from energy principles. The Mori-Tanaka back stress analysis has, in turn, been extended by Taya and Chou (1981) to include two types of inhomogeneities.

As pointed out by Hill (1965a) in his self-consistent analysis of polycrystalline plasticity, the matrix instantaneous stiffness, rather than the elastic stiffness, should be used in the solution of the "auxiliary problem" of a single grain embedded in an elastic-plastic matrix. Following this recommendation, Tandon and Weng (1988) corrected the Mori-Tanaka method by replacing the elastic stiffness C_{ijkl}^m in equation (10) with the instantaneous stiffness L_{ijkl}^m and removing the plastic strain ϵ_{kl}^p from the equation. The resulting equivalency condition in the incremental form is

$$C_{ijkl}^i (d\epsilon_{kl}^0 + d\bar{\epsilon}_{kl} + d\epsilon_{kl}) = L_{ijkl}^m (d\epsilon_{kl}^0 + d\bar{\epsilon}_{kl} + d\epsilon_{kl} - d\epsilon_{kl}^*) \quad (11)$$

where $d\bar{\epsilon}_{kl}$ is the increment of the Mori-Tanaka "back strain." We note that the Mori-Tanaka formulation for an elastic matrix is recovered if the instantaneous stiffness L_{ijkl}^m is replaced by the elastic stiffness C_{ijkl}^m .

Following Hill (1963), we write the "direct approach" to the composite elastic stiffness C_{ijkl} as

$$C_{ijkl} = C_{ijkl}^m + c^i \{ C_{ijmn}^i - C_{ijmn}^m \} A_{mnkl} \quad (12)$$

where c^i is the reinforcement volume fraction and the brackets denote the orientation average. The composite elastic stiffness can be obtained following the determination of the orientation dependent "strain concentration factor" A_{ijkl} , which gives the average inhomogeneity strain in terms of the uniform composite strain. The determination of A_{ijkl} is the essential difficulty in the micromechanics method. For dilute concentrations of inhomogeneities, the tensor $A_{ijkl} = T_{ijkl}$ can be obtained from Eshelby (1957) as

$$T_{ijkl} = [I_{ijkl} + S_{ijmn} (C_{mnop}^m)^{-1} (C_{opkl}^i - C_{opkl}^m)]^{-1} \quad (13)$$

where S_{ijmn} is the Eshelby tensor, and I_{ijkl} is the identity tensor. For a non-dilute concentration of inhomogeneities, the strain concentration tensor should be derived in a manner which takes into account the particle interaction. Hill (1965b) obtained such a concentration tensor in his "direct

approach" to the self-consistent scheme for two-phase composites.

The Eshelby tensor is a function of the particle aspect ratios and the instantaneous matrix stiffness. Mura (1982) has given single integral equations for the Eshelby tensor corresponding to the case of a transversely isotropic matrix with its crystalline directions coincident with the principal directions of a spheroidal inhomogeneity of any aspect ratio. For the case of a generally orthotropic matrix containing spherical inhomogeneities, Morris (1970) has given double integrals for the Eshelby tensor.

In order to use Mura's integrals for the Eshelby tensor, the inhomogeneities are assumed to be aligned in the x_3 direction. The macroscopic loading is constrained to render the instantaneous matrix stiffness, at most, transversely isotropic about the x_3 axis. This condition is not overly restrictive, as it allows for the application of hydrostatic pressure and combined tension/torsion, and triaxial stress states in which $\dot{\epsilon}_{11} = \dot{\epsilon}_{22}$, $\dot{\epsilon}_{33} = 0$.

Recently, Benveniste (1987) made the remarkable observation that the non-dilute strain concentration tensor could be obtained from a reexamination of the elastic Mori-Tanaka method in terms of equations (12) and (13). Benveniste et al. (1989) subsequently extended the analysis to predict the effective elastic stiffness of composites with two types of inhomogeneities. Recall from equation (11) that the elastic-plastic form of the Mori-Tanaka method is obtained by replacing the matrix elastic stiffness with the instantaneous stiffness. Therefore, the elastic-plastic form of the Benveniste et al. (1989) method can be written in terms of instantaneous stiffness L_{ijkl}^m . In the remainder of the paper, equations will be cast in rate, rather than incremental form. Under an applied uniform strain rate $\dot{\epsilon}_{ij}^0$, the composite instantaneous tangent stiffness L_{ijkl} is given as

$$L_{ijkl} = \left[\sum_r c^r L_{ijmn}^r T_{mnop}^r \right] \left[\sum_r c^r T_{opkl}^r \right]^{-1} \quad (14)$$

where $r = 1$ denotes the first particle type,
 $r = 2$ denotes the second particle type, and
 $r = m$ denotes the matrix phase.

The average phase strain rates are given by

$$\dot{\epsilon}_{ij}^r = A_{ijkl}^r \dot{\epsilon}_{kl}^0, \quad r = 1, 2, m \quad (15)$$

or

$$\dot{\epsilon}_{ij}^r = T_{ijkl}^r \dot{\epsilon}_{kl}^m, \quad r=1,2 \quad (16)$$

where the matrix strain rate is written in terms of the applied strain rate $\dot{\epsilon}_{ij}^0$ as

$$\dot{\epsilon}_{ij}^m = [\sum_r c^r T_{ijkl}^r]^{-1} \dot{\epsilon}_{kl}^0, \quad r=1,2,m \quad (17)$$

The dilute strain concentration tensors T_{ijkl}^r are given in the form

$$T_{ijkl}^r = [I_{ijkl} + S_{ijmn}^r (L_{mnop}^m)^{-1} (L_{opst}^r - L_{opst}^m)]^{-1}, \quad r=1,2 \quad (18)$$

$$T_{ijkl}^m = I_{ijkl} \quad (19)$$

where the fourth-order unit tensor is defined by

$$I_{ijkl} = \frac{1}{2} (\delta_{ik}\delta_{jl} + \delta_{il}\delta_{jk}) \quad (20)$$

Similarly, under an applied traction giving rise to a uniform stress rate $\dot{\sigma}_{ij}^0$, the composite instantaneous compliance M_{ijkl} ($= -\frac{1}{\dot{\sigma}_{ij}^0}$) is given as

$$M_{ijkl} = [\sum_r c^r M_{ijmn}^r W_{mnop}^r] [\sum_r c^r W_{opkl}^r]^{-1}, \quad r=1,2,m \quad (21)$$

with

$$\dot{\sigma}_{ij}^r = B_{ijkl}^r \dot{\sigma}_{kl}^0, \quad r = 1, 2, m \quad (22)$$

or

$$\dot{\sigma}_{ij}^r = W_{ijkl}^r \dot{\epsilon}_{kl}^m, \quad r = 1, 2 \quad (23)$$

where the matrix stress rate is written in terms of the applied stress rate $\dot{\sigma}_{ij}^0$ as

$$\dot{\sigma}_{ij}^m = [\sum_r c^r W_{ijkl}^r]^{-1} \dot{\sigma}_{kl}^0, \quad r = 1, 2, m \quad (24)$$

The dilute stress concentration tensors are

$$W_{ijkl}^r = L_{ijmn}^r T_{mnop}^r M_{opkl}^m, \quad r = 1, 2, m \quad (25)$$

Substitution of equation (9) into (14) results in

$$W_{ijkl}^m = I_{ijkl} \quad (26)$$

For a given composite stress rate $\dot{\sigma}_{ij}^0$, the composite total strain rate $\dot{\epsilon}_{ij}^0$ follows from the composite compliance M_{ijkl} , equation (21). The micromechanics leading to M_{ijkl} is based on the fact that the composite total strain rate is equal to the volume average of the phase total strain rates. As pointed out by Hill (1967), the elastic and inelastic components of the composite total strain rate are not direct averages of their microscopic counterparts when the composite stress rate $\dot{\sigma}_{ij}^0$ maintains inelastic flow in an elastically heterogeneous medium. The composite inelastic strain is typically obtained from an elastic unloading. Because the unified equations do not allow for regions of purely elastic deformation we will consider only

imaginary "instantaneous" elastic unloading. In other words, we assume that during the infinitesimal period of unloading static recovery has insufficient time to induce inelastic flow. With this assumption, we associate with each real state an imaginary elastic state of zero applied stress. The composite inelastic strain rate is then given by

$$\dot{\epsilon}_{ij}^{OI} = [M_{ijkl} - (C_{ijkl})^{-1}] \dot{\epsilon}_{kl}^C \quad (27)$$

However, the composite inelastic strain rate may be obtained without calculating the composite compliance. Suquet (1985) has given the composite inelastic strain as the volume average of the product of the phase stress concentration factors and the phase inelastic strains. When inelastic flow occurs only in the matrix the result is simply

$$\dot{\epsilon}_{ij}^{OI} = c^m B_{ijkl}^m \dot{\epsilon}_{kl}^{ml} \quad (28)$$

The proof follows from the decomposition of strain and the equivalence of micro and macro virtual power, also known as Hill's Macromogeneity Equality.

The model accounts only for the particle volume fraction and not the individual particle size. We make the implicit assumption that the individual particles "see" a statistically homogeneous polycrystalline matrix. SiC whiskers of 1-2 μm diameter, however, are embedded within single grains. Walker and Jordan (1989) have developed unified constitutive equations for single crystals. The inversion of single crystal equations to the total strain form may be of limited utility, however, due to the presence of multiple corners on a single crystal SCISR. Fortunately, continuous fibers of 150 μm diameter may be at least one order of magnitude larger than the surrounding grains [Kim et al. (1989)]. But the Mori-Tanaka method may have limited applicability to typical continuous fiber reinforced metal matrix composites, which are often no more than eight plies thick. In this case, the fiber diameter is of the same order of magnitude as the composite thickness. The rigorous form of the micromechanics may not then reduce to the simple common form (see, for instance, Mori and Tanaka (1973), the appendix).

The model presented herein provides the mechanical equation of state for the composite and the growth law for the composite inelastic strain. The damage state is treated as known. The Mori-Tanaka method has been used [Taya (1981)] to obtain the strain energy release rates of cracks in elastic composites. The concept of strain energy release rate is of limited utility for bodies beyond general yield. Also, proportional macro-loading may result in non-proportional micro-loading. The J integral is therefore not useful for calculating microcrack strain energy release rates.

The Mori-Tanaka method has also been used [Taya (1981)] to study ductile void growth in viscous metals. Ductile void growth is primarily a finite deformation phenomenon and is of limited consequence in composites. Indeed, experimental studies of SiC reinforced aluminum composites indicate that no measurable increase of porosity occurs in loading to failure [Flom and Arsenault (1989)].

III. RESULTS AND DISCUSSION

A. Composite Hardening Equations

The composite inelastic strain rate can be obtained from a composite SCISR in σ_{ij}^0 space. Hill (1967) has identified the constraints on the composite yield function in terms of the constituent yield functions. For the simple case at hand, overall yielding occurs simultaneously with matrix yielding. Furthermore, the composite yield function is smooth and convex, and the macroscopic plastic strain increment is in the direction of the outward normal.

Substitution of (22) into the matrix SCISR (4) defines the initial SCISR in composite stress space:

$$F = \frac{1}{2} (B_{ijkl}^{me} \sigma_{kl}^0)' (B_{ijuv}^{me} \sigma_{uv}^0)' - \frac{1}{3} D_0^2 = 0 \quad (29)$$

where B_{ijkl}^{me} is the elastic stress concentration tensor. In defining the initial SCISR we make the usual assumption that the back stress is initially zero and the drag stress is of initial value D_0 . The concentration tensor B_{ijkl}^{me} induces a rotation and an anisotropic expansion of the SCISR. The SCISR (29) is the equation for an ellipse in the deviatoric plane, and the initial SCISR may now exhibit pressure dependence. The stress concentration tensors are defined in terms of stress rates, whereas the SCISR is defined in space of current stress. A simple substitution such as (29) will therefore not enable the determination of subsequent SCISRs.

Dvorak and Bahei-El-Din (1982) have derived composite kinematic hardening rules for fiber reinforced kinematically hardening metals. We use this method to obtain the macroscopic back stress σ_{ij}^B . The back stress σ_{ij}^B corresponding to a yield function has a different meaning than the Mori-Tanaka back stress $\tilde{\sigma}_{ij}$. The Mori-Tanaka back stress is given by the difference of the applied stress and the resulting matrix stress as

$$\tilde{\sigma}_{ij} = \sigma_{ij}^m - \sigma_{ij}^0 \quad (30)$$

or, using (22),

$$\tilde{\sigma}_{ij} = (B_{ijkl}^m - I_{ijkl}) \sigma_{kl}^0 \quad (31)$$

The Mori-Tanaka back stress will develop under purely elastic loading, whereas the back stress responsible for kinematic hardening gives the yield function translation due only to inelastic flow.

The location of the SCISR in composite stress space is given by σ_{ij}^B . The back stress rate $\dot{\sigma}_{ij}^B$ is obtained by subtracting the elastic response from the total response. For instance, during a time increment dt we apply a load $d\sigma_{ij}^C$, followed immediately by an instantaneous, and therefore elastic, unloading $-d\sigma_{ij}^C$. Due to the matrix inelastic deformation, the matrix stress

will not return to its pre-load-cycle value. The resulting matrix residual stress increment is

$$d\sigma_{ij}^r = (B_{ijkl}^m - B_{ijkl}^{me}) d\sigma_{kl}^0 \quad (32)$$

The composite and matrix SCISR translations due to the load increment are related by

$$B_{ijkl}^{me} d\sigma_{kl}^B = d\sigma_{ij}^B - d\sigma_{ij}^r \quad (33)$$

Thus, the composite back stress is seen to depend explicitly on the "material" hardening stress $d\sigma_{ij}^B$ and the "mechanical" hardening stress $d\sigma_{ij}^r$ due to constraint hardening. If the inhomogeneities are voids, $d\sigma_{ij}^r$ is a mechanical softening stress.

The composite back stress increment is given by (32) and (33):

$$d\sigma_{kl}^B = (B_{ijkl}^{me})^{-1} d\sigma_{ij}^B - [(B_{ijkl}^{me})^{-1} B_{ijuv}^m - I_{kluv}] d\sigma_{uv}^0 \quad (34)$$

The incremental equation (34) may be rewritten in rate form as

$$\dot{\sigma}_{kl}^B = (B_{ijkl}^{me})^{-1} \dot{\sigma}_{ij}^B - [(B_{ijkl}^{me})^{-1} B_{ijuv}^m - I_{kluv}] \dot{\sigma}_{uv}^0 \quad (35)$$

The evolution of the composite back stress is thus seen to depend explicitly on the evolution of the matrix back stress and the applied stress rate.

B. Composite Creep Equations

During creep or stress hold (strain transient) tests, the composite stress is constant, i.e. $\dot{\sigma}_{ij}^0 = 0$, and the composite strain rate cannot be determined by the compliance (21). Also, the phase stress rates cannot be determined from (22). The composite strain rate must be obtained from an equation relating $\dot{\epsilon}_{ij}^0$ directly to the matrix stress rate. To derive such an equation we begin with the composite stress/elastic strain equation

$$\dot{\epsilon}_{kl}^0 = (C_{kluv})^{-1} \dot{\sigma}_{uv}^0 + \dot{\epsilon}_{kl}^{0I} = \dot{\epsilon}_{kl}^{0I} \quad (36)$$

Substitution of (28) yields

$$\dot{\epsilon}_{kl}^0 = \dot{\epsilon}_{kl}^{0I} = c^m B_{kluv}^m \dot{\epsilon}_{uv}^{mI} \quad (37)$$

Next, we substitute equation (17) to obtain

$$c^m c^{m-1} B_{ijkl}^m \dot{\epsilon}_{ij}^{mI} = c^m B_{kluv}^m \dot{\epsilon}_{uv}^{mI} \quad n = 1, 2, m. \quad (38)$$

Now decomposing the matrix strain rate and making use of the matrix elastic compliance,

$$[\sum_r c^r T_{ijk}^r] (M_{ijop}^{me} \dot{\epsilon}_{op}^m + \epsilon_{ij}^{ml}) = c^m B_{kluv}^m \dot{\epsilon}_{uv}^{ml} \quad (39)$$

We solve for the matrix stress rate as

$$\dot{\sigma}_{op}^m = [\sum_r c^r T_{ijk}^r] M_{ijop}^{me}^{-1} c^m B_{kluv}^m - [\sum_r c^r T_{uvk}^r] (c^m B_{stuv}^m)^{-1} \dot{\epsilon}_{st}^{ml} \quad (40)$$

The matrix stress rate may be written in terms of the composite strain rate as

$$\dot{\sigma}_{op}^m = [\sum_r c^r T_{ijk}^r] M_{ijop}^{me}^{-1} c^m B_{kluv}^m - [\sum_r c^r T_{uvk}^r] (c^m B_{stuv}^m)^{-1} \dot{\epsilon}_{st}^0 \quad (41)$$

Equation (41) gives the matrix stress rate in terms of material hardening (softening) and constraint hardening (softening). The composite creep response contrasts sharply with the creep response of the in situ matrix. From (37), (40) and (1.2) it is apparent that constraint hardening precludes composite steady state creep if the matrix is undergoing steady state creep. A composite may obtain a steady state only when the sum of void-induced constraint softening and matrix thermal softening equals the sum of reinforcement-induced constraint hardening and matrix strain hardening. Under steady creep conditions, a SCISR is fixed in stress space, i.e. it does not translate, rotate, or expand (contract). Interestingly, a fixed matrix SCISR will generate a dynamic composite SCISR.

The "fading memory" of neat metal SCISRs has been experimentally verified by Blass and Findley (1971) and analytically modelled by Robinson (1985). Fading memory implies that, regardless of mechanical history, a metal will eventually reach a steady state flow rate unique to the current fixed stress state. The concept of a unique pairing of the stress and steady state inelastic strain rate is the foundation of Hart's (1970) framework, upon which Miller's model is predicated. Fortunately, the composite will exhibit fading memory. Recall that our model assumes all inhomogeneities to be separated by a continuous viscoplastic matrix. Furthermore, stress fields are uniform in the inhomogeneities. Therefore, residual stresses in the inhomogeneities must be balanced by residual stresses in the matrix. The matrix exhibits fading memory with respect to the deviatoric component of residual stress, which will eventually totally relax through static recovery. Equilibrium then demands total relaxation of the inhomogeneity residual deviatoric stress. Inelastic incompressibility of the matrix precludes the existence of residual hydrostatic stress.¹

¹ We do not consider thermal residual stress.

3. Initial Yield Surface

Recall that the inhomogeneities are aligned in the x_3 direction. For macroscopic axisymmetric loading the initial yield surfaces of SiC ($E=430$ GPa, $\nu=0.2$) reinforced aluminum ($E=63$ GPa, $\nu=0.33$) composites are shown in Figures 2 and 3 for 20% and 30% reinforcement volume fraction, respectively. The axisymmetric transverse stress is given as

$$\sigma_1^0 = \frac{1}{2} (\sigma_1^0 + \sigma_2^0) \quad (42)$$

For spherical reinforcement, the yield surface is a cylinder aligned along the hydrostatic axis. For whiskers and fibers, the cylinder rotates in the direction of reinforcement and is now an ellipse in the deviatoric plane. The yield surfaces corresponding to whiskers and fibers do not differ substantially. The surfaces take the shape of a cylinder because the matrix is modelled only in terms of an average stress. Dvorak and Baneh-El-Din (1979) have used the modified self-consistent method to obtain yield surfaces for fibrous composites with non-hardening matrices. In that case, the yield surfaces were elliptical in the axisymmetric plane because the modified self-consistent method allows for two different (but uniform) matrix stress fields. Therefore, we expect the Mori-Tanaka method to predict an unrealistically large elastic region for large values of hydrostatic stress.

For macroscopic plane stress, the initial yield surface of a 50% boron fiber ($E=400$ GPa, $\nu=0.2$) reinforced aluminum ($E=72.5$ GPa, $\nu=0.33$) composite is shown in Figure 4. Also shown are the yield surfaces predicted by the matrix dominated mode (MDM) and the self-consistent fiber dominated mode [FDM(SCM)] for the bimodal theory of Dvorak and Baheh-El-Din (1987). For B/AI the bimodal theory has been experimentally shown to predict extremely accurate results for plane stress loading in the $\sigma_{32} - \sigma_{33}$ and $\sigma_{32} - \sigma_{22}$ planes. Apparently, the Mori-Tanaka method underestimates the yield strength of fibrous composites. This conclusion is supported by Figure 4 and also Figures 2 and 3, which indicate little strengthening of the fiber composite over the whisker composite. For whisker and particulate composites, however, the Mori-Tanaka method should predict more accurate results than the bimodal theory.

The rigorous theory of "effective modulus" elastic micromechanics involves the exact solution of a localization boundary value problem taken over a representative volume element. The resulting microscopic field variables are then transformed to the macroscopic values through a suitable homogenization procedure. Usually, the localization problem must be solved using the finite element method. Micromechanics models were developed to provide physical insight and predictive capability using approximate methods of localization and homogenization. In general, these methods involve exact solutions to elastic boundary value problems formulated over an approximate representative volume element. For example, the localization problem in the Mori-Tanaka method is the "auxiliary" problem of Eshelby's "equivalent inclusion" solution for a single ellipsoidal inhomogeneity in an infinite matrix. The approximate localization scheme in the Generalized Self-Consistent Method [Christensen and Lo (1979)] involves the solution to a concentric spheres or a concentric cylinders problem. Unfortunately, the properties of history dependent materials vary with strain. Exact solutions cannot be obtained for localization problems involving inelastically hardening materials in the presence of strain gradients. Under these circumstances, Eshelby's "equivalent inclusion" solution is merely an approximation.

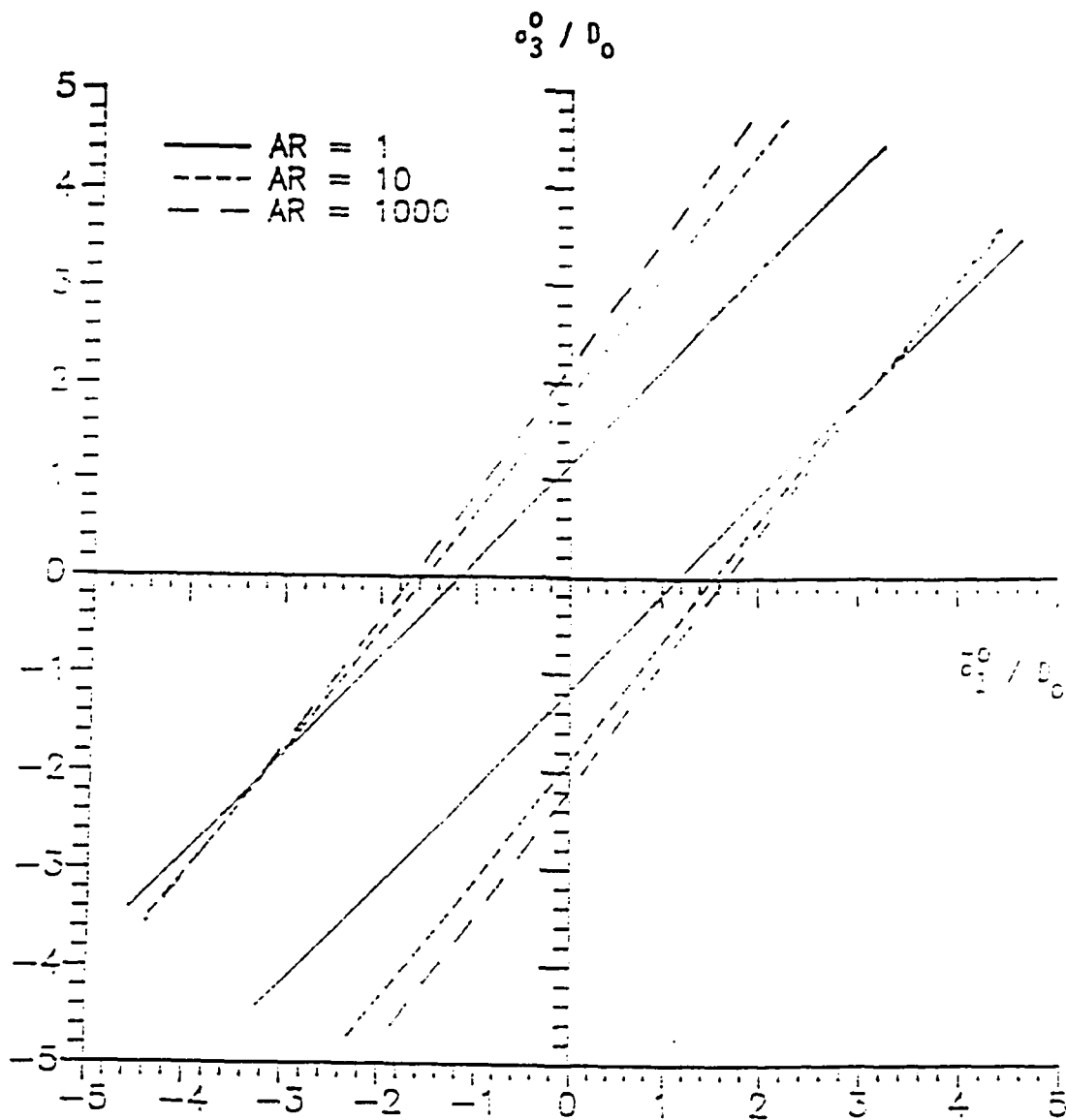


Figure 2. Initial yield surfaces for 20% SiC/Al in the axisymmetric plane.

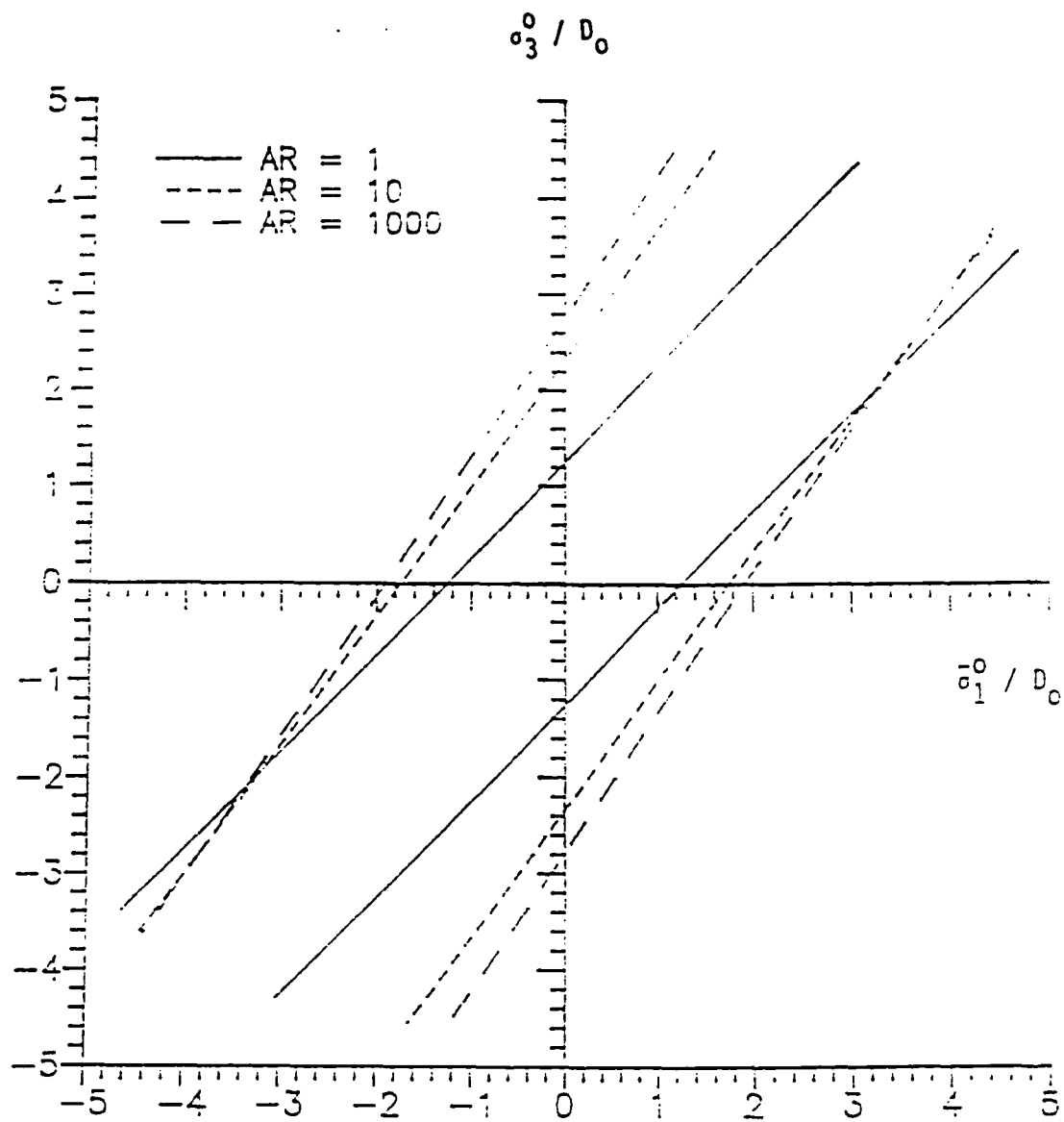


Figure 3. Initial yield surfaces for 30% SiC/Al in the axisymmetric plane.

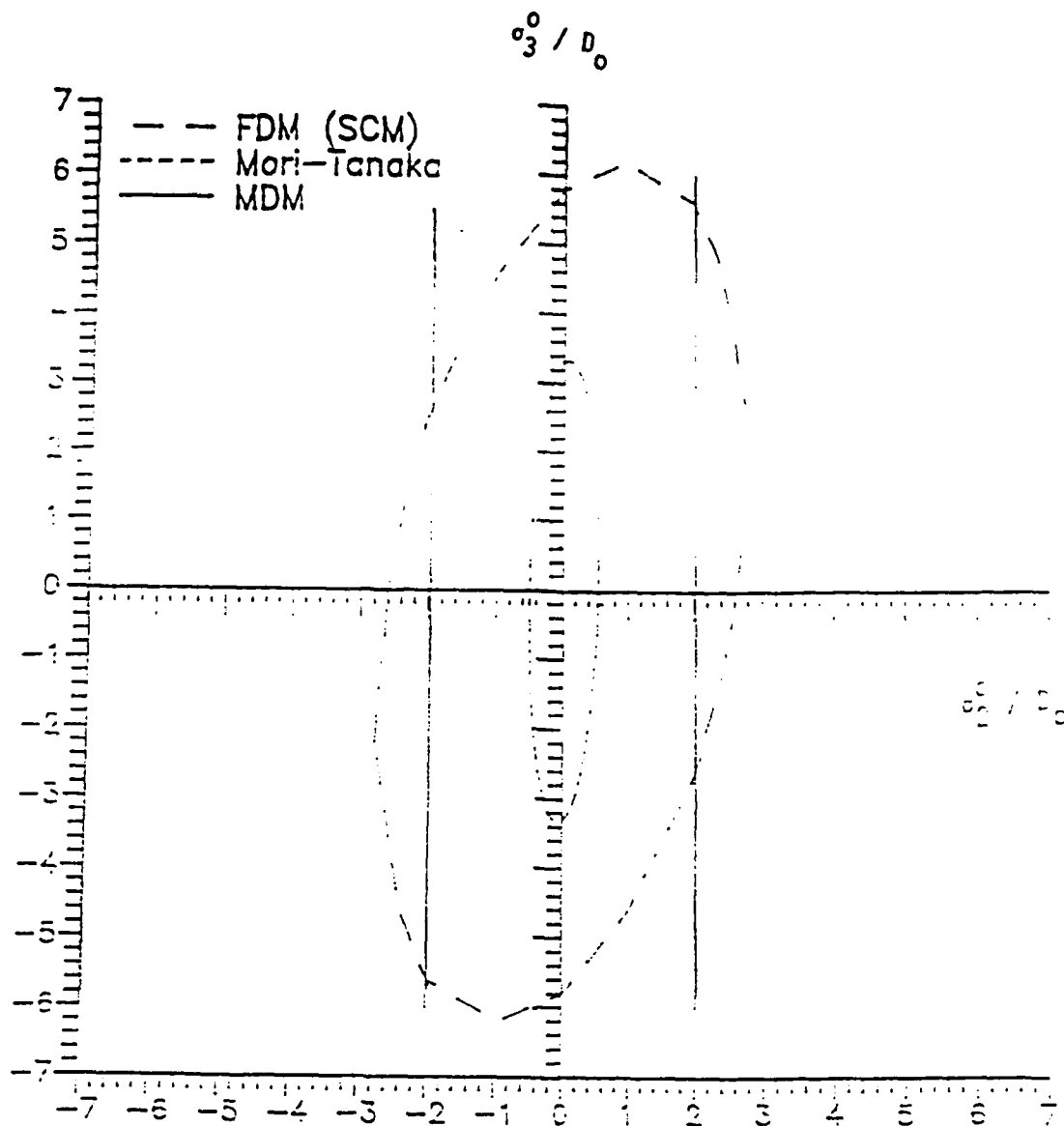


Figure 4. Initial yield surfaces for 50% B/Al, plane stress.

In a recent comparison, Christensen (1990) determined that the Generalized Self Consistent Scheme is qualitatively superior to the Mori-Tanaka method. It was shown that the Mori-Tanaka method involved no solution of the basic particle interaction problem in the non-dilute case, and the method is essentially "an estimate of the solution form guided only by the requirement of the dilute solution at one end of the concentration scale and at the opposite end of the scale by the requirement that as $C_2 \rightarrow 1$, the effective property identify with that of the inclusion phase." In the dilute limit as $C_2 \rightarrow 0$ the Mori-Tanaka method takes the form of Eshelby's method, which for inelastically hardening materials does not yield an exact solution.

IV. SUMMARY

A micromechanics model for the viscoplastic behavior of a metal matrix composite has been developed. The composite consists of a thermoviscoplastic matrix reinforced by linear elastic particles. Voids are also included in the analysis. The micromechanics model has been used to develop constitutive equations for the composite. Specifically, strain hardening equations and initial SCISR for the composite have been obtained. In addition, the micromechanics model has been used to generate equations describing creep of the composite.

The micromechanics model presented herein provides a general framework for predicting composite response based on constituent behavior. For example, while Miller's unified thermoviscoplasticity theory was used to describe the thermomechanical behavior of the matrix in the present study, other constitutive theories could have been used. In the future residual stresses due to thermal expansion mismatch will be included and the analysis extended to predict thermoviscoplastic response of the composite.

ACKNOWLEDGEMENT

The authors gratefully acknowledge the citizens of Texas for funding this research under the Texas Advanced Research Program.

REFERENCES

- Aboudi J., "Constitutive Relations for Cracked Metal Matrix Composites," Mechanics of Materials, vol. 6, 1987, pp. 303-315.
- Achenbach, J.D., and Sun, C.-T., in Dynamics of Composite Materials, E.H. Lee, ed., American Society of Mechanical Engineers, N.Y., 1972.
- Arsenault, R.J., and Taya, M., "Thermal Residual Stress in Metal Matrix Composite," Acta Metallurgica, vol. 35, no. 3, 1987, pp. 651-659.
- Benveniste, Y., "A New Approach to the Application of Mori-Tanaka's Theory in Composite Materials," Mechanics of Materials, vol. 6, 1987, pp. 147-157.
- Benveniste, Y., Dvorak, G.J., and Chen, T., "Stress Fields in Composites with Coated Inclusions," Mechanics of Materials, vol. 7, 1989, pp. 305-317.
- Blass, J.J. and Findley, W.N., "Short-Time, Biaxial Creep of an Aluminum Alloy with Abrupt Changes in Temperature and State of Stress," Journal of Applied Mechanics, vol. 38, no. 2, 1971, pp. 489-501.
- Boedner, S.R., "Review of a Unified Elasto-Viscoplastic Theory," AFOSR-84-0042, 1984.
- Christensen, R.M., "A Critical Evaluation for a Class of Micromechanics Models," Journal of Mechanics and Physics of Solids, Vol. 38, No. 3, 1990, pp. 379-404.
- Christensen, R.M., and Lo, K.H., "Solutions for Effective Shear Properties in Three Phase Sphere and Cylinder Models," Journal of Mechanics and Physics of Solids, Vol. 27, 1979, pp. 315-330.
- Chu, T.Y., and Hashin, Z., "Plastic Behavior of Composites and Porous Media Under Isotropic Stress," International Journal of Engineering Science, vol. 9, 1971, pp. 971-994.
- Dvorak, G.J., and Bahei-El-Din, Y.A., "Plasticity Analysis of Fibrous Composites," Journal of Applied Mechanics, vol. 49, 1982, pp. 327-335.
- Dvorak, G.J., and Bahei-El-Din, Y.A., "A Bimodal Plasticity Theory of Fibrous Composite Materials," Acta Mechanica, vol. 69, 1987, pp. 219-241.
- Dvorak, G.J., and Bahei-El-Din, Y.A., "Elastic-Plastic Behavior of Fibrous Composites," Journal of the Mechanics and Physics of Solids, vol. 27, 1979, pp. 51-72.
- Dvorak, G.J. and Rao, M.S.M., "Axisymmetric Plasticity Theory of Fibrous Composites," International Journal of Engineering Science, vol. 14, 1976, pp. 361-373.
- Eshelby, J.D., "The Determination of the Elastic Field of the Ellipsoidal Inclusion, and Related Problems," Proceedings of the Royal Society, London vol. A241, 1957, pp. 376-396.
- Flom, Y., and Arsenault, R.J., "Effect of Particle Size on Fracture Toughness of SiC/Al Composite Material," Acta Metallurgica, vol. 37, no. 9, 1989, pp. 2413-2423.
- Hart, E.W., "A Phenomenological Theory for Plastic Deformation of Polycrystalline Metals," Acta Metallurgica, vol. 18, 1970, pp. 599-610.
- Hashin, Z., "Analysis of Composite Materials," Journal of Applied Mechanics, vol. 50, 1983, pp. 481-505.
- Hill, R., "Elastic Properties of Reinforced Solids: Some Theoretical Principles," Journal of Mechanics and Physics of Solids, vol. 11, 1963, pp. 357-372.

Hill, R., "Continuum Micro-Mechanics of Elastoplastic Polycrystals," Journal of the Mechanics and Physics of Solids, vol. 13, 1965, pp. 89-101.

Hill, R., "A Self-Consistent Mechanics of Composite Materials," Journal of the Mechanics and Physics of Solids, vol. 13, 1965, pp. 213-222.

Hill, R., "The Essential Structure of Constitutive Laws for Metal Composites and Polycrystals," Journal of the Mechanics and Physics of Solids, vol. 15, 1967, pp. 79-95.

Kim, J.S., Verrill, M.C., and Gabe, T.A., "Characterization of Failure Processes in Tungsten-Copper Composites Under Fatigue Loading Conditions," NASA Technical Memorandum 102371, 1986.

Miller, A.K., "A Unified Phenomenological Model for Monotonic, Cyclic and Creep Deformation of Strongly Work-Hardening Materials," Ph.D. Dissertation, Stanford University, Department of Materials Science and Engineering, May 1975.

Miller, A.K., "The MATMOD Equations," in Unified Constitutive Equations for Creep and Plasticity, A.K. Miller, ed., Elsevier, 1987, pp. 139-212.

Mori, T., and Tanaka, K., "Average Stress in Matrix and Average Elastic Energy of Materials with Misfitting Inclusions," Acta Metallurgica, vol. 21, 1973, pp. 571-574.

Morris, P.R., "Elastic Constants of Polycrystals," International Journal of Engineering Science, vol. 8, 1970, pp. 49-61.

Mura, T., Micromechanics of Defects in Solids, Martinus Nijhoff, 1982.

Nemat-Nasser, S., and Shokoh, A., "On Finite Plastic Flows of Compressible Materials With Internal Friction," International Journal of Solids and Structures, vol. 16, 1980, pp. 455-514.

Robinson, D.N., "On Thermomechanical Testing in Support of Constitutive Equation Development for High-Temperature Alloys," NASA Contractor Report 174879, 1985.

Robinson, D.N., Duffy, S.F., and Ellis, J.R., "A Viscoplastic Constitutive Theory for Metal Matrix Composites at High Temperature", Thermal Stress, Material Deformation and Thermomechanical Fatigue, H. Senitoglu and S.Y. Zamrik, eds., ASME-PVP, vol. 123, 1987, pp. 49-56.

Sun, C.-T., Achenbach, J.D., and Herrmann, G., "Continuum Theory for a Laminated Medium," Journal of Applied Mechanics, vol. 35, 1968, pp. 467-475.

Suquet, P.M., "Local and Global Aspects in the Mathematical Theory of Plasticity," in Plasticity Today, A. Sawczuk, ed., Elsevier, 1985, pp. 279-310.

Tandon, G.P., and Weng, G.J., "A Theory of Particle-Reinforced Plasticity," Journal of Applied Mechanics, vol. 55, 1988, pp. 126-135.

Taya, M., "On Stiffness and Strength of an Aligned Short-Fiber Reinforced Composite Containing Penny-Shaped Cracks in the Matrix," Journal of Composite Materials, vol. 15, 1981, pp. 198-210.

Taya, M., and Arsenault, R.J., Metal Matrix Composites, Pergamon, N.Y., 1989.

Taya, M., and Ono, T.-K., "On Two Kinds of Ellipsoidal Inhomogeneities in an Infinite Elastic Body: An Application to a Hybrid Composite," International Journal of Solids and Structures, vol. 17, 1981, pp. 555-565.

Taya, M., and Seidel, E.D., "Void Growth in a Viscous Metal," International Journal of Engineering Science, vol. 19, 1981, pp. 1083-1094.

Walker, K.P., and Jordan, E.M., "Biaxial Constitutive Modelling and Testing of a Single Crystal Superalloy at Elevated Temperatures," in Biaxial and Multiaxial Fatigue, M.W. Brown, ed., Mechanical Engineering Publications, Ltd., London, 1989, pp. 145-170.

Walker, K.P., and Wilson, D.A., "Creep Crack Growth Prediction in INCO 718 Using a Continuum Damage Model," Proceedings of the 2nd Symposium on Nonlinear Constitutive Relations for High Temperature Applications, Cleveland, Ohio, 1984.

Zhu, Z.G., and Weng, G.D., "Creep Deformation of Particle - Strengthened Metal-Matrix Composites," Journal of Engineering Materials and Technology, vol. 111, 1989, pp. 99-105.

APPENDIX

Substitute the stress/elastic strain equation (3) and the flow rule (5) into the consistency condition (6) to obtain

$$\frac{\partial F}{\partial \sigma_{ij}} C_{ijkl} (\dot{\epsilon}_{kl} - \lambda \frac{\partial F}{\partial \sigma_{kl}}) - \frac{\partial F}{\partial \sigma_{ij}} \dot{\epsilon}_{ij}^b = \frac{2}{3} \dot{D} \quad (A.1)$$

Rewrite the flow rule (5) as

$$\frac{\partial F}{\partial \sigma_{ij}} = \frac{\dot{\epsilon}_{ij}^I}{\lambda} \quad (A.2)$$

and substitute into (A.1) to obtain

$$\frac{\partial F}{\partial \sigma_{ij}} C_{ijkl} (\dot{\epsilon}_{kl} - \lambda \frac{\partial F}{\partial \sigma_{kl}}) - \lambda \left(\frac{\dot{\epsilon}_{ij}^I}{\lambda} \frac{\dot{\epsilon}_{ij}^b}{\lambda} \right) = \lambda \left(\frac{2\dot{D}}{3\lambda} \right) \quad (A.3)$$

From (A.3) obtain the following implicit solution for λ ,

$$\lambda = \frac{\frac{\partial F}{\partial \sigma_{uv}} C_{uvrs} \dot{\epsilon}_{rs}}{\frac{\dot{\epsilon}_{mn}^I}{\lambda} \frac{\dot{\epsilon}_{mn}^b}{\lambda} + \frac{2\dot{D}}{3\lambda} + \frac{\partial F}{\partial \sigma_{mn}} C_{mnop} \frac{\partial F}{\partial \sigma_{op}}} \quad (A.4)$$

Substitute the flow rule (5) and (A.4) into the stress/elastic strain equation (3) to yield

$$\begin{aligned} \dot{\epsilon}_{ij} &= C_{ijkl} \dot{\epsilon}_{kl} \\ &= C_{ijkl} \left(\frac{\partial F}{\partial \sigma_{uv}} C_{uvrs} \dot{\epsilon}_{rs} \right) \\ &= C_{ijkl} \left(\frac{\dot{\epsilon}_{mn}^I}{\lambda} \frac{\dot{\epsilon}_{mn}^b}{\lambda} + \frac{2\dot{D}}{3\lambda} + \frac{\partial F}{\partial \sigma_{mn}} C_{mnop} \frac{\partial F}{\partial \sigma_{op}} \right) \end{aligned} \quad (A.5)$$

Now assume that there exists a scalar C such that

$$\frac{\partial F}{\partial \sigma_{ij}} (\dot{\sigma}_{ij} - C \dot{\epsilon}_{ij}^I) = 0 \quad (A.6)$$

The consistency condition (6) may be combined with (A.6) to obtain

$$C = \frac{\partial F}{\partial \sigma_{ij}} \dot{\epsilon}_{ij}^I = \frac{\partial F}{\partial \sigma_{ij}} \dot{\epsilon}_{ij}^b - \frac{2}{3} \dot{D} \quad (A.7)$$

With flow rule (A.2) - (A.7) may be rewritten as

$$C \frac{\partial F}{\partial \sigma_{ij}} \frac{\partial F}{\partial \sigma_{ij}} = \frac{\dot{\epsilon}_{ij}^b \frac{\partial F}{\partial \sigma_{ij}}}{\lambda} + \frac{2\dot{D}}{3\lambda} \quad (A.8)$$

Substitute (A.8) into (A.5) to obtain the instantaneous tangent stiffness tensor

$$L_{ijkl}^m = C_{ijkl} - \frac{C_{ijuv} \frac{\partial F}{\partial \sigma_{uv}} \frac{\partial F}{\partial \sigma_{qr}} C_{qrkl}}{C \frac{\partial F}{\partial \sigma_{mn}} \frac{\partial F}{\partial \sigma_{mn}} + \frac{\partial F}{\partial \sigma_{mn}} C_{mnop} \frac{\partial F}{\partial \sigma_{op}}} \quad (A.9)$$

The scalar C may be obtained from (A.6) and (A.2) as

$$C = \frac{\dot{\epsilon}_{op}^I \frac{\partial F}{\partial \sigma_{op}}}{\dot{\epsilon}_{st}^I \frac{\partial F}{\partial \sigma_{st}}} = \frac{\dot{\epsilon}_{op}^I \dot{\epsilon}_{op}^I}{\dot{\epsilon}_{st}^I \dot{\epsilon}_{st}^I} \quad (A.10)$$

ADDENDUM

Three papers directly relevant to the present research were presented at the recent IUTAM Symposium on Inelastic Deformation of Composite Materials, Rensselaer Polytechnic Institute, Troy, N.Y., 29 May-1 June, 1990.

The "vanishing fiber diameter model" of Dvorak and Bahei-El-Din (1982) was used by Krempl and Yeh² to predict thermal residual stresses in unified viscoplasticity type metal matrix.

Wang and Weng³ modelled the primary and secondary creep of composites using a combination of Eshelby's equivalent inclusion method, Kroner's elastic constraint, the Mori-Tanaka method, and Luo and Weng's local solution of a three-phase cylindrically concentric solid.

Dvorak et al.⁴ presented research that is similar to the present paper. The Mori-Tanaka method was used to predict composite yield surfaces and composite stress-strain curves for B-Al and SiCw-Al composites. The aluminum matrix was modelled by a rate-independent incremental plasticity theory using the Phillips kinematic hardening rule. The authors pointed out that Eshelby's "equivalent inclusion" solution is not exact for a plastically hardening matrix. A more complete paper [Lagoudas et al.⁵] has been submitted for publication. In addition, Gavazzi and Lagoudas⁶ have developed a numerical algorithm for the evaluation of Eshelby's tensor corresponding to a generally anisotropic matrix containing inclusions of any aspect ratio. The authors have offered to provide a copy of the code via electronic mail or floppy disk.

- ² Krempl, E. and Yeh, K.M., "Residual Stresses in Fibrous Metal Matrix. A Thermoviscoplastic Analysis," RPI Report MML 90-3, March 1990.
- ³ Wang, Y.M., and Weng, G.J., "A Local-Field Theory for the Overall Creep of Fiber-Reinforced Metal Matrix Composites"
- ⁴ Dvorak, G.J., Gavazzi, A.C., Lagoudas, D.C., and Nigam, H., "Elastoplastic Behavior of Metal Matrix Composites Based on Incremental Plasticity and the Mori-Tanaka Averaging Scheme"
- ⁵ Lagoudas, D.C., Gavazzi, A.C., and Nigam, H., "Elastoplastic Behavior of Metal Matrix Composites Based on Incremental Plasticity and the Mori-Tanaka Averaging Scheme," submitted to the Journal of Computational Mechanics, June 1990.
- ⁶ Gavazzi, A.C., and Lagoudas, D.C., "On the Numerical Evaluation of Eshelby's Tensor and its Application to Elastoplastic Fibrous Composites," in print, Journal of Computational Mechanics.

Appendix 7.4

Application of Current Unified Viscoplastic Constitutive Models to Hastelloy X at Elevated Temperatures

APPLICATION OF CURRENT UNIFIED VISCOPLASTIC
CONSTITUTIVE MODELS TO HASTELLOY X
AT ELEVATED TEMPERATURES

by

L.D. McCrea, P.K. Imbrie, D.H. Allen
Aerospace Engineering Department
College Station, Texas 5123

ABSTRACT

The unified viscoplastic constitutive theories of Bodner and Walker are investigated to determine their predictive capabilities using experimentally obtained data for Hastelloy X, at 1100 and 1700°F, as the basis of comparison. Material parameters for these models have been obtained using an iterative approach, unlike the traditional explicit approach. Instead, the nonlinear form of the constitutive equations are numerically integrated using physical insight, as well as knowledge of the parameters, until acceptable values are obtained. The iterative method for determining the material constants is shown to be a viable alternative, proving to be much simpler and less time consuming than previously developed procedures.

Comparisons to experimental data reveal that the constitutive theories are not able to simultaneously model the initial and fully saturated condition for a material which has undergone a considerable amount of cyclic hardening, although, a power law based strain rate equation is shown to model this material system best overall.

INTRODUCTION

Over the last several decades, technological advances in areas such as gas turbines, rocket engines, solar energy conversion devices, nuclear reactors, and the like, have forced engineers to reevaluate traditional methods of structural analysis. This, in part, is a result of attempting to make better use of natural resources through improved design and fabrication techniques. In addition, materials used in the aforementioned applications are exposed to hostile thermal environments where temperature and rate dependent phenomena are significant. To this end, a number of unified thermoviscoplastic constitutive theories have been developed which accurately predict the response of a material subjected to thermal and/or mechanical loading. However, use of these models is still not commonplace and additional research is necessary in order to understand their full potential, as well as their limitations.

The purpose of this research will be to assess the viability of an iterative approach for material parameters evaluation, as well as to perform a qualitative and quantitative analysis of the predictive capabilities of the models proposed by Bodner [1] and Walker [2]. Numerical simulations from selected theories in uniaxial form, and experimental data using Hastelloy X, will provide the basis for the evaluations.

SELECTED CONSTITUTIVE THEORIES

The constitutive theories chosen for this investigation are those of Bodner [1,3-15] and Walker [2,13,14,16,17]. Selection was based upon several considerations, namely: 1) these models have been scrutinized very carefully in the literature and are now considered to be in a mature form.

2) these models have been previously used to model the behavior of Hastelloy X; 3) parameter evaluation schemes are more readily available for obtaining "initial" estimates to the material constants; and 4) continued development of these models requires a thorough understanding of their full potential, as well as their limitations. Thus, in the paragraphs that follow, a brief overview of these theories is presented which will include a discussion of their forms and general characteristics. However, the complete derivation of the equations will not be reviewed herein since this information has appeared on numerous occasions in the literature.

Bodner Model

Bodner's model [1] is a unified viscoplastic theory which does not require the use of a yield criterion. The constitutive equations are cast in a continuum mechanics format and make use of many microphysical considerations based on the concepts of dislocation dynamics. The form of the model presented herein is capable of characterizing behavior such as isotropic and directional hardening, thermal recovery, and general temperature dependence of plastic flow [14]. The model has two internal state variables: an isotropic hardening parameter, and a kinematic hardening parameter. Bodner makes use of the plastic work rate ($\sigma \dot{\epsilon}^I$) as a scalar measure of hardening, which enables more accurate modeling of a strain rate jump test [1]. The uniaxial differential form of this constitutive theory is presented below as [1]:

$$\dot{\epsilon}^I = \frac{2}{\sqrt{3}} D_0 \exp(-0.5 |(D_p B)/\sigma|^{2n}) \operatorname{sgn}(\sigma) \quad (1)$$

$$\dot{B} = m_2 (Z_3 \text{sgn}(\sigma) - B) \sigma \dot{\epsilon}^I - A_2 Z_1 (|B|/Z_1)^{r_2} \text{sgn}(B) \quad (2)$$

$$\dot{D} = m_1 (Z_1 - D) \sigma \dot{\epsilon}^I - A_1 Z_1 (|D - Z_2|/Z_1)^{r_1} \quad (3)$$

$$\text{where: } D_p B = D + B \text{sgn} \sigma, \text{ and} \quad (4)$$

$$m_2 = \bar{m}_2/2 (1 + \exp\{-m_3 B \text{sgn}(\sigma)\}) . \quad (5)$$

In equations (1)-(5) the variables D_0 , n , m_1 , Z_1 , Z_2 , A_1 , r_1 , \bar{m}_2 , Z_3 , A_2 , m_3 , and r_2 represent material parameters which can be obtained through a series of uniaxial isothermal constitutive experiments.

An exponential function is used as the form of the basic equation for the inelastic strain rate, eq. (1). This function yields a very small value at low stress levels and provides a limiting value of inelastic strain rate in shear (D_0). These properties appear to be particularly useful for predicting material behavior at a variety of strain rates. This flow law contains a scalar coefficient ($D_p B$) which is a function of both the isotropic (D) and directional hardening (B) variables.

The growth laws, eq.'s (2) and (3), for the theory are in the standard Bailey-Orowan format of competing hardening and recovery terms. Cyclic hardening/softening characteristics are represented through the isotropic evolution equation (3). Hardening and/or softening is included in this growth law by the term $m_1 Z_1 (\sigma \dot{\epsilon}^I)$. Hardening is modeled when Z_1 is greater than the initial value of D , whereas softening is modeled when Z_1 is less than the initial value of D . The term $-m_1 D (\sigma \dot{\epsilon}^I)$ accounts

for the dynamic recovery, while the term $-A_1 Z_1 [(D-Z_2) Z_1^{-1}]^{r_1}$ represents the static thermal recovery.

Bodner's model does not make use of the back stress concept to include directional hardening effects; instead, an anisotropic form of the flow law is used. This flow law is assumed to behave isotropically on an incremental basis. This growth law, eq. (2), includes hardening through the term $m_2 Z_3 \text{sgn} \sigma (\dot{\sigma} \dot{\epsilon}^I)$. In the evolution equation for directional hardening, the term $-m_2 B (\dot{\sigma} \dot{\epsilon}^I)$ is the dynamic recovery term, and $-A_2 Z_1 [(|B|/Z_1)^{r_2} \text{sgn} B]$ is the static thermal recovery term. Cross softening effects are avoided by using the stress as the directional index of hardening.

Walker Model

Walker's model [2], is a unified viscoplastic constitutive theory which is based upon a nonlinear modification of a three parameter solid containing a Voigt element in series with a spring. However, during the development of this theory, Walker included many microphysical considerations. The form of Walker's theory used herein is seen to be capable of modeling isotropic and directional hardening, and includes one internal state variable, the back stress. The growth law for the back stress is of the standard Bailey-Orowan format. The scalar measure of hardening used by Walker is seen to be the inelastic strain rate. The uniaxial differential form of Walker's model is given below [2]:

$$\dot{\epsilon}^I = \frac{|\sigma - B|^{n-1}}{D^n} (\sigma - B) \quad (6)$$

$$\dot{B} = (n_1 + n_2) \dot{\epsilon}^I - (B - B_0 - n_1 \epsilon^I) \dot{\epsilon}^I$$

$$D = D_1 - D_2 \exp(-n_7 R) \quad (8)$$

$$\text{where: } \dot{G} = (n_3 + n_4 \exp(-n_5 R)) |\dot{\epsilon}|^I + n_6 |B|^{m-1}, \text{ and} \quad (9)$$

$$R = \int \dot{\epsilon}^I dt \quad (10)$$

In equations (6)-(10), the variables D_1 , D_2 , E , n_1 , n_2 , n_3 , n_4 , n_5 , n_6 , n_7 , n , m , and B_0 represent material parameters, which can be obtained through a set of isothermal uniaxial constitutive experiments. It should be noted that Walker's constants are temperature dependent.

The form of the basic equation for the inelastic strain rate, eq. (6), is a power law function which accurately predicts material behavior such as creep, relaxation and strain rate effects for strain rates below 10^{-2} sec^{-1} . However, at higher strain rates the power law expression appears to predict stress levels which are much larger than those actually measured during a constant strain rate tensile test [18,19]. Walker has also proposed an exponential form of the flow law [2].

The drag stress models isotropic hardening and accounts for cyclic hardening/softening of the material. The equation for the drag stress (D), eq. (8), is assumed to be a function only of the accumulated effective inelastic strain (R). Initially the drag stress is $D_1 - D_2$, which eventually saturates to a value of D_1 as the inelastic strain increases. The hardening in this evolution equation is given by the term $D_2 \exp(-n_7 R)$. No recovery, dynamic or static, has been included in the drag stress growth law.

Nonlinear kinematic hardening and the Bauschinger effect are represented by the back stress. The growth law for the back stress, eq. (7), includes hardening via the term $n_2 \dot{\epsilon}^I$. Dynamic recovery is modelled by the term $B(n_3 + n_4 \exp(-n_5 R))$, and the term $B n_6$ models the back stress static thermal recovery.

EXPERIMENTAL PROGRAM

This section details the experimental program used for developing isothermal uniaxial constitutive data for Hastelloy X. Data were obtained for temperatures of 1100 and 1700°F using four different mechanical testing modes. These include monotonic tension, fully reversed cyclic, stress drop, and complex history experiments. In the following paragraphs both the procedures and apparatus used to conduct these experiments are presented.

Experimental Procedures

All of the tests performed during this program were carried out in the Solid Mechanics Laboratory of the Aerospace Engineering Department at Texas A&M University using an MTS 880 servo-hydraulic closed-loop testing machine. The load frame was configured with a closed-loop heating chamber, water-cooled hydraulic grips, an externally mounted load cell, an axial extensometer, and a mini computer for controlling testing operations. The heating chamber had a maximum operating range of 180°F and was of the three zone, resistive heating, clam shell type design. Temperature feedback for each longitudinal set of heating coils was provided by 24/28 gauge K-type bead welded thermocouple wire. The temperature at the center of each zone was monitored by its own process and power controller and enabled the user to establish and maintain a spatially uniform

temperature profile (within ASTM specifications for a short term test) along the gauge length of the specimen. A set of Fiberfrax® insulating plugs placed on the top and bottom access ports of the furnace and grips which extended into the hot zone were used to reduce and/or minimize the effect of convective and conductive heat losses, respectively.

A high temperature specimen grip system was utilized for this series of experiments and, as stated above, extended into the main body of the furnace. The grips were designed to accept threaded type specimens through the use of an inside/outside threaded adapter. Backlash in the specimen/adapter assembly was removed via a hydraulically operated piston which could be loaded to a specified amount. Grip alignment was performed prior to and during testing (failure of one of the specimen adapters necessitated a realignment during the course of the experimental program). This included a check of both concentricity and angularity of the load train with respect to the actuator rod movement. The alignment procedure yielded a total indicated run-out of 0.0008" at an angle of 0.022°, as measured by a digital dial indicator accurate to 0.00005". However, since the adapter assembly contained a number of threaded components, it was not reasonable to expect any degree of repeatability of these measured quantities, however; they are stated for the sake of completeness. It should also be noted that there was no explicit measurement of specimen bending strains to ensure compliance with ASTM specifications.

The primary measured data of interest included load, displacement, and temperature. The load data were obtained via a 10 KIP load cell mounted in the load train. Displacement data were measured using a one inch gauge length, air cooled, axial extensometer. The extensometer was mounted outside the furnace and used a set of conical tipped quarter extender rods

to make contact with the specimen. Signal conditioning for both of these transducers was part of the MTS 880 load frame system and possessed a multiple range select feature which provided maximum data resolution. Load and displacement data were measured using a 12 bit A/D system which had a ± 5 mV resolution and was an integral part of the controlling and measuring computer system. Temperature data were obtained using three 24/28 gauge K type thermocouples equally spaced along the gauge length of the specimen. The thermocouples were connected to a multi-channel digital thermometer which was not an integral part of the A/D measuring system. Therefore, temperature data were not automatically recorded on a regular basis, as were the load and displacement measurements. Instead, temperature values at the beginning of a test were entered by hand into the data acquisition program and simply monitored thereafter. The thermocouples were attached to the specimen using the self-supporting method. This method of attachment provided sufficient thermal contact with the material to yield accurate temperature measurements and did not flaw the specimen (which in general can result in premature failure), as is common with welding thermocouples to the surface.

The Hastelloy X material used to fabricate the specimens was purchased in bar stock form (heat ID 2G6782) from Atek Metals Center of Houston Texas. This was a solution strengthened material conforming to ASM specification number 5754H. The design of the specimen was that of a standard, constant gauge section, low cycle fatigue geometry having a nominal one inch gauge length and quarter inch diameter circular cross-section. The specimens were fabricated to meet ASTM E606-77T specifications except for the surface finish and post machining heat treatment. A 32μ finish was used instead of the typical 8μ for cost considerations. In addition, the

specimens were used in an "as received" condition with no additional heat treatment to remove microstructural damage resulting from the machining process.

A total of 27 tests were conducted in fulfillment of this isothermal constitutive test program. Two cyclic tests were carried out at 1200 and 1600°F, respectively, and served as a basis of comparison to previously obtained data and for uniaxial constitutive code verification. Specific details of the remaining 25 experiments are as follows. Monotonic tension and fully reversed cyclic tests were performed at 1100 and 1700°F, using a variety of strain rates, ranging from 1×10^{-5} to $3 \times 10^{-3} \text{ sec}^{-1}$, under strain controlled conditions. Strain amplitudes for the tension and cyclic test were 4.0% and 0.8%, respectively. However, the strain amplitude of 0.8% was subsequently reduced to 0.4% during the course of the 1100°F experiments because specimen buckling became a problem. This was apparently the result of a material instability at the selected temperature and strain rate.

The fully reversed cyclic experiments were carried out until a saturated condition was achieved. For the purpose of this test program, cyclic saturation was defined as a change in stress amplitude of less than 100 psi, from one cycle to the next. The stress drop tests, used to measure values of back stress, were performed by inserting a hold time on the unloading branch of a fully reversed saturated hysteresis loop, and monitoring the creep response. When positive creep was observed, the hold stress was greater than the back stress and vice versa, when negative creep was seen. Since it is very difficult to obtain the exact hold stress which results in no creep, the general procedure was to bracket the positive and negative creep responses and use a linear regression scheme

to estimate the values of the back stress. Additional stress drops were made on a specimen after it had been recycled to saturated condition.

Finally, two experiments, one each at 1100 and 1700°F, were performed in order to verify the predictive capabilities of the constitutive models considered herein. These complex history tests included mechanical effects such as strain rate jumps, relaxation, cyclic behavior, and strain holds. A listing of each segment defining these experiments can be found in Table 1. In conclusion, a complete summary of the entire test matrix can be found in Table 2.

Experimental Results

Based upon an inspection of the experimental data presented in Figs. 1-4, the following general observations can be made regarding the behavior of Hastelloy X at 1100 and 1700°F. For the range of temperatures tested, the material exhibits a positive strain rate sensitivity, that is, stress amplitude increases with an increase in strain rate (see Figs. 1 and 3). However, Fig. 1 also shows that there is an inversion of the rate sensitivity between a strain rate of 10^{-4} and 10^{-3} sec^{-1} , which would indicate that strain aging effects are present at 1100°F (Strain aging is a thermally activated solute effect which generally changes the rate sensitivity of a material). This phenomenon is further demonstrated in Fig. 2 and appears to be more pronounced once the material undergoes cyclic deformation. While no explanation for this type of behavior can be made, other researchers [2] have reported that the rate sensitivity changes from negative to positive between 1000 and 1200°F. Therefore, one can conclude that the material is undergoing a significant microstructural change in this temperature range which may result in the strain aging effect observed herein.

The fully-reversed hysteresis loop data, shown in Figs. 2 and 4, indicate that Hastelloy X undergoes cyclic hardening up through 1600°F and cyclic softening thereafter. The amount of hardening and/or softening, as indicated by the difference between peak stress levels at initial loading and cyclic saturation, appears to be a function of both temperature and strain rate and, in general, increases with strain rate, but decreases with temperature. This type of material response is again typical of that reported by other researches [2]. In addition, the saturated cyclic data can also be used to make one other observation regarding symmetry of the data in tension and compression. A Bauschinger-like effect was noted during testing, which resulted in an asymmetric cyclic response with respect to the strain axis as the material was going through its initial cycling. However, no specific trends were observed regarding this asymmetry as a function of strain rate or temperature. In addition, as a saturated condition was achieved, the material generally exhibited little or no asymmetric characteristics. This is contrary to what has been previously reported in the literature [2], wherein Hastelloy X is shown to have a higher stress amplitude in compression than in tension. It is believed however, that this discrepancy is simply a result of how long the material was cycled and therefore does not represent a significant constitutive behavior variation.

MATERIAL PARAMETER EVALUATION

Evaluation of the material parameters for the unified constitutive theories represents one of the most difficult aspects of their implementation. These difficulties generally stem from the fact that a clear mathematical description of an experiment used to determine a

constant cannot always be achieved as well in the laboratory. Thus, without accurate constants, characterizing material behavior, even with the best of models is not possible. To this end, one can take several approaches: 1) make use of least squares optimization techniques and neglect the real physical aspects of the theory; 2) simplify or recast the original constitutive equations, through a series of judicious assumptions, so that the different phenomena being modelled can be individually examined; and 3) numerically integrate the nonlinear form of the theories directly, using physical incite, as well as knowledge of the equations in an iterative approach, incrementing the parameters until acceptable values are determined. The first approach mentioned above may provide constants which adequately predict material behavior within the limits of the data base used to generate them. However, there is no guarantee that under more complex conditions accurate results will be obtained. The second approach, on the other hand, represents the present and more traditional form of determining the material parameters. However, obtaining unique values of the constants directly from a discretization and linearization of the constitutive equations generally requires additional data manipulation in order to accurately characterize a given material response [20]. Therefore, presented below is the third method, which is a simpler and much less time consuming iterative style procedure for determining the material parameters.

The iterative method described herein attempts to provide the reader with physical incite about the various parameters used in both the Bodner and Walker theories, so that final forms of the constants can be obtained directly by this method. The procedure requires the user to assume some initial estimates of the constants, based upon a knowledge of

the material and model behavior, in order to begin the process.

Computer Iterations

A detailed explanation of the order of determination of parameters, experimental data requirements, and a description of the constants for each model will be presented later. However, some general observations can be made which are applicable to other models as well. The order in which the material parameters are evaluated is an important factor in determining the ease and speed at which these constants are obtained. The hardening parameters were determined first, and the recovery constants determined last, with the order within these categories being determined by the amount of influence each constant had. The constants with the most effect were determined first. Experimental data requirements were both high and low strain rate tests. The hardening constants required the use of the experimental results from high strain rate tests. These tests were used based on the assumption that at high strain rates the thermal recovery is negligible. The recovery constants were evaluated using slow strain rate tests based on the same previously mentioned assumption.

The first step in the evaluation of the material parameters was to study experimental data in order to determine points on the curve at which it was desired for the model to predict most accurately. In this case, the points most generally used were a point directly following yield, a point in the middle of the plastic behavior, and the maximum and minimum strain amplitudes. The general shape and cyclic hardening or softening characteristics were also observed, as well as strain rate sensitivity, and thermal recovery behavior. Studying the experimental data and becoming familiar with it was found to be very important for determining the constants most expeditiously. The information obtained from the above

observations was used to develop a physical feel for each of the constants and their influence on the model.

All of the constants for these models, except the elastic modulus, E , were obtained starting with provisional values and using an iterative procedure. The iterative procedure began by first assigning a value of zero to all of the constants except for the exponents. Initial values for the exponents were selected so as to avoid any numerical overflow conditions. The iteration proceeded by assuming a provisional value of one constant, and adjusting that constant until satisfactory results were obtained. Satisfactory results in this case implies that a desired stress amplitude for a given strain point was achieved using the constants invoked at that time. Next, another constant was given a value and subsequently adjusted. Each time another constant was enabled or a different experiment was used, all provisional values of constants were updated. Iteration proceeded in this manner until all applicable constants were evaluated and the experimental data was satisfactorily predicted for the required tests. It should be noted that when iterating between a fast and a slow strain rate test, care should be taken not to update the hardening constants too much. It was found that "over-updating" these constants caused problems when switching between these tests, which resulted in performing unnecessary iterations.

Bodner Model: The iterative procedure for this model began by evaluating the isotropic hardening constants. Z_0 was the first parameter of interest and represents the initial value of the isotropic hardening variable. This constant is seen to affect the yield point location, translating it up or down the stress axis as shown in Fig. 5a. In addition, this parameter, in conjunction with Z_1 , determines whether cyclic hardening

$(Z_0 < Z_1)$ or softening $(Z_0 > Z_1)$ will be modeled. The strain rate exponent, n , was determined next. This constant appears to be related to the velocity of dislocations in the crystalline lattice [1] and as a result, is highly temperature dependent. In general, this constant is determined using rapid strain rate data, where thermal recovery effects are not present. This parameter physically shows the dependence of the flow stress with strain rate and affects the predicted stress-strain response as shown in Fig. 5b, noting that the yield point does not change, but rather the rate at which a saturated value of the flow stress is attained. The limiting or maximum value of the isotropic hardening variable, Z_1 , is used to raise or lower the stress amplitudes during cyclic hardening and softening, respectively, and was set next. Figure 5c shows the effect of changing Z_1 for a given value of Z_0 . The last of the isotropic hardening constants, m_1 , was then determined. This parameter is seen to affect the rate at which D reaches a saturated condition. In general, once the inelastic strain becomes significant, increasing the value of m_1 makes $d\sigma/d\epsilon$ larger and vice versa, as shown in Fig. 6a. Some summary observations regarding these three hardening constants are that the difference between Z_0 and Z_1 , in conjunction with m_1 , sets the rate and amount of cyclic hardening/softening. However, Z_0 alone determines the initial yield point, whereas Z_1 sets an upper limit on the predicted stress levels. The constant m_1 , on the other hand, the rate at which these conditions are met.

Values of the directional hardening evolution equation were determined next. The limiting value of the directional hardening, Z_3 , was found first using a provisional value of m_2 . The purpose of this hardening term is mainly to account for a Bauschinger type effect, but was also seen to

introduce a more nonlinear stress-strain response. Z_3 , coupled with m_2 and m_3 , the directional hardening rate coefficient and shape factor constants, respectively, tend to add more shape to the predicted behavior, reducing the typical "oversquare" problem associated with many other models (see Fig. 6b).

The thermal recovery constants were the last parameters to be determined. As a general rule, the value of Z_2 , which represents the fully recovered value of isotropic hardening, is simply set to that of Z_0 as was the case during this iterative procedure. The value of A_1 , the recovery coefficient for isotropic hardening, was then determined using a provisional value of r_1 . This constant is seen to be most effective once B is of sufficient strength; that is, once a significant amount of plastic deformation has occurred. Adjusting the value of A_1 should be performed with slow strain rate test data when recovery mechanisms are generally active. Figure 6c depicts the effect of varying A_1 , noting that this constant has little influence at the low inelastic strain levels. However, under cyclic conditions this parameter will reduce the overall stress amplitudes appreciably as its value is increased. The recovery coefficient r_1 was then found. Figure 6d shows the effect of increasing r_1 for a given value of A_1 and basically indicates that increasing the value of this coefficient enhances the rate of application of recovery (i.e., active at lower plastic strain values). Chan [13] reports that for most metallic materials, the value of r_1 can be set to a number between 2 and 3. Lastly, the directional hardening recovery parameters are, in general, set equal to the respective isotropic constants.

Walker's Model: First, the hardening parameters were investigated, beginning with B_1 . This constant represents the drag stress or isotropic

hardening. Adjustment of this constant results in changing the height of the stress-strain curve. Increasing D_1 raises the stress level, whereas decreasing the values lowers the stress response. Next, the strain rate sensitivity parameter, n , was put into play. The effect of adjusting the value of n on the stress-strain response shown in Fig. 7a. This value was adjusted based on experimental observations of the strain rate sensitivity. Next, the back stress or kinematic hardening parameters, n_1 and n_2 , were enabled. The combination n_1+n_2 was found to determine the shape of the curve as shown in Fig. 7b. The value of n_1 adjusts the slope of the stress-strain curve after yield. For this material, n_1 had negligible effect and was therefore disabled. Figure 8 shows the effect of n_2 on the curve. Since the material behavior studied was governed by hardening effects for the most part, n_2 was found to be very important in the prediction of this material response.

Next, the values for the recovery constants were obtained. First, the parameter B_0 was initialized, which accounts for the difference between tensile and compressive creep. The effects of adjusting this parameter are shown in Fig. 9. The exponent on the back stress thermal recovery term, m , was then evaluated. The results of manipulating this constant are shown in Fig. 10. The back stress recovery constant, n_3 was then investigated. This constant was seen to be responsible for the Bauschinger effect. Adjusting n_3 effected the asymmetry of the stress strain response, as shown in Fig. 11. Observation of the experimental data showed that the data exhibited no Bauschinger effect. Therefore, this parameter was not enabled. Next, the constants D_2 and n_7 , were simultaneously evaluated. These constants allow the model to predict isotropic cyclic hardening/softening. Increasing the value of D_2 appears to reduce the cyclically

saturated stress level and the opposite trend results when D_2 is decreased. The constant n_7 simply appears to magnify the stated trends of D_2 . This trend is shown in Fig. 12. From the investigation of experimental data it was observed that enabling these constants did not produce accurate predictions of cyclic response. It was therefore concluded that these constants have little effect on the response for this material, and they were subsequently disabled. The ability of this model to predict cyclic hardening and softening will be addressed later.

Next, the parameters n_4 and n_5 were investigated. These parameters account for dynamic recovery of the back stress. Fig. 13a shows the effect that n_4 has on the stress-strain response with the value of n_5 serving as a magnifier of this term. In this figure it can be seen that the material exhibits tri-linear behavior when n_4 is decreased. This behavior can be explained by the fact that decreasing the value of n_4 results in a decrease in the amount of dynamic recovery, thus leaving only static thermal recovery. The first linear portion of the curve is the elastic loading region. The second linear portion of the curve comes about because thermal recovery is small at the onset of inelastic behavior and thus, the back stress grows linearly with strain. The final portion of the trilinear curve results when the back stress becomes large enough to activate thermal recovery. The thermal recovery term increases until it balances out the linear hardening term. However, because this material exhibited little recovery, these constants were found to be unnecessary, and were subsequently disabled. Finally, the constant n_6 was evaluated, which accounts for thermal recovery of back stress hardening. The effect of varying n_6 is shown in Fig. 13b. This constant was found to be unnecessary because the material showed only a small amount of thermal

recovery, and it was set to zero. The material parameters for both the Bodner and Walker models were obtained for Hastelloy X at 1100 and 1700°F, using the computer iteration scheme. Provisional values of the constants were established using a knowledge of the material behavior and model characteristics as a guideline. Final values of the parameters can be seen in Tables 3 and 4. In the following section, the ability of these models/constants to predict the behavior of Hastelloy X under more complex conditions will be investigated.

RESULTS

This section provides results, which show the response and predictive capabilities of Bodner's and Walker's theory for Hastelloy X. Experimental data, as well as material parameters obtained by the iterative procedure described herein for temperatures of 1100 and 1700°F, are used as the basis of comparison.

Figure 14 presents the response of both models at 1100°F in comparison to the experimental data. Bodner's theory models the behavior of Hastelloy at 1100°F fairly well. However, significant discrepancy can be found in the estimation of the sharpness and height of the initial yield point. The smoothness of the response characterized by Bodner's model is governed by the kinematic hardening variable term in eq (2). For this application, it was found that the parameter m_3 helps to smooth the response as its value is increased. However, referring to eq. (5), it can be seen that this constant will result in numerical difficulties if increased too much. Thus, it was concluded that the sharpness of this response is due to the fact that m_3 could not be raised to a large enough value. The cause of underestimation of the yield point can be seen by examining Bodner's avo-

lution law for isotropic hardening, eq. (3). The constant Z_0 , the initial value of the isotropic hardening parameter, sets the value of the initial yield point. However, the value of Z_0 must also be low enough for the term $(Z_1 - D)$ to account for cyclic hardening. Therefore, a compromise was reached that allowed for characterization of both responses. Other researchers also experienced similar problems when working with this material [21].

Walker's model generally overestimated the stress levels for the first quarter cycle by as much as 50 percent ($\dot{\epsilon} = 1.19\text{E-}03 \text{ sec}^{-1}$). This overestimation can be explained by the fact that Hastelloy X cyclically hardens at 1100°F. Walker's model was unable to accurately predict cyclic hardening/softening effects, primarily because the constants D_2 , and n_7 , which govern this behavior, were found to be ineffective for the case studied. Disabling these parameters causes the evolution law for the drag stress, eq. (7), to be a constant. Therefore, the stress response was forced to be near the cyclically saturated stress level. Walker also found that his model did not accurately characterize monotonic tension behavior of this material at other temperatures [2].

Figures 15 shows a comparison of the initial response of both models to experiments at 1700° F. For this case, Bodner's model is seen to underestimate the stress response for the high strain rate test, and overestimate for the slow strain rate test, with the yield point staying approximately the same. This response is explained by observing that a fairly rigid upward shift of the experimental curve occurs with increasing strain rate. Recall that the parameter, Z_0 , is set at a value which allows both the yield point and cyclic hardening/softening characteristics to be modelled (See Fig. 5a). In addition, the constant, n , which accounts for

strain rate sensitivity, does not respond to changes in strain rate by rigidly shifting the entire curve. Thus, once the parameter Z_0 is set, attempts at modelling the peak stress amplitude result in changing the rate at which the flow stress saturates.

Walker's model characterizes the first quarter cycle at 1700°F well. It can be seen that Hastelloy X cyclically softens only slightly at 1700°F, and therefore, the initial stress level is near the final saturated stress value. Thus, the model does not have to capture a large cyclic softening response. This theory models the material behavior at high strain rates (Fig. 15) even more accurately because the assumption is made that at high strain rates thermal recovery is negligible. With no thermal recovery, even less softening occurs, and the initial value is almost exactly the same as the saturated stress level. As the strain rate is decreased, thermal recovery is initiated, causing more softening. Therefore, Walker's model begins to overestimate slightly with decreasing strain rate.

The cyclic response at 1100°F is shown in Fig. 16. As was previously discussed in the experimental section, this material was shown to display the strain aging phenomenon at this temperature (See Fig. 2). Therefore, it should first be noted that the forms of both models used in this study did not incorporate strain aging correction terms, and thus, the strain aging effects are not accurately captured. In general, the peak saturated hysteresis values for high and low strain rate tests were accurately modelled. However, for intermediate cases, the stress levels were overestimated. This response is presumably the result of the strain aging phenomenon, as shown in Fig. 2. However, it can be seen that even with the strain aging effects, Bodner's theory is capable of modeling the general

shape, the yield point, and saturated stress levels for this application.

On the other hand, Walker's model demonstrates some difficulty in modelling the general form of the curve for the slow strain rate test, and presents an "oversquare" response. In order to explain the inability to model the form, it should be noted that the curve changes considerably from high to low strain rate tests. For the form of Walker's model used herein, only one parameter, n_2 , is available to govern this type of shape change (See Figure 8). Thus, modeling two curves which are very different in form is difficult. "Oversquareness" of the response is typical of Walker's model at slow strain rates, as was demonstrated by Walker [2].

Figure 17 presents the cyclic response of both models, in comparison with measured values, at 1700°F. For this case it is seen that Walker's model accurately characterizes the material behavior. Bodner's model predicts well also, but has a few discrepancies resulting from the same problems as were discussed for the initial load up case. Specifically, Bodner's model overestimates at the slow strain rate and underestimates at the high strain rate.

Figures 18 and 19 demonstrate the predictive capabilities of the models compared to complex history tests performed on Hastelloy X at 1700°F. Experimental results were compared to Bodner's theory at 1700°F, as seen in Fig. 18. This figure shows that Bodner's model predicts an extremely "oversquare" response. This response is not in keeping with the observations made previously in this study, where Bodner's theory accurately represented the general shape of the stress-strain curve. Also, this model demonstrates insensitivity to relaxation and strain rate jumps. This response is contrary to information given by Bodner [1], where it is stated that use of the plastic strain rate as the measure of hardening

enables the model to better predict strain rate jump behavior. This inconsistency is possibly due to the fact that the hardening terms in the evolution equations, eq. (2) and eq. (3), saturate too quickly.

Figure 19 presents a comparison of Walker's theory to measured values at 1700°F. Walker's model predicts the overall response accurately, including general shape, strain jumps, and relaxation. This outcome is congruent with previous results.

CONCLUSIONS

The purpose of this research was to perform an analysis of the ability of the Bodner and Walker theories to model the behavior of Hastelloy X at 1100 and 1700°F using experimentally obtained data as a basis. The constitutive behavior of the material was characterized using material parameters determined by a simple iterative approach described previously. This iterative approach appears to be a viable alternative to the more traditional evaluation methods used by other researchers. In addition, listed below are some other pertinent conclusions:

- 1) The main objective of the experimental program was to obtain uniaxial test data for Hastelloy X at 1100 and 1700°F and it is believed that this has been achieved. However, at these temperatures significant microstructural changes in the material are taking place. Since the form of the constitutive theories considered herein cannot accurately predict the type of transient phenomena observed, evaluation of the material parameters was made more difficult. In retrospect therefore, utilizing the models considered herein at these temperatures is not advisable.

- 2) Both models fail to accurately characterize the initial quarter cycle of a hysteresis loop, when the material exhibits significant cyclic

hardening/softening effects. Bodner's theory demonstrated more capability to model the growth of isotropic hardening than did Walker's theory. However, Bodner's model was generally unable to capture the yield point properly.

3) Both models provided a good representation of peak stress amplitudes of the fully reversed cyclic experiments at 1100 and 1700°F. However, at 1100°F Walker's model gave an "oversquare" response. This was attributed to the fact that strain aging effects were present which significantly altered the stress-strain response as a function of strain rate.

4) From the complex history experiments at 1700°F, it is seen that Walker's model accurately predicts the stress-strain response for cyclic, strain jumps, and relaxation behavior. Bodner's model on the other hand, does not provide an adequate simulation, even though the theory was reported to be capable of handling these types of conditions.

ACKNOWLEDGEMENTS

The authors gratefully acknowledge the support provided for this research by the Air Force Office of Scientific Research under grant no. F49620-86-K-0016.

REFERENCES

1. Bodner, S.R., "Review of a Unified Elastic-Viscoplastic Theory (the Bodner Equations)," Interim Report No. AFOSR-84-0042, Air Force Office of Scientific Research, October 1984.
2. Walker, K.P., "Research and Development Program for Nonlinear Structural Modeling With Time-Temperature Dependent Constitutive Relationships," NASA Report No. CR-165533, 1981.
3. Bodner, S.R., and Partom, Y., "Constitutive Equations for Elastic-Viscoplastic Strain-Hardening Materials," J. Appl. Mech., Vol. 42, p. 385-389, 1975.
4. Bodner, S.R., "A Procedure for Including Damage in Constitutive Equations for Elastic Viscoplastic Work-Hardening Materials," Proc IUTAM Symposium, Springer-Verlag, pp. 21-28, 1981.
5. Bodner, S.R. and Partom, Y., "Constitutive Equations for Elastic-Viscoplastic Strain-Hardening Materials," J. Appl. Mech., Vol. 42, No. 2, p. 285, 1975.
6. Merzer, A. and Bodner, S.R., "Analytical Formulation of a Rate and Temperature Dependent Stress-Strain Relation," J. Eng. Mat. Tech., Vol. 101, p. 254, 1979.
7. Bodner, S.R., "Representation of Time Dependent Mechanical Behavior of Rene 95 by Constitutive Equations," Air Force Materials Laboratory, AFML-TR-4116, 1979.
8. Bodner, S.R., and Partom, Y., "A Large Deformation Elastic-Viscoplastic Analysis of a Thick-Walled Spherical Shell," J Appl. Mech., Vol. 39, pp. 751-757, 1972.
9. Bodner, S.R., Partom I., and Partom, Y., "Uniaxial Cyclic Loading of Elastic-Viscoplastic Materials," J. Appl. Mech., Vol. 46, pp. 805-810, 1979.
10. Stouffer, D.C., and Bodner, S.R., "A Constitutive Model for the Deformation Induced Anisotropic Plastic Flow of Metals," Int. J. Eng. Science, Vol. 17, pp. 757-764, 1979.
11. Bodner, S.R., and Stouffer, D.C., "Comments on Anisotropic Plastic Flow and Incompressibility," Int. J. Eng. Science, Vol. 21, pp. 211-215, 1983.

12. Bodner, S.R., "Evolution Equations for Anisotropic Hardening and Damage of Elastic-Viscoplastic Materials," Plasticity Today: Modeling, Methods and Applications, Elsevier Applied Science Pub., Barking, England, 1984.
13. Lindholm, U.S., Chan, K.S., Bodner, S.R., Weber, R.M., Walker, K.P., and Cassenti, B.N., "Constitutive Modeling for Isotropic Materials (HOST)," NASA Report No. CR-174718, 1984.
14. Lindholm, U.S., Chan, K.S., Bodner, S.R., Weber, R.M., Walker, K.P., and Cassenti, B.N., "Constitutive Modeling for Isotropic Materials (Host)," NASA Report No. CR-174980, 1985.
15. Chan, K.S., Lindholm, U.S., and Bodner, S.R., "Constitutive Modeling for Isotropic Materials (HOST)," NASA Report No. CR-182132, 1988.
16. Walker, K.P., "Representation of Hastelloy-X Behavior at Elevated Temperature with a Functional Theory of Visco-plasticity," ASME Pressure Vessels Conference, San Francisco, California, 1980.
17. Freed, A.D., and Walker, K.P., "Refinements in a Viscoplastic Model," NASA TM-102338, 1989.
18. Krempl, E., "The Role of Servocontrolled Testing in the Development of the Theory of Viscoplasticity Based on Total Strain and Overstress," Presented at the ASTM Symposium on Mechanical Testing for Deformation Model Development, Bal Harbour, Florida, November 12-13, 1980.
19. Cernocky, E.P., and Krempl, E., "A Nonlinear Uniaxial Integral Constitutive Equation Incorporating Rate Effects, Creep, and Relaxation," Int. J. Nonlinear Mechanics, Vol. 14, pp. 183-202, 1979.
20. James, G.J., "An Experimental Comparison of Current Viscoplastic Constitutive Models at Elevated Temperature," M.S. Thesis, Texas A&M University, 1986.
21. Tong, Mike, Sverdrup Technology, Inc., Brook Park, Ohio, Personal Correspondance, 1990

Table 1. Complex History Test Information.

Strain Rate (sec ⁻¹)	Strain (%)	Change in Strain (%)	Time (sec)	Change in Time (sec)
1.90738E-05	0.2	0.2	104.856	104.856
1.99795E-04	0.3	0.1	109.860	5.050
1.99984E-03	0.4	0.1	110.360	0.500
0.00000E-00	0.4	0.0	301.010	109.647
1.90738E-06	0.6	0.2	1349.370	1048.560
1.85969E-05	0.3	-0.3	1510.890	161.317
0.00000E-00	0.3	0.0	1859.410	348.520
1.85969E-05	0.0	-0.3	2020.720	161.317
1.99989E-03	-0.2	-0.2	2021.720	1.000
1.98367E-04	-0.6	-0.4	2041.890	20.165
1.98367E-04	-0.2	0.4	2062.050	20.165
0.00000E-00	-0.2	0.0	2761.090	699.040
1.99798E-03	0.3	0.5	2763.590	2.502
1.99798E-04	0.4	0.1	2768.600	5.005
1.90738E-05	0.6	0.2	2873.450	104.856
1.71664E-03	-0.6	-1.2	3572.490	699.040
5.72213E-04	0.6	1.2	5669.610	2097.120
5.72213E-04	-0.6	-1.2	7766.730	2097.120
5.77213E-04	0.6	1.2	9863.850	2097.120

Table 2. Test Matrix.

Test	Specimen	Temp. (F)	Strain Rate (sec ⁻¹)	Strain Amp. (%)	Type of Test
4	4	1100	1.1921E-05	2.5	Monotonic Tension
5	5	1100	1.1921E-05	0.8	Cyclic
6	6	1700	1.1921E-05	0.8	Cyclic
7	7	1700	1.2207E-04	0.8	Cyclic
8	8	1700	1.1903E-03	0.8	Cyclic
9	9	1700	5.0362E-04	0.8	Stress Hold
10 *	10			0.6	Monotonic Tension
11	11	1700	1.1903E-03	4.0	Monotonic Tension
12	12	1700	5.8148E-03	0.8	Cyclic
13 *	13	1100	3.8148E-03	0.8	Cyclic
14	14	1100	1.2207E-04	0.8	Cyclic
15 *	15	1100	1.1903E-03	0.8	Cyclic
16	16	1100	1.1903E-03	4.0	Monotonic Tension
17	17				
18 *	18	1100	1.1903E-03	0.8	Cyclic
19	19				
20	20				
21	21	1100	5.3047E-05	0.8	Stress Hold
22 *	22 *	1100	5.0362E-04	0.8	Cyclic
23	23	1100	5.0355E-04	0.6	Stress Hold
24	24	1100	1.1902E-03	0.4	Stress Hold
25	25				
26	26				
27 @	27	1100		0.6	Complex History
28 @	28	1700		0.6	Complex History

Table 3. Material Parameters for Bodner's
Model at 1100°F and 1700°F.

Parameter	1100°F	1700°F
A_1, sec^{-1}	0.6500E-04	0.6500E-04
A_2, sec^{-1}	0.6500E-04	0.6500E-04
D_0, sec^{-1}	0.1000E+05	0.1000E+05
E, psi	0.2394E-08	0.1900D+08
r_1	0.9800E-00	0.9800E-00
r_2	0.9800E-00	0.9800E-00
m_1, psi^{-1}	0.5500E-03	0.5500E-03
m_2, psi^{-1}	0.1100E-01	0.1100E-02
m_3, psi^{-1}	0.3477E-04	0.3477E-03
n	0.1000E+01	0.7000E-00
Z_0, psi	0.1000E+06	0.2500E+06
Z_1, psi	0.2900E+06	0.2200E+06
Z_2, psi	0.1000E+06	0.2500E+06
Z_3, psi	0.1300E+06	0.8200E+05

Table 4. Material Parameters for Walker's
Model at 1100°F and 1700°F.

Parameter	1100°F	1700°F
D_1 , psi	0.8580E+05	0.1080E+06
D_2 , psi	0.0000E-00	0.0000E-00
E , psi	0.2394E+08	0.1900E+08
n_1 , psi	0.0000E-00	0.0000E-00
n_2 , psi	0.4200E+07	0.2500E+06
n_3	0.0000E-00	0.0000E-00
n_4	0.0000E-00	0.0000E-00
n_5	0.0000E-00	0.0000E-00
n_6 , psi ^(1-m) sec ⁻¹	0.0000E-00	0.0000E-00
n_7 , sec	0.0000E-00	0.0000E-00
n	0.1420E+02	0.5000E+01
m	0.1160E+01	0.1160E+01
B_0 , psi	-0.2000E+04	-0.1000E+04

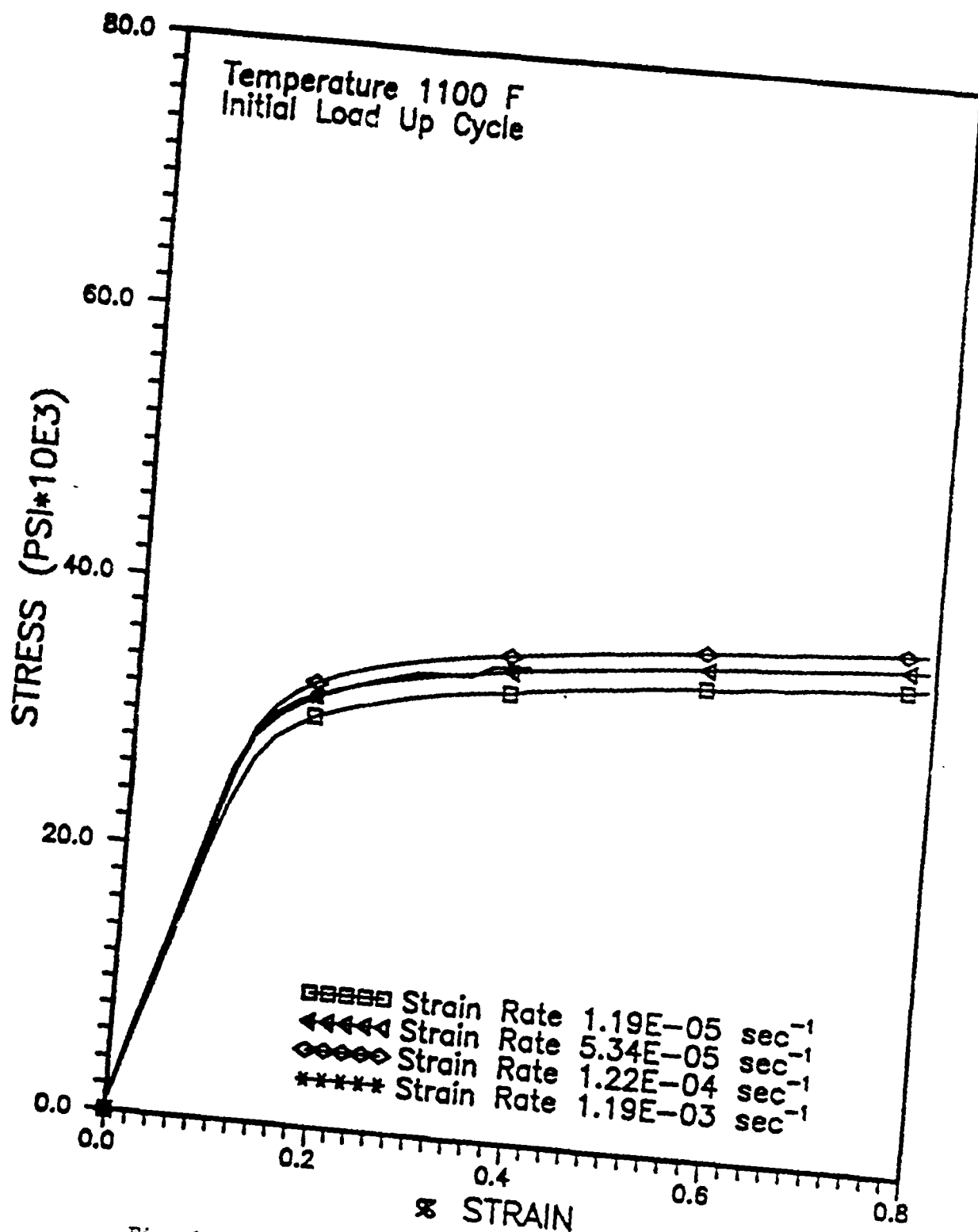


Fig. 1 Comparison of Experimental Data at 1100°F at Different Strain Rates for Initial Load Up.

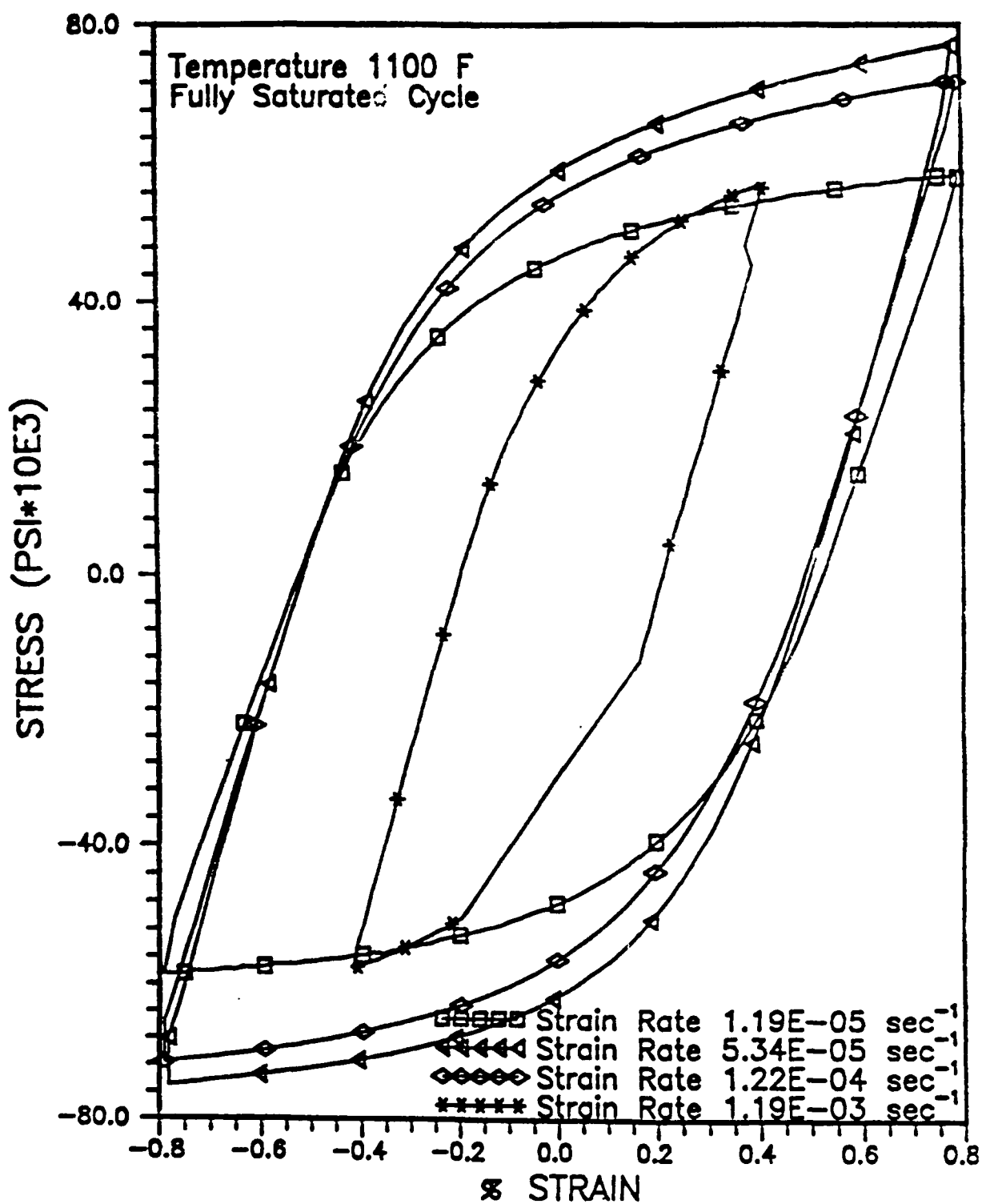


Fig. 2 Comparison of Experimental Data at 1100°F at Different Strain Rates for the Fully Saturated Case.

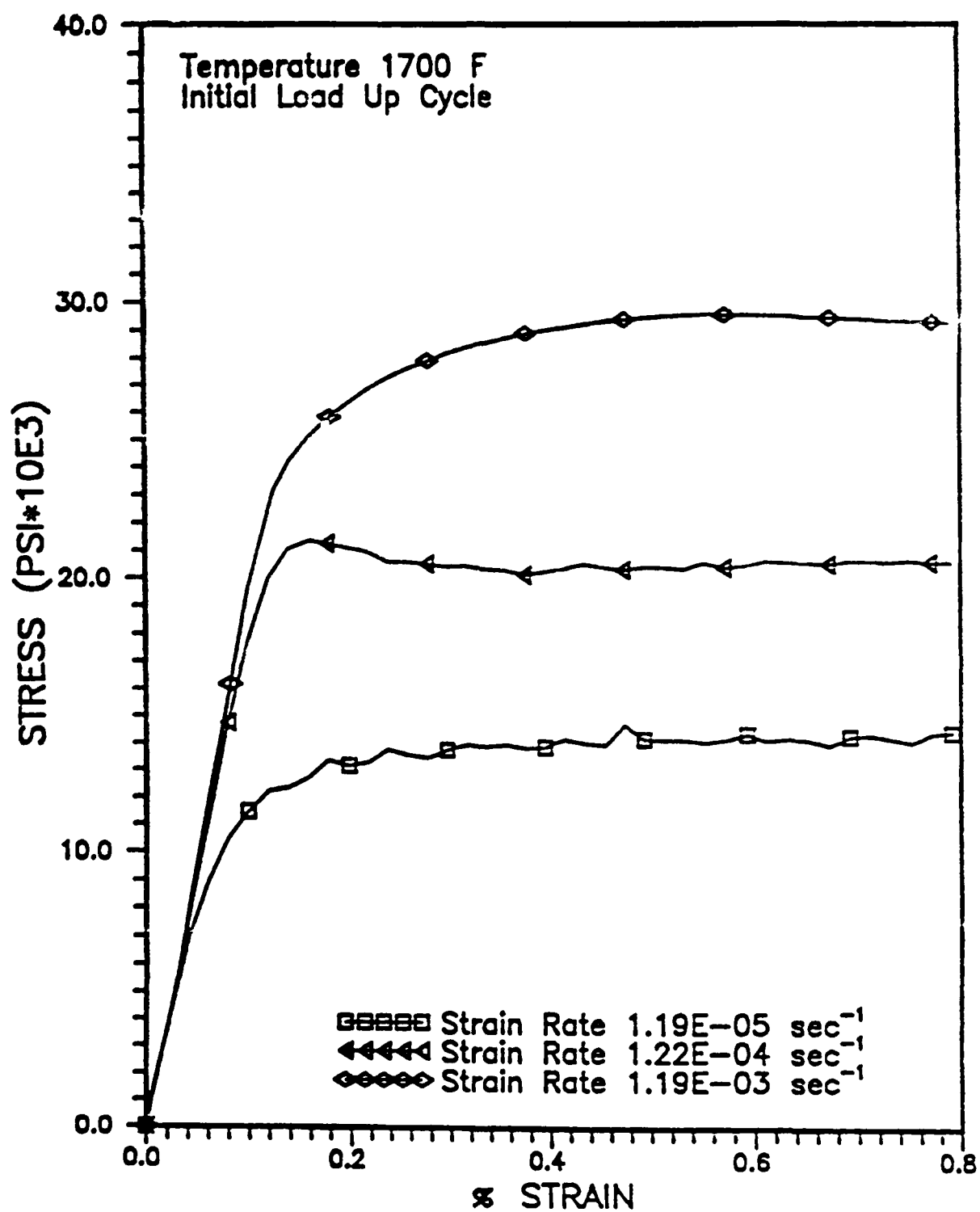


Fig. 3 Comparison of Experimental Data at 1700°F at Different Strain Rates for Initial Load Up.

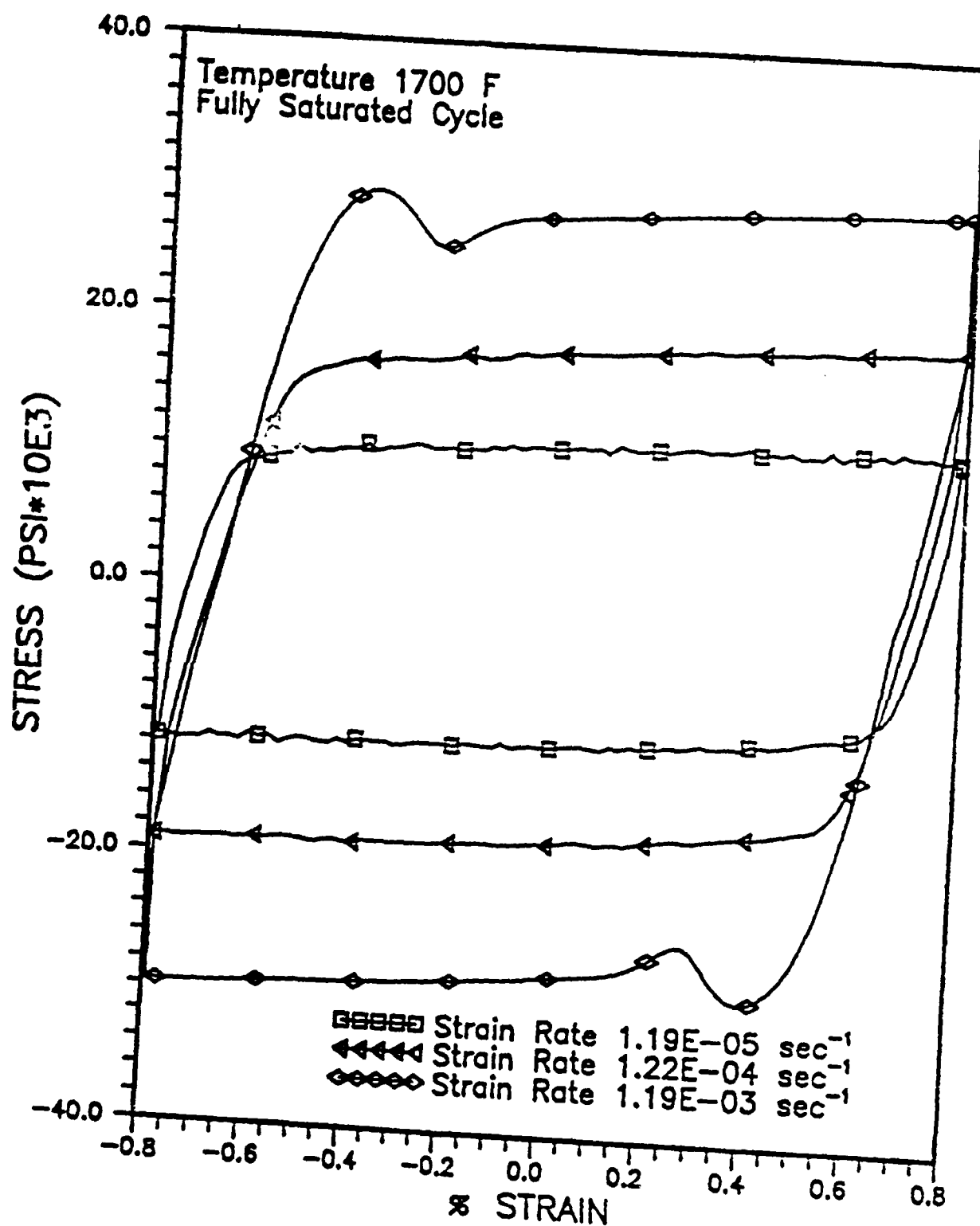
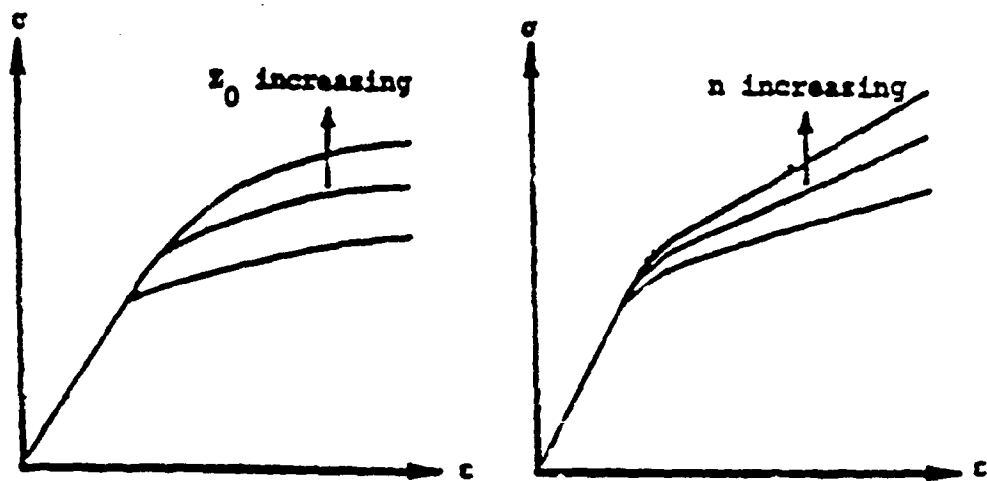
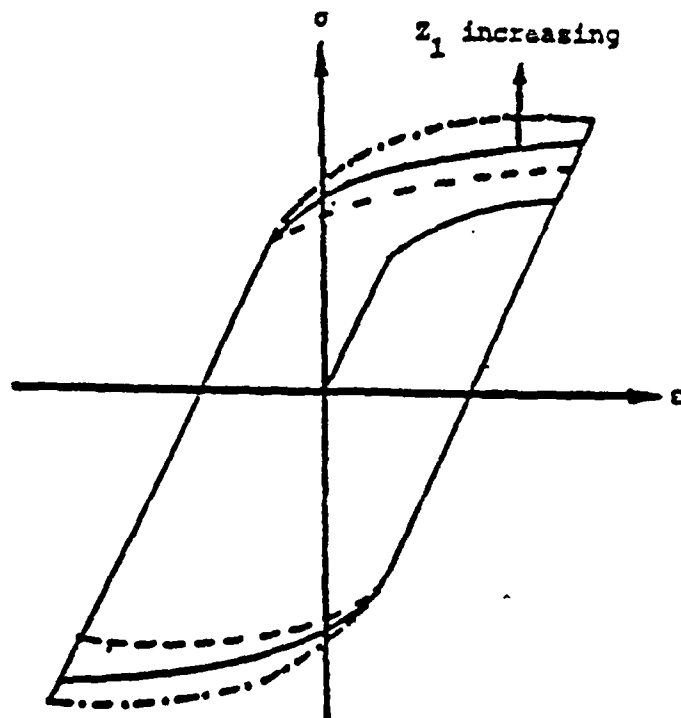


Fig. 4 Comparison of Experimental Data at 1700°F at Different Strain Rates for the Fully Saturated Case.



a) Response to Changing Material Parameter Z_0 .

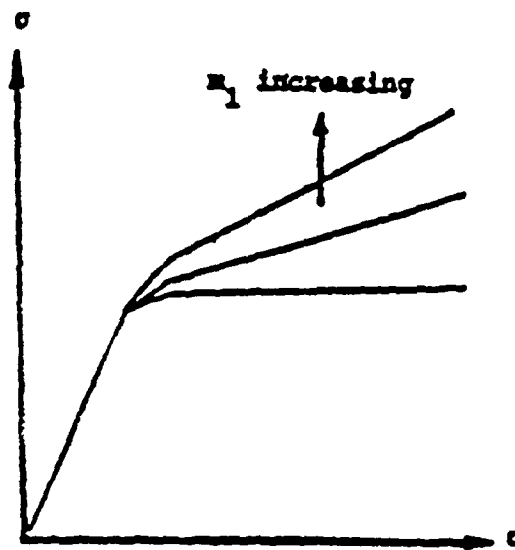
b) Response to Changing Material Parameter n .



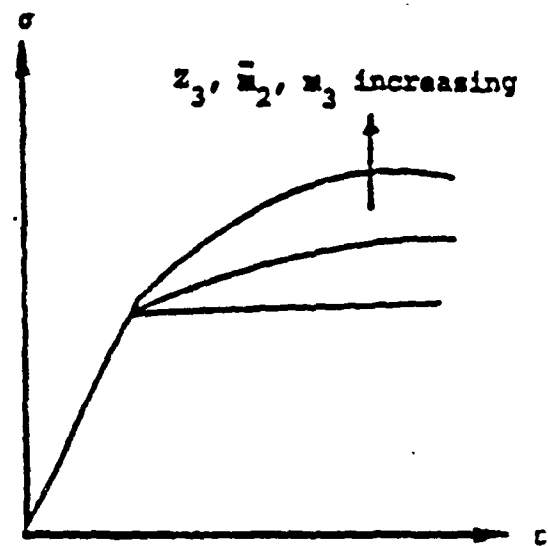
c) Response to Changing Material Parameter Z_1 .

Fig. 5 Stress-Strain Response for Bodner-Partom's Model:

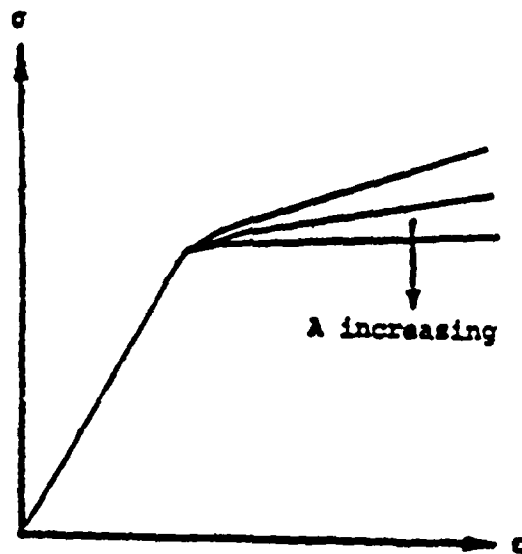
- a) Response to Changing Material Parameter Z_0 .
- b) Response to Changing Material Parameter n .
- c) Response to Changing Material Parameter Z_1 .



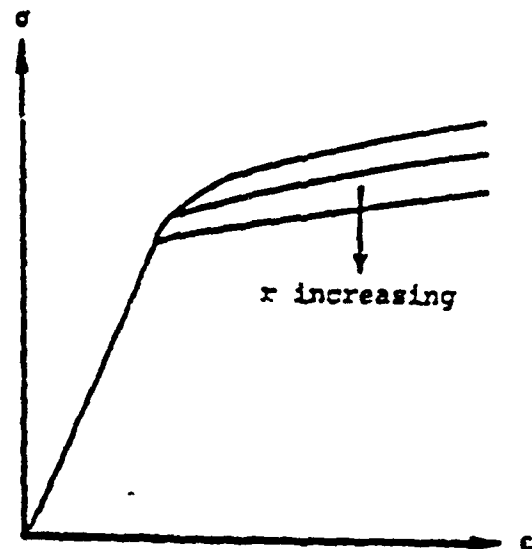
a) Response to Changing Material Parameter m_1 .



b) Response to Changing Material Parameter Z_3 , m_2 , and m_3 .



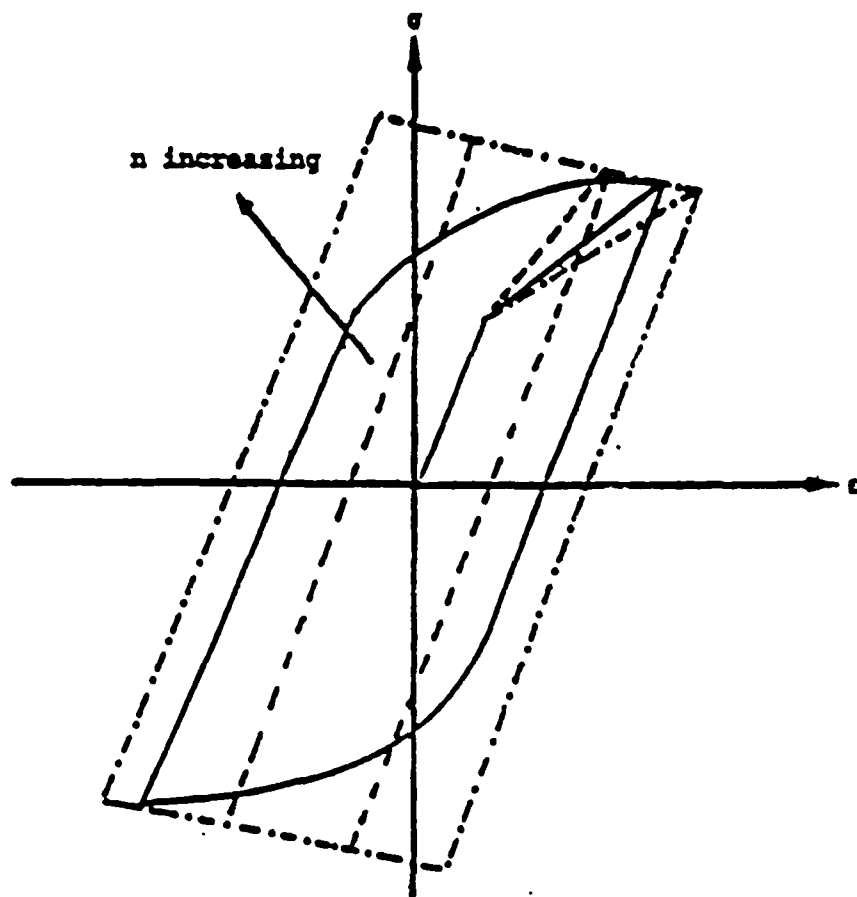
c) Response to Changing Material Parameter A .



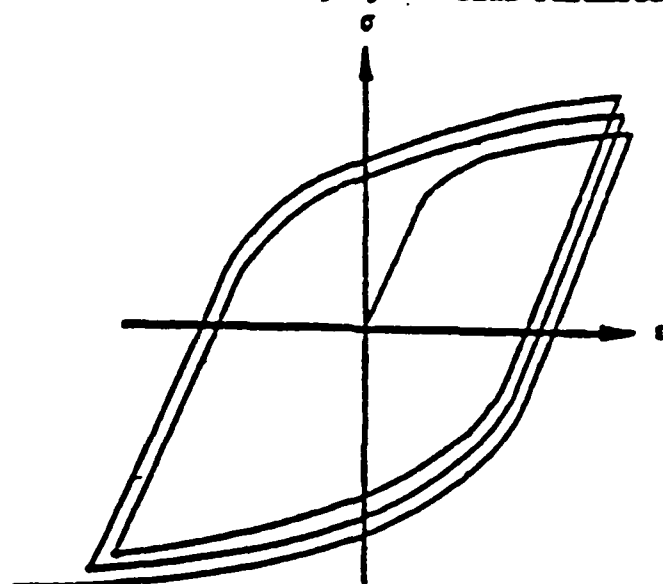
d) Response to Changing Material Parameter r .

Fig. 6 Stress-Strain Response for Bodner-Partom's Model:

- a) Response to Changing Material Parameter m_1 .
- b) Response to Changing Material Parameters Z_3 , m_2 , m_3 .
- c) Response to Changing Material Parameter A .
- d) Response to Changing Material Parameter r .



a) Response to Changing Material Parameter n .



b) Response to Changing Material Parameter $(n_1 + n_2)$.

Fig. 7 Stress-Strain Response for Walker's Model:
a) Response to Changing Material Parameter n .
b) Response to Changing Material Parameters $(n_1 + n_2)$.

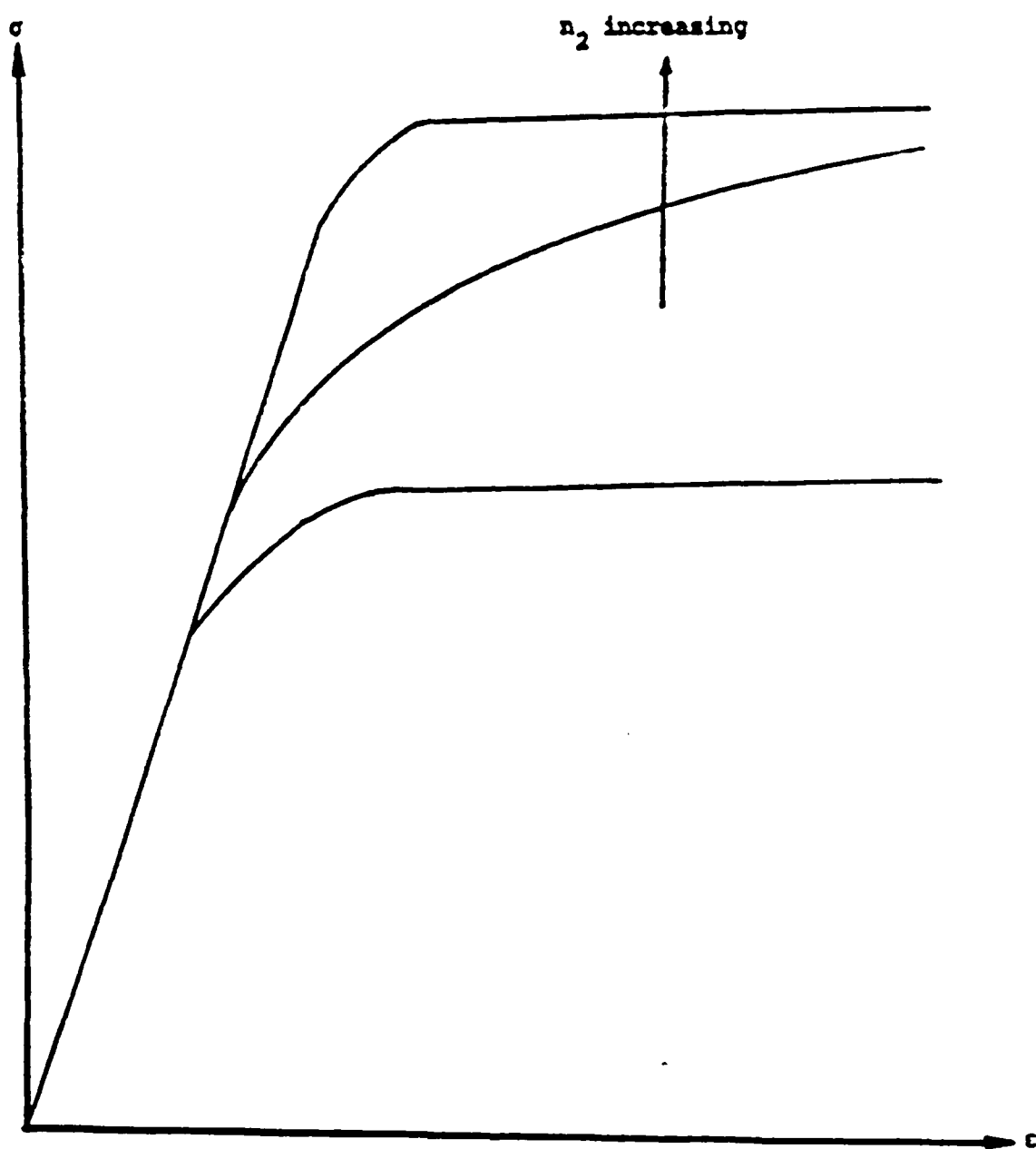
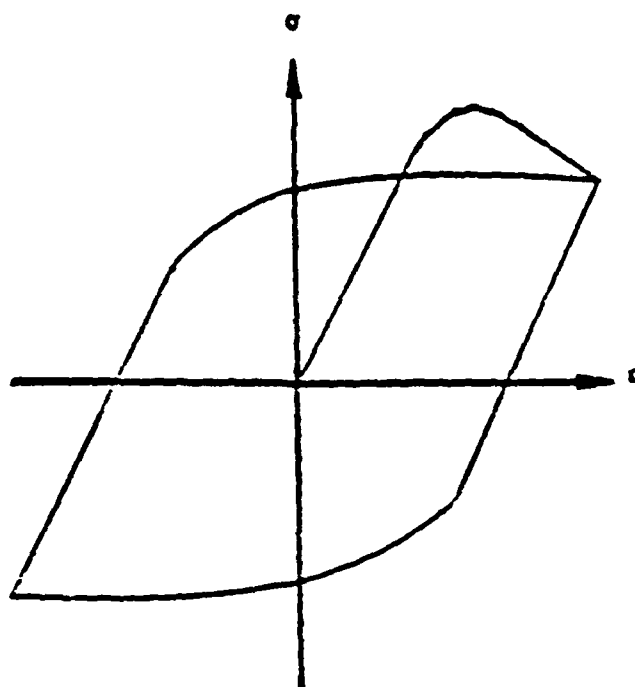
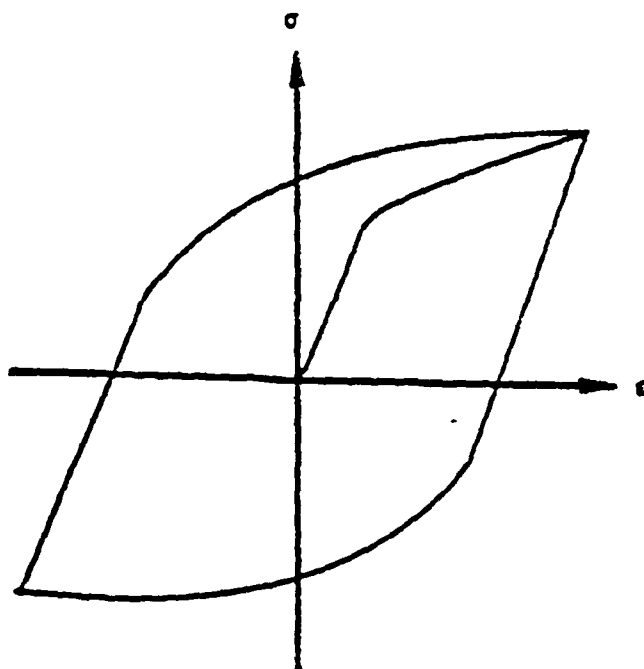


Fig. 8 Stress-Strain Response for Walker's Model to Changing Material Parameter n_2 .



a) B_0 Decreasing.



b) B_0 Increasing.

Fig. 9 Stress-Strain Response for Walker's Model to Changing Material Parameter B_0 .

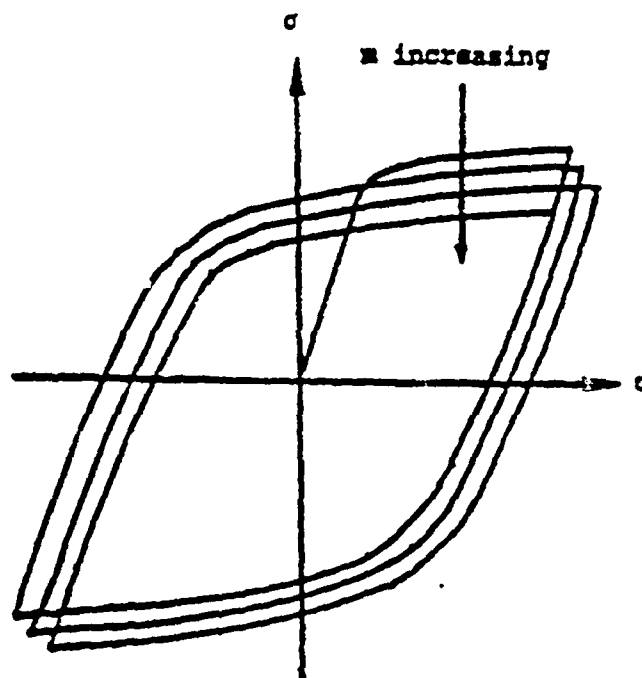
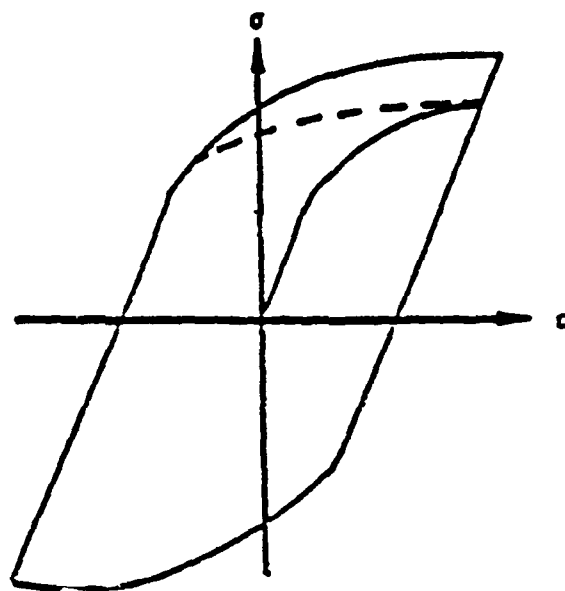
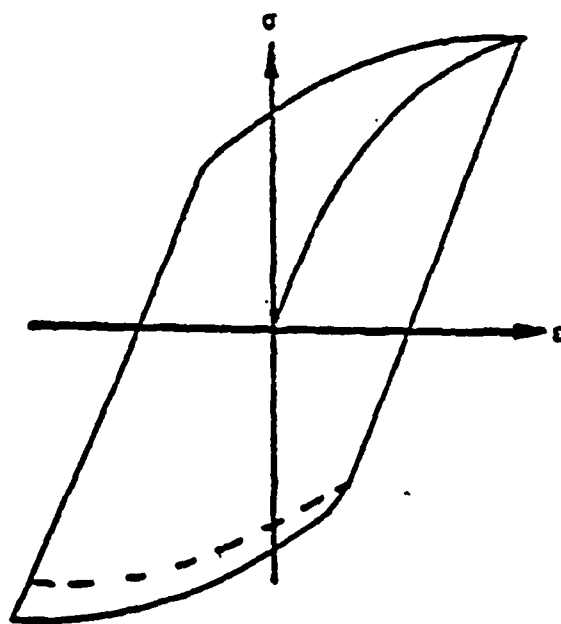


Fig. 10 Stress-Strain Response for Walker's Model to Changing Material Parameter m .



a) n_3 Decreasing.



b) n_3 Increasing.

Fig. 11 Stress-Strain Response for Walker's Model to Changing Material Parameter n_3 .

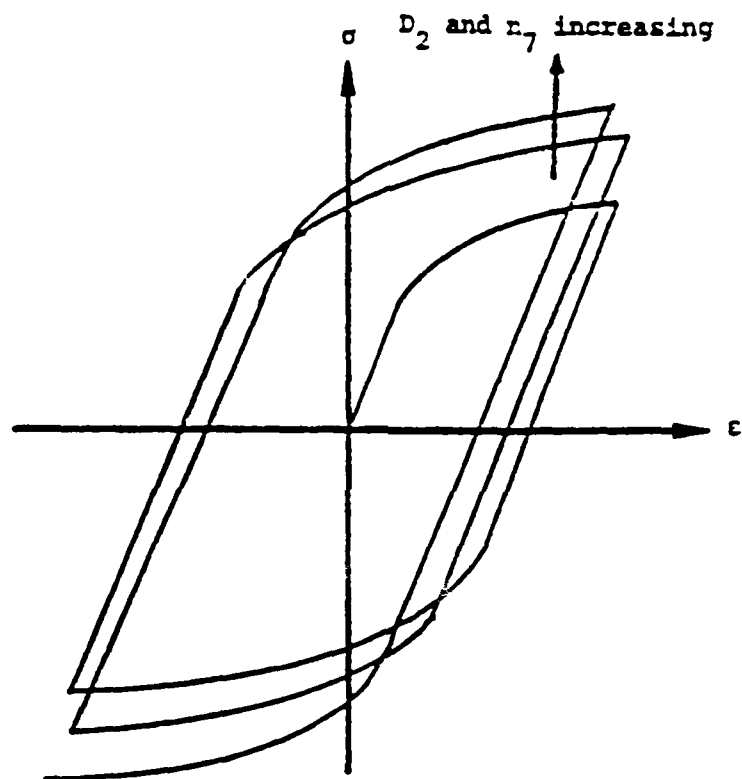
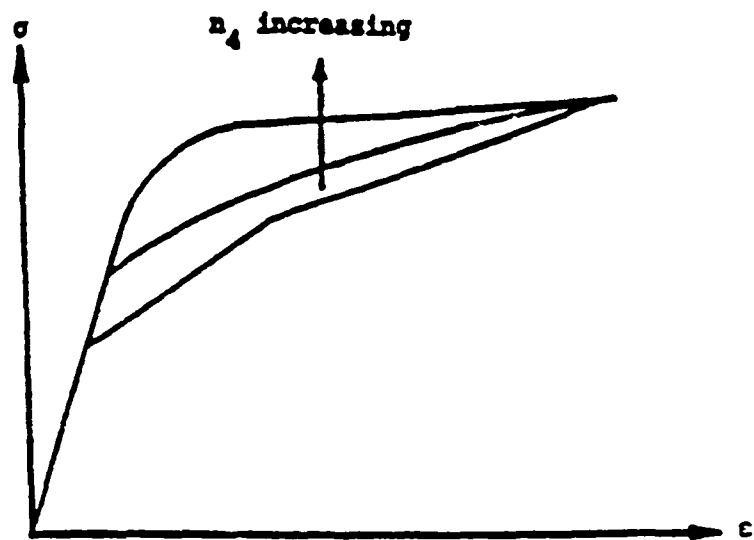
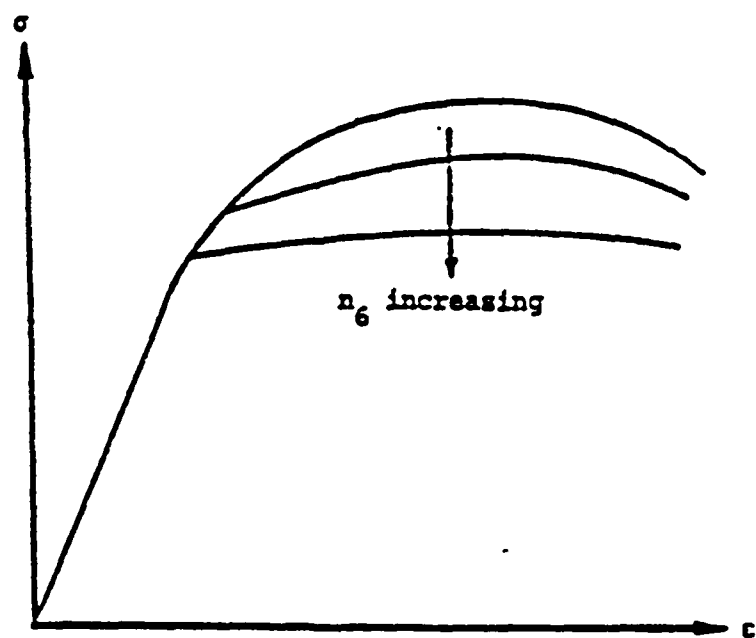


Fig. 12 Stress-Strain Response for Walker's Model to Changing Material Parameters D_2 and n_7 .



a) Response to Changing Material Parameter n_4 .



b) Response to Changing Material Parameter n_6 .

Fig. 13 Stress-Strain Response for Walker's Model:
a) Response to Changing Material Parameter n_4 .
b) Response to Changing Material Parameter n_6 .

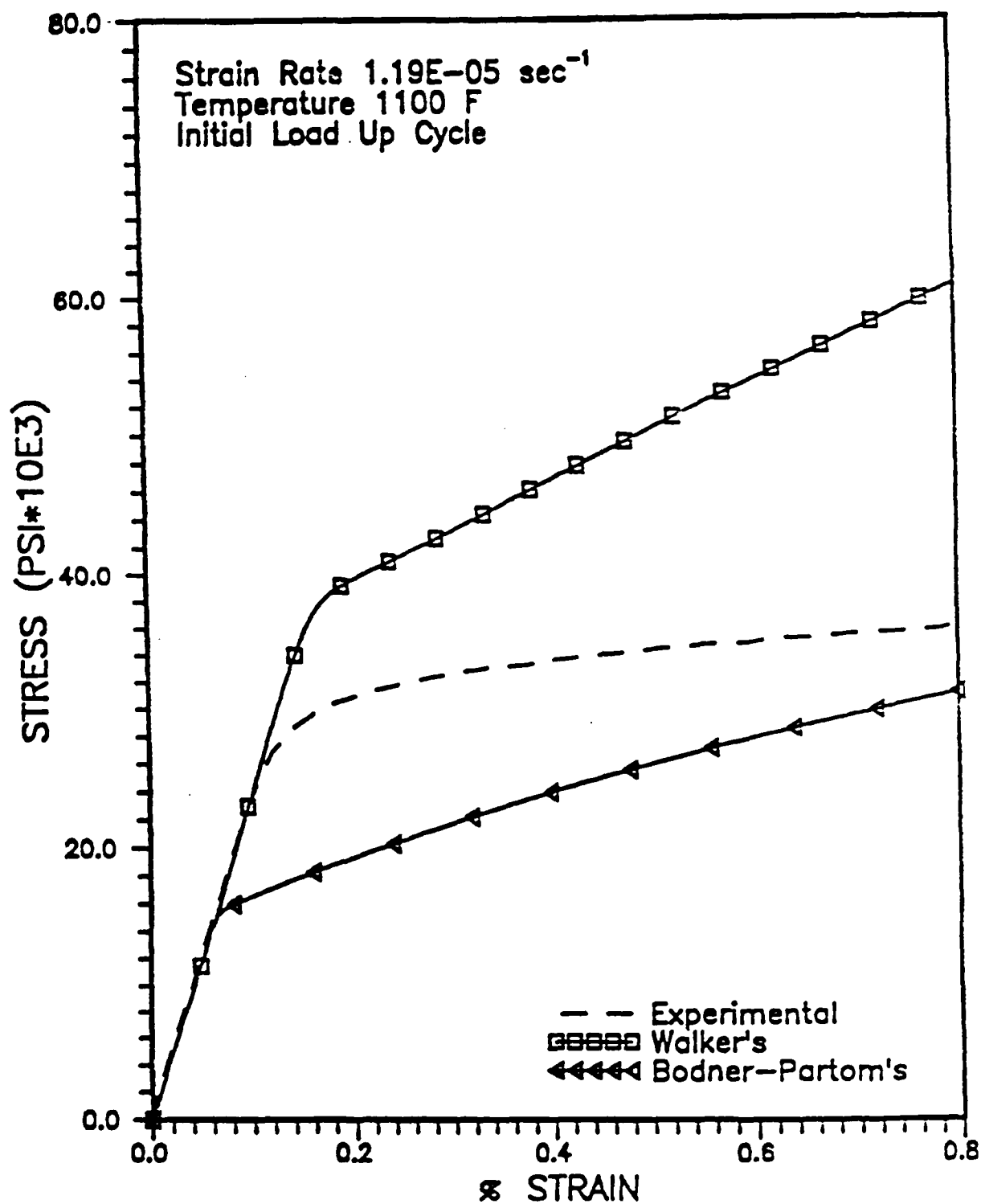


Fig. 14 Comparison of Models to the Experimental Data for 1100°F at a Strain Rate of $1.19\text{E}-03 \text{ sec}^{-1}$ for Initial Load up.

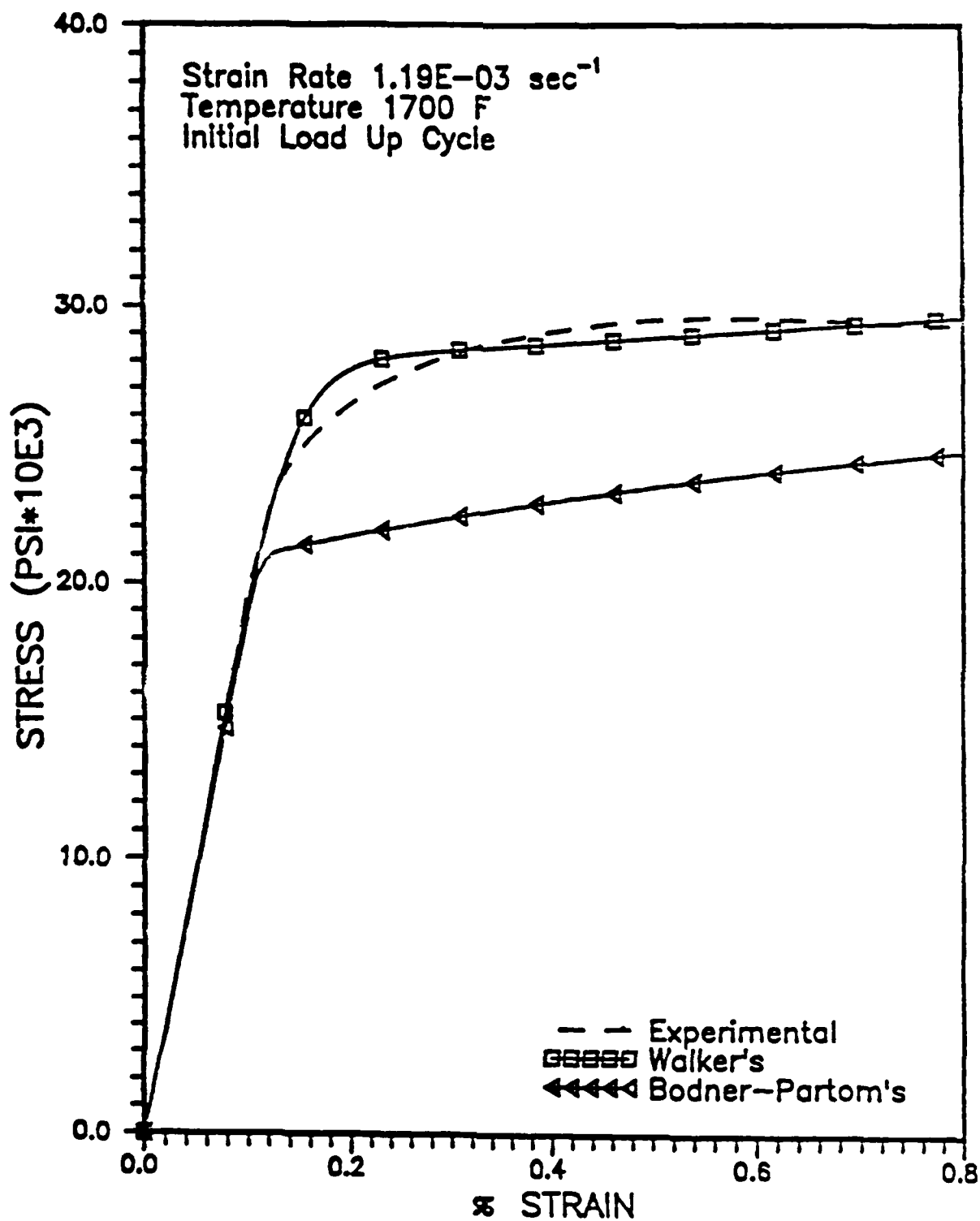


Fig. 15 Comparison of Models to the Experimental Data for 1700°F at a Strain Rate of $1.19\text{E}-03 \text{ sec}^{-1}$ for Initial Load up.

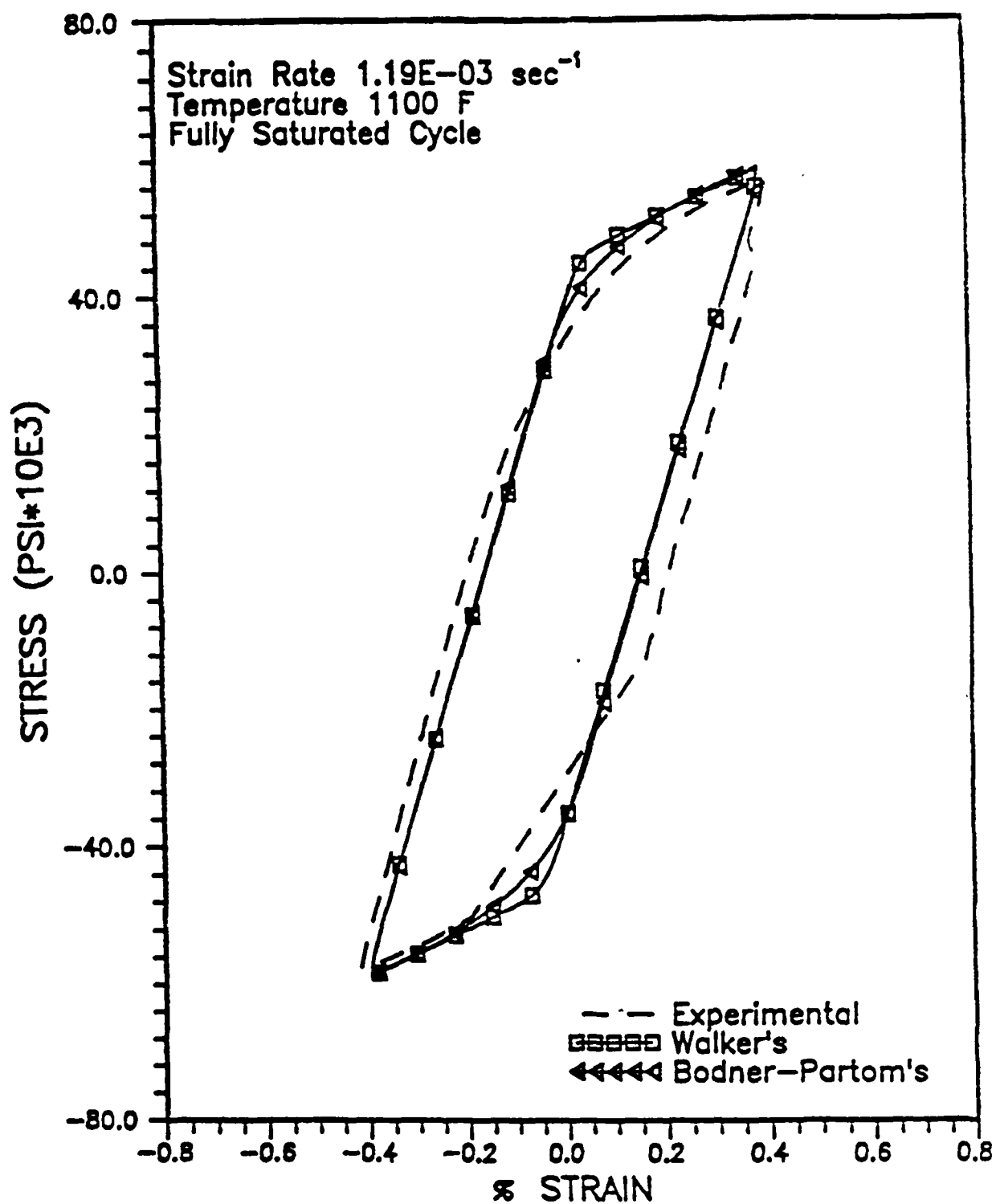


Fig. 16 . Comparison of Models to the Experimental Data
for 1100°F at a Strain Rate of $1.19\text{E}-03 \text{ sec}^{-1}$
for the Fully Saturated Case.

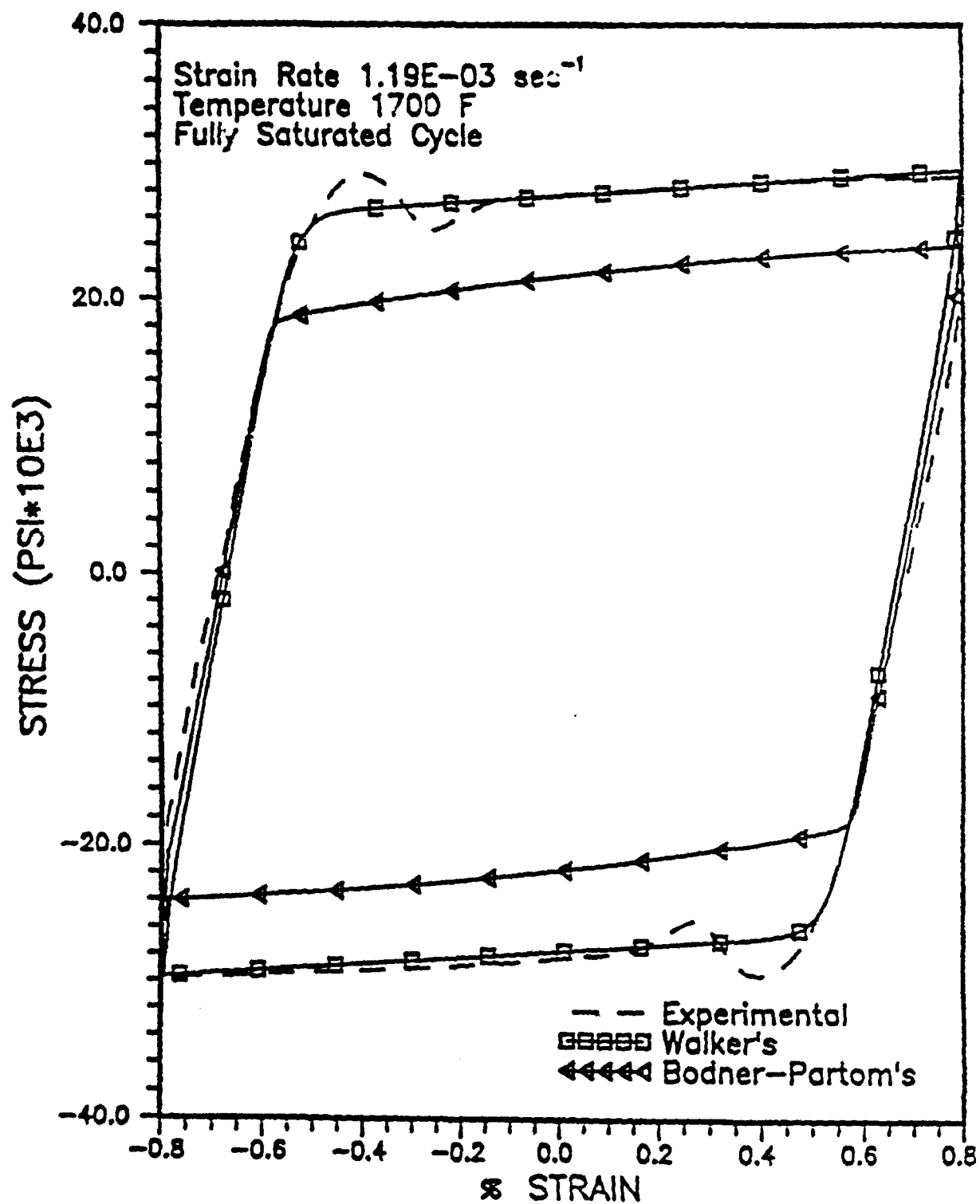


Fig. 17 Comparison of Models to the Experimental Data for 1700°F at a Strain Rate of $1.19\text{E}-03 \text{ sec}^{-1}$ for the Fully Saturated Case.

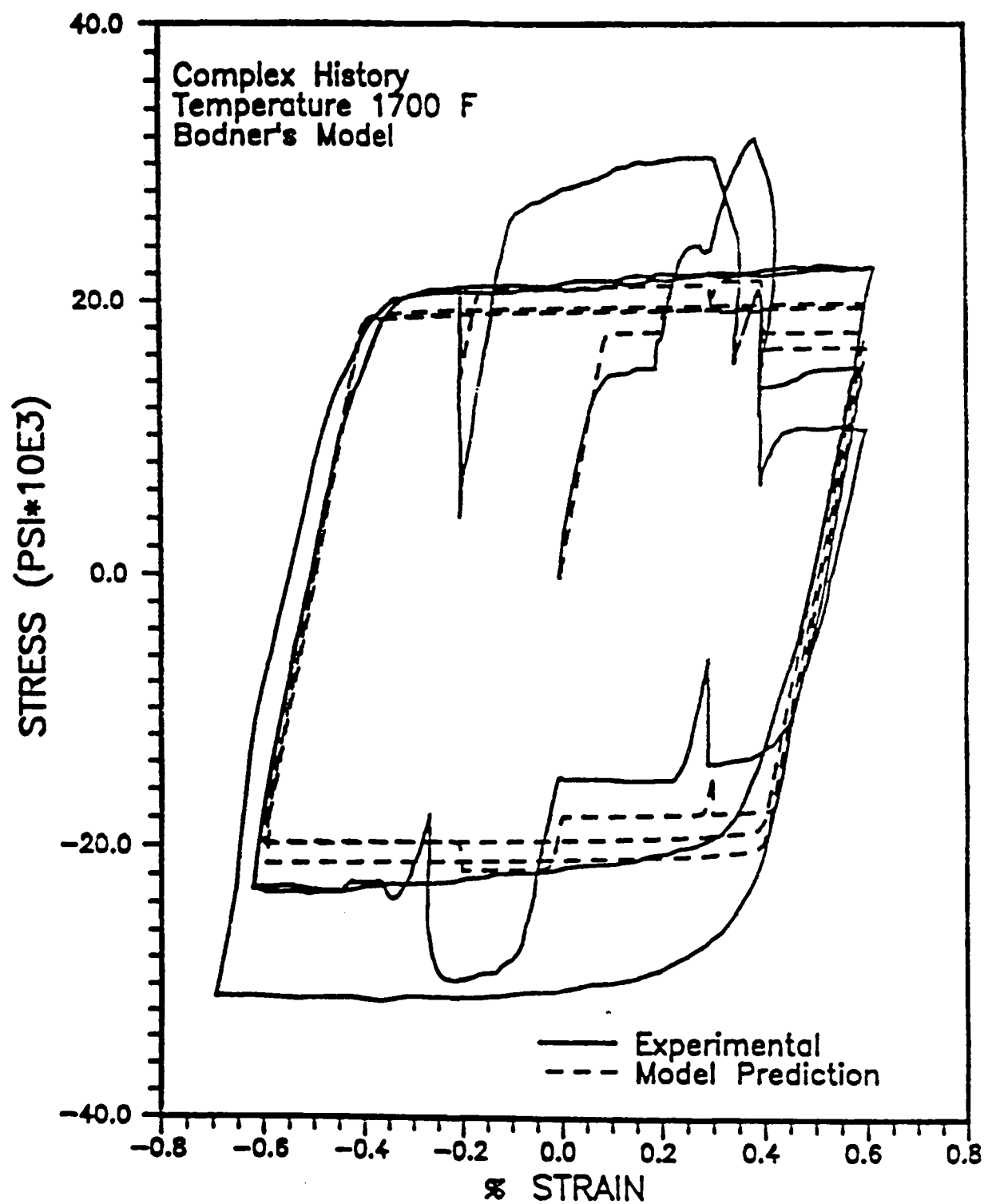


Fig. 18 Comparison of Bodner's Model to Experimental data at 1700°F for a Complex Strain Input History.

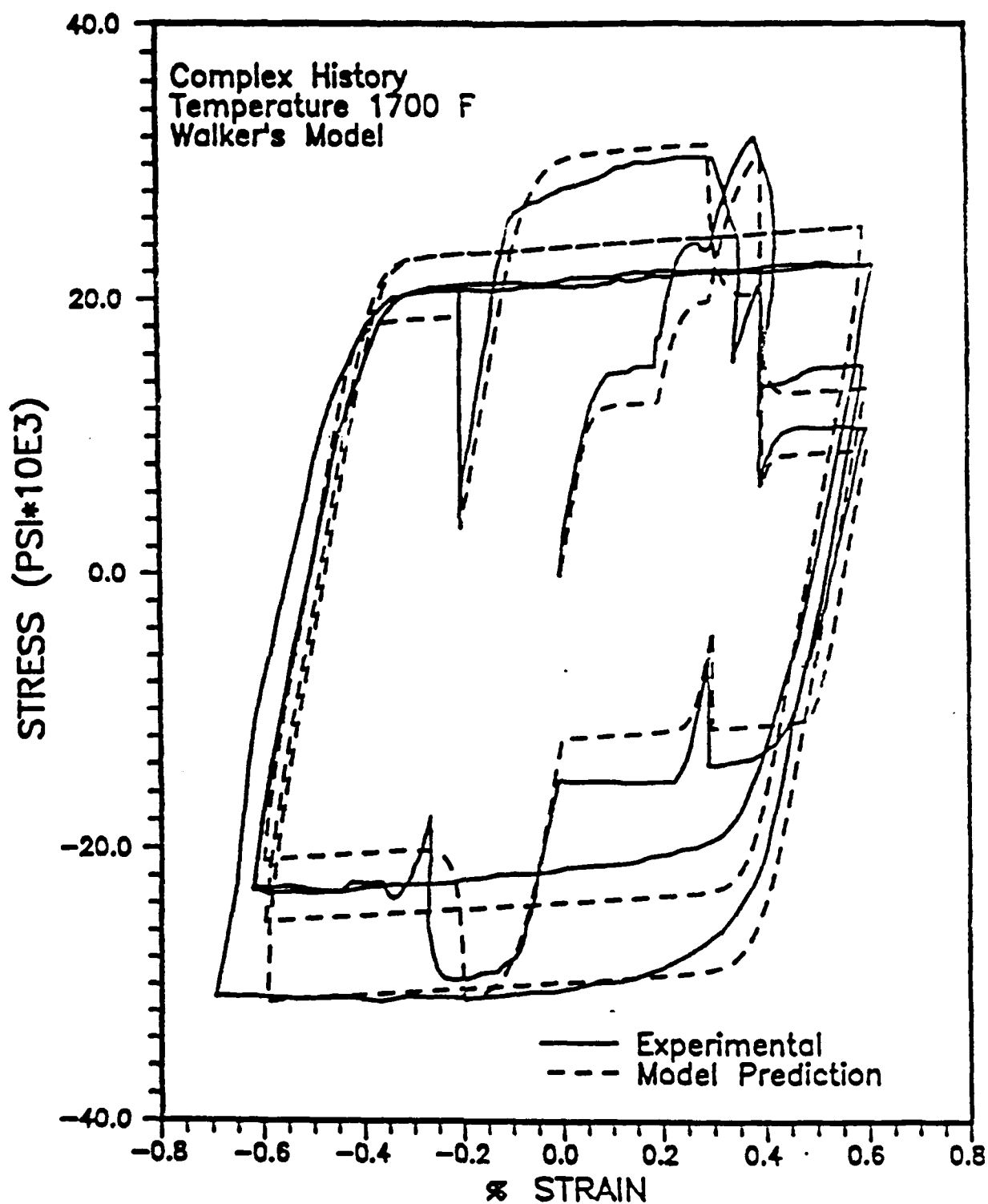


Fig. 19 Comparison of Walker's Model to Experimental data at 1700°F for a Complex Strain Input History.

Appendix 7.5

A Review of the Theory
of Thermomechanical Coupling
in Inelastic Solids

A Review of the Theory of
Thermomechanical Coupling in Inelastic Solids

by

David H. Allen
Aerospace Engineering Department
Texas A&M University
College Station, TX 77843

ABSTRACT

Coupling between mechanical and thermodynamic processes can be significant in solid media when material inelasticity occurs. Significant mechanical energy may be converted to heat via hysteretic loss, and this coupling may be significant even under quasi-static conditions. Important advances have been made since the second world war in modelling this thermomechanical coupling. This paper reviews many of the major achievements on this subject.

The paper opens with a short review of historical milestones on this subject. A theoretical model is then reviewed, including both conservation laws and constitutive models for certain classes of solids. The paper concludes with a discussion of recent attempts to solve the inelastic coupled thermomechanical field problem.

INTRODUCTION

The phenomenon of coupling between thermodynamic and mechanical processes in solid media was first predicted by Duhamel [1837]. The significance of this coupling depends on the type of material behavior encountered during the process, as well as the time required to perform the process. In the case of elastic solids, this coupling is for most materials insignificant except under conditions wherein inertial effects are not negligible. However, in inelastic media circumstances may arise wherein this coupling is significant even under quasi-static conditions.

This phenomenon can be illustrated with a simple experiment: take a coat hanger and bend it until permanent deformations occur. Now note that additional mechanical energy must be supplied in order to restore the coat hanger to its original configuration. Since mechanical energy must be applied throughout the entire process, the question becomes: where has the mechanical energy gone? The answer can be found by repeating the process several times and then touching the coat hanger where the permanent deformations have occurred. Of course, anyone who has ever performed this experiment knows that the coat hanger heats up, so that it is clear that at least some of the mechanical energy has gone into heat.

While the above example represents a somewhat simplistic viewpoint of thermomechanical coupling, it nevertheless verifies the existence of the phenomenon, and whereas this example is of purely academic interest, there are numerous physical situations occurring in science and engineering today wherein this coupling may be so significant as to be unavoidable in order to accurately model mechanical response. This paper endeavors to lay out the important developments that are necessary in order to go about solving a

problem involving thermomechanical coupling. This is accomplished in three parts: a historical review; theoretical foundations; and applications of the theory for certain problems.

HISTORICAL REVIEW

Historically, the foundations of continuum mechanics appear to have been formulated just after the turn of the nineteenth century at the Ecole Polytechnique in Paris. Although their research did not appear in print until sometime later, two students of Laplace appear to have successfully formulated the boundary value problem for isotropic linear elastic media by the year 1822 [Navier, 1827, Cauchy, 1823]. Navier is credited with the initial formulation of the field problem, but Cauchy was the first to introduce the concept of stress. At the same time, Fourier was proposing a model for the transfer of heat [Fourier, 1822]. These early models did not recognize the coupling between mechanical and thermal energy.

It remained for Duhamel to propose the first model of thermomechanical coupling in 1837 [Duhamel, 1837, 1838]. Thereafter, the fundamental advances in thermodynamics by Caratheodory [1909], as well as the research of Neumann [1885] provided further credence to the theory of thermomechanical coupling, so that by the start of the first world war this phenomenon was well known in elastic media [Voigt, 1910].

During the first quarter of this century the phenomenological theory of plasticity was solidified by a number of scientists including Prandtl [1924], Von Mises [1913], and others. These achievements in plasticity helped to spawn an interest in thermomechanical coupling in inelastic solids, such as the landmark experimental works of Farren and Taylor [1925] and Taylor and

Quinney [1934]. These works demonstrated that nearly all of the hysteretic loss in elastic-plastic solids is converted to heat. These experiments have been verified by more recent and precise experiments [Halford, 1966, 1987; Dillon, 1962, 1962, 1966; Tauchert, 1967, Tauchert and Afzal, 1967; Kratochvil and DeAngelis, 1971].

Although great advances had been previously made in the theory of thermomechanical coupling, the necessary framework to construct a theory applicable to inelastic solids did not appear until the 1950's. The first work appears to have been reported by Biot [1956], utilizing developments in irreversible thermodynamics achieved by Prigogine in the late 1940's [1947]. This paper was then followed by a number of works dealing with thermodynamics of coupled thermomechanical processes in inelastic solids [Boley and Weiner, 1960; Coleman, 1964; Coleman and Gurtin, 1967; Schapery, 1964, 1964; Olszak and Perzyna, 1968; Green and Naghdi, 1965; Dillon; 1963] most notably those by Kratochvil and Dillon [1969, 1970], and Lehmann [1972, 1977, 1980]. In the following section a general formulation of the field problem as constructed by these authors is reviewed.

THEORETICAL FORMULATION

Consider a continuous domain with interior V and boundary B . The body $V+B$ may be either simply or multiply connected. The objective is to predict to a predetermined degree of accuracy the mechanical response (such as deformation field) of the body to some arbitrary input. It is assumed that although thermal effects on mechanical properties may be significant, electric and magnetic effects produce negligible mechanical response [Coleman and Noll, 1963]. Furthermore, in the current model development, it is assumed that all

deformations are infinitesimal (although the theory applies with minor modifications to media undergoing finite deformations). Under these conditions it is postulated that the following physical quantities are necessary to characterize the thermomechanical response at all points x_k and for all times t in the body $V+B$ [Coleman and Noll, 1963]:

- 1) the deformation field

$$u_i = u_i(x_k, t)$$

- 2) the stress tensor

$$\sigma_{ij} = \sigma_{ij}(x_k, t)$$

- 3) the body force per unit mass

$$f_i = f_i(x_k, t)$$

- 4) the internal energy per unit mass

$$u = u(x_k, t)$$

- 5) the heat supply per unit mass

$$r = r(x_k, t)$$

- 6) the entropy per unit mass

$$s = s(x_k, t)$$

- 7) the absolute temperature

$$T = T(x_k, t)$$

8) the heat flux vector

$$q_i = q_i(x_k, t)$$

and

9) the mass density

$$\rho = \rho(x_k, t)$$

Also, recall that the deformation field u_i is related to the infinitesimal strain tensor by

$$\epsilon_{ij} \equiv \frac{1}{2}(u_{i,j} + u_{j,i}) \quad (1)$$

Statements 1) through 9) above, along with equation (1) describe 32 state variables to be determined for each material point and at all times in order to characterize the state of the body V+B. Now consider what is available to obtain the 32 state variables postulated above:

1) Conservation of mass (assuming infinitesimal deformations in a closed system):

$$\frac{\partial \rho}{\partial t} = 0 \quad (2)$$

2) Conservation of linear momentum:

$$\sigma_{ji,j} + \rho f_i = \rho \ddot{u}_i \quad (3)$$

3) Conservation of angular momentum (assuming no body moments):

$$\sigma_{ji} = \sigma_{ij} \quad (4)$$

4) Conservation of energy:

$$\rho \dot{u} = \dot{\sigma}_{ij} \epsilon_{ij} - q_{i,i} + \rho \dot{r} \quad (5)$$

5) The entropy production inequality:

$$\rho \dot{s} + \left(\frac{q_i}{T} \right)_{,i} - \frac{\rho \dot{r}}{T} \geq 0 \quad (6)$$

When tallied, the above are a set of seventeen equations and one inequality. Since the number of available equations (17) exceeds the number of state variables (32), one must assume that additional equations are required in order to produce a complete model. On reflection, this would seem obvious due to the fact that none of the above equations recognizes the material makeup of different media. In other words, if the information already supplied were sufficient to describe the state of a body, two different bodies of identical shape but different makeup (such as steel and silly putty) would respond the same to identical inputs. Since this is obviously not the case, it will be necessary to construct additional equations describing the material makeup (or constitution) of the body.

In order to accomplish this, first recall the 32 unknown quantities to be determined: u_i , σ_{ij} , f_i , ρ , u , q_i , s , r , T , and ϵ_{ij} .

In physical practice the field variables f_i and r are normally specified

as input data. However, suppose that as a thought experiment the variables u_i and T are specified. It is common to call these variables the independent variables. However, it is preferable to call them "specified variables" since all of the state variables are in fact independent of one another. Although any four variables could be chosen, it is propitious to choose u_i and T because they are directly measurable quantities in laboratory experiments. This leaves a total of 32 (variables) minus 17 (field equations) minus 4 (specified variables) or eleven equations to be determined.

These last eleven equations are termed constitutive equations. In order to obtain a complete solution, then, it is possible to proceed in the following stepwise fashion:

- 1) Specify as input variables $u_i = u_i(x_k, t)$, $T = T(x_k, t)$ at all points in $V+B$, thus reducing to 28 unknowns;
- 2) utilize the conservation of angular momentum equations (4) to symmetrize the stress tensor, reducing to 25 unknowns;
- 3) use strain-displacement equations (1) to obtain ϵ_{ij} , thus reducing to 16 unknowns;
- 4) use the conservation of mass equation (2) to determine ρ , reducing to 15 unknowns;
- 5) assume that the following eleven equations can be determined at all points in $V+B$:

$$\sigma_{ij}(x_m, t) = \sigma_{ij}(\epsilon_{kl}(x_m, t), T(x_m, t), g_k(x_m, t)) \quad (7a)$$

$$u(x_m, t) = u(\epsilon_{kl}(x_m, t), T(x_m, t), g_k(x_m, t)) \quad (7b)$$

$$s(x_m, t) = s(\epsilon_{kl}(x_m, t), T(x_m, t), g_k(x_m, t)) \quad (7c)$$

$$q_i(x_m, t) = q_i(\epsilon_{kl}(x_m, t), T(x_m, t), g_k(x_m, t)) \quad (7d)$$

where $\{ \}$ signify history dependence, spanning the interval of time between which the quantities are initially known and the current time of interest, and $g_k \equiv T_{,k}$. Note that ϵ_{ij} is utilized instead of u_i in order to exclude dependence on rigid body motions;

6) use the conservation of linear momentum equations (3) to determine f_i , reducing to 1 unknown;

7) use the conservation of energy equation (5) to determine r ; and

8) impose entropy production inequality (6).

Thus, the constitutive equations (7), subject to the constraints imposed by the entropy production inequality, comprise a sufficient number of equations to solve the boundary value problem of interest when adjoined with the other seventeen equations described above. The above procedure is impractical for actually solving problems analytically because in practice one cannot normally specify u_i and T a priori at all points in $V+B$. The point of the method is to form a reasonable approach for constructing the general form

of constitutive equations (7). Once the precise form of these equations has been determined, it is then possible to utilize the most expedient solution procedure for the problem at hand.

Unfortunately, the form of equations (7) is still quite general, and further constraints are available only via the entropy production inequality, physical intuition, and experimental evidence. Since the last is often cumbersome and expensive, the first two should be utilized to maximum advantage.

Note that although higher order spatial derivatives in the displacement field $u_i(x_k)$ and temperature $T(x_k)$ could in principle be included in constitutive equations (7), their inclusion would yield a non-local theory. Such a non-local theory is generally only necessary when the scale of the microstructural features of the medium is large relative to the boundary value problem of interest. It will be assumed in the balance of this discussion that all microstructural features are very small, thus rendering a local model acceptable. Note also that equations (7) are not equations of state, since they require information at times other than the current time. Thus, the inclusion of time derivatives would be redundant.

Constitutive equations (7) are called the functional formulation. Alternatively, we could propose an internal state variable (ISV) formulation:

$$\sigma_{ij} = \sigma_{ij}(\epsilon_{kl}, T, g_k, \alpha_{kl}^\mu) \quad (8a)$$

$$u = u(\epsilon_{kl}, T, g_k, \alpha_{kl}^\mu) \quad (8b)$$

$$s = s(\epsilon_{kl}, T, g_k, \alpha_{kl}^\mu) \quad (8c)$$

$$q_i = q_i(\epsilon_{kl}, T, g_k, a_{kl}^\mu) \quad (8d)$$

$$\dot{a}_{ij}^n = \dot{a}_{ij}^n(\epsilon_{kl}, T, g_k, a_{kl}^\mu) \quad n=1, \dots, n; \mu=1, \dots, n \quad (8e)$$

where n is a sufficiently large number to characterize the material at hand. Equations (8e) are called internal state variable (ISV) evolution (or growth) laws. From the above description it can be inferred that an internal state variable is any state variable which cannot be obtained from an equation of state in terms of the specified variables (u_i and T). Instead, it must be obtained from an evolution law which is necessarily a differential equation in time.

It can be shown that when equations (8e) are continuously integrable in time the above are a special case of the functional formulation described by equations (7) [Lubliner, 1972].

Although constitutive equations (8) satisfy the principles of equipresence, determinism for stress, and local action, they do not actually satisfy the principle of material frame-indifference, but are in approximate agreement for infinitesimal displacements.

Now, to summarize, the problem is to solve for the $32+9n$ state variables u_i , σ_{ij} , f_i , ρ , u , q_i , r , s , T , ϵ_{ij} , and a_{ij}^n . To obtain these quantities, equations (1) through (5), (8) and inequality (6), or $28+9n$ equations are available, together with appropriate thermal and mechanical boundary conditions. Since the remaining four degrees of freedom (f_i and r) can be specified, this formulation constitutes a well-posed boundary value problem.

Constitutive equations (8) represent a general framework which is a formidable task to quantify for each material. Fortunately, there are two steps that can be taken before it becomes necessary to proceed to the

laboratory and perform (usually expensive) experiments. First, it is necessary to satisfy the entropy production inequality, and this will provide constraints on the allowable form of equations (8). Second, it is possible to perform "thought" experiments imposing such restrictions as material symmetry which will further constrain the form of equations (8).

To perform these two steps, first define the Helmholtz free energy:

$$h \equiv u - Ts \quad (9)$$

Thus, the free energy represents the recoverable energy during any process. Note that due to the above and definition (8), the Helmholtz free energy may be written as follows:

$$h = h(\epsilon_{kl}, T, g_k, \alpha_{kl}^\mu) \quad (10)$$

Therefore, according to the chain rule of differentiation

$$\dot{h} = \frac{\partial h}{\partial \epsilon_{kl}} \dot{\epsilon}_{kl} + \frac{\partial h}{\partial T} \dot{T} + \frac{\partial h}{\partial g_k} \dot{g}_k + \frac{\partial h}{\partial \alpha_{kl}^\mu} \dot{\alpha}_{kl}^\mu \quad (11)$$

Thus, solving (9) for u , differentiating in time and substituting this result into (5) results in

$$\rho(\dot{h} + \dot{T}s + T\dot{s}) = \sigma_{ij} \dot{\epsilon}_{ij} - q_{i,i} + \rho \dot{r} \quad (12)$$

Finally, substituting (12) into (11) and this result into entropy production inequality (6) gives

$$\begin{aligned}
& [\sigma_{ij}(\epsilon_k, T, g_k, \alpha_{kl}^\mu) - \rho \frac{\partial h}{\partial \epsilon_{ij}}(\epsilon_k, T, g_k, \alpha_{kl}^\mu)] \dot{\epsilon}_{ij} \\
& - [\rho \frac{\partial h}{\partial T}(\epsilon_k, T, g_k, \alpha_{kl}^\mu) + \rho s(\epsilon_k, T, g_k, \alpha_{kl}^\mu)] \dot{T} \\
& - [\rho \frac{\partial h}{\partial g_i}(\epsilon_k, T, g_k, \alpha_{kl}^\mu)] \dot{g}_i \\
& - [\frac{\partial h}{\partial \alpha_{ij}^\eta}(\epsilon_k, T, g_k, \alpha_{kl}^\mu)] \dot{\alpha}_{ij}^\eta(\epsilon_k, T, g_k, \alpha_{kl}^\mu) \\
& - [q_i(\epsilon_k, T, g_k, \alpha_{kl}^\mu)/T] g_i \geq 0
\end{aligned} \tag{13}$$

where the specified variables $\dot{\epsilon}_{ij}$, T , \dot{g}_i , $\dot{\alpha}_{ij}^\eta$, and g_i are taken outside the brackets.

Thermodynamic constraints on constitutive equations (8) are now obtained in a manner similar to that employed by Coleman and Mizel [1963]. To do this, note that inequality (13) must hold for any and all processes. Therefore, important constraints can be obtained by considering several thought experiments. For example, at time $t=t_0$:

THOUGHT EXPERIMENT I: a) CASE A: let $\dot{\epsilon}_{ij}$, T , $g_i = 0$, $\dot{g}_1 = k_1 = \text{constant}$; or

b) CASE B: let $\dot{\epsilon}_{ij}$, T , $g_i = 0$, $\dot{g}_1 = -k_1 = \text{constant}$.

It follows that

$$- \frac{\partial h}{\partial g_1} (\epsilon_{kl}(t_0), T(t_0), g_k(t_0)) \cdot k_1 \geq 0 \text{ and}$$

$$\frac{\partial h}{\partial g_1} (\epsilon_{kl}(t_0), T(t_0), g_k(t_0)) \cdot (-k_1) \geq 0 \Rightarrow$$

$$\frac{\partial h}{\partial g_1} = 0$$

Similarly,

$$\frac{\partial h}{\partial g_i} = 0 \Rightarrow h = h(\epsilon_{kl}, T, a_{kl}^\mu) \quad (14)$$

and the above must hold for any and all processes since u_i , ϵ_{ij} , T , and g_i are specified (and mutually independent) state variables.

THOUGHT EXPERIMENT II: let $g_i, \dot{g}_i, \dot{T} = 0$. Similarly, it follows that for all processes:

$$\sigma_{ij} = \rho \frac{\partial h}{\partial \epsilon_{ij}} \Rightarrow \sigma_{ij} = \sigma_{ij}(\epsilon_{kl}, T, a_{kl}^\mu) \quad (15)$$

Note that although (15) is similar to the result obtained for elastic materials, h is not a potential for the stress tensor for this class of materials since the inclusion of the internal state variables, a_{ij}^η , causes the Helmholtz free energy to be path dependent.

THOUGHT EXPERIMENT III: let $g_i, \dot{g}_i, \dot{\epsilon}_{ij} = 0$. It follows that for all processes:

$$s = - \frac{\partial h}{\partial T} \Rightarrow s = s(\epsilon_{ij}, T, \alpha_{kl}^u) \quad (16)$$

Due to equations (14) through (16) inequality (13) now reduces to

$$- \rho \frac{\partial h}{\partial \alpha_{ij}^u} \dot{\alpha}_{ij}^u - q_i g_i / T \geq 0 \quad (17)$$

where the first term represents internal dissipation and the last term is heat conduction dissipation. Note that the internal dissipation cannot be set to zero because although the rate of change of the internal state variables may be specified, the actual internal state at any time cannot be specified.

It can also be shown that [Coleman and Mizel, 1963]

$$q_i = -k_{ij} g_j + \text{H.O.T.} \quad (18)$$

where the thermal conductivity tensor, k_{ij} , may depend on ϵ_{kl} , T , and α_{kl}^u .

Thus, if internal state variable evolution laws (8e) can be determined experimentally, the problem will be completely specified by construction of the Helmholtz free energy function (equation (10)).

Now consider a special case of equation (10) which is found to be suitable for many materials. Let

$$h = h(\epsilon_{kl}, T, \epsilon_{kl}^I) \quad (19)$$

where ϵ_{kl}^I , called the inelastic strain tensor, is equivalent to α_{kl}^1 and is in the case of metals a locally averaged representor of dislocation movement. A material behaving according to equations (8) and (19) is termed a viscoplastic material [Kratochvil and Dillon, 1970].

Expanding h in a second order Taylor series in its arguments gives

$$h = \frac{1}{\rho} \left[A + BT' + C_{ij} \epsilon_{ij} + \frac{1}{2} D_{ijkl} \epsilon_{ij} \epsilon_{kl} + E_{ij} \epsilon_{ij}^I + F_{ijkl} \epsilon_{ij} \epsilon_{kl}^I + \right. \\ \left. + \frac{1}{2} G_{ijkl} \epsilon_{ij}^I \epsilon_{kl}^I + H_{ij} \epsilon_{ij} T' + I_{ij} \epsilon_{ij}^I T' + \frac{1}{2} K T'^2 \right] \quad (20)$$

where

$$T' \equiv \frac{T - T_0}{T_0} \quad (21)$$

and T_0 is the reference temperature at which no strain is observed.

Substituting the above into (15) results in

$$\sigma_{ij} = C_{ij} + D_{ijkl} \epsilon_{kl} + F_{ijkl} \epsilon_{kl}^I + H_{ij} T' \quad (22)$$

Experimental evidence suggests that in viscoplastic materials, during isothermal processes, the inelastic strain produces negligible free energy, or

$$\frac{\partial h}{\partial \epsilon_{ij}^I} = - \frac{\partial h}{\partial \epsilon_{ij}} \quad (23)$$

so that, at constant temperature

$$\dot{h} = \frac{\partial h}{\partial \epsilon_{ij}} \dot{\epsilon}_{ij} + \frac{\partial h}{\partial \epsilon_{ij}^I} \dot{\epsilon}_{ij}^I = \frac{\partial h}{\partial \epsilon_{ij}} (\dot{\epsilon}_{ij} - \dot{\epsilon}_{ij}^I) \quad (24)$$

Substituting (20) into (23) results in

$$\begin{aligned} E_{ij} + F_{ijk1}\epsilon_{k1} + G_{ijk1}\epsilon_{k1}^I + I_{ij}T' = & -C_{ij} - D_{ijk1}\epsilon_{k1} \\ & - F_{ijk1}\epsilon_{k1}^I - H_{ij}T' \end{aligned} \quad (25)$$

Therefore, by inspection

$$E_{ij} = -C_{ij} \equiv \sigma_{ij}^R \quad (26)$$

$$F_{ijk1} = -D_{ijk1} \quad (27)$$

$$G_{ijk1} = -F_{ijk1} = D_{ijk1} \quad (28)$$

$$I_{ij} = -H_{ij} \equiv D_{ijk1}\beta_{k1} \quad (29)$$

It follows that equations (22) may be written

$$\sigma_{ij} = \sigma_{ij}^R + D_{ijk1}[\epsilon_{k1} - \epsilon_{k1}^I - \beta_{k1}(T - T_0)] \quad (30)$$

where σ_{ij}^R is called the residual stress at zero strain and temperature change, D_{ijk1} is the elastic modulus tensor and β_{k1} is called the thermal expansion tensor. The Prandtl-Reuss equations [Prandtl, 1924] can be obtained as a special case of (30) by differentiating (30) in time and substituting an appropriate evolution law for the inelastic strain tensor.

To obtain the coupled heat conduction equation differentiate (9) in time

and substitute into the first law of the thermodynamics (equation (5)) to obtain:

$$\rho(\dot{h} + T\dot{s} + T\dot{s}) = \sigma_{ij}\dot{\epsilon}_{ij} - q_{j,j} + \rho\dot{r} \quad (31)$$

Substituting (11) into (31) gives

$$\begin{aligned} & -(\sigma_{ij} - \rho \frac{\partial h}{\partial \epsilon_{ij}}) \dot{\epsilon}_{ij} + \rho (\frac{\partial h}{\partial T} + s) \dot{T} + \rho T\dot{s} \\ & + \rho \frac{\partial h}{\partial g_i} \dot{g}_i + \rho \frac{\partial h}{\partial \alpha_{ij}^n} \dot{\alpha}_{ij}^n + q_{j,j} - \rho\dot{r} = 0 \end{aligned} \quad (32)$$

Thus, utilizing (14) through (16) results in

$$\rho T\dot{s} + \rho \frac{\partial h}{\partial \alpha_{ij}^n} \dot{\alpha}_{ij}^n + q_{j,j} - \rho\dot{r} = 0 \quad (33)$$

Manipulating (8c) and (16) gives

$$\dot{s} = \frac{\partial s}{\partial \epsilon_{ij}} \dot{\epsilon}_{ij} + \frac{\partial s}{\partial T} \dot{T} + \frac{\partial s}{\partial \alpha_{ij}^n} \dot{\alpha}_{ij}^n \quad (34)$$

Substituting (35) into (34) thus gives

$$\begin{aligned} & \rho T \frac{\partial s}{\partial \epsilon_{ij}} \dot{\epsilon}_{ij} + \rho T \frac{\partial s}{\partial T} \dot{T} + \rho T \frac{\partial s}{\partial \alpha_{ij}^n} \dot{\alpha}_{ij}^n + \rho \frac{\partial h}{\partial \alpha_{ij}^n} \dot{\alpha}_{ij}^n \\ & + q_{j,j} - \rho\dot{r} = 0 \end{aligned} \quad (35)$$

Finally, utilizing (16) gives

$$\begin{aligned}
 & - \rho T \frac{\partial^2 h}{\partial \epsilon_{ij} \partial T} \dot{\epsilon}_{ij} - \rho T \frac{\partial^2 h}{\partial T^2} \dot{T} + \rho T \frac{\partial^2 h}{\partial \alpha_{ij}^n \partial T} \dot{\alpha}_{ij}^n + \rho \frac{\partial h}{\partial \alpha_{ij}^n} \dot{\alpha}_{ij}^n \\
 & = -q_{i,i} + \rho \dot{r}
 \end{aligned} \tag{36}$$

so that substitution of (15) and (18) into the above will give

$$\begin{aligned}
 & \rho \frac{\partial h}{\partial \alpha_{ij}^1} \dot{\alpha}_{ij}^1 - \rho T \frac{\partial^2 h}{\partial \alpha_{ij}^1 \partial T} \dot{\alpha}_{ij}^1 - T \frac{\partial \sigma_{ij}}{\partial T} \dot{\epsilon}_{ij} - \rho T \frac{\partial^2 h}{\partial T^2} \dot{T} \\
 & - (k_{ij} T_{,j})_{,i} - \rho \dot{r} = 0
 \end{aligned} \tag{37}$$

Substituting (20) into the above and utilizing (26) through (29) gives

$$\begin{aligned}
 & - \sigma_{ij} \dot{\epsilon}_{ij}^I + \rho_{ijkl} \beta_{kl} T (\dot{\epsilon}_{ij} - \dot{\epsilon}_{ij}^I) \\
 & + \rho C_v \dot{T} - (k_{ij} T_{,j})_{,i} - \rho \dot{r} = 0
 \end{aligned} \tag{38}$$

where $C_v \equiv \partial^2 h / \partial T^2$ is the specific heat at constant volume. The above is the coupled heat conduction equation for anisotropic thermoviscoplastic media. Note that for an elastic material $\dot{\epsilon}_{ij}^I = 0$ and the above reduces to the coupled heat conduction equation for linear thermoelastic media. Since terms 1 and 2 could be large even under non-inertial conditions, they should be considered carefully in inelastic problems.

In the case of uniaxial stress states the inelastic coupling term reduces to $\sigma \dot{\epsilon}^I$, which is the rate of hysteretic energy loss, as shown in the cyclic stress-strain curve in Fig. 1. As pointed out by Taylor and Quinney [1934],

not all of this energy is transformed into heat. For example, some mechanical energy may be lost to dislocation rearrangement, phase change or microfracture processes. Thus, Lee [1969] has proposed that the inelastic loss term should be modified to

$$\eta \sigma_{ij} \dot{\epsilon}_{ij}^I \quad (39)$$

where $\eta \leq 1$ is a positive scalar function of inelastic deformation. Similar expressions have been proposed by Lehmann [1979], Raniechi and Sawczuk [1973], Mroz and Raniechi [1976] and Nied and Batterman [1972]. However, due to the experimental difficulties encountered in measuring such small energy losses, this remains an open issue at this time. Since for stable materials the term in equation (39) is never negative, setting $\eta=1$ will slightly overestimate the predicted temperature.

For the case where the material is initially isotropic and viscoplastically incompressible ($\dot{\epsilon}_{kk}^I=0$), equation (38) reduces to

$$kT_{,ij} = \rho C_V \dot{T} + \rho \dot{r} + (3\lambda + 2\mu) B T_0 \dot{\epsilon}_{kk} - \eta \sigma_{ij} \dot{\epsilon}_{ij}^I \quad (40)$$

Thus, it can be seen that whereas for the elastic case ($\dot{\epsilon}_{ij}^I=0$) all thermomechanical coupling in isotropic materials results from bulk deformations, heating can occur in shear in inelastic media.

One can now briefly review the thermoviscoplastic boundary value problem for the case of infinitesimal deformations. The following state variables: σ_{ij} , ϵ_{ij} , T , u_i , and α_{ij}^η , or $16+9n$ variables are sought. The variables u , s , h and q_i are not normally included in this list since they need not be determined in order to perform stress analysis. To obtain these

16 + 9n variables the following equations are utilized:

1) conservation of linear momentum

$$\sigma_{ji,j} + \rho f_i = \rho \ddot{u}_i \quad (41)$$

2) strain-displacement equations

$$\epsilon_{ij} = \frac{1}{2} (u_{i,j} + u_{j,i}) \quad (42)$$

3) stress-strain-temperature relations

$$\sigma_{ij} = \sigma_{ij}^R + D_{ijkl} [\epsilon_{kl} - \epsilon_{kl}^I - \beta_{kl} (T - T_0)] \quad (43)$$

4) ISV evolution laws

$$\dot{\alpha}_{ij}^n = \alpha_{ij}^n(\epsilon_{kl}, T, g_k, \alpha_{kl}^\mu, \dot{\alpha}_{kl}^\mu) \quad (44)$$

5) conservation of energy

$$-\sigma_{ij} \dot{\epsilon}_{ij}^I + D_{ijkl} \beta_{kl} T (\dot{\epsilon}_{ij} - \dot{\epsilon}_{ij}^I) + \rho C_v \dot{T} - (k_{ij} T_{,j})_{,i} - \rho \dot{r} = 0 \quad (45)$$

Thus, these are a total of 16+9n equations. The variables ρ , f_i , T_0 , r , and σ_{ij}^R are specified data, and D_{ijkl} , β_{kl} , α_{ij}^n , k_{ij} , and C_v are input material properties. The above equations, together with appropriate boundary conditions, constitute a well-posed boundary value problem. Unfortunately, α_{ij}^n may be very difficult to construct based on experimental observation, and the introduction of nonlinearities via α_{ij}^n causes solutions to be very difficult to obtain analytically.

APPLICATIONS OF THE THEORY

Few applications of the theory have been reported in the literature for the case where inelastic material behavior occurs [Oden et al., 1973; Cernocky and Krempf, 1980; Argyris et al., 1981; Nicholson, 1984; Allen, 1985, 1986; Allen and Haisler, 1986; Van der Lugt, 1986; Hsu, 1986; Banas et al., 1987; Ghoneim, 1986; Ghoneim and Dalo, 1987; Ghoneim and Matsuoka, 1987]. This is due in part to the fact that the elastic and inelastic coupling terms in equation (45) are in many cases for all practical purposes negligible. When this occurs, the problem is said to be one-way coupled, since equation (45) becomes a single equation in temperature which can be solved independently of the mechanical problem and the resulting temperature field can be utilized as input to equations (43) and (44).

There is a second reason that few applications of the theory have been reported: because they are extremely difficult to work with. This is due to a number of reasons, not the least of which is that there are several sources of nonlinearity in the resulting problem. The most common nonlinearities occur in the ISV evolution laws (44), and these are often numerically stiff for polycrystalline metals. Additional sources of nonlinearity may arise from radiation boundary conditions and large deformations. In fact, the nonlinearities appear to preclude analytic (closed-form) solutions to the two-way coupled problem in all cases reported to date, with the exceptions of Lee et al. [1980], Reddy [1976], and Mukherjee [1973], and in these three cases the applications are to linear viscoelastic media. Thus, the two-way coupled nonlinear problems lends itself well to computational solutions, in particular the finite element method. The balance of the paper then deals with this procedure and results obtained using this approach.

Chronologically, the first computational algorithm to appear in the open literature was reported by Oden et al. [1973]. While the authors do not elucidate in great detail the algorithm used, they do introduce a time marching scheme which allows partitioning of the coupled equations during each time step. This procedure, which appears to be used by most subsequent researchers, bears further discussion here.

In the method proposed by Oden et al. [1973] the governing field equations are first recast in a weakened variational form and applied over a sub-domain denoted as an element. It is then assumed that the coupling terms in equations (45) are negligible over a small time increment, and this term is dropped from the variational heat equation. Orthogonal basis functions are then introduced as an approximation for the displacement and temperature fields in each element during the time increment. The resulting equations are of the form:

$$[M]\{\ddot{U}\} + [K]\{\Delta U\} = \{F\} + \{F^I\} + \{F^T\} \quad (46)$$

and

$$[K_T]\{T\} + [C]\{\dot{T}\} = \{Q\} + \{Q^I\} \quad (47)$$

Equations (46) are the mechanical equations and equations (47) are the thermal equations. The ordinary time derivatives in equations (46) and (47) are obtained using finite differencing. The coupling enters the mechanical equations via $\{F^T\}$, which depends on the temperature field. Conversely, the coupling enters (47) via $\{Q^I\}$, which depends on ϵ_{ij}^I . On each time step this term is initially assumed to be zero and the resulting deformations are

calculated. An iterative procedure is then used during the time step to account for $\{Q^I\}$.

Unfortunately, because the numerical results obtained by the authors do not contain a comparison of two-way coupled and one-way coupled results, no results are reviewed here. However, the approach utilized in this paper has been utilized by most succeeding authors.

Cernocky and Krempl proposed a coupled theory in 1980, and while the reported work considers only spatially invariable responses, it does represent the first attempt to utilize a recently developed rate dependent viscoplastic constitutive model in a two-way coupled analysis.

Argyris et al. [1981] produced perhaps the most exhaustive study of computational schemes for solving the two-way coupled problem. Like Oden, the authors utilize the semi-discretized finite element method for both the thermal and mechanical analyses. Furthermore, they utilize partitioning, with the thermal analysis performed first on each time step and then utilized to approximate the mechanical response. Although they point out that for weakly coupled problems no interaction is required on each step, they include in their algorithm an iterative procedure for strongly coupled applications.

The authors discuss in some detail the importance of the so-called " β - effect," in which the effect of thermal contraction causes a perceived "heating effect." This effect can be seen by first defining the elastic strain tensor as follows:

$$\epsilon_{ij}^E = \epsilon_{ij} - \epsilon_{ij}^I - \beta_{ij}(T - T_0) \quad (48)$$

Thus, for an inelastically incompressible material contracting the above and rearranging results in

$$\epsilon_{kk} = \epsilon_{kk}^E + \beta_{KK}(T - T_0) \quad (49)$$

Differentiating the above in time and substituting into (40) gives

$$kT_{,ij} = \rho \hat{C} \dot{T} + \rho \dot{r} + (3\lambda + 2\mu) \alpha T_0 \epsilon_{kk}^E - n \sigma_{ij} \dot{\epsilon}_{ij}^I \quad (50)$$

where

$$\hat{C} \equiv \rho C_V \left[1 + \frac{3(3\lambda + 2\mu) \beta^2 T_0}{\rho C_V} \right] \quad (51)$$

Thus, the thermal expansion effect can cause the apparent heat capacity \hat{C} to be magnified considerably. The authors advise that this term should be handled in the form described by equation (50) because the form given in equation (45) can lead to numerical instability of the time marching scheme.

An interesting numerical result is obtained in the paper by Argyris et al. [1981]. The time marching iterative scheme described above is applied to a thick-walled cylinder that is pressurized with an internal pressure $p_i = 200 \text{ N/mm}^2$ and subsequently quenched from an initial temperature $T = 320^\circ\text{C}$ to a final temperature $T = 20^\circ\text{C}$. A simplified model is used for the ISV evolution laws. Temperature, radial displacement, and equivalent stress histories are shown at the outside wall in Figs. 2 through 4. Similar results are obtained at the inside wall. It is interesting to note that the coupled thermoviscoplastic result is significantly different at long times from the uncoupled result, thus indicating the importance of including two-way coupling in relatively slow processes such as are found in this example. However, the authors point out that a substantial part of the coupling results from the β effect.

Beginning in 1985, Allen published a series of three papers dealing with thermomechanical coupling in viscoplastic uniaxial bars. Using the viscoplastic constitutive theory proposed by Bodner and Partom [1975], he predicts the stress in a uniaxial bar as shown in Fig. 5 for the input strain history shown. Since the uniaxial bar is assumed to be adiabatic, the response is spatially invariable, and the predicted temperature shown in Fig. 6 represents an upper bound of the actual temperature for $n=1$ [Allen, 1985].

Recognizing that there is significant heat loss in a uniaxial bar, Allen [1986] produced a one-dimensional fully coupled finite element model for the uniaxial bar problem. The spatial discretization was accomplished by assuming a second order displacement function in each element, along with a first order temperature field. This insured numerical stability and accuracy via compatibility of the total and thermal strains in each element. Unlike the computational approach taken previously [Oden et al. 1973; Argyris et al. 1981], the author chose to retain full coupling in the governing equations so that the resulting finite element equations are of the form

$$[K] \left\{ \frac{\Delta U}{\Delta T} \right\} = \{\Delta F\} \quad (52)$$

Thus, unlike equations (46) and (47), the temperature and displacements occur on the left-hand side of the equations. Unfortunately, this procedure results in a highly complex algorithm which is sufficiently complicated that existing uncoupled codes cannot be utilized. For example, the stiffness matrix $[K]$ is not symmetric. The author found this approach cumbersome and does not recommend it, especially for multidimensional problems.

Using the above computational scheme Allen compared results for a fully insulated uniaxial bar to one imbedded in massive grips at 1005°K. The

resulting predicted temperatures for two different monotonic strain rates are shown in Figs. 7 and 8 [1986]. As expected, the non-adiabatic temperature change is bounded by the adiabatic result. A typical plot of temperature vs. axial location in the bar, as shown in Fig. 9, demonstrates that the temperature gradient occurs in a very small boundary layer near the grip. The final result in this paper, shown in Figs. 10 and 11, is for the case of a uniaxial bar subjected to low cycle fatigue. It is found that, whereas the temperature rise is approximately 3.7°K for each cycle in the adiabatic case, the bar with fixed temperature at the ends heats up only about 1.0°K per cycle, thus indicating that flux of heat at the boundary can significantly diminish the effect of thermomechanical coupling.

In the third paper of the series, Allen and Haisler [1989] included the effects of radiation boundary conditions on the cylindrical surface of the bar. They determined that inspite of the significant heat loss provided by radiation boundary conditions, an aluminum bar subjected to cyclic loading as shown in Figs. 12 and 13 experiences substantial heating both with anodized surface (CASE II) and when painted with a high emissivity coating (CASE I). The authors concluded from this research that material inelasticity in large space structures should be considered carefully as a means of passive damping because it is difficult to dissipate heat generated via thermomechanical coupling.

Recent results have been reported also by Ghoneim and coworkers [Ghoneim, 1986; Ghoneim and Matsuoka, 1987, Ghoneim and Dalo, 1987]. Ghoneim uses essentially the same finite element discretization procedure as that developed by Oden. Using a simplified viscoplasticity model he obtains results for the uniaxial bar problem [Ghoneim and Matsuoka, 1987] similar to that previously obtained by Allen. However, he goes a step further by producing a two-

dimensional prediction of the response of a flat coupon during a compression test. Figure 14 depicts effective stress and temperature contours in one quadrant of the specimen for successive strains $\epsilon=0.3, 0.6, 0.9$ and 1.2% , respectively (Contour lines 1, 2, 3,... are 300, 350, 400,...MPa for the stress and 0.0, 0.5, 1.0, 1.5°K ,... for the temperature, respectively).

Ghoneim [1986] modelled a thick-walled cylinder similar to that previously considered by Argyris et al. [1981]. However, Ghoneim considers the response of the cylinder to an instantaneous thermal pulse. Since the time duration is very short, he points out that the predicted change in temperature is strictly due to thermomechanical coupling. Figures 15 and 16 show the stress history and temperature history at the inner surface of the cylinder (σ^E is the effective stress). The large difference between the temperature predicted for the elastic and viscoplastic cases is remarkable.

The final result to be discussed herein is due to Hsu [1986]. He uses essentially the same fully coupled algorithm as that reported by Allen. However, he has developed a two-dimensional finite element code using four-node quadrilateral isoparametric elements. He models one quarter of a rod in uniaxial tension and considers the temperature rise in the bar for a monotonic load and unload sequence. As shown in Fig. 17, he reports the effects caused by the η factor discussed in equation (39) ($\lambda=1-\eta$). As expected, the predicted temperature rise decreases with increasing λ .

CONCLUSION

Significant advances in the theory and analysis of thermomechanical coupling have been made in this century. However, although thermomechanical coupling is now a well-known phenomenon in inelastic solids, several issues remain open at this time. Among these are:

- 1) the thermodynamics of nonequilibrium processes have not yet been clearly identified;
- 2) the relative contribution of the η factor is not yet resolved;
- 3) computational algorithms, though proposed, have not been studied for a broad array of problems; and
- 4) the important issue of when coupling can be neglected has not been resolved.

For these reasons, further research would appear to be fruitful on this subject.

ACKNOWLEDGMENT

The author gratefully acknowledges the support provided for this research by the Air Force Office of Scientific Research under contract no. F49620-86-K-0016.

REFERENCES

- Allen, D.H., "A Prediction of Heat Generation in a Thermoviscoplastic Uniaxial Bar," Int. J. Solids Structures, Vol. 21, No. 4, pp. 325-342, 1985.
- Allen, D.H., "Predicted Axial Temperature Gradient in a Viscoplastic Uniaxial Bar Due to Thermomechanical Coupling," Int. J. Num. Methods Engrg., Vol. 23, No. 5, pp. 903-917, 1986.
- Allen, D.H. and Haisler, W.E., "Predicted Temperature Field in a Thermomechanically Heated Viscoplastic Space Truss Structure," J. Spacecraft and Rockets, Vol. 23, No. 2, pp. 178-183, 1986.

Argyris, J.H., Vaz, L.E., and William, K.J., "Integrated Finite Element Analysis of Coupled Thermoviscoplastic Problems," J. Thermal Stresses, Vol. 4, pp. 121-153, 1981.

Banas, A., Hsu, T.R., and Sun, N.S., "Coupled Thermoelastic-Plastic Stress Analysis of Solids by Finite Element Method," J. Thermal Stresses, Vol. 10, pp. 319-344, 1987.

Biot, M.A., "Thermoelasticity and Irreversible Thermodynamics," J. Applied Physics, Vol. 27, No. 3, pp. 240-254, 1956.

Bodner, S.R. and Partom, Y. "Constitutive Equations for Elastic-Viscoplastic Strain-Hardening Materials" J. Appl. Mech, Vol. 42, pp. 385-389, 1975.

Boley, B.A. and Weiner, J.H., Theory of Thermal Stresses, Wiley, New York, 1960.

Cauchy, A., "Recherches Sur L'Equilibre Et Le Mouvement Interieur Des Corps Solides Ou Fluides, Elastiques Ou Non Elastiques," Bulletin...Philomatique, pp. 9-13, 1823.

Caratheodory, C., "Untersuchungen uber die Grundlagen der Thermodynamik," Math. Annalen, Vol. 67, pp. 355-386, 1909.

Cernocky, E.P. and Krempl, K., "A Theory of Thermoviscoplasticity Based on Infinitesimal Total Strain," Int. J. Solids Structures, Vol. 16, pp. 724-741, 1980.

Coleman, B.D., "Thermodynamics of Materials with Memory," Archive for Rational Mechanics and Analysis, Vol. 17, pp. 1-46, 1964.

Coleman, B.D. and Gurtin, M.E., "Thermodynamics with Internal State Variables," Journal of Chemical Physics, Vol. 47, pp. 597-613, 1967.

Coleman, B.D. and Mizel, V.J., "Thermodynamics and Departures from Fourier's Law of Heat Conduction," Arch. Rat. Mech. Anal., Vol. 13, pp. 245-261, 1963.

Coleman, B.D. and Noll, W., "The Thermodynamics of Elastic Materials with Heat Conduction and Viscosity," Arch. Rat. Mech. Anal., Vol. 13, p. 167, 1963.

Dillon, O.W., Jr., "An Experimental Study of the Heat Generated in Aluminum Rods Undergoing Torsional Oscillations," J. Mech. Phys. Solids, Vol. 10, pp. 224-235, 1962.

Dillon, O.W., Jr., "Coupled Thermoplasticity," J. Mech. Phys. Solids, Vol. 11, pp. 21-33, 1963.

Dillon, O.W., Jr., "Temperature Generated in Aluminum Rods Undergoing Torsional Oscillations," J. Appl. Mech., Vol. 33, pp. 3100-3105, 1962.

Dillon, O.W., Jr., "The Heat Generated During the Torsional Oscillations of Copper Tubes," Int. J. Solids Struct., Vol. 2, pp. 181-204, 1966.

Lehmann, Th., "Coupling Phenomena in Thermoplasticity," Nucl. Engng. & Des., Vol. 57, pp. 323-332, 1980.

Lehmann, Th., "Coupling Phenomena in Thermoplasticity," Trans. 5th Int. Conf. Structure Mech. Reactor Technol., Berlin, Paper L1/1, 1979.

Lehmann, Th., "On the Theory of Large, Non-Isothermic, Elastic-Plastic and Elastic-Visco-Plastic Deformation," Arch. Mech., Vol. 29, No. 3, pp. 393-409, 1977.

Lehmann, Th., "Some Thermodynamic Considerations of Phenomenological Theory Non-Isothermal Elastic-Plastic Deformations," Arch. Mech., Vol. 24, pp. 975-989, 1972.

Lubliner, J., "On the Thermodynamic Foundation of Non-Linear Solid Mechanics," Intl. J. Non-Linear Mech., Vol. 7, pp. 237-254, 1972.

Mroz, Z. and Raniecki, B., "On The Uniqueness Problem in Coupled Thermoplasticity," Int. J. Engng. Sci., Vol. 14, pp. 211-221, 1976.

Mukherjee, S., "Variational Principles in Dynamic Thermoviscoelasticity," Int. J. Solids Structures, Vol. 9, pp. 1301-1316, 1973.

Nagahi, S., Cui, W., and Abe, T., "Coupled Thermo-Deformation Analysis of Strain-Rate Dependent Materials with Work Hardening," JSME International Journal, Series I, Vol. 32, No. 1, pp. 88-93, 1989.

Navier, "Memoire sur les Lois de l'Equilibre et du Mouvement des Corps Solides Elastiques," Memoire...de l'Institut, Vol. 7, pp. 375-393, 1827.

Neumann, F.E., Vorlesungen uber die Theorie der Elasticitat der Festen Korper und des Lichtathers, Leipzig, pp.107-120, 1885.

Nicholson, D.W., "Adiabatic Temperature Rise in a Viscoplastic Rod under Impact," Mech. Res. Commun., Vol. 11, No. 5, pp. 317-329, 1984.

Nied, H.A. and Batterman, S.C., "On The Thermal Feedback Reduction of Latent Energy in the Heat Conduction Equation", Material Sci. Engrg., Vol. 9, pp. 243-245, 1972.

Oden, J.T., Bhandari, D.R., Yagawa, G., and Chung, T.J., "A New Approach to the Finite-Element Formulation and Solution of a Class of Problems in Coupled Thermoviscoplasticity of Crystalline Solids," Nuclear Engr. Des., Vol. 24, pp. 420-430, 1973.

Olszak, W. and Perzyna, P., "Thermal Effects in Viscoplasticity," IUTAM Symposium, East Kilbride, pp. 206-212, Springer-Verlag, New York, 1968.

Prandtl, L., "Spannungsverteilung in Plastischen Korpern," Proc. 1st Int. Congr. Appl. Mech., p. 43, 1924.

Prigogine, I., Etude Thermodynamique des Phenomenes Irreversibles, Desoor, Liege, 1947.

Raniechi, B. and Sawczuk, A., "Problems of Thermoplasticity," Nucl. Engng. & Des., Vol. 24, pp. 1-55, 1973.

Rebelo, U. and Kobayashi, S., "A Coupled Analysis of Viscoplastic Deformation and Heat Transfer-I, II," Int. J. Mech. Sci., Vol. 22, pp. 699, 1980.

Reddy, J.N., "Variational Principles for Linear Coupled Dynamics Theory of Thermoviscoelasticity," Int. J. Engng. Sci., Vol. 14, pp. 605-616, 1976.

Schapery, R.A., "Application of Thermodynamics to Thermomechanical, Fracture, and Birefringent Phenomena in Viscoelastic Media," Journal of Applied Physics, Vol. 35, pp. 1451-1465, 1964.

Schapery, R.A., "Effect of Cyclic Loading on the Temperature in Viscoelastic Media with Variable Properties," AIAA Journal, Vol. 2, pp. 827-835, 1964.

Tauchert, T.R., "The Temperature Generated During Torsional Oscillation of Polyethylene Rods," Int. J. Engng. Sci., Vol. 5, pp. 353-365, 1967.

Tauchert, T.R. and Afzal, S.M., "Heat Generated During Torsional Oscillations of Polymethylmethacrylate Tubes," J. Appl. Phys., Vol. 38, pp. 4568-4572, 1967.

Taylor, G.I. and Quinney, H., "The Latent Energy Remaining in a Metal After Cold Working," Proc. Royal Society, Vol. 143, pp. 307-326, 1934.

Van der Lugt, J. and Huetink, J., "Thermal Mechanically Coupled Finite Element Analysis in Metal-Forming Processes," Comput. Methods Appl. Mech. Eng., Vol. 54, pp. 145-160, 1986.

Voigt, W., Lehrbuch der Krystallophysik, Teubner, Leipzig, 1910.

Von Mises, R., "Mechanik der Festen Körper im Plastisch Deformablen Zustand," Göttingen Nachr. Math. Phys., Vol. K1, p. 582, 1913.

Fig. 1. Hysteretic Strain Energy Loss During a Cyclic Uniaxial Test

Fig. 2. Temperature History at the Inside Wall of Quenched Cylinder
(Courtesy of Hemisphere Publishing)

Fig. 3. Radial Displacement History at the Inside Wall of Quenched Cylinder
(Courtesy of Hemisphere Publishing)

Fig. 4. Equivalent Stress History at the Inside Wall of Quenched Cylinder
(Courtesy of Hemisphere Publishing)

Fig. 5. Stress-Strain Behavior of IN100 at 1005°K (1350°F) Under Cyclic Load with Stress Relaxation (Courtesy of Pergamon Journals Ltd.)

Fig. 6. Predicted Temperature Change for IN 100 at 1005°K (1350°F) Subjected to Cyclic Load History Shown in Fig. 5 (Courtesy of Pergamon Journals Ltd.)

Fig. 7. Predicted Temperature vs. Absolute Strain for Monotonic Deformation Histories ($\dot{\epsilon} = \pm 0.00142 \text{ sec}^{-1}$) (Courtesy of John Wiley & Sons, Ltd.)

Fig. 8. Predicted Temperature vs Absolute Strain for Monotonic Deformation Histories ($\dot{\epsilon} = \pm 0.00142 \text{ sec}^{-1}$) (Courtesy of John Wiley & Sons, Ltd.)

Fig. 9. Temperature vs. Spatial Location for Various Times for Constant Strain Rate $\dot{\epsilon} = 0.00142 \text{ sec}^{-1}$ ($x = 0.3175$ is the midpoint of the bar) (Courtesy of John Wiley & Sons, Ltd.)

Fig. 10. Stress-Strain Curve and Strain Input Curve for Cyclic Load (Courtesy of John Wiley & Sons, Ltd.)

Fig. 11. Temperature Change at $x = L/2$ vs. Time for the Cyclically Loaded Bar Described in Fig. 10 (Courtesy of John Wiley & Sons, Ltd.)

Fig. 12. Cyclic Stress-Strain Curve at $x = L/2$ for Case I Coating Loaded at 5Hz. (Courtesy of American Institute of Aeronautics and Astronautics)

Fig. 13. Temperature vs. Time Curves at $x=L/2$ for Loading at 5Hz (Courtesy of American Institute of Aeronautics and Astronautics)

Fig. 14. The Predicted Stress and Temperature Change Fields for the Compression Test at Different Stages of Loading (Courtesy of Pergamon Journals Ltd.)

Fig. 15. Transient Response of the Radial and Hoop Stresses at the Inner Surface of Thick Walled Cylinder (Courtesy of Hemisphere Publishing)

Fig. 16. Transient Response of the Effective Stress (τ^E) and Temperature at the Inner Surface of Thick Walled Cylinder (Courtesy of Hemisphere Publishing)

Fig. 17. Temperature Rise in the Rod Induced by Applied Mechanical Load (Courtesy of Allen & Unwin, Inc.)

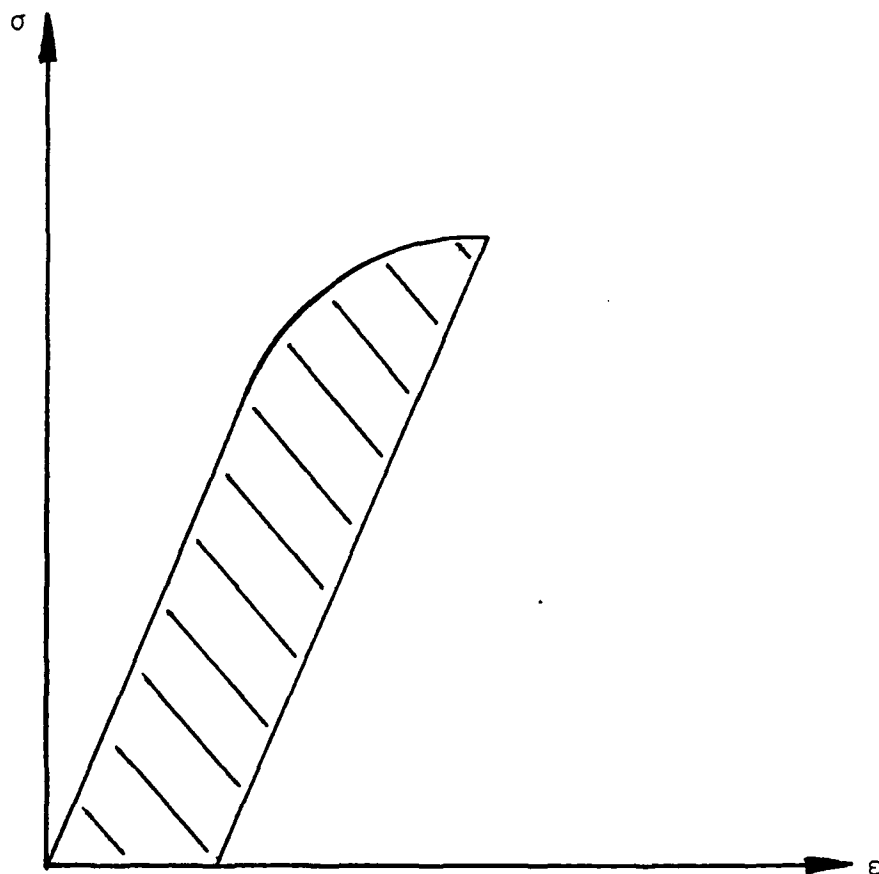


Fig. 1. Hysteretic Strain Energy Loss During a Cyclic Uniaxial Test

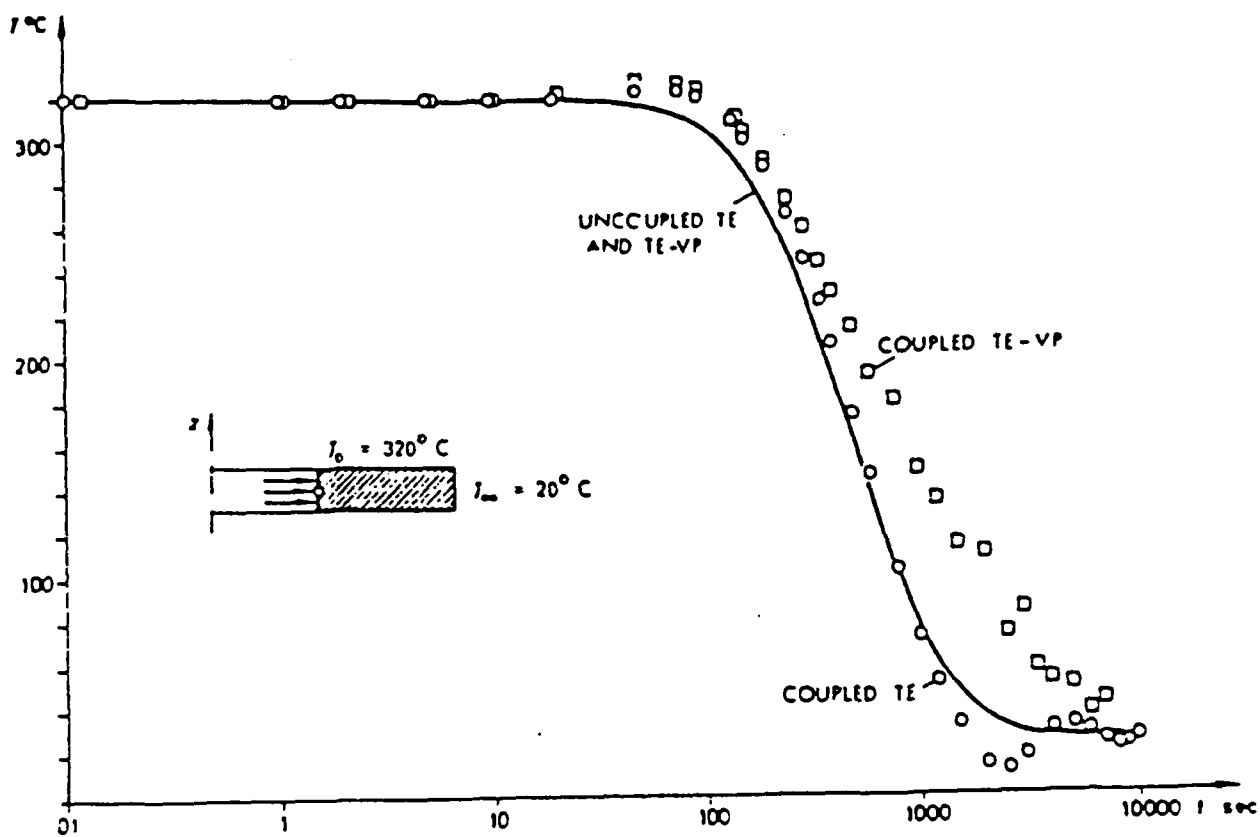


Fig. 2. Temperature History at the Inside Wall of Quenched Cylinder
(Courtesy of Hemisphere Publishing)

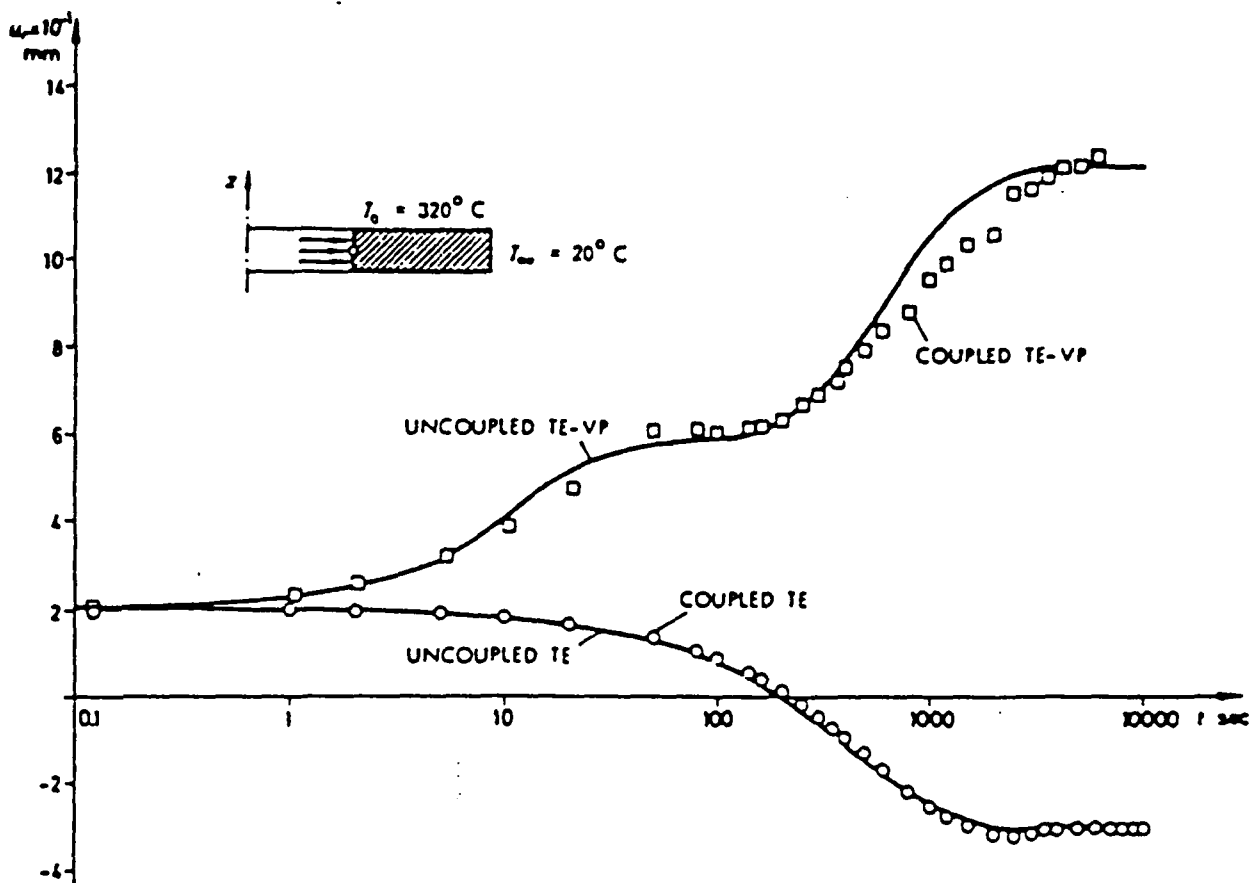


Fig. 3. Radial Displacement History at the Inside Wall of Quenched Cylinder
(Courtesy of Hemisphere Publishing)

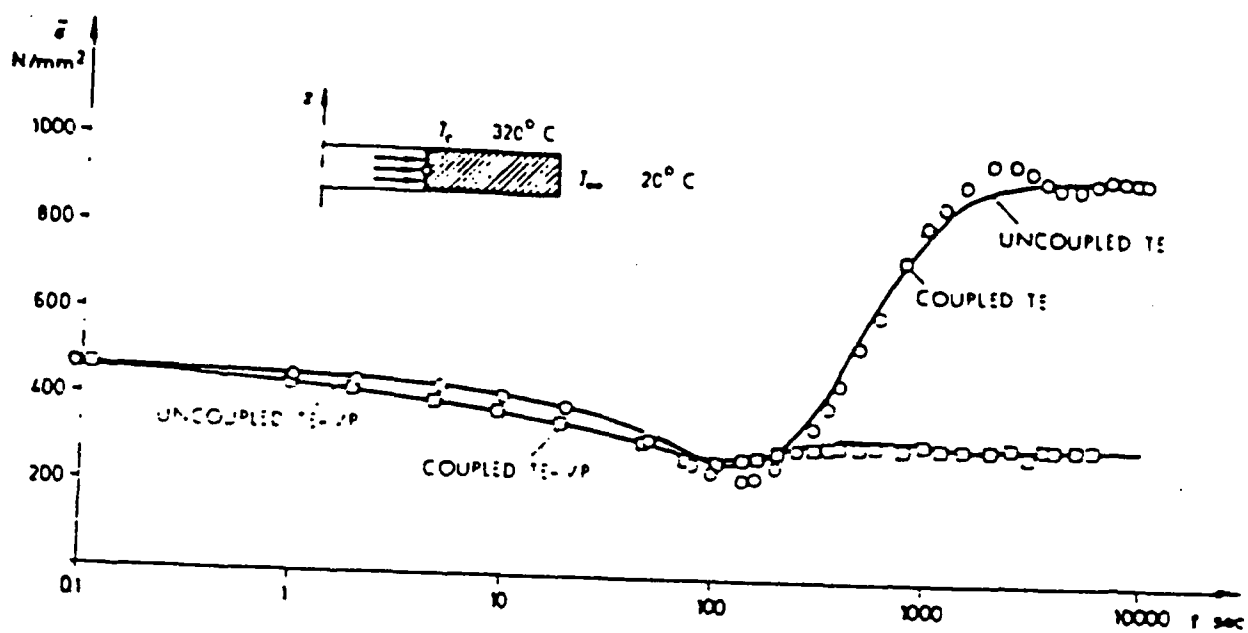


Fig. 4. Equivalent Stress History at the Inside Wall of Quenched Cylinder
(Courtesy of Hemisphere Publishing)

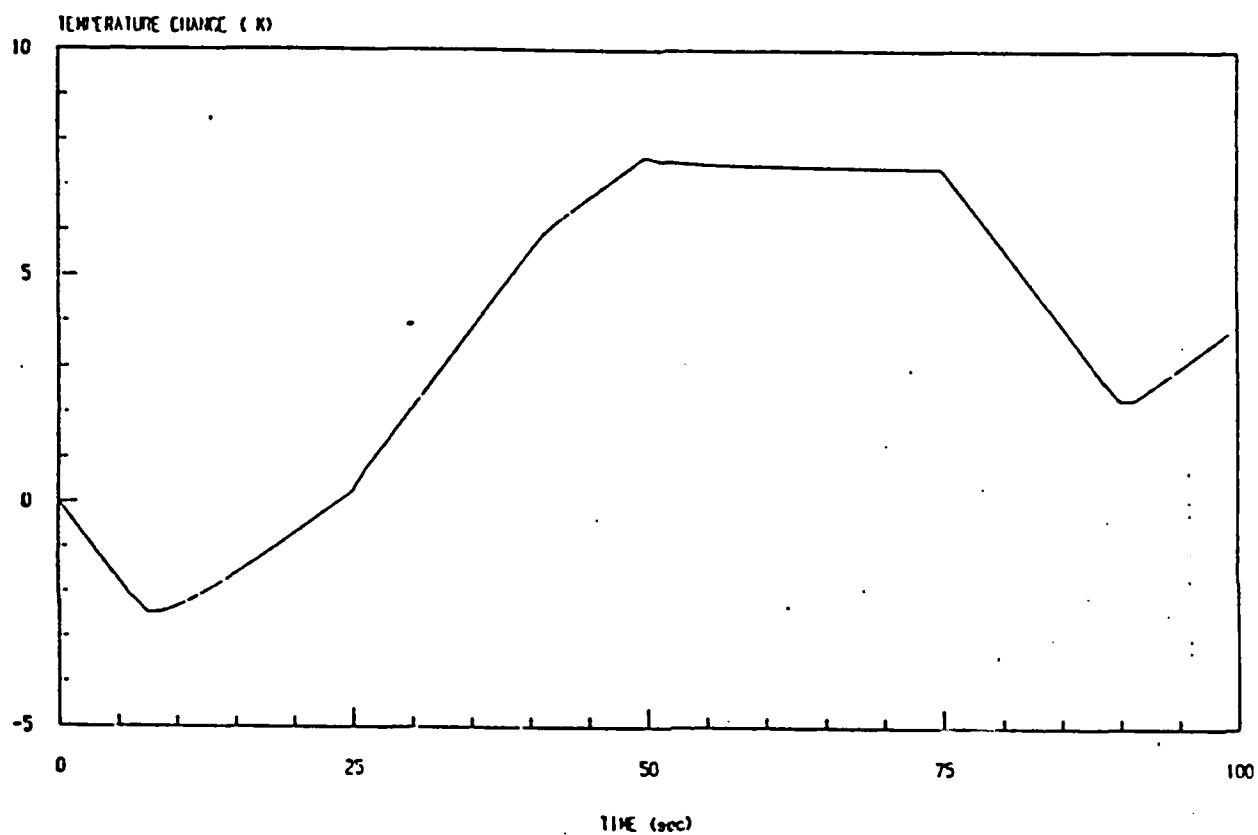


Fig. 6. Predicted Temperature Change for IN 100 at 1005°K (1350°F) Subjected to Cyclic Load History Shown in Fig. 5 (Courtesy of Pergamon Journals Ltd.)

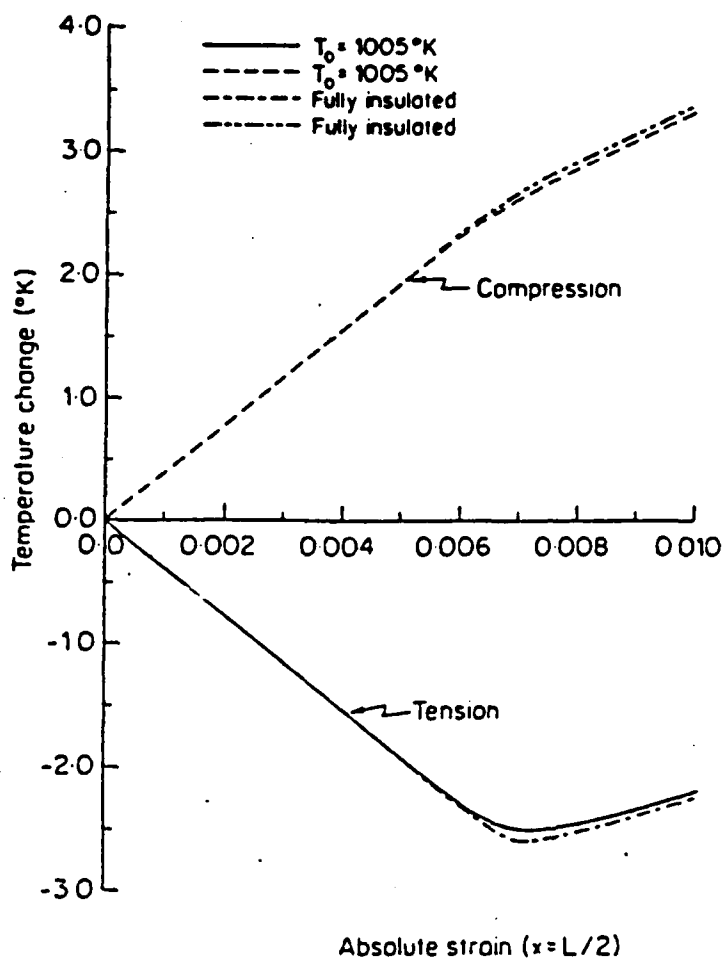


Fig. 7. Predicted Temperature vs. Absolute Strain for Monotonic Deformation Histories ($\dot{\epsilon} = \pm 0.00142 \text{ sec}^{-1}$) (Courtesy of John Wiley & Sons, Ltd.)

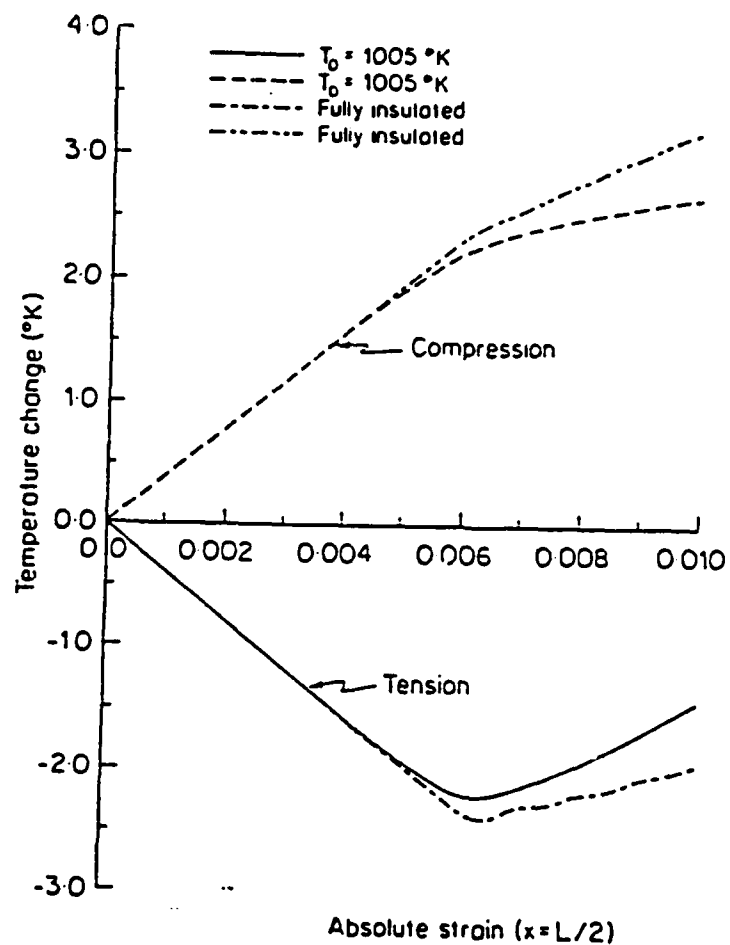


Fig. 8. Predicted Temperature vs Absolute Strain for Monotonic Deformation Histories ($\dot{\epsilon} = \pm 0.000142 \text{ sec}^{-1}$) (Courtesy of John Wiley & Sons, Ltd.)

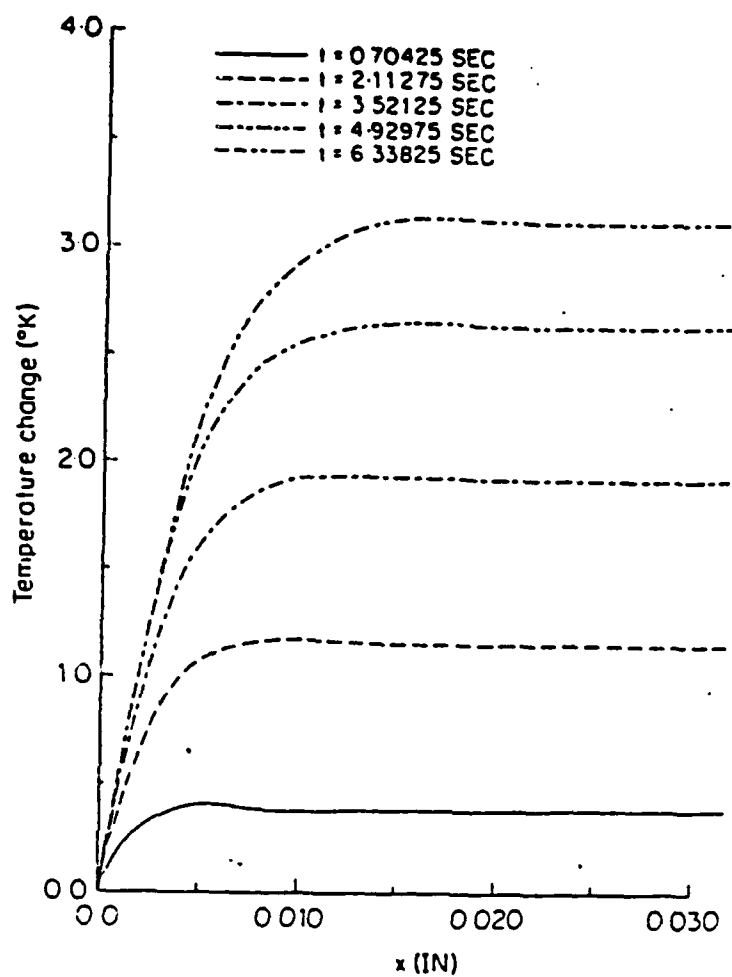


Fig. 9. Temperature vs. Spatial Location for Various Times for Constant Strain Rate $\dot{\epsilon}=0.00142 \text{ sec}^{-1}$ ($x=0.3175$ is the midpoint of the bar) (Courtesy of John Wiley & Sons, Ltd.)

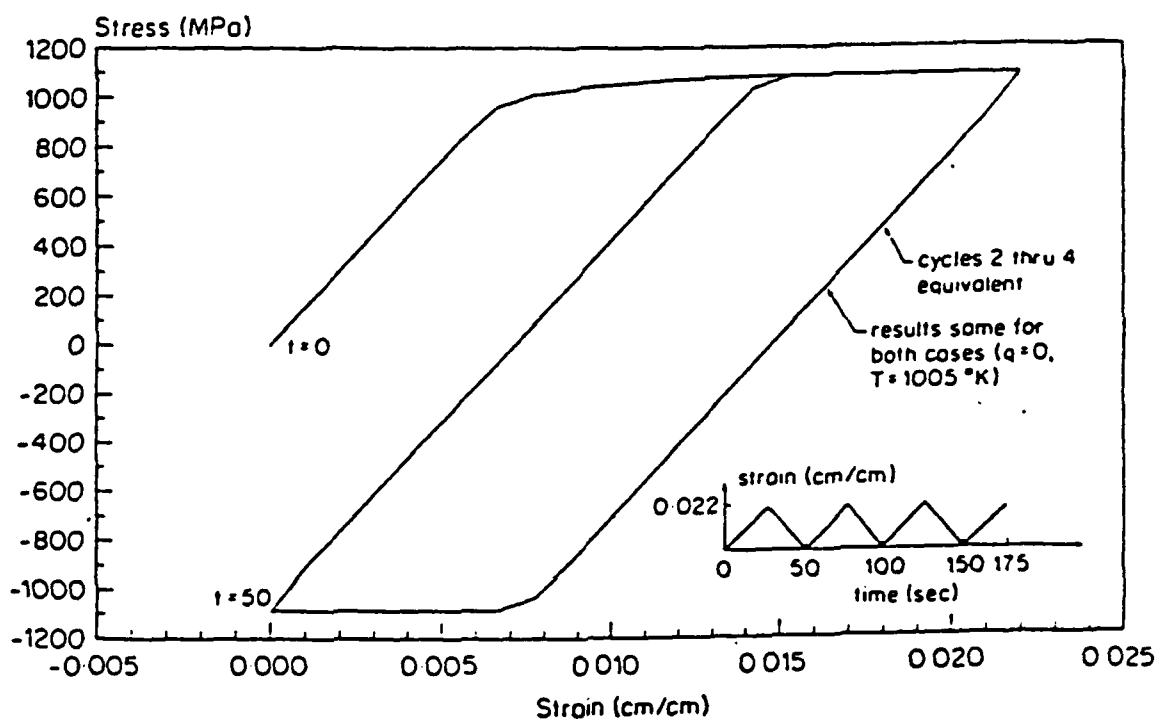


Fig. 10. Stress-Strain Curve and Strain Input Curve for Cyclic Load (Courtesy of John Wiley & Sons, Ltd.)

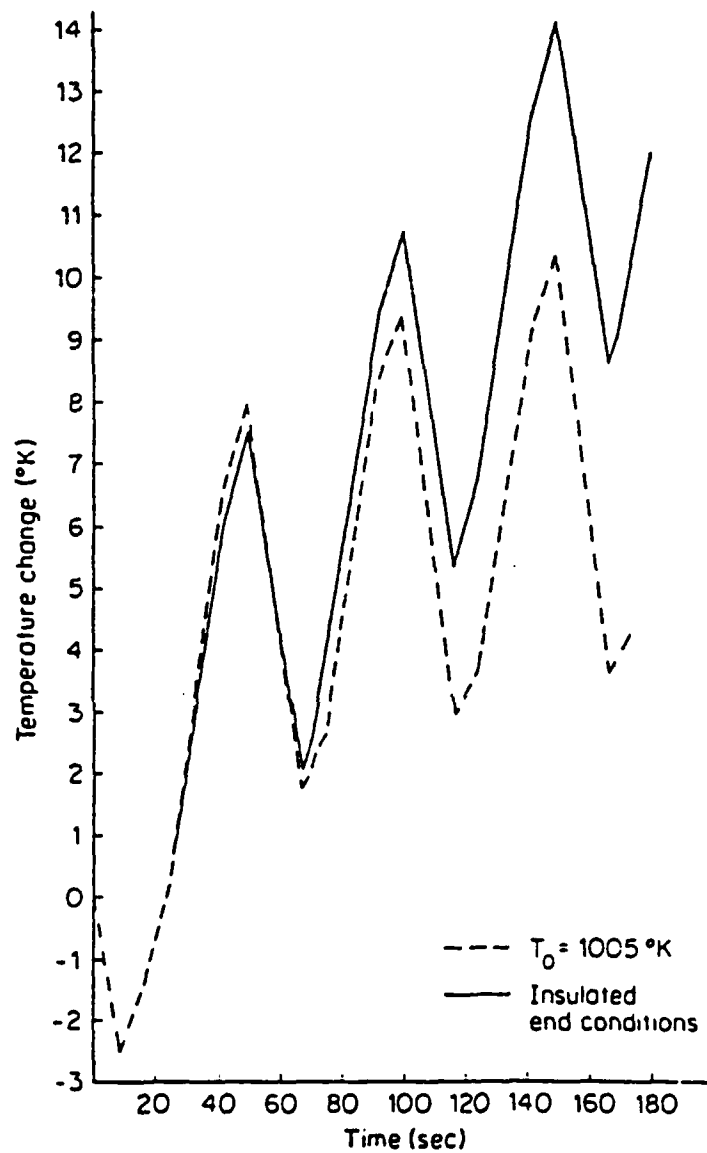


Fig. 11. Temperature Change at $x=L/2$ vs. Time for the Cyclically Loaded Bar Described in Fig. 10 (Courtesy of John Wiley & Sons, Ltd.)

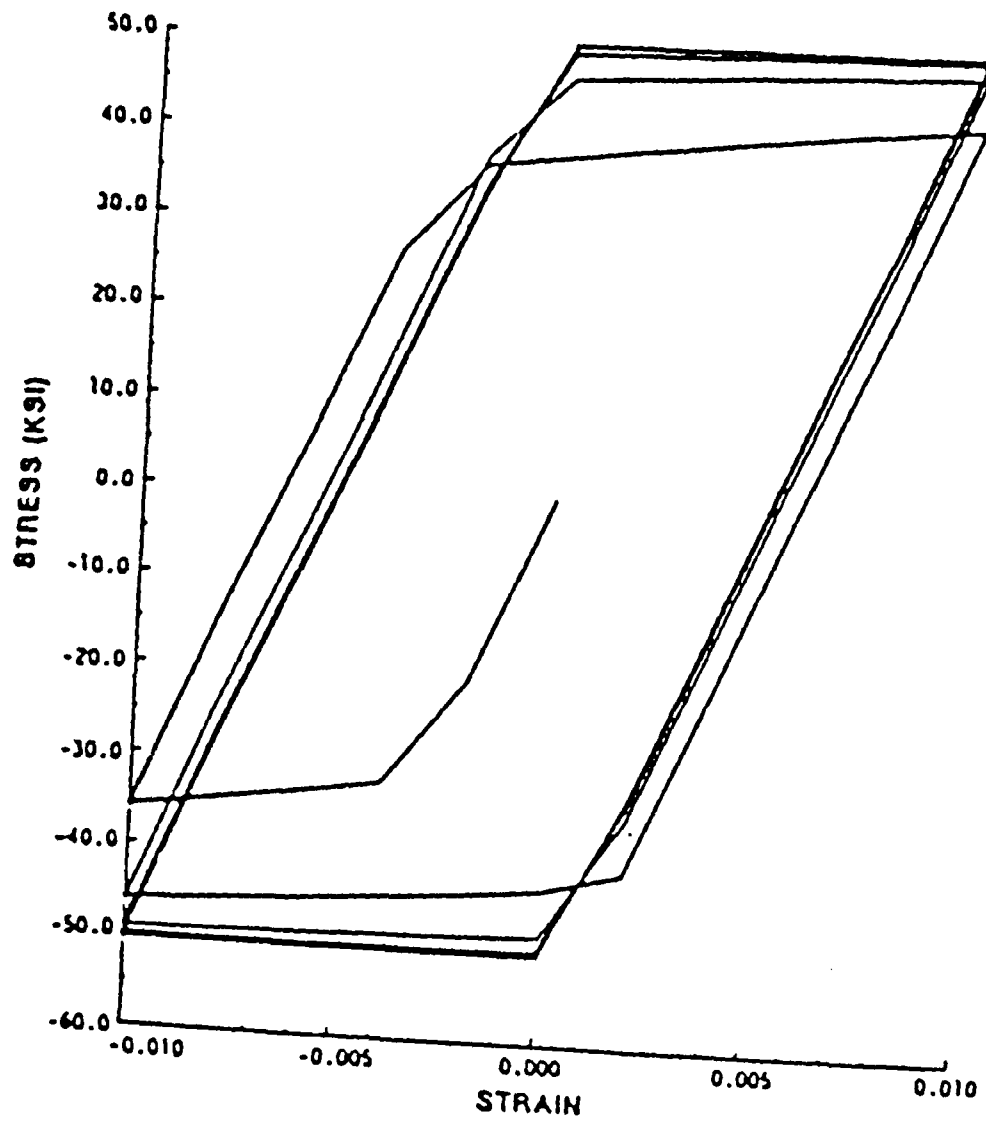


Fig. 12. Cyclic Stress-Strain Curve at $x=L/2$ for Case I Coating Loaded at 5Hz. (Courtesy of American Institute of Aeronautics and Astronautics)

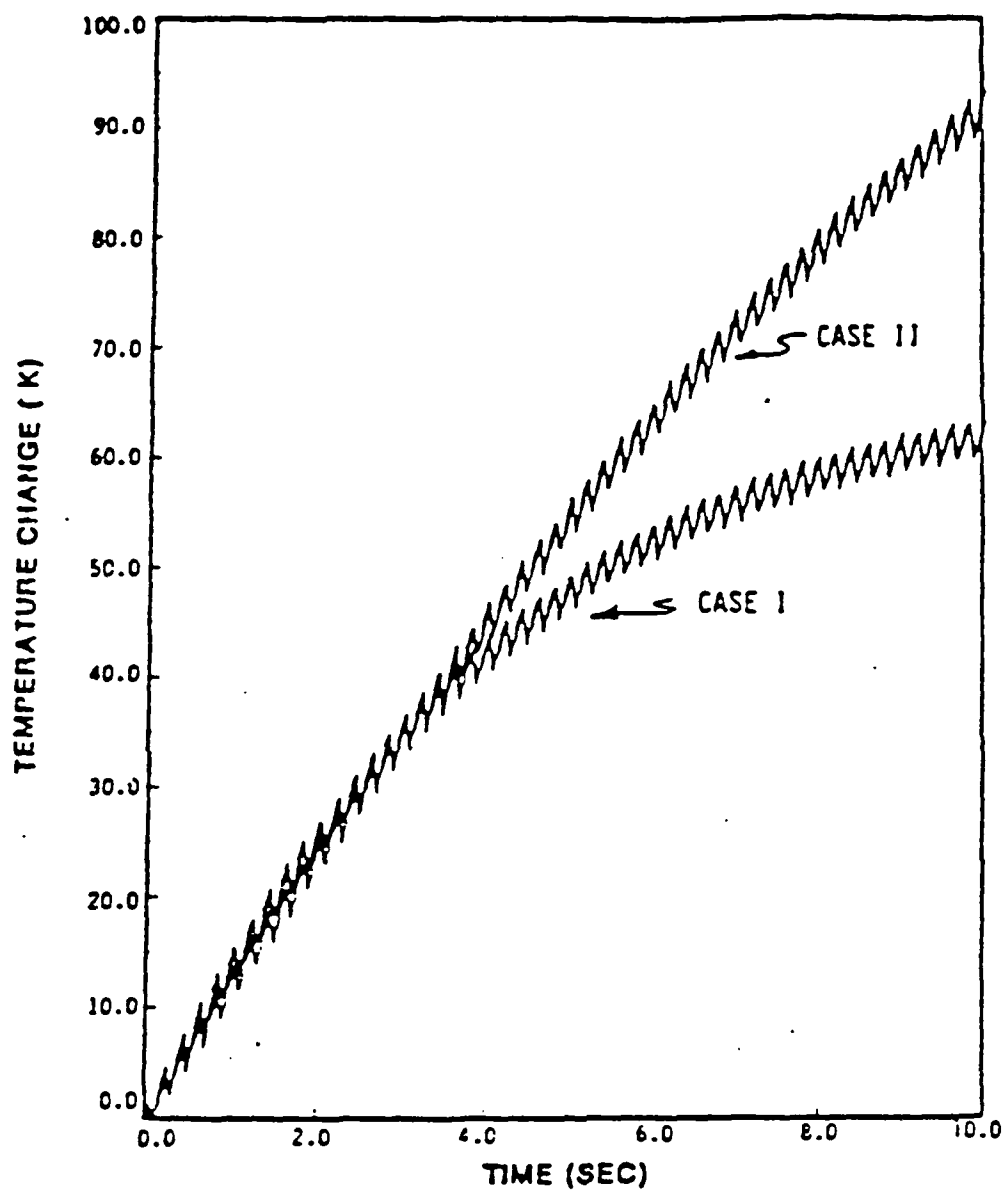
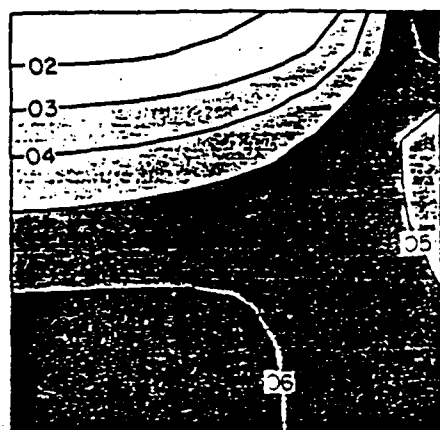
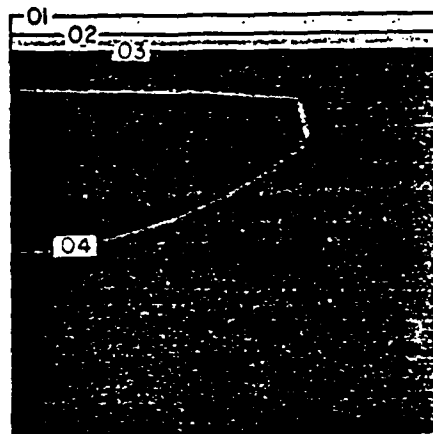


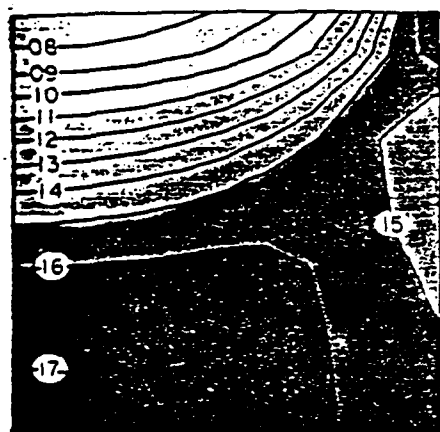
Fig. 13. Temperature vs. Time Curves at $x=L/2$ for Loading at 5Hz (Courtesy of American Institute of Aeronautics and Astronautics)



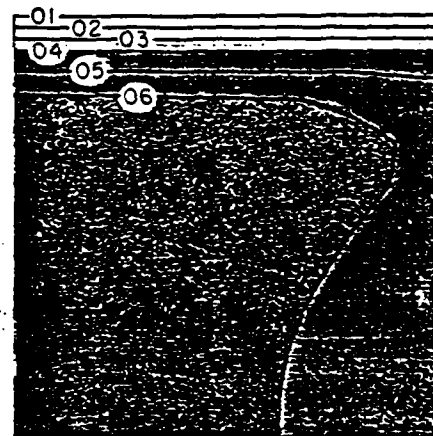
STRESS
(a)



TEMP

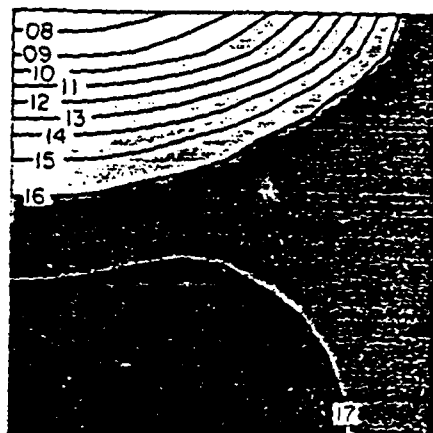


STRESS
(b)

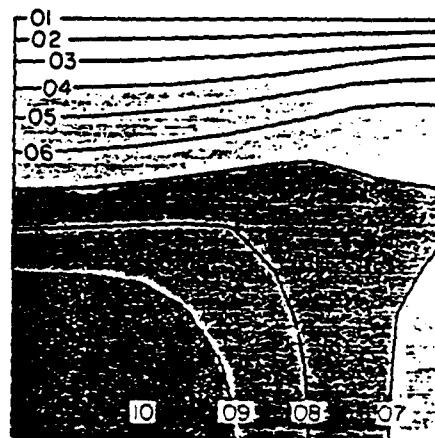


TEMP

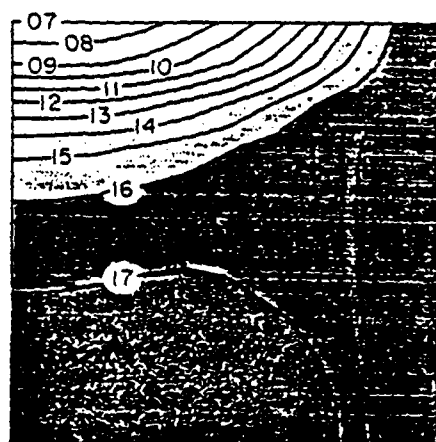
Fig. 14. The Predicted Stress and Temperature Change Fields for the Compression Test at Different Stages of Loading (Courtesy of Pergamon Journals Ltd.)



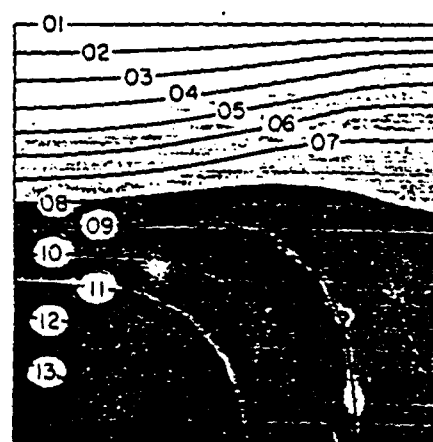
STRESS
(c)



TEMP



STRESS
(d)



TEMP

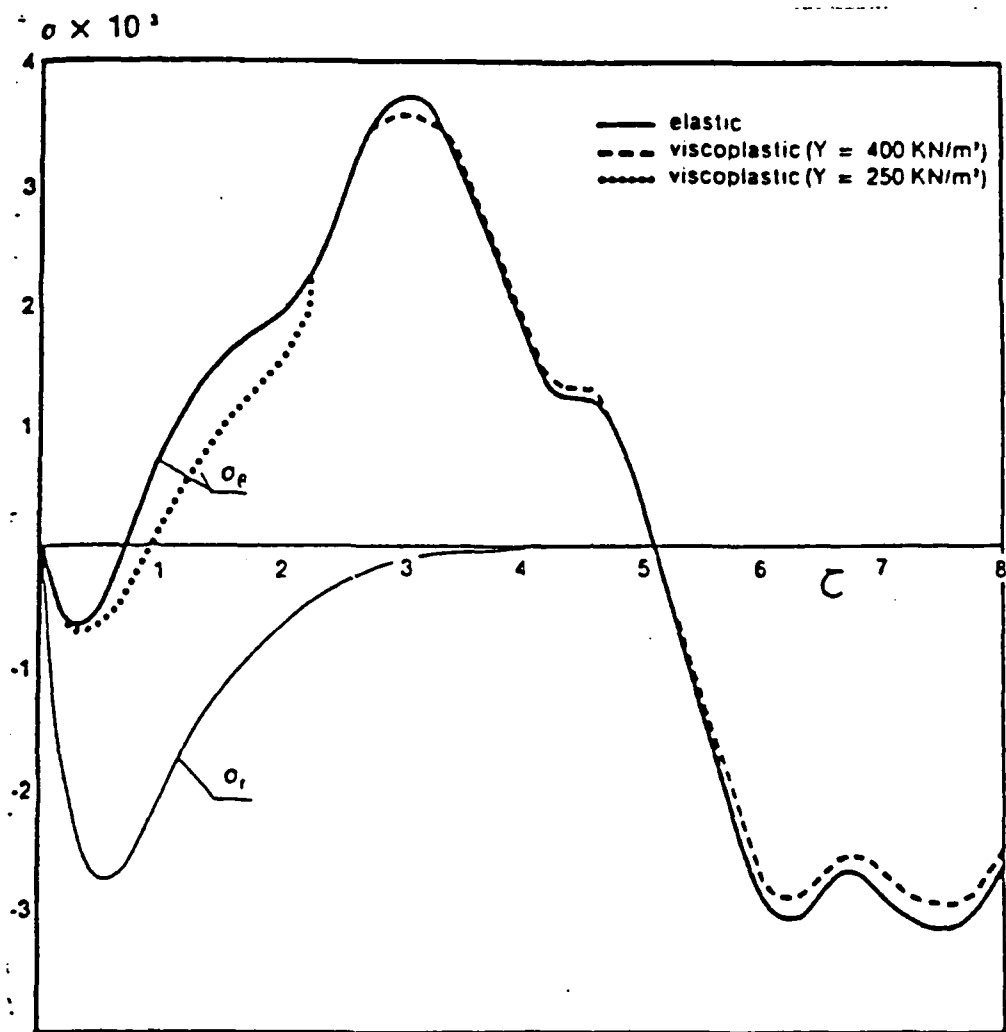


Fig. 15. Transient Response of the Radial and Hoop Stresses at the Inner Surface of Thick Walled Cylinder (Courtesy of Hemisphere Publishing)

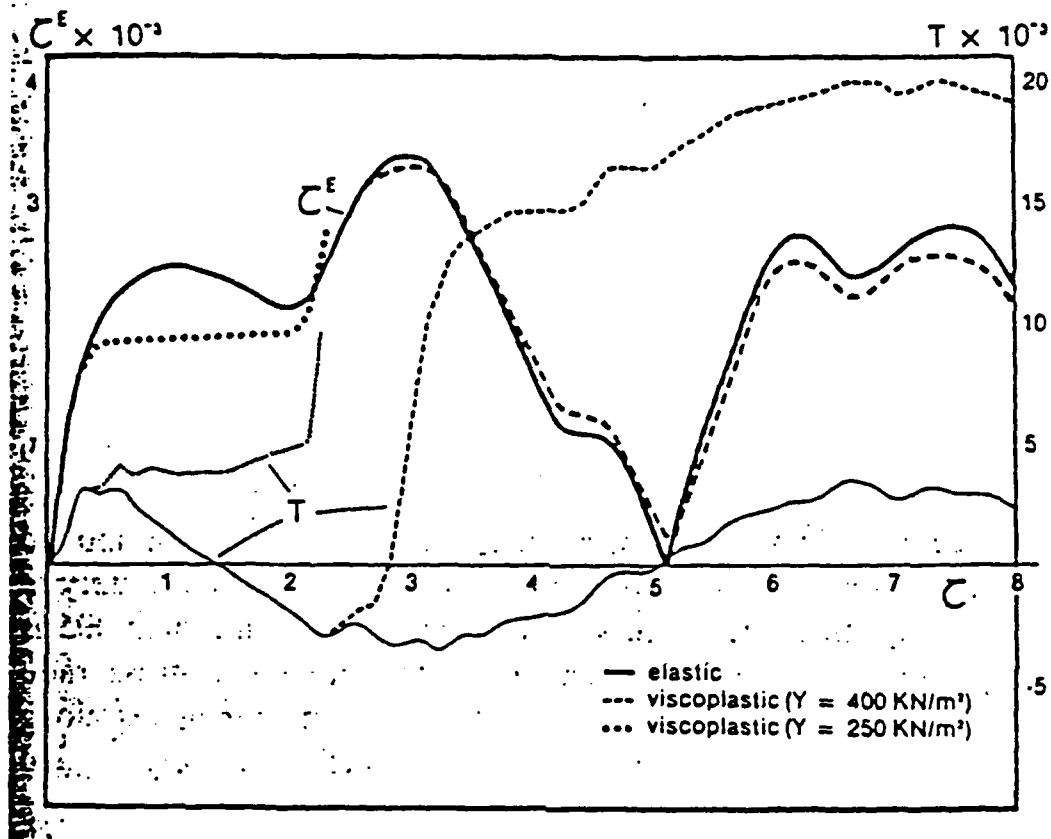


Fig. 16. Transient Response of the Effective Stress (τ^E) and Temperature at the Inner Surface of Thick Walled Cylinder (Courtesy of Hemisphere Publishing)

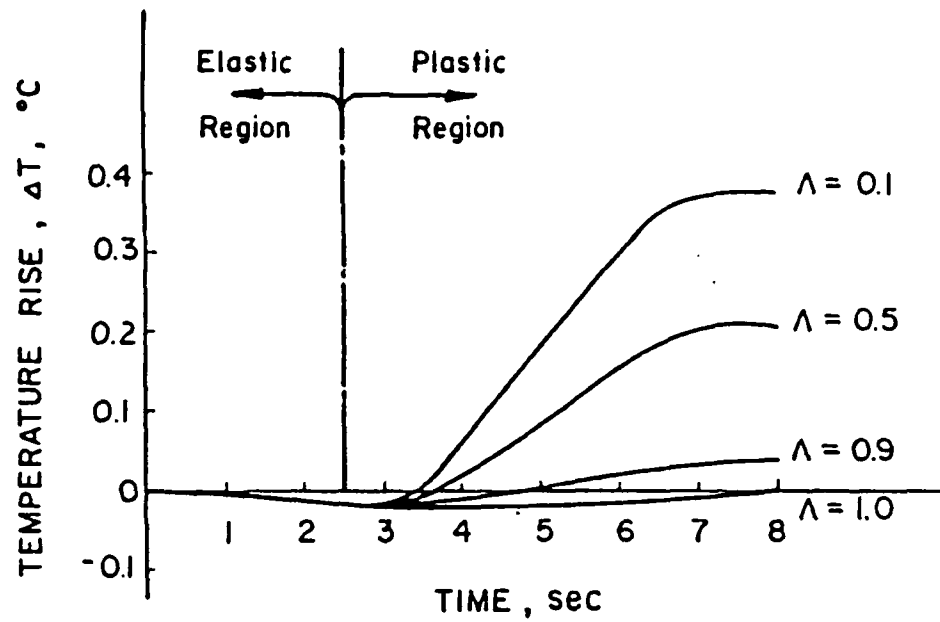


Fig. 17. Temperature Rise in the Rod Induced by Applied Mechanical Load
(Courtesy of Allen & Unwin, Inc.)

Appendix 7.6

Nonlinear Constitutive Behavior of Metals

NONLINEAR CONSTITUTIVE BEHAVIOR OF METALS

by

Professor David H. Allen
Aerospace Engineering Department
Texas A&M University

and

Dr. Charles E. Harris, Head
Mechanics of Materials Branch
NASA Langley Research Center

ABSTRACT

Over the past two decades a number of thermomechanical constitutive theories have been proposed for viscoplastic metals. These models are in most cases similar in that they utilize a set of internal state variables which are locally averaged representors of microphysical phenomena such as dislocation rearrangement and grain boundary sliding. The state of development of several of these models has now matured to the point that accurate theoretical solutions can be obtained for a wide variety of structural applications at elevated temperatures.

The purpose of this paper is threefold. First, the fundamentals of viscoplasticity are briefly reviewed and a general framework is outlined. Second, several of the more prominent models are reviewed in some detail. Finally, some comparative results are given to experimental evidence for a few of the models, and conclusions about the efficacy of the models are drawn from these comparisons.

INTRODUCTION

Since World War II there have been an increasing number of circumstances wherein structural materials are required to operate at very high temperatures. Perhaps the first large scale example of this occurred in the nuclear power industry, wherein temperatures in excess of 2000°F are common. Recently, interest in the National Aerospace Plane, wherein hypersonic shock interaction causes predicted temperatures in excess of 3000°F, has enhanced interest in this subject. The quest for more efficient gas turbines has also forced operating temperatures up. Thus, since experimentation in such hostile environments is extremely expensive, it is desirable to produce accurate theoretical models for structural components constructed from viscoplastic metals.

In all of these cases the structural materials commonly in use experience a substantial amount of inelastic constitutive behavior. Indeed, they are history, temperature, and rate dependent, as well as highly nonlinear. Hence, it is clear that any successful modelling attempt will be extremely complex in nature.

The most recent advances in constitutive theories to predict the inelastic behavior of structural materials have been the incorporation of the effects of temperature and rate dependence into the stress-strain relationships. The ability to predict the temperature and rate dependence of structural materials used in elevated temperature applications is especially important to the aerospace industry wherein substantial weight savings can be accomplished if safety factors can be reduced by the use of accurate analytic models. Most metals become viscoplastic, i.e., exhibit rate dependent inelasticity at temperatures above about four-tenths of their melting temperature. These materials are more intricate than elastic-plastic

materials in that the inclusion of rate dependence represents a significant increase in complexity of the mathematical model required to describe the observed material behavior. This is evident because in the classical rate-independent plasticity theory of metals the only parameter required to characterize the plastic strain is $\dot{\lambda}$, a history dependent scalar material property that relates inelastic strain rate to stress through the flow rule, which may be obtained experimentally from a single phenomenological uniaxial stress-strain curve. However, when the material becomes significantly rate dependent the uniaxial monotonic stress-strain curve is no longer unique. Therefore, it becomes necessary to construct a mathematical equation governing $\dot{\lambda}$. This equation can only be constructed by obtaining considerable experimental information about the response of the material to changes in the independent variables such as strain, strain rate, and temperature. The experiments required to obtain this information are usually cumbersome and expensive.

Historically, there have been two distinct approaches to the modelling of inelastic materials: 1) the functional theory [1], in which all dependent state variables are assumed to depend on the entire history of the specified observable state variables; and 2) the internal state variable (ISV) approach [2], wherein history dependence is postulated to appear explicitly in a set of ISV's. Lubliner [3] has shown that in most circumstances ISV models can be considered to be special cases of functional models. Because the internal state variables are readily identifiable in metals, most models currently under development are of the ISV type. This form has the added benefit that it is also usually more computationally tractable than the functional form.

This article will focus on several of these models which have shown promise for predicting the complex stress-strain response of metals at

elevated temperature. After establishing the general framework for a constitutive model using the ISV formulation, several state-of-the-art thermoviscoplastic models will be reviewed along with examples of the model predictions compared to experimental results.

SYMBOLS

σ_{ij}	stress tensor
D_{ijkl}	elastic modulus tensor
ϵ_{kl}	strain tensor
ϵ_{kl}^C	creep strain tensor
ϵ_{kl}^I	inelastic strain tensor
ϵ_{kl}^P	plastic strain tensor
ϵ_{kl}^T	thermal strain tensor
α_2	drag stress
α_{3ij}	back stress tensor
α_{kl}^μ	general set of internal state variables
h_2, h_3	hardening parameters
r_2, r_3	recovery parameters
$\dot{\lambda}$	inelastic flow parameter
T	temperature
α_{4ij}	damage tensor
σ_{ij}^d	deviatoric stress tensor
α_{3ij}^d	deviatoric back stress tensor
J_2	second deviatoric stress invariant
\dot{W}_p	rate of inelastic work = $\sigma_{ij} \dot{\epsilon}_{ij}^I$

GENERAL THERMOVISCOPLASTIC CONSTITUTIVE MODEL FRAMEWORK

The concept of ISV's, sometimes called hidden variables, was apparently first utilized in thermodynamics by Onsager [4,5], and numerous applications have been recorded in the literature over the last forty years [2,6-14]. A general framework for an ISV formulation of a thermoviscoplastic constitutive model can be developed by following the thermodynamic approach described by Coleman and Gurtin [2]. Historically, attempts to model rate dependence began with extensions of rate-independent classical plasticity theory. In these attempts the inelastic strain was "uncoupled" into rate-independent plastic and rate-dependent creep components to obtain

$$\sigma_{ij} = D_{ijkl} (\epsilon_{kl} - \epsilon_{kl}^P - \epsilon_{kl}^C - \epsilon_{kl}^T) \quad (1)$$

Ultimately, these attempts failed due to the fact that rate-independent and rate-dependent inelastic deformations are caused by the same microphysical mechanism, predominately dislocation movement. Thus, a more salient approach evolved using an approach in which the plastic strain and creep strain are "unified" into a single inelastic strain, ϵ_{kl}^I . The general form of the model for a metal is thus described by the following stress-strain equation of state:

$$\sigma_{ij} = D_{ijkl} (\epsilon_{kl} - \epsilon_{kl}^I - \epsilon_{kl}^T) \quad (2)$$

Although the strain, ϵ_{kl} , and the thermal strain, ϵ_{kl}^T , are normally specifiable, the inelastic strain tensor, representing a locally averaged measure of the distance traversed by dislocations, is not. Therefore, equation (2) must be augmented by an ISV evolution law (also sometimes called the flow law) of the form:

$$\dot{\epsilon}_{ij}^I = \dot{\lambda} (\sigma_{ij}' - \alpha_{3ij}') \quad (3)$$

where $\dot{\lambda}$ is a complicated history dependent function of state. For example, the Prandtl-Reuss equations [15,16] utilized in rate independent applications may be obtained as a special case by differentiating (2) in time, substituting (3) into this result, and setting α_{3ij}' to zero.

For rate dependent circumstances, however, the equations must be further augmented by additional ISV evolution laws to account for the diffusive nature of dislocation mechanisms at elevated temperatures. These are of the form:

$$\dot{\alpha}_2 = h_2 (\epsilon_{kl}, T, \alpha_{kl}^\mu) - r_2 (\epsilon_{kl}, T, \alpha_{kl}^\mu) \quad (4)$$

$$\dot{\alpha}_{3ij} = h_3 (\epsilon_{kl}, T, \alpha_{kl}^\mu) - r_3 (\epsilon_{kl}, T, \alpha_{kl}^\mu) \quad (5)$$

where the drag stress, α_2 , is an ISV related to the number or density of dislocations and the backstress, α_{3ij} , is an ISV related to the residual stresses at the microstructural level produced by the dislocation arrangement. The functions h_2 and h_3 represent the hardening terms in the drag stress and backstress, respectively, due to loss of dislocation mobility, whereas the functions r_2 and r_3 represent the recovery terms in the drag stress and backstress, respectively, due to recovery of dislocation mobility. In some applications it may be necessary to append an additional internal variable, α_{4ij} , called a damage parameter and representing the effects of grain boundary sliding and microfracture [17-20].

The mathematical expressions for the ISV's and the flow rule, equations 3 through 5, are typically determined phenomenologically by curve fitting data

obtained from a prescribed set of complicated experiments to this form. The precise experiments required to obtain the models depend on the theory being utilized. However, these experiments are typically complex in nature [21-23]. Since they are normally performed at temperatures in excess of 1000°F, they require that sophisticated furnaces be used, such as the one shown in Fig. 1. In addition, many of the models require that cyclic tension-compression tests be performed such as the one shown in Fig. 2, so that a highly aligned testing machine is required in order to avoid buckling of the specimens.

REVIEW OF CURRENT MODELS

In this section several of the more prominent unified models will be reviewed, and because the uncoupled models possess limited modelling ability, they will not be covered. The first concerted attempt to model the inelastic strain rate in a rate-dependent setting appears to have been due to Bodner and co-workers [17,18,24-36]*, and an indication of the complexity of this problem is that they are still actively pursuing this model. Since 1975, there has been a veritable explosion of models such as Hart [36,37], Miller and co-workers [19,38-48], Valanis [49,50], Robinson [51-57], Walker and co-workers [20,32,35,36,58,59,60], Krempl and co-workers [61-66], Krieg and co-workers [36,67], as well as others [68-78]. Doubtless there are numerous efforts we have overlooked, and the authors apologize for any oversight on our part.

In a paper of this limited scope it is unrealistic to expect that an in-depth review can be reported on each of the models. Therefore, we have chosen what we hope is a reasonable and expedient dissemination method. First, we

*Although a promising model proposed by Valanis had been previously reported, it was rate-independent at the time of Bodner's work.

will discuss each of the models briefly, and we have encapsulated a summary of each of the models mentioned above (in uniaxial form) in Table I. Because many of the models have appeared in several forms, in this table we have chosen a relatively simple version of each of the models. Second, we have attempted to summarize the capabilities of the models in Table II, and to review the experimental requirements in Table III. Finally, we have undertaken to discuss recent advances and review in somewhat greater detail the models of Bodner, Miller, and Walker.

Because the scope of this paper is limited, we are unable to pursue all of the important issues regarding this subject. Readers who are interested in further study on this subject will find a far more detailed discussion of recent advances in viscoplasticity in reference 36, as well as in the bibliography at the end of this paper.

In this discussion the models are reviewed only in uniaxial form because in virtually all cases they are converted to multiaxial form by using J_2 theory in conjunction with Drucker's postulate [79]. We should also point out that we have utilized a common terminology due to the fact that each author uses different notation.

Probably the simplest model to date was proposed by and Krempl and co-workers [61-66]. Because this model does not contain evolution laws for the back stress and drag stress, it is best used for monotonic loadings.

The model proposed by Valanis [49,50] is built on a single integral framework which makes it quite different in form from equations (2) and (3). However, as pointed out by Schapery [80], when this so-called "endochronic" theory is used with an exponential kernel function, the Prandtl-Reuss [15,16] equations can be recovered. Although Valanis' model is actually capable of producing much more general results, a single exponential is usually used, so

that it reduces to equations (2) and (3) when Laplace transformed in the endochronic time scale.

An interesting and potentially very useful model has been proposed by Krieg, et al. [67]. The model appears to have been one of the first to include both drag stress and back stress terms. However, the authors moved on to other things and the model was not improved for about a decade. Recently, a second generation of the model has been proposed [36].

Robinson [51-57] has proposed one of the most complex and advanced models to date. His model is distinguished from the other current models both in that it possesses a yield criterion similar to that used in classical plasticity, and that it has been proposed in multiaxial form for orthotropic media such as metal-matrix composites.

Hart's model [37] is distinguished by the fact that the drag stress is assumed to be a constant, and it possesses an ISV called hardness which affects the back stress evolution law. Recent advances of this model have also been reported in reference 36.

Bodner's Model

As mentioned earlier, Bodner's model [17,18,24-36] appears to have been the first viable unified model proposed for viscoplastic metals. Although early versions of the model were somewhat primitive, it has remained at the forefront of technology via timely modifications. The initial model did not contain a drag stress, σ_{3ij} , and although the current version does include one, it is included in a significantly different way from other current models. Bodner calls it an anisotropic hardening parameter, α_3 , and it occurs in the inelastic strain rate equation as a scalar variable. Thus, the resulting evolution laws are:

$$\dot{\epsilon}^I = \frac{2}{\sqrt{3}} D_0 \exp \left\{ -\frac{1}{2} \left[\frac{Z}{\sigma} \right]^{2n} \right\} \operatorname{sgn} \sigma \quad (6)$$

$$Z \equiv \alpha_2 - \alpha_2 + \alpha_3 \operatorname{sgn} \sigma \quad (7)$$

$$\dot{\alpha}_2 = m_1 [Z_1 - Z_1] \dot{W}_p - A_1 Z_1 \left[\frac{\alpha_2 - Z_2}{Z_1} \right]^{r_1} \quad (8)$$

$$\dot{\alpha}_3 = m_2 [Z_3 \operatorname{sgn} \sigma - \alpha_3 \operatorname{sgn} \sigma] \dot{W}_p - A_2 Z_1 \left[\frac{\alpha_3}{Z_1} \right]^{r_2} \operatorname{sgn} \alpha_3 \quad (9)$$

where D_0 , n , m_1 , Z_1 , Z_2 , A_1 , r_1 , m_2 , Z_3 , A_2 , and r_2 are material constants.

The flow law is exponentially based as seen in equation (6). The model gives a limiting strain rate in shear of D_0 . The term $-m_1 Z^I \dot{W}_p$ is a dynamic recovery term for α_3 in the isotropic growth law (8) and $-A_1 Z_1 [(\alpha_2 - Z_2) Z_1^{-1}]^{r_1}$ is a static thermal recovery term. B is a uniaxial representation of a second order tensor in the multiaxial state which models directional or anisotropic hardening. α_3 is assumed to act as an isotropic variable on an incremental basis. Equation (7) shows that Z can experience large changes in magnitude due to the $\operatorname{sgn} \sigma$ function as the stress changes sign. This could cause numerical problems if the B variable is of the same order of magnitude as the α_2 variable. The evolution law for B has the same components as the evolution law for D .

Bodner's model is seen to use the rate of plastic work, \dot{W}_p , instead of inelastic strain rate as the measure of work hardening. This is designed to allow for better modelling of strain rate jump tests. The modification used to account for the strain aging effects was patterned after Schmidt and Miller's solute strengthening correction. The constant Z_3 in the α_3 evolution law was written in the following form:

$$Z_3 = Z_4 + Z_5 f(\dot{\epsilon}^I) \quad (10)$$

$$f(\dot{\epsilon}^I) = F \exp \left\{ - \left[\frac{\log(|\dot{\epsilon}^I|) - \log(J)}{\beta} \right]^2 \right\} \quad (11)$$

where F is the maximum correction, J is the strain rate of maximum correction, and β is the width of correction.

Miller's Model

Miller's model [19,36,39-48] is probably the most complex model available at the time of this writing. It is capable of accounting for a wide range of physical phenomena, including solute strengthening and cyclic strain softening.

Schmidt and Miller's evolution laws have the following form:

$$\dot{\epsilon}^I = B' \left\{ \sinh \left(\frac{\alpha_3}{\alpha_2 + F_{sol}} \right)^{1.5} \right\}^n \operatorname{sgn}(\sigma - \alpha_3) \quad (12)$$

$$\dot{\alpha}_3 = H_1 \dot{\epsilon}^I - H_1 B' \left\{ \sinh(A_1 |\alpha_3|) \right\}^n \operatorname{sgn}(\alpha_3) \quad (13)$$

$$\dot{\alpha}_2 = H_2 [|\dot{\epsilon}^I| (C_2 + |\alpha_3| - \frac{A_2}{A_1} \alpha_3) - H_2 C_2 B' \left\{ \sinh(A_2 \alpha_2^3) \right\}^n] \quad (14)$$

$$F_{sol} = F \exp \left\{ - \left(\frac{\log(|\dot{\epsilon}^I|) - \log(J)}{\beta} \right)^2 \right\} \quad (15)$$

where B' , n , H_1 , A_1 , H_2 , C_2 , A_2 , F , J , and β are material constants.

The flow law has the form of a hyperbolic sine. This form was chosen to model creep response better. The same form is found in the static thermal recovery terms of the backstress and drag stress evolution laws. The drag

stress hardening term contains a hardening term, a dynamic recovery term, and a term which couples drag stress hardening to backstress magnitude. These three terms provide the proper cyclic, hardening, softening and saturation behavior. The same non-interactive solute strengthening correction (F_{s01}) as mentioned earlier is seen in this model.

Walker's Exponential Model

The growth laws for Walker's exponential model [20,32,35,36,58,59,60] have the following form:

$$\dot{\epsilon}^I = \frac{\exp\left(\frac{\sigma - \alpha_3}{\beta}\right) - 1}{\beta} \operatorname{sgn}(\sigma - \alpha_3) \quad (16)$$

$$\dot{\alpha}_3 = n_2 - B \{ [n_3 + n_4 \exp(-n_5 |\log(\dot{R}/\dot{R}_0)|)] \dot{R} + n_6 \} \quad (17)$$

$$\alpha_2 = D_1 + D_2 \exp(-n_7 R) \quad (18)$$

$$\dot{R} = |\dot{\epsilon}^I| \quad (19)$$

where β , n_2 , n_3 , n_4 , n_5 , \dot{R}_0 , n_6 , D_1 , D_2 , and n_7 are material constants.

This version of Walker's flow law is based on an exponential function. The term $n_2 \dot{\epsilon}^I$ is seen to be a work hardening term in the back stress growth law. The term $\alpha_3 [n_3 + n_4 \exp(-n_5 |\log(\dot{R}/\dot{R}_0)|)] \dot{R}$ is a dynamic recovery term. Negative strain rate sensitivity effects can be modelled with the term $n_4 \exp(-n_5 |\log(\dot{R}/\dot{R}_0)|)$. Back stress thermal recovery is handled by the $\alpha_3 n_6$ term. Drag stress hardening is modelled through the $D_2 \exp(-n_7 R)$ term. No provision is made for drag stress recovery in this model.

COMPARISON OF MODEL PREDICTIONS TO EXPERIMENTAL RESULTS

In most cases, the models are described by a set of ordinary differential equations in time which are mathematically "stiff". The definition of mathematical stiffness is that if the solution is expanded in an exponential series in time, at least two of the eigenvalues will differ by many orders of magnitude. A characteristic of stiff differential equations is that they cannot be efficiently integrated in time by standard integration schemes such as Runge-Kutta methods. Numerous intricate algorithms have been developed for integrating equations (3) through (5) in time [81-86]. Oftentimes, it is most efficient to use a simple Euler forward or backward scheme, where accuracy is achieved by taking very small time steps, as shown in Fig. 3 [81]. When solving boundary value problems using the finite element method, it is normally possible to obtain convergence on each displacement increment by subincrementing the Euler integration at each integration point.

Many of the models mentioned in the previous section have been compared both qualitatively and quantitatively to one another as well as to experimental results for a variety of materials [87-92]. The accuracy of several of the models is demonstrated for INCONEL 718 under two constant strain rate conditions at 1100°F (593°C) in Figs. 4 and 5 [92]. A complex load history is demonstrated in Figs. 6 through 8. In this example INCONEL 718 is subjected to the strain history shown at the bottom right hand corner of each figure [92].

CONCLUSION

The complex task of predicting the response of viscoplastic metals has now reached a state wherein reliable structural analysis is sometimes possible [93]. However, the accuracy of predictions still depends on a number of

complicated factors such as material type, loading conditions, thermal environment, numerical accuracy, and the constitutive model being utilized. Although this area of research has certainly reached fruition, it has not yet reached full maturity.

REFERENCES

1. Coleman, B.D., "Thermodynamics of Materials with Memory," Archive Rational Mechanics and Analysis, Vol. 17, pp. 597-613, 1967.
2. Coleman, B.D. and Gurtin, M.E., "Thermodynamics with Internal State Variables," J. Chem. Phys., Vol. 47, pp. 597-613, 1967.
3. Lubliner, J., "On Fading Memory in Materials of Evolutionary Type," Acta Mech., Vol. 8, pp. 75-81, 1969.
4. Onsager, L., "Reciprocal Relations in Irreversible Processes I.," Physics Review, Vol. 37, pp. 405-426, 1931.
5. Onsager, L., "Reciprocal Relations in Irreversible Processes II.," Physics Review, Vol. 38, pp. 2265-2279, 1931.
6. Eckhart, C., "Thermodynamics of Irreversible Processes, I. The Simple Fluid," Physics Review, Vol. 58, p. 267, 1940.
7. Meixner, J., "Die thermodynamische Theorie der Relaxationserscheinungen und ihr Zusammenhang mit der Nachwirkungstheorie.," Kolloid-Z, Vol. 134, p. 2, 1953.
8. Biot, M.A., "Theory of Stress-Strain Relations in Anisotropic Viscoelasticity and Relaxation Phenomena," J. Appl. Phys., Vol. 25, pp. 1385-1291, 1954.
9. Biot, M.A., "Variational Principles in Irreversible Thermodynamics with Application to Viscoelasticity," Physics Review, Vol. 97, p. 1463, 1955.
10. Ziegler, H., "An Attempt to Generalize Onsager's Principle, and Its Significance for Rheological Problems," Z. Angew. Math Phys., Vol. 9, p. 748, 1958.
11. Valanis, K.C., "Unified Theory of Thermomechanical Behavior of Viscoelastic Materials," Mechanical Behavior of Materials Under Dynamic Loads, p. 343, Springer, 1968.
12. Kestin, J. and Rice, J.R., "Paradoxes in the Application of Thermodynamics to Strained Rods," A Critical Review of Thermodynamics, p. 275, Mono Book Corp., 1970.

13. Schapery, R.A., "Application of Thermodynamics to Thermomechanical, Fracture and Bierefringent Phenomena in Viscoelastic Media," Journal of Applied Physics, Vol. 35, p. 1941, 1964.
14. Schapery, R.A., "A Theory of Non-linear Viscoelasticity Based on Irreversible Thermodynamics," Proc. 5th U.S. National Congress of Applied Mechanics, ASME, pp. 511-530, 1966.
15. L. Prandtl, "Spannungsverteilung in Plastischen Koerpen," Proceedings of the First International Congress on Applied Mechanics, Delft, Technische Boekhandel en Drukkerij, J. Waltman, Jr., pp. 43-45, 1925.
16. E. Reuss, "Bereucksichtigung der Elastischen Formaenderungen in der Plastaizitaetstheorie," Zeitschrift fuer Angewandte Mathematic and Mechanik, Vol. 10, pp. 266-274, 1930.
17. Bodner, S.R., "A Procedure for Including Damage in Constitutive Equations for Elastic-viscoplastic Work-hardening Materials," Proceedings of the IUTAM Symposium on Physical Nonlinearities in Structural Analysis, Senlis, France, pp. 21-28, 1981.
18. Bodner, S.R., "Evolution Equations for Anisotropic Hardening and Damage of Elastic-viscoplastic Materials," Plasticity Today: Modelling, Methods, and Applications, Elsevier Applied Science Pub., Barking, England, 1984.
19. Miller, A.K., Obalucki, A.O., Lee, C.W., Tanaka, T.G., and Lee, S.B., "A Unified Model for Fatigue Crack Initiation and Growth, with Emphasis on Short-Crack Behavior, Crack Closure Effects Variable - Temperature Fatigue and Creep-Fatigue Iteration," Mat. Science Engr., Vol. A103, pp. 71-93, 1988.
20. Walker, K.P., and Wilson, D.A., "Creep Crack Growth Predictions in INCO 718 Using a Continuum Damage Model," Nonlinear Constitutive Relations for High Temperature Applications - 1984, NASA CP 2369, pp. 65-82, 1984.
21. Krempl, E., "An Experimental Study of Room-temperature Rate-sensitivity, Creep, and Relaxation of AISI Type 304 Stainless Steel," J. Mech. Phys. Solids, Vol. 27, pp. 363-375, 1979.
22. Krempl, E., "The Role of Servocontrolled Testing in the Development of the Theory of Viscoplasticity Based on Total Strain and Overstress," Mechanical Testing for Deformation Model Development, STP 765, ASTM, 1982.
23. Ellis, J.R. and Robinson, D.N., "Some Advances in Experimentation Supporting Development of Viscoplastic Constitutive Models," Nonlinear Constitutive Relations for High Temperature Applications - 1984, NASA CP 2369, pp. 237-272, 1984.
24. Bodner, S.R. and Partom, Y., "Constitutive Equations for Elastic-viscoplastic Strain-hardening Materials," J. Appl. Mech., Vol. 42, pp. 385-389, 1975.

25. Bodner, S.R., Partom, I., and Partom, Y., "Uniaxial Cyclic Loading of Elastic-viscoplastic Materials," J. Applied Mech. Vol. 46, p. 805, 1979.
26. Stouffer, D.C. and Bodner, S.R., "A Relationship Between Theory and Experiment for a State Variable Constitutive Equation," Mechanical Testing for Deformation Model Development, STP 765, ASTM, pp. 239-250, 1982.
27. Bodner, S.R. and Stouffer, D.C., "Comments on Anisotropic Plastic Flow and Incompressibility," Int. J. Eng. Sci., Vol. 21, pp. 211-215, 1983.
28. Bodner, S.R., "Review of a Unified Elastic-viscoplastic Theory," AFOSR-84-0042, 1984.
29. Bodner, S.R., "Evolution Equations for Anisotropic Hardening and Damage of Elastic-viscoplastic Materials," Plasticity Today: Modelling, Methods, and Applications, Elsevier Applied Science Pub., Barking, England, 1984.
30. Bodner, S.R., "Constitutive Equations-directional Hardening with Incrementally Isotropic Flow Law," Unpublished Research, Department of Materials Sciences, Southwest Research Institute, 1984.
31. Lindholm, U.S., Chan, K.S., Bodner, S.R., Weber, R.M., Walker, K.P., Cassenti, B.N., "Constitutive Modeling for Isotropic Materials (HOST)," CR-174718, NASA, 1984.
32. Chan, K.S., Lindholm, U.S., Bodner, S.R., and Walker, K.P., "High Temperature Deformation Under Uniaxial Loading: Theory and Experiment," J. Engr. Mat. Tech., ASME, Vol. 111, No. 4, pp. 345-353, 1989.
33. Bodner, S.R., "Review of a Unified Elastic-viscoplastic Theory," AFOSR-84-0042, 1984.
34. Chan, K.S., Bodner, S.R., and Lindholm, U.S., "Phenomenological Modeling of Hardening and Thermal Recovery in Metals," Journal of Engineering Materials and Technology, American Society of Mechanical Engineers, Vol. 110, pp. 1-8, 1988.
35. Lindholm, U.S., Chan, K.S., Bodner, S.R., Weber, R.M., Walker, K.P., and Cassenti, B.N., "Constitutive Modelling for Isotropic Materials (HOST)," Second Annual Contract Report, NASA CR-174980, 1985.
36. Miller, A.K., Ed., Unified Constitutive Equations for Creep and Plasticity, Elsevier, London, 1987.
37. Hart, E.W., "Constitutive Relations for the Nonelastic Deformation of Metals," J. Eng. Mater. Tech., Vol. 98-H, p. 193, 1976.
38. Lowe, T.C. and Miller, A.K., "Improved Constitutive Equations for Modelling Strain Softening - Part 1: Conceptual Development and Part 2: Predictions for Aluminum," J. Eng. Mat. Tech., Vol. 106, pp. 337-348, 1984.

39. Sherby, O.D. and Miller, A.K., "Combining Phenomenology and Physics in Describing the High Temperature Mechanical Behavior of Crystalline Solids," J. Eng. Mat. Tech., Vol. 101, pp. 387-395, 1979.
40. Schmidt, C.G. and Miller, A.K., "The Effect of Solutes on the Strength and Strain Hardening Behavior of Alloys," Acta Met., Vol. 30, pp. 615-625, 1982.
41. Miller, A.K., Kassner, and Ruibin, "Verification of a Microstructurally-based Equation for Elevated-temperature Transient Isotropic Hardening," Strength of Metals and Alloys, Vol. 2, Pergamon Press, Oxford, pp. 581-587, 1982.
41. Miller, A.K., "Modelling of Cyclic Plasticity: Improvements in Simulating Normal and Anomalous Bauschinger Effects," J. Eng. Mat. Tech., Vol. 102, pp. 215-220, 1980.
42. Miller, A.K. and Ziaai-Moayyed, A.A., "Some Critical Experimental Tests of the MATMOD Constitutive Equations with Respect to Directional Hardening and Cyclic Deformation," Mechanical Testing for Deformation Model Development, STP 765, ASTM, pp. 202-222, 1982.
42. Miller, A.K., Kassner, and Sherby, O.D., "The Separate Roles of Subgrains and Forest Dislocations in the Isotropic Hardening of Type 304 Stainless Steel," Met. Trans. A, vol. 13A, 1982.
43. Schmidt, C.G., "A Unified Phenomenological Model for Solute Hardening, Strain Hardening, and Their Interactions in Type 316 Stainless Steel," Ph.D. Dissertation, Stanford University, Department of Materials Science and Engineering, 1979.
44. Ruano, Miller, A.K., and Sherby, O.D., "The Influence of Pipe Diffusion on the Creep of Fine-grained Materials," Mat. Sci. Eng., Vol. 51, pp. 9-16, 1981.
45. Schmidt, C.G. and Miller, A.K., "A Unified Phenomenological Model for Non-elastic Deformation of Type 316 Stainless Steel - Part I: Development of the Model and Calculation of the Material Constants - Part II: Fitting and Predictive Capabilities," Res Mech., Vol. 3, pp. 109-129; 175-193, 1981.
46. Schmidt, C.G. and Miller, A.K., "The Effect of Solutes on the Strength and Strain Hardening Behavior of Alloys," Acta Met., Vol. 30, pp. 615-625, 1982.
47. Lowe, T.C. and Miller, A.K., "Improved Constitutive Equations for Modelling Strain Softening - Part 1: Conceptual Development and Part 2: Predictions for Aluminum," J. Eng. Mat. Tech., Vol. 106, pp. 337-348, 1984.
48. Hedling, D.E., Miller, A.K., "The Incorporation of Yield Surface Distortion into a Unified Constitutive Model, Part I: Equation Development," Acta Mechanica, Vol. 69, pp. 9-23, 1987.

49. Valanis, K.C., "A Theory of Viscoplasticity Without a Yield Surface Part I. General Theory," Archives of Mechanics, Vol. 23, pp. 535-551, 1971.
50. Valanis, K.C., "A Theory of Viscoplasticity Without a Yield Surface Part II. Application to Mechanical Behavior of Metals," Archives of Mechanics, Vol. 23, pp. 535-551, 1971.
51. Robinson, D.N., "Developments Toward Refined Constitutive Laws for Reactor System Metals," ORNL-5136, pp. 15-23, 1975.
52. Robinson, D.N., "Tests for Examining the Concept of a Flow Potential in the Stress-strain Relations of Reactor System Metals," ORNL-5235, pp. 23-25, 1976.
53. Robinson, D.N., "On the Concept of a Flow Potential and the Stress-strain Relations of Reactor System Metals," TM-5571, ORNL, 1976.
54. Robinson, D.N., "Developments Toward Refined Constitutive Laws," ORNL-5339, pp. 5-16, 1977.
55. Robinson, D.N., "A Unified Creep-Plasticity Model for Structural Metals at High Temperature," TM-5969, ORNL, 1978.
56. Robinson, D.N. and Swindeman, R.W., "Unified Creep-plasticity Constitutive Equations for 2-1/4 Cr-1 Mo Steel at Elevated Temperature," TM-8444, ORNL, 1982.
57. Robinson, D.N. and Bartolotta, P.A., "Viscoplastic Constitutive Relationships with Dependence on Thermomechanical History," NASA CR-174836, 1985.
58. Walker, K.P., "Representation of Hastelloy-X Behavior at Elevated Temperature with a Functional Theory of Visco-Plasticity," ASME Pressure Vessels Conference, San Francisco, California, 1980.
59. Walker, K.P., "Research and Development Program for Non-linear Structural Modelling with Advanced Time-temperature Dependent Constitutive Relationships," CR-165533, NASA, 1981.
60. Freed, A.D. and Walker, K.P., "Refinements in a Viscoplastic Model," NASA TM 102338, 1989.
61. Liu, M.C.M., Krempl, E., and Nairn, D.C., "An Exponential Stress-strain Law for Cyclic Plasticity," J. Eng. Mat. Tech., pp. 322-329, 1976.
62. Cernocky, E.P. and Krempl, E., "Construction of Nonlinear Monotonic Functions of Almost Constant or Linear Behavior," J. Appl. Mech., Vol. 45, pp. 781-784, 1978.
63. Liu, M.C.M. and Krempl, E., "A Uniaxial Model Based on Total Strain and Overstress," J. Mech. Phys. Solids, Vol. 27, pp. 377-391, 1979.
64. Cernocky, E.P. and Krempl, E., "A Nonlinear Uniaxial Integral Constitutive Equation Incorporating Rate Effects, Creep, and Relaxation," Int. J. Nonlinear Mech., Vol. 14, pp. 183-203, 1979.

65. Cernocky, E.P. and Krempl, E., "A Theory of Viscoplasticity Based on Infinitesimal Total Strain," Acta Mech., Vol. 36, pp. 263-289, 1980.
66. Yao, D. and Krempl, E., "Viscoplasticity Theory Based on Overstress. The Prediction of Monotonic and Cyclic Proportional and Nonproportional Loading Paths of an Aluminum Alloy," Int. J. of Plasticity, Vol. 1, No. 3, pp. 259-274, 1985.
67. Krieg, R.D., Sweekren, J.C., and Rhode, R.W., "A Physically-based Internal Variable Model for Rate-dependent Plasticity," Proc. ASME/CSME PVP Conference, pp. 15-27, 1978.
68. Zienkiewicz, O.C. and Corneau, I.C., "Visco-plasticity - Plasticity and Creep in Elastic Solids - a Unified Numerical Approach," International Journal of Numerical Methods in Engineering, Vol. 78, pp. 821-845, 1974.
69. Chaboche, J.L., "Viscoplastic Constitutive Equations for the Description of Cyclic and Anisotropic Behavior of Metals," Bulletin de L'Academie des Sciences, Serie des Science Techniques, Vol. 25, p. 33, 1977.
70. Ghosh, A.K., "A Physically Based Constitutive Model for Metal Deformation," Acta Met., Vol. 28, p. 1443, 1980.
71. Cescotto, S. and Leckie, F., "Determination of Unified Constitutive Equations for Metals at High Temperature," Proc. International Conference on Constitutive Laws for Engineering Materials, pp. 105-111, 1983.
72. Jones, W.B. Rhode, R.W., and Sweekren, J.C., "Deformation Modelling and the Strain Transient Dip Test," Mechanical Testing for Deformation Model Development, STP 765, ASTM, pp. 102-118, 1982.
73. Jones, W.B. and Rhode, R.W., "An Evaluation of the Kinematic Variable (Back Stress) Response of Metals," 7th International Conference on Structural Mechanics in Reactor Technology, Chicago, Illinois, 1983.
74. Lee, D. and Zaverl, Jr., "A Generalized Strain Rate Dependent Constitutive Equation for Anisotropic Metals," Acta Met., Vol. 26, p. 385, 1975.
75. Lin, H.C. and Wu, H.C., "Strain-rate Effect in the Endochronic Theory of Viscoplasticity," J. Appl. Mech., Vol. 43, pp. 92-96, 1976.
76. P. Perzyna, "The Constitutive Equations for Work-hardening and Rate-sensitive Plastic Materials," Proc. Vibr. Probl., Vol. 4, pp. 281-290, 1963.
77. P. Perzyna, "Fundamental Problems in Viscoplasticity," Advan. Appl. Mech., Vol. 9, pp. 243-377, 1966.
78. P. Perzyna, "On Physical Foundations of Viscoplasticity," Polska Akademia Nauk, 1BPt. Report 28, 1968.
79. Drucker, D.C., "A Definition of Stable Inelastic Materials," J. Appl. Mech., Vol. 26, pp. 101-106, 1959.

80. Schapery, R.A., "On a Thermodynamic Constitutive Theory and Its Application to Various Nonlinear Materials," Proceedings of the IUTAM Symposium, East Kilbride, pp. 260-285, 1968.
81. Imbrie, P.K., Haisler, W.E., and Allen, D.H., "Evaluation of the Numerical Stability and Sensitivity to Material Parameter Variations for Several Unified Constitutive Models," MM 4998-85-61, Department of Aerospace Engineering, Texas A&M University, 1985.
82. Imbrie, P.K., James, G.H., Hill, P.S., Haisler, W.E., and Allen, D.H., "An Automated Procedure for Material Parameter Evaluation for Viscoplastic Constitutive Models," Nonlinear Constitutive Relations for High Temperature Applications - 1986, NASA CP 10010, pp. 317-352, 1986.
83. Miller, A.K. and Tanaka, T.G., "NONSS: A New Method for Integrating Unified Constitutive Equations Under Complex Histories," J. Eng. Mat. Tech., ASME, Vol. 110, pp. 205-211, 1988.
84. Henshall, G.A., Tanaka, T.G., and Miller, A.K., "Numerical Differentiation for Use in Integrating Unified Constitutive Equations," Int. J. Num. Methods Engr., Vol. 28, pp. 1115-1129, 1989.
85. Tanaka, T.G. and Miller, A.K., "Development of Method for Integrating Time-Dependent Constitutive Equations with Large, Small or Negative Strain Rate Sensitivity," Int. J. Num. Methods engr., Vol. 26, pp. 2457-2488, 1988.
86. Krieg, R.D., "Numerical Integration of Some New Unified Plasticity-creep Formulations," 4th International Conference on Structural Mechanics in Reactor Technology, San Francisco, California, 1977.
87. Delph, T.J., "A Comparative Study of Two State-variable Constitutive Theories," J. Eng. Mat. Ttech., Vol. 102, pp. 327-336, 1980.
88. Milly, T.M., and Allen, D.H., "A Comparative Study of Non-linear Rate-dependent Mechanical Constitutive Theories for Crystalline Solids at Elevated Temperatures," API-E-5-82, Department of Engineering Science and Mechanics, Virginia Polytechnic Institute and State University, 1982.
89. Cernocky, E.P., "An Examination of Four Viscoplastic Constitutive Theories in Uniaxial Monotonic Loading," Int. J. Solids Structures, Vol. 18, pp. 989-1005, 1982.
90. Beek, J.M., Allen, D.H., and Milly, T.M., "A Qualitative Comparison of Current Models for Nonlinear Rate-dependent Material Behaviour of Crystalline Solids," MM 4246T-83-14, Department of Aerospace Engineering, Texas A&M University, 1983.
91. Beek, J.M., A Comparison of Current Models for Nonlinear Rate-dependent Material Behavior of Crystalline Solids, M.S. Thesis, Texas A&M University, 1986.

92. James, G.H., Imbrie, P.K., Hill, P.S., Allen, D.H., and Haisler, W.E., "An Experimental Comparison of Current Viscoplastic Models at Elevated Temperature," Journal of Engineering Materials and Technology, Vol. 109, pp. 130-139, April, 1987.
93. Moreno, V. and Jordan, E.H., "Prediction of Material Thermomechanical Response with a Unified Viscoplastic Constitutive Model," Pro. of the 26th Structures, Structural Dynamics, and Materials Conference, Orlando, Florida, 1985.

TABLE I. COMPARISON OF UNIAXIAL MODELS

Theory	Stress-Strain Relation	Internal State Variable Evolution Laws	Comments	Material Parameters
Cernocky and Krempf	$\sigma = E (\epsilon - \epsilon^I - \epsilon^T)$	$\dot{\epsilon}^I = \frac{\sigma - G}{E k}$	1. $G = G(\epsilon, T)$ from extrapolation of relaxation data. 2. k is curve-fit to $-\left(\frac{ \sigma - G }{R_2}\right) R_3$ $k = R_0 e^{R_1 e}$	E, R_0, R_1 R_2, R_3
Krieg, Swarengen, and Rohde	$\sigma = E (\epsilon - \epsilon^I - \epsilon^T)$	$\dot{\epsilon}^I = C_1 \left(\frac{ \sigma - \alpha_2 }{\alpha_3}\right)^2 \text{sgn}(\sigma - \alpha_2)$ $\dot{\alpha}_2 = C_3 \epsilon^I - C_4 \alpha_2^2 C_3 \alpha_2^2 - 1 \text{sgn}(\sigma_2)$ $\dot{\alpha}_3 = C_6 \dot{\epsilon}^I - C_7 (\alpha_3 - \alpha_3^0)^n$		$E, C_1, C_2, C_3, C_4,$ $C_5, C_6, C_7, \alpha_3^0, n$
Bodner et al.	$\sigma = E (\epsilon - \epsilon^I - \epsilon^T)$	$\dot{\epsilon}^I = \frac{2}{\sqrt{3}} D_0 e^{-\left(\frac{n+1}{2n}\right) \left(\frac{\sigma}{\alpha_3}\right)^{-2n}} \text{sgn}(\sigma)$ $\dot{\alpha}_3 = (Z_1 - \alpha_3) \dot{\alpha}_p - A Z_1 \left(\frac{\alpha_3 - Z_1}{Z_1}\right)^r$	1. $\dot{\alpha}_p = \sigma \dot{\epsilon}^I$	$E, D_0, n, m,$ Z_1^I, A, Z_1, r

Walker

$$\sigma = E (\epsilon - \epsilon^I - \epsilon^T)$$

$$\dot{\epsilon}^I = \left(\frac{|\sigma - \alpha_2|}{\alpha_3} \right)^n \operatorname{sgn} (\sigma - \alpha_2)$$

$$\dot{\alpha}_2 = (n_1 + n_2) \dot{\epsilon}^I$$

$$-(\dot{\alpha}_2 - \alpha_2 - n_1 \dot{\epsilon}^I) \cdot \left(\dot{\epsilon}^I \left| \frac{\partial}{\partial R} \right| (n_3 + n_4 R) \right)$$

$$\ln \left(\frac{n_5 R}{1 + n_6 R} + 1 \right) + n_7 |\alpha_2 - \alpha_2^0|^{n-1}$$

$$\dot{\alpha}_3 = n_8 |\dot{\epsilon}^I| - n_9 |\dot{\epsilon}^I| \alpha_3 - n_{10} (\alpha_3 - \alpha_3^0)^q$$

1. R is the cumulative inelastic strain:

$$R = \int_0^t \left| \frac{\partial \epsilon}{\partial \tau} \right| d\tau$$

$E, n, n_1, n_2, \alpha_2^0, n_3, n_4, n_5, n_6, n_7, n_8, n_9, n_{10}, \alpha_3^0, q$

Miller

$$\sigma = E (\epsilon - \epsilon^I - \epsilon^T)$$

$$\dot{\epsilon}^I = B \theta^I \left| \operatorname{SINH} \left(\frac{|\sigma - \alpha_2|}{\alpha_3} \right) \right|^{1.5 n} \operatorname{sgn} (\sigma - \alpha_2)$$

$$\dot{\alpha}_2 = -H_1 \dot{\epsilon}^I - H_1 B \theta^I \left| \operatorname{SINH} (A_1 |\alpha_2|) \right|^n \operatorname{sgn} (\alpha_2)$$

$$\dot{\alpha}_3 = H_2 |\dot{\epsilon}^I| \left[C_2 + |\alpha_2| - \frac{A_2}{A_1} \alpha_3^3 \right] - H_2 C_2 B \theta^I \left| \operatorname{SINH} (A_2 \alpha_3^3) \right|^n$$

$1. \theta^I = e^{-\frac{Q}{kT}}$ for $T > 0.6 T_m$
 $\theta^I = B e^{\left(\frac{-Q}{0.6 k T_m} \right) \left(\ln \left(\frac{0.6 T_m}{T} \right) + 1 \right)}$ for $T \leq 0.6 T_m$

$E, B, n, H_1, A_1, H_2, C_2, A_2, \theta$

T_m is the melting temp.

k is the gas constant.

Hart

$$\sigma = E (\epsilon - \epsilon^I - \epsilon^T)$$

$$\dot{\epsilon}^I = \alpha^* \left(\frac{2}{3} \right)^{\frac{M}{2}} \left(\frac{|\sigma - \alpha_2|}{\alpha} \right)^M \operatorname{sgn} (\sigma - \alpha_2)$$

$$\dot{\alpha}_2 = \frac{3}{2} \nu \dot{\epsilon}^I - \frac{\alpha_3^I \left(\frac{2}{3} \right)^M e^{-\frac{Q}{RT}}}{\ln \frac{3 \alpha_3^I I / \lambda}{2 |\alpha|}} \operatorname{sgn} (\alpha_2)$$

$$\dot{\alpha}_3 = c \left(\frac{2}{3} \right)^{\frac{k}{2}} \nu e^{-\frac{Q}{RT}} \left(\frac{\alpha}{\alpha_3^I} \right)^k \frac{\alpha_3^I}{\ln \frac{\alpha_3^I}{\sqrt{\frac{2}{3}} \alpha_2}} \frac{1}{\sqrt{\frac{2}{3}} \alpha_2}$$

1. The drag stress is taken to be a constant. ν
Hence there is no α_3 as in other models. There is, however, a third internal state variable termed α_3^I .

$E, \alpha^*, M, \nu, G, m, f, Q, k, \lambda, c$

2. R is the gas constant.
T is the absolute temp.

Robinson $\sigma = E(\epsilon - \epsilon^I - \epsilon^T)$

$$\dot{\epsilon}^I = \frac{1}{2u} \left(\frac{1}{\sqrt{3}} \left| \frac{\sigma - \alpha_2}{K} \right| \right)^{n-1} (\sigma - \alpha_2)$$

1. G_0 is the initial
value of $\frac{\alpha_2^2}{3K^2}$

$E, u, K, m,$
 θ, H, R, c

$$\dot{\alpha}_2 = \frac{2uH}{\left(\frac{1}{\sqrt{3}} \left| \frac{\alpha_2}{K} \right| \right)^\beta} \dot{\epsilon}^I - R \left(\frac{1}{\sqrt{3}} \left| \frac{\alpha_2}{K} \right| \right)^{n-\theta-1} \alpha_2$$

Valanis $\sigma = E(\epsilon - \epsilon^I - \epsilon^T)$

$$\dot{\epsilon}^I = k_1 f_1(\epsilon, \sigma) \epsilon + k_2 f_2(\epsilon, \sigma) \alpha_1$$

1. Represents
simplified
form of
Valanis' model.

E, k_1, k_2
 f_1, f_2

TABLE II. ABILITY TO MODEL CERTAIN PHENOMENA

Theory	Unified	History Dependence	Bauschinger Effect	Temperature Dependence	Anelasticity	Multiaxial Representation
Cernocky and Krempf	X			X		X
Krieg, Swearengen, and Rhode	X	X	X	X	X	X
Bodner <u>et.al</u>	X	X	X	X	X	X
Walker	X	X	X	X	X	X
Miller	X	X	X	X	X	X
Hart	X	X	X	X	X	X
Robinson	X	X	X		X	X
Valanis	X	X		X		X

TABLE III. REQUIRED MATERIAL PARAMETER CHARACTERIZATION

Cernocky and Kremp1	Constant Strain Rate Tensile Tests with Intermittent Hold Times Relaxations Tests
Krieg, Swearingen, and Rohde	Stress Drop Tests Constant Strain Rate Tensile Tests
Bodner <u>et al.</u>	Constant Strain Rate Tensile Tests* Creep Tests
Walker	Constant Strain Rate Cyclic Tests Constant Strain Rate Tensile Tests
Miller	Creep Tests Constant Strain Rate Cyclic Tests Constant Strain Rate Tensile Test
Hart	Relaxation Tests
Robinson	Stress Drop Tests
Valanis	Constant Strain Rate Tensile Test*

*Represents Simplest Form of the Model

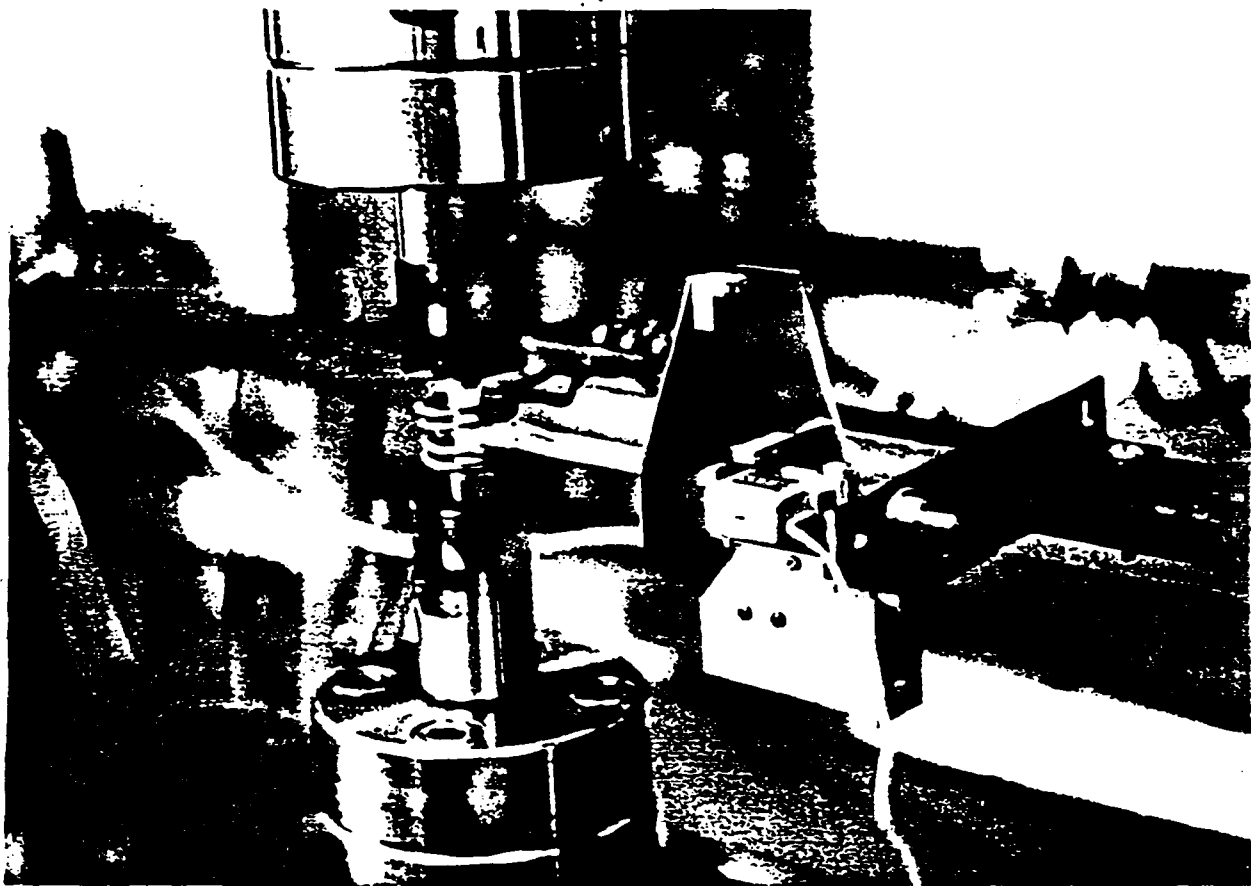


Fig. 1 Inconel 100 Specimen Tested at 1100°F in MTS-810 110 Kip Load Frame with MTS Quartz Rod Diametral Extensometer and Lepel Induction Heating Furnace

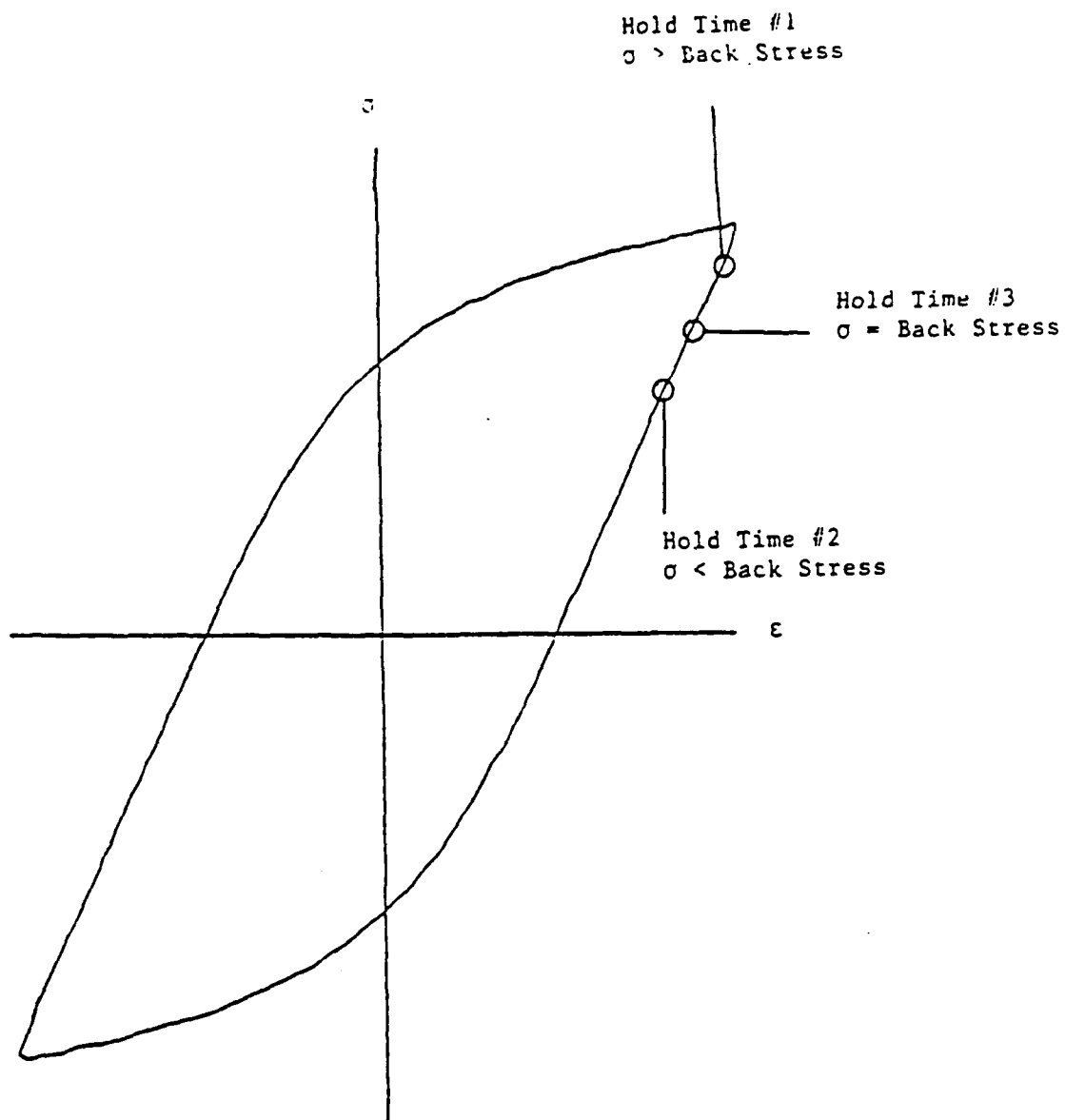


Fig. 2 Cyclic Hysteresis Loop with Hold Times

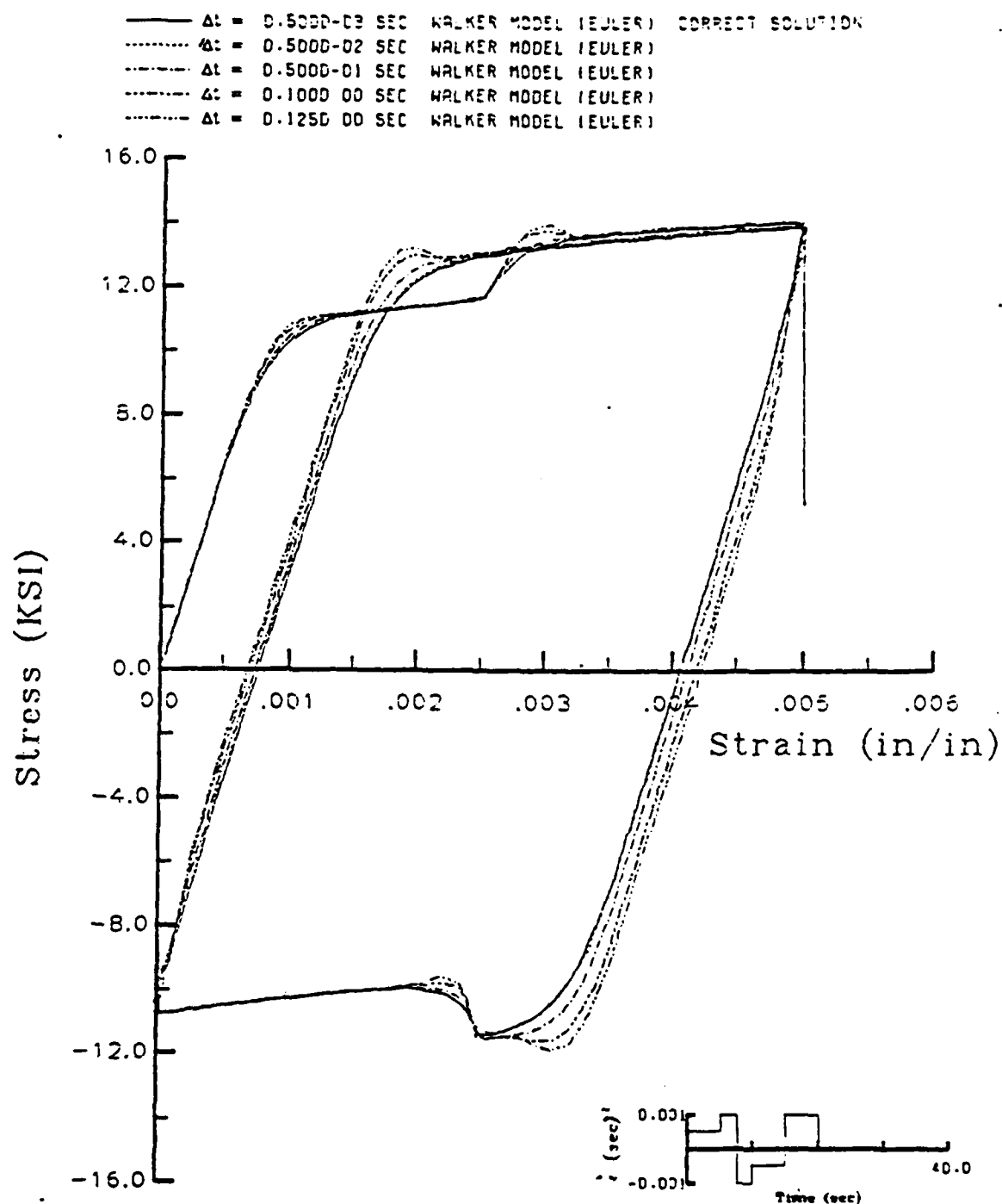


Fig. 3 Stability and Accuracy of Euler Integration
 for Walker's Model Using Various Step Sizes
 (Hastelloy-X at 1800°F)

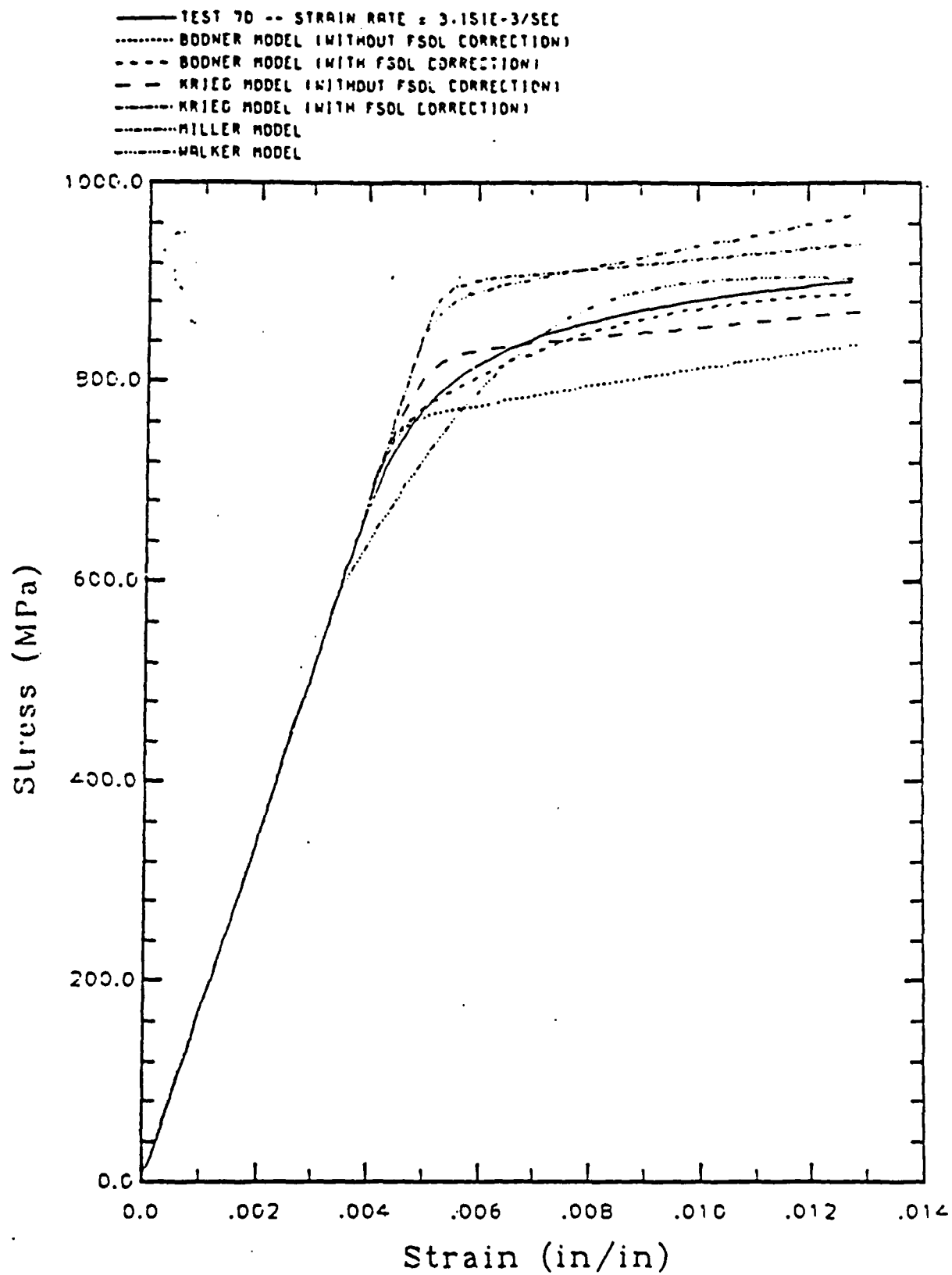


Fig. 4 Model Response as Compared to Test 70
 (Courtesy American Society of Mechanical Engineers)

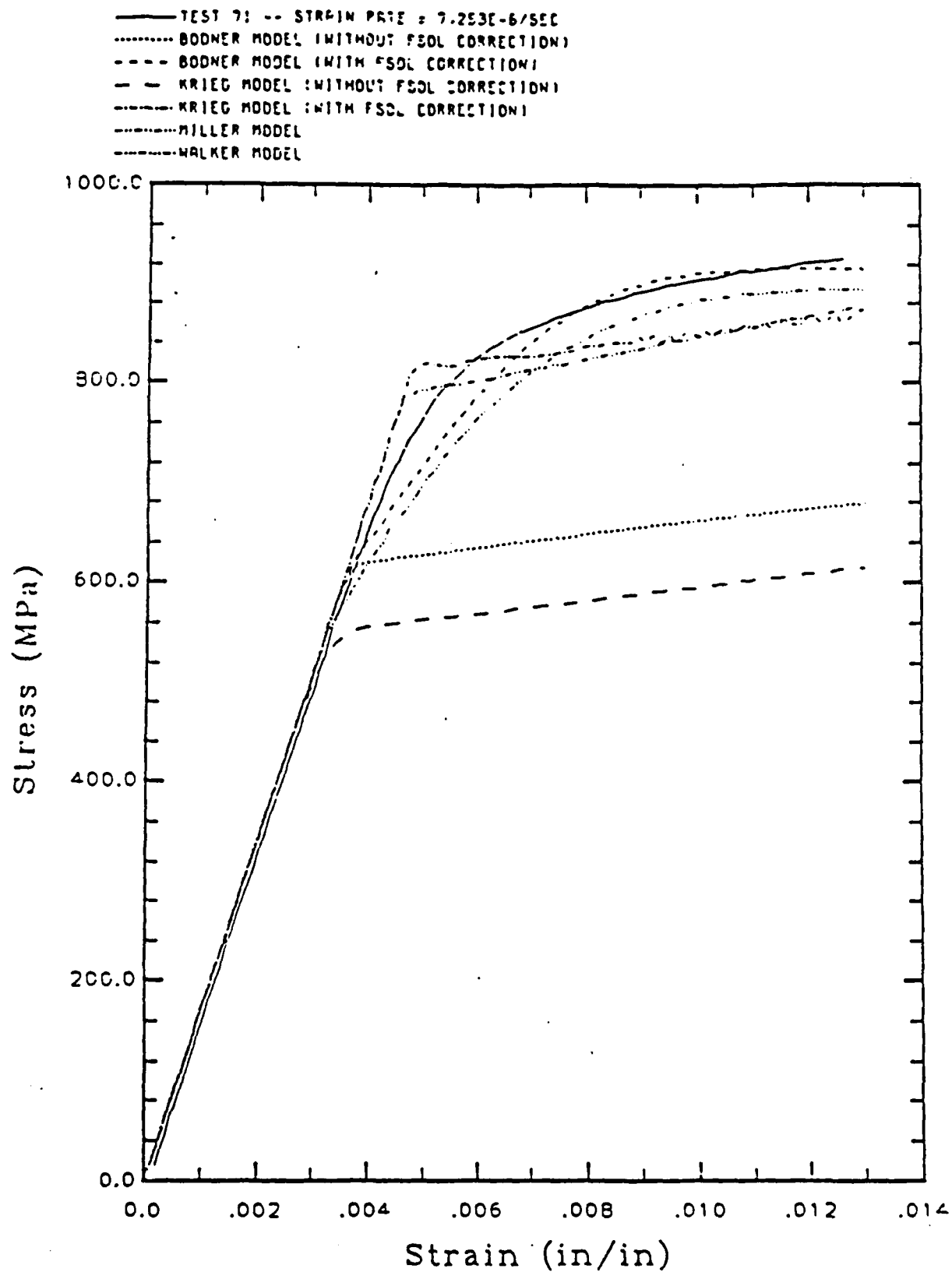


Fig. 5 Model Response as Compared to Test 71
 (Courtesy American Society of Mechanical Engineers)

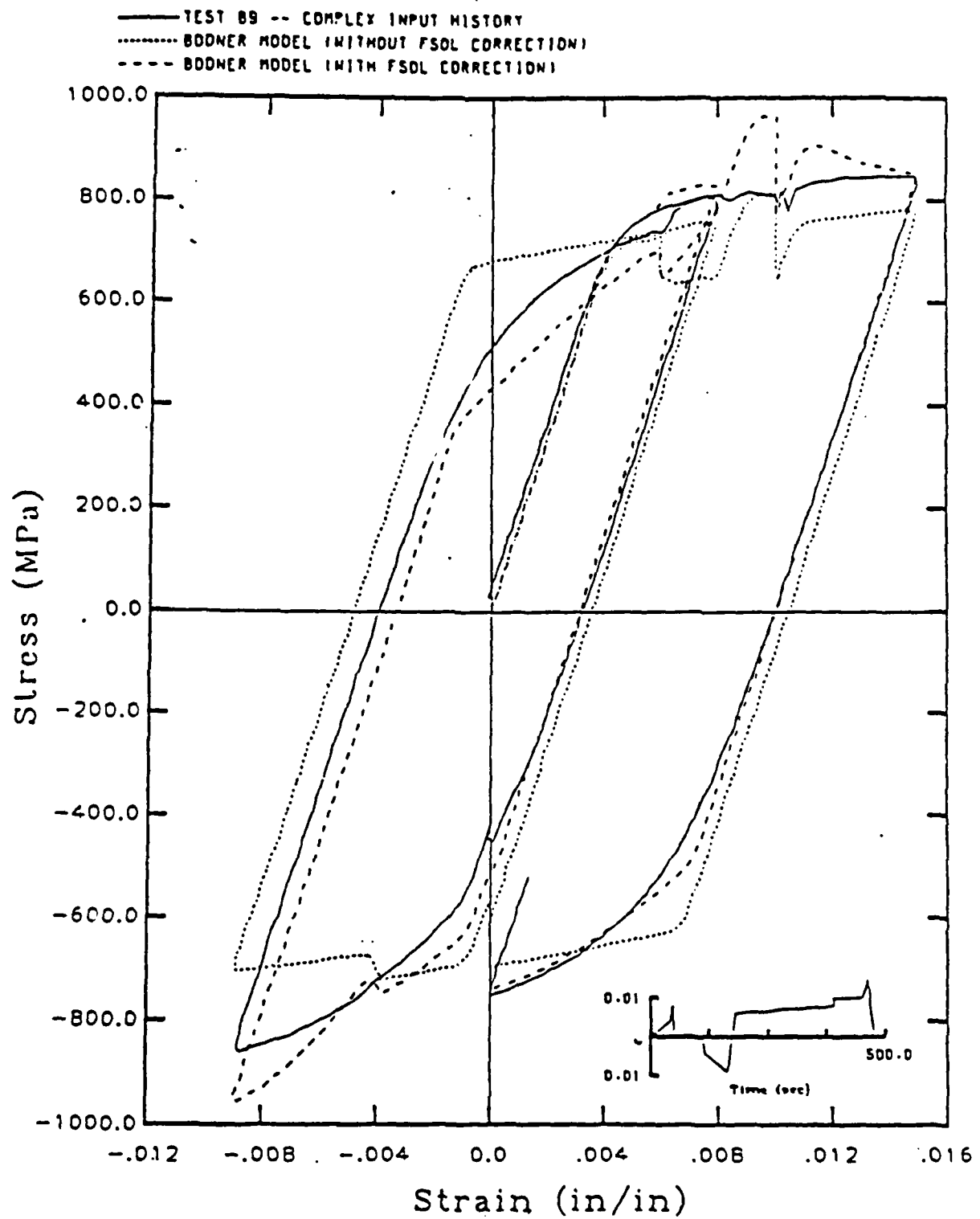


Fig. 6 Complex History-Bodner's Model
 (Courtesy American Society of Mechanical Engineers)

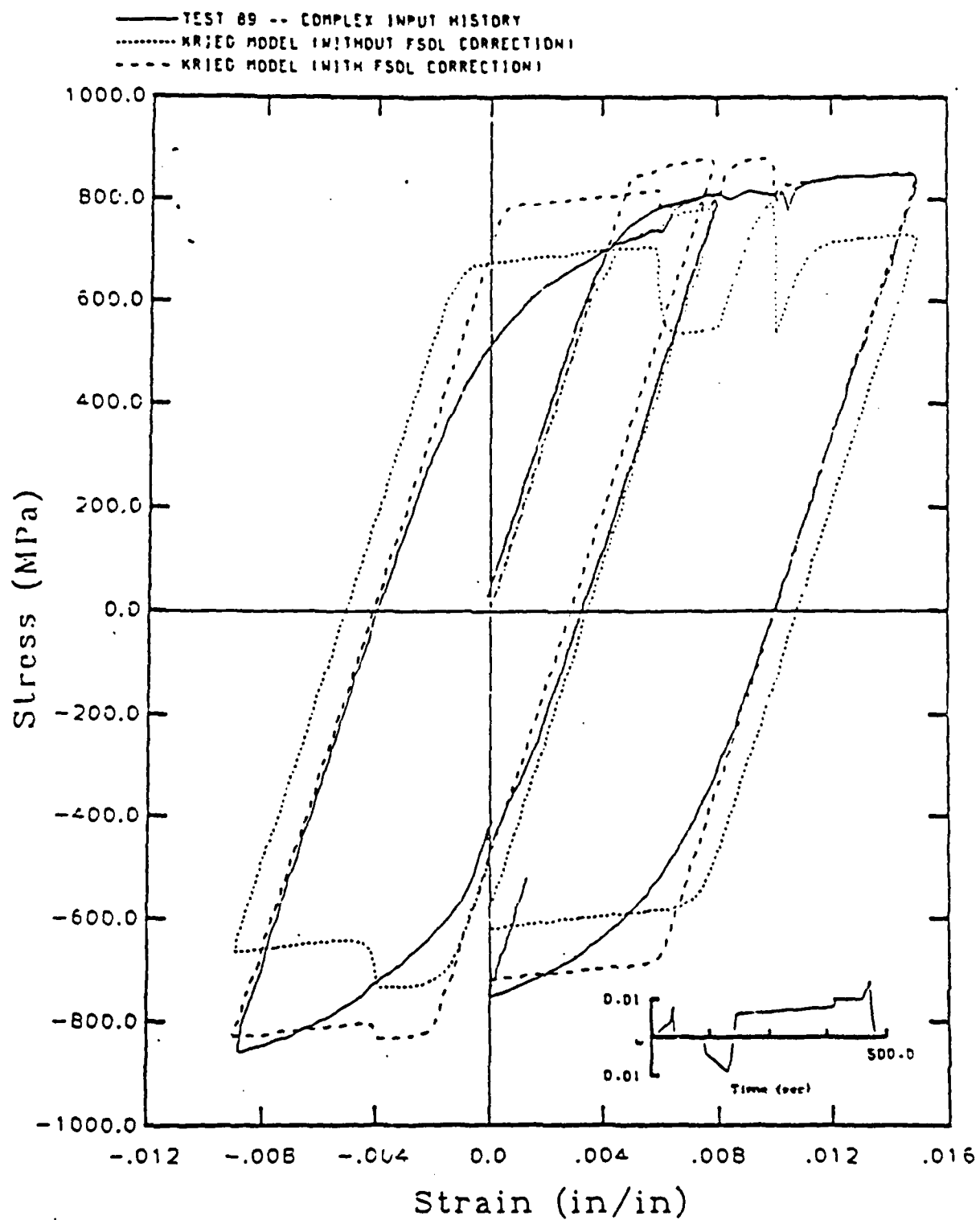


Fig. 7 Complex History-Model of Krieg, et al.
 (Courtesy American Society of Mechanical Engineers)

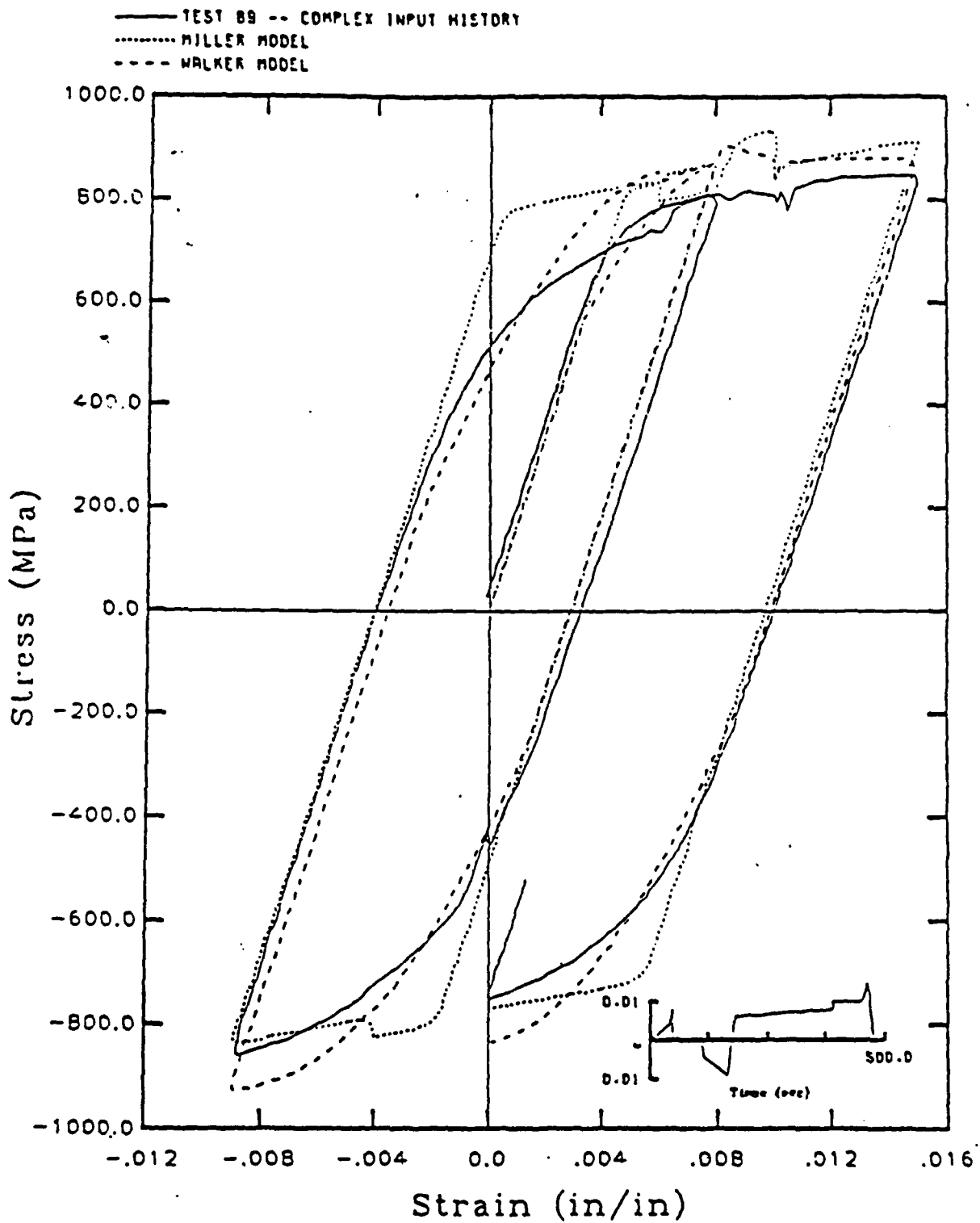


Fig. 8 Complex History-Schmidt and Miller's and Walker's Model
 (Courtesy American Society of Mechanical Engineers)

Appendix 7.7

Laser/Structure Interaction - A Comparison of Theory to Experiment

LASER/STRUCTURE INTERACTION - A COMPARISON OF THEORY TO EXPERIMENT

P.K. Imbrie*

D.H. Allen**

H.T. Chang***

Texas A&M University
College Station, Texas 77843

Abstract

A comprehensive experimental program has been developed to study the transient response of a viscoplastic plate subjected to rapid heat input. The experiments consisted of irradiating a clamped plate of Hastelloy X with a high energy 15 kW c.w. CO₂ laser, with displacement and temperature serving as measured data. A theoretical model is also being developed for comparison to the experimental results. The model assumes one-way thermomechanical coupling; that is, it is assumed that the temperature field is independent of deformation but not vice versa. The thermal analysis is nonlinear via radiation boundary conditions and temperature dependent thermal conductivities. The structural analysis includes geometric nonlinearity and material viscoplasticity. The experimental procedure and an abbreviated development of the model are described in this paper.

Nomenclature

A_e - area of two-dimensional finite element
 $[B_L]$ - matrix relating linear components of strain and deformation
 $[B_{NL}]$ - matrix relating nonlinear components of strain and deformation
 C_p - coefficient of specific heat at constant pressure
 D_{ij} - elastic modulus matrix
 f_i - components of body force per unit mass
 k - thermal conductivity
 m_{ij} - components of finite element mass matrix
 n_r, n_z - components of unit outer normal vector in cylindrical coordinates
 N, M - components of plate midsurface forces and moments per unit length
 N_i - finite element shape functions
 q - heat flux input

r - radial coordinate direction
 R_i - finite element external force components
 t - time
 T - temperature
 T_r - reference temperature at which radiation is zero
 u, v, w - components of plate displacement
 u_i - components of displacement in Cartesian coordinates
 z - axial coordinate direction
 $\bar{\alpha}$ - thermal absorptivity
 σ_1 - drag stress
 σ_{2ij} - back stress tensor
 θ_x, θ_y - components of plate rotation
 Γ - boundary of a domain
 Γ_e - boundary of a finite element
 ϵ - thermal emissivity
 ϵ_{ij} - strain tensor
 κ_{ij} - plate mid-surface rotations
 ϵ_{ij}^E - elastic strain tensor
 ϵ_{ij}^I - inelastic strain tensor
 ϵ_{ij}^T - thermal strain tensor
 θ_x, θ_y - nodal components of plate rotation
 λ - normality coefficient for inelastic strain rate
 ρ - mass density
 k - Boltzman's constant
 σ_{ij} - stress tensor

* Lecturer, Aerospace Engineering
 ** Professor, Aerospace Engineering
 Member AIAA
 *** Research Engineer, Aerostructures, Inc.,
 Arlington, Virginia

σ_{ij} - deviatoric stress tensor

Ω - interior of a domain

Introduction

The transient response of an aerospace structure exposed to rapid heating may be vastly different from that produced under steady state conditions. For applications such as gas-turbine combustors, rocket nozzles, space structures, and the like, large temperature gradients are commonly induced in a very short period of time. However, due to the complex and severe environment, little experimental data are available for use in developing new methods of analysis where material inelasticity occurs in the structure. Therefore, an experimental program was established to investigate the response of a metallic plate undergoing rapid heating with temperature and displacement as the primary variables of interest. The parameters varied in the experiment included: 1) plate thickness; 2) heat flux; and 3) duration of heat flux.

A solution algorithm has been developed by the authors for predicting the transient response of plates when subjected to rapid heat input. While the model itself is not the subject of this paper, it is presented in abbreviated form and is used to compare theory to experiment. The solution algorithm makes use of one-way thermomechanical coupling (it is assumed that the temperature field is independent of deformation), thermoviscoplastic response, and geometric nonlinearities. The finite element method is used in a two step process to compute the plate response. The thermal analysis is performed first, taking into account such things as nonlinear effects due radiation heat exchange and temperature dependent material properties. The results are then used as input to the structural analysis where nonlinear material response, using Bodner's¹ and Walker's² constitutive models and large rotational plate theory are used to compute plate deformation as well as stress and strain. Both the experimental and modelling programs are described in the following sections.

Model Development

The model is presented in abbreviated form in this section. Further details can be found in references 3 and 4. As shown in the flowchart in Fig. 1, the solution algorithm is constructed in two stages: the thermal analysis and the structural analysis. On a given time step, the thermal loads are evaluated. Then the temperature field is solved by the finite element method. Using this temperature field, along with the inelastic strain increment evaluated from the previous time step, yields the thermal strain. The thermal strain results in an unbalanced load from which the deformation field is approximated. An iterative procedure is utilized to bring the solution to convergence for a given time step. The solution is described in further detail below.

Thermal Analysis

An axisymmetric finite element model, developed to include nonlinear radiation boundary conditions, is used to construct the temperature field as a function of r and z for each time step. A typical two-dimensional axisymmetric heat transfer mesh is shown in Fig. 2.

The governing heat transfer equations are as follows:

$$\rho C_p r \frac{\partial T}{\partial t} - \frac{\partial}{\partial r} (kr \frac{\partial T}{\partial r}) - \frac{\partial}{\partial z} (kr \frac{\partial T}{\partial z}) = 0 \text{ in } \Omega \quad (1)$$

$$kr \frac{\partial T}{\partial r} n_r + kr \frac{\partial T}{\partial z} n_z = q_0 r + \cos(T_r^4 - T^4) \text{ on } r \quad (2)$$

Equations (1) and (2) may be cast into a Galerkin finite element formulation. Since this part of the model exists in the open literature³, it is not covered in detail here.

The resulting element equations are of the form

$$C_{ij} \dot{T}_j + a_{ij} T_j = q_i \quad (3)$$

where

$$C_{ij} = \int_{A_e} \rho C_p N_i N_j r dA_e \quad (4a)$$

$$a_{ij} = \int_{A_e} \left(\frac{\partial N_i}{\partial r} r k \frac{\partial N_j}{\partial r} + \frac{\partial N_i}{\partial z} r k \frac{\partial N_j}{\partial z} \right) dA_e + \int_{r_e} N_i (N_k T_k)^3 N_j r dr \quad (4b)$$

$$q_i = \int_{r_e} N_i q_0 r dr + \int_{r_e} N_i \cos T_r^4 r dr \quad (4c)$$

A linear triangular axisymmetric element is used in the analysis. Equation (3) for each element is assembled to give the following global system of ordinary differential equations:

$$[C] (\dot{T}) + [A] (T) = [Q] \quad (5)$$

The Crank-Nicholson scheme is then applied temporally to obtain the temperature field with time.

Structural Analysis

In the structural analysis, Von Karman theory⁷ is assumed for the thin plate bending motion, and material nonlinearity and viscoplastic constitution are included in the model. The material nonlinearity is introduced via the inelastic strain tensor, ϵ_{ij} , which is described in the next section.

The strain components are defined as

$$\epsilon_{ij} = \epsilon_{ij}^0 + \alpha_{ij} = \frac{1}{2} (u_{i,j} + u_{j,i}) + \frac{1}{2} (u_{3,i} u_{3,j}) + \alpha_{ij} \quad i, j = 1, 2 \quad (6)$$

Utilizing the above in a standard laminate scheme will result in

$$N = \bar{A} \bar{B} \quad \epsilon^0 - \epsilon^I - \epsilon^T \quad (7)$$

where

$$(\bar{A}_{ij}, \bar{B}_{ij}, \bar{D}_{ij}) = \int_{-\frac{h}{2}}^{\frac{h}{2}} D_{ij}(1, z, z^2) dz \quad (8)$$

Note that the coupling matrix $|\bar{B}|$ does not disappear due to the through thickness variation of elastic modulus, D_{ij} , which is temperature dependent.

The governing equations for the plate motion are thus derived by satisfying the conservation of linear and angular momentum $[B]$:

$$N_{x,x} + N_{yx,y} - \rho u_{,tt} = 0 \quad (9)$$

$$N_{xy,x} + N_{y,y} - \rho v_{,tt} = 0 \quad (10)$$

$$[D_{1j} \epsilon_j + \bar{B}_{1j}(\epsilon_j^0 - \epsilon_j^I - \epsilon_j^T)]_{,xx} +$$

$$[D_{2j} \epsilon_j + \bar{B}_{2j}(\epsilon_j^0 - \epsilon_j^I - \epsilon_j^T)]_{,yy} +$$

$$2[D_{3j} \epsilon_j + \bar{B}_{3j}(\epsilon_j^0 - \epsilon_j^I - \epsilon_j^T)]_{,xy} +$$

$$p + N_{x,w,xx} + 2N_{xy,w,xy} + N_{y,w,yy} - \rho w_{,tt} = 0 \quad (11)$$

Integrating equations (9) through (11) against variations in the components of the displacement field will result in the following variational principle.

$$\int_A \delta u (N_{x,x} + N_{yx,y} - \rho u_{,tt}) dx dy +$$

$$\int_A \delta v (N_{xy,x} + N_{y,y} - \rho v_{,tt}) dx dy +$$

$$\int_A \delta w ([D_{1j} \epsilon_j + \bar{B}_{1j}(\epsilon_j^0 - \epsilon_j^I - \epsilon_j^T)]_{,xx} +$$

$$[D_{2j} \epsilon_j + \bar{B}_{2j}(\epsilon_j^0 - \epsilon_j^I - \epsilon_j^T)]_{,yy} +$$

$$2[D_{3j} \epsilon_j + \bar{B}_{3j}(\epsilon_j^0 - \epsilon_j^I - \epsilon_j^T)]_{,xy} + p) +$$

$$N_{x,w,xx} + 2N_{xy,w,xy} + N_{y,w,yy} - \rho w_{,tt}) dx dy = 0 \quad (12)$$

Incrementing the field variables, neglecting the third and higher order terms of the displacement increment, and applying finite element discretization results in

$$[M](\dot{u})^{t+\Delta t} + [K](\Delta u) = \{R\}^{t+\Delta t} - \{F_1\} - \{F_2\} \quad (13)$$

where $[M]$ is the mass matrix and

$$[K] = [K_{NL}] + [K_L] \quad (14)$$

$$[K_L] = \sum_{n=1}^n \int_V [B_{NL}]^T [D]^{t+\Delta t} [B_L] dV_e \quad (15)$$

$$[K_{NL}] = \sum_{n=1}^n \int_V [B_{NL}]^T [S]^{t+\Delta t} [B_{NL}] dV_e \quad (16)$$

Also, $\{R\}$ is the external load vector and

$$\{F_1\} = \sum_{n=1}^n \int_V [B_L]^T \{(\epsilon) - [D]^{t+\Delta t} (\Delta \epsilon^I + \Delta \epsilon^T) +$$

$$[\Delta D] (\epsilon^0 + \epsilon^I - \epsilon^T - \epsilon^I) \} dV_e \quad (17)$$

$$\{F_2\} = \sum_{n=1}^n \int_V [B_{NL}]^T \{ -[D]^{t+\Delta t} (\Delta \epsilon^I + \Delta \epsilon^T) +$$

$$[\Delta D] (\epsilon^0 + \epsilon^I - \epsilon^T - \epsilon^I) \} dV_e \quad (18)$$

Solving equation (13) by the Newmark integration scheme will give the first approximation of (Δu) at time $t+\Delta t$. The Newton Raphson iteration method will give convergence to the nonlinear solution⁹.

Thermomechanical Constitutive Models

In order to prescribe the forcing functions $\{F_1\}$ and $\{F_2\}$ defined in equations (17) and (18) it is necessary to determine the inelastic strain increment, $\Delta \epsilon_{ij}^I$. This is accomplished by integration of the selected viscoplastic constitutive model. The authors are currently using Walker's model¹⁰, as well as the anisotropic hardening form of Bodner's model¹¹. These models are compared critically in reference 11.

Bodner's model assumes

$$\dot{\epsilon}_{ij}^I = \lambda \sigma_{ij}^I \quad (19)$$

whereas Walker's model proposes

$$\dot{\epsilon}_{ij}^I = \lambda (\epsilon_{ij}^I - \alpha_{2ij}) \quad (20)$$

where

$$\lambda = \lambda (\sigma_{ij}, \alpha_1, \alpha_{2ij}) \quad (21)$$

and the above is supplemented by an additional set of evolution laws of the form

$$\dot{\alpha}_{ij}^n = \rho_{ij} (\sigma_{k\ell}, \alpha_{k\ell}^n) \quad (22)$$

Equations (19) and (22) are typically numerically stiff, so that numerical integration to obtain ϵ_{ij}^I is not straightforward¹². Bodner's model is currently being integrated using Euler's forward method, whereas Walker's model is integrated using Euler's backward method¹³. Both models are subincremented on each time step in order to produce accurate values for $\Delta \epsilon_{ij}^I$ on each time increment.

Experimental Program

In order to verify analytical models currently being constructed, an experimental program has been developed to investigate the transient response of a viscoplastic plate subjected to rapid heat input. Of particular interest is the measurement of displacement and

temperature fields for a rectangular plate specimen undergoing rapid heating. The experimental program is divided into two phases: 1) a low energy ($<100\text{W/in}^2$) input phase being conducted at Texas A&M University; and 2) a high energy ($>1\text{KW/in}^2$) input phase being performed at the Air Force Wright Aeronautics Laboratories using the LMEL I (Laser-Hardened Materials Evaluation Laboratory) facility.

Low Energy Testing

The low energy, semi-rapid heating experiments make use of a bank of quartz lamps, to irradiate the plate specimens. The purpose of these experiments is two fold: first, they serve as a simulation of the high energy experiments; and second, they produce temperature and displacement fields which change at a much slower rate. Therefore, valuable information with regard to expected experimental results can be gained, in addition to verifying model predictions under less severe conditions.

The heat source for these experiments are tubular quartz lamps with tungsten emitters. A circular heat target zone is obtained by shielding excess energy from the specimen via a water cooled orifice plate, which is fitted with a variable size aperture. This apparatus is attached directly to the specimen support fixture as shown in Fig. 3. The support fixture imposes clamp-like boundary conditions along each edge of a rectangular specimen (details on the support fixture are discussed later in the paper). Insulation shields enclose both sides of the specimen, in order to reduce the amount of heat transfer due to free convection.

Displacement and temperature data are obtained using a PC based data acquisition system, which also serves as the quartz lamp controller. A single DC-operated LVDT, which can be positioned at various radial locations, is used to measure displacements. A coupling tang enables dual measurement of displacement with the LVDT and a precision dial indicator. Measurement of the in-plane temperature field and transverse temperature gradients are made using K-type 30 gage thermocouples intrinsically mounted to the plate specimen. The specimens for this phase of testing were made of 6061-T6 aluminum. This material was selected because it exhibits inelastic deformation at relatively low temperatures ($<500^\circ\text{F}$).

Testing to date has not yielded a high enough input energy to produce a significant specimen temperature rise. In addition, the current aperture system has failed to generate a well defined target zone. Therefore, the orifice plate is being refitted with a lens system that will serve to both condense available heat energy and focus it on the target spot.

High Energy Testing

The high energy, rapid heating experiments made use of an electric discharge 15 KW continuous-wave carbon dioxide laser operating at a wave length of $10.6\text{ }\mu\text{m}$ with a flat-top beam profile, to irradiate the plate specimens. The test apparatus was placed in a nitrogen flood box during irradiation in order to prevent oxidation

of the specimen surface while it was being heated. In addition, instrumentation for measuring temperature and displacement fields, as well as high speed photographic documentation were used and will be discussed in detail below.

A specimen support fixture was designed to impose clamp-like boundary conditions along each edge of a rectangular plate specimen. The superstructure of the fixture was fabricated from 6061-T6 aluminum to support the specimen in the vertical position, as shown in Figs. 4a and 4b. An insert made of 304 stainless steel serves both as a support stiffener and water jacket. A total waste water cooling system is used to provide a uniform and constant plate boundary temperature. Thermocouples were attached to each half of the insert at the mid-position, approximately 0.5 in away from the specimen, to record any temperature variations.

The two piece (with the inserts in place) picture frame style fixture securely clamps the specimen in position, using 24 socket head cap screws torqued to 120 in-lbs. An off-set, staggered screw pattern is used to ensure a uniform clamping zone. In addition, the fixture is indexed with hardened dowel pins so that alignment between the fixture and specimen remains consistent from test to test.

The material selected for this research is Hastelloy X. Hastelloy X is a nickel-chromium-iron-molybdenum alloy that possesses a combination of oxidation resistance and high strength at temperatures in excess of 2200°F . It was selected for this test program primarily for its high temperature characteristics, but also because it is widely used in the research community in conjunction with high temperature constitutive modeling and testing.

The Hastelloy X material was obtained in plate form in nominal thicknesses of $1/16$ in, $1/8$ in, and $1/4$ in, and was used to fabricate a total of 18 specimens (6 of each thickness). The material was received in an annealed condition specified by ASTM 5536 and used without further heat treatment. No micrographic studies were performed to investigate the variations in grain structure or size that existed between the different plate thicknesses.

All specimens were machined to finished dimensions of 13×13 in, corresponding to the outer edge of support fixture. Therefore, taking into account the support fixture clamping zone, the effective plate dimensions were reduced to 10×10 in. Each specimen was hand sanded with #320 grit sand paper and glass bead blasted to produce a low luster finish. No other special surface treatment, such as anodizing, blueing, or the like, was performed to enhance the thermophysical properties of the material.

An integrated instrumentation package was used to simultaneously measure the displacement and temperature fields of a plate specimen undergoing laser irradiation. The primary instrumentation included: 1) LVDT's (Linear Variable Differential Transformers) for measuring displacement; 2) thermocouples for measuring temperature; 3) a radiant pyrometer for measuring surface brightness temperature; and 4) strain

gages for measuring the plate vibration frequency. A 12 bit, high speed data system (called the PCM) was used to convert the analog output of these transducers and thermocouples to an equivalent binary form at an approximate rate of 1.2 KHz. Once converted, the data were stored on magnetic tape for subsequent conversion to engineering units and any other post-processing. Described below is a more detailed discussion on the implementation of the various pieces of instrumentation.

A total of 11 DC-operated LVDT's were used to sense the out-of-plane displacements resulting from the laser deposition. The outputs of the LVDT's were scaled via the data system, to detect displacements as small as 0.0001 in, at a published maximum frequency response of 15 Hz. The LVDT's were arranged in a symmetric pattern around the heat zone and were rigidly mounted to a support system which was positioned directly behind the specimen, as shown in Fig.'s 5a and 5b. In addition, 2 LVDT's were used to monitor relative movement between the LVDT support system and plate fixture.

Measurement of the in-plane temperature field, through-thickness temperature gradients, and non-contact plate surface temperatures, were made using 21 K-type 30 gage thermocouples. The thermocouples were concentrated in a 1 in diameter circle around the heat zone and were arranged in a symmetric pattern for measuring the in-plane temperature field. The through-thickness temperature gradients were measured using thermocouples positioned at the same coordinate locations, but mounted on the front and back of the specimen. All thermocouples were intrinsically mounted to the specimen via a welding operation with the exception of 4 thermocouples. These thermocouples were bead welded junctions which were mounted approximately 0.050 in from the surface of the plate. All thermocouples mounted on the front surface of the plate (the heat side) were Inconel 600 sheathed to withstand the extreme temperatures, whereas the thermocouples mounted on the back side of the specimen were insulated using high temperature glass braid. The thermocouples were connected to the data system via a 150°F reference oven, which for this test was left open to room temperature. For thermocouple input, the data system was scaled to record voltage changes on the order of 0.03 mV, which corresponds to a measured temperature resolution of approximately 1.4°F. Thus, taking into account the NBS wire error specification and the above resolution, a maximum temperature uncertainty between 5.36°F and 18.5°F can be expected.

A germanium radiation pyrometer was used to obtain relative measurements of the plate surface brightness temperature. The pyrometer is a high speed transducer, having a peak spectral response at a wavelength of 1.5 μ m and an effective temperature range between 900°F and 5400°F, within a target area of approximately 0.0491 in². The pyrometer was aligned to record temperatures within the laser irradiated spot diameter in conjunction with a thermocouple. The output of the pyrometer was fed into the data system for use later in developing an appropriate transfer function for the slower responding thermocouples.

A 350 μ strain gage was used to measure the dynamic response of the specimen resulting from the rapid heating. The strain gage was mounted parallel with the edge of the plate specimen approximately 2.5 in off center. Since vibration frequencies and not strain magnitudes were of interest, the output of the strain gage was displayed on a visicorder strip chart recorder.

A total of 4 laser/structure interaction experiments have been conducted thus far, representing approximately one third of those planned under this phase of testing. All 4 tests utilized the same 1/16 in thick plate specimen with heat flux and exposure time serving as input test variables (as shown in Table 1) and displacement and temperature fields serving as measured or output quantities. Before testing, the laser beam was characterized in terms of the amount of energy being delivered on target, in addition to the beam width and density. Target energy was measured by reflecting approximately 7% of the total available energy into a torpedo calorimeter. The beam profile was determined by ablation of plexiglass samples as shown in Fig. 6. By measuring the plexiglass burn patterns, both the laser target area and beam uniformity in the radial direction can be found. For this experiment, the laser contact spot was found to be ellipsoidal, having major and minor axis length equal to 0.5235 in and 0.5276 in, respectively (this is a result of the beam striking the specimen at a 10° incidence angle in order to prevent energy feedback through the laser pattern).

Figures 7 through 10 show typical output of the thermocouples and LVDT's at discrete locations during laser irradiation (with and without time averaging). In particular, Figs. 7 and 9 show raw data (in engineering units) where there is an apparent electrical noise problem. A power spectrum density analysis indicates that 60 Hz and its harmonics, were present in the data. This resulted in peak-to-peak variations of approximately 44°F and 0.0074 in for temperature and displacement, respectively. Future tests will incorporate real time analog filtering and/or post test digital filtering, in order to resolve this problem. Figures 8 and 10 present the same data as discussed above, except that time averaging has been used.

No comment is made about the validity of the data, except to note the following. First, the typical temperature profile shown in Figs. 7 and 8, indicates the thermocouple did not respond during the laser shot. This should not be interpreted as thermocouple lag. For intrinsically mounted thermocouples, one would expect a response time in the msec time frame. It is presumed that the laser firing sequence caused a voltage shift and saturated the A to D system low. Second, a target zone temperature of 800-1000°F was generally encountered, which was far below the 1500-2000°F temperature expected. Lastly, Figs. 9 and 10 show a typical LVDT data that indicates a drastic displacement reversal during irradiation. That is, the specimen initially deforms in the positive direction (towards the heat source) and then reverse itself, going through a neutral point to assume a negative displacement. The authors are awaiting photographic confirmation, via high speed

cameras, to see if this phenomena actually exists.

The primary objective of this first phase of testing was to establish a baseline experimental procedure which would verify analytical models currently under construction. To this end, that objective has been met, with the exception of the following problem areas (which are currently being corrected): 1) energizing and/or firing the laser adversely affected the measured data, both with noise and voltage shifts; 2) there was no explicit indication of when the laser power was on and off the target area; 3) the nitrogen flood box did not provide an inert environment and made photographic documentation difficult; 4) the thermocouple reference junction needed to be below room temperature; 5) a constant aperture setting on the video and high speed cameras made photographic interpretation difficult as the specimen heated up; 6) the pyrometer data was inappropriately scaled; and 7) there was apparent movement of the LVDT support stand during laser deposition.

Comparison of Model to Experiment

Limited results have been obtained with the model for comparison to the experimental results given in the previous section. Experimental constants for Bodner's model have been obtained for Hastelloy X¹⁴ as shown in Table 2. The model has been used to predict the response of the square plate of 1/16 in thickness with spatially and temporally constant heat input of 12.2 Btu/in² sec over a 0.25 in radius spot at the center of the plate. Predicted temperature at the front center of the plate versus time is shown for the first 0.08 sec in Fig. 11, where it can be seen that the plate is heated rapidly to a temperature of about 1300°F. This heating is sufficient to cause a center displacement of approximately 0.02 in (about 33% of the plate thickness), as shown in Fig. 12. The displacement field in turn produces radial and hoop stresses near the plate center which rapidly exceed the material yield point on the front surface, as shown in Figs. 13 and 14. These stresses are induced, in large measure, by the plate bending which occurs near the center of the plate, as shown in Fig. 15.

A comparison between Figs. 8 and 11 shows that the predicted and experimentally observed temperatures are not in agreement. Furthermore, Figs. 10 and 12 demonstrate that the displacement predictions are also not in accord with experimental observations. The authors hasten to point out that both the experimental and theoretical results are first passes, and, as such, no attempt has been made to "massage" either result to match the other. Given the complex nature of both the model and experiment, the discordant results are to be expected. Since there are numerous sources for the disagreement, our current emphasis is on uncovering the most important sources in such a way as to enhance the accuracy of the model.

Briefly, we suspect the following sources of disagreement between the model and experiment:

1) We have reason to suspect that both the LVDT's and thermocouples are giving spurious results for short time spans. We are currently studying this problem.

2) The model assumes that the input source commences instantaneously, whereas the laser output indicates an approximately linear rise time of .003 sec. We are modifying the model to account for this.

3) Initial indications are that the input heat source is not spatially homogeneous, thus producing a temperature field which is not axisymmetric.

4) Currently, we can measure only the amount of heat energy being delivered on target, future tests will try to measure the amount of energy being reflected by the specimen.

5) The very rapid heat input may cause thermal waves which are not predicted by our parabolic heat equation. We are thus considering various hyperbolic forms of the heat equation.

6) The computer code currently requires one CPU day on a VAX 8880 (3 real time days) to produce the first 0.08 sec of predicted response. We are attempting to improve the computational efficiency of the model so that longer term predictions can be obtained.

Conclusion

It is obvious that the experimental results are not in agreement with the model at this point in time. While the authors cannot say with certainty what the causes for discrepancy are, it is the general feeling here that the experimental program needs to be refined considerably before a critical comparison of the model and experiments will yield fruitful results. We are currently making progress in both directions.

Acknowledgement

This research was sponsored by the Air Force Office of Scientific Research under contract no. F49620-86-K-0016. The authors would especially like to thank Dr. George P. Sendeckyj and his support technicians at AFWAL. Their continued efforts brought the experimental phase of this research to fruition.

References

1. Bodner, S.R. and Partom, Y., "Constitutive Equations for Elastic-Viscoplastic Strain-Hardening Materials," Journal of Applied Mechanics, Vol. 42, No. 2, pp. 365-369, 1975.
2. Walker, K.P., "Representation of Hastelloy-X Behavior at Elevated Temperature with a Functional Theory of Viscoplasticity," ASME J. Eng. Mat. & Tech., 1982.
3. Chang, H.T. and Allen, D.H., "A Finite Element Analysis of a Viscoplastic Plate Subjected to Rapid Heating," to appear in Mechanics of Structures and Machines an International Journal, 1988.

4. Chang, H.T. and Allen, D.H., "Analysis of Viscoplastic Plates Subjected to Rapid External Heating," Proceedings 29th AIAA/ASME/ASCE/AHS Structures, Structural Dynamics and Materials Conference, Part III, pp. 1640-1647, 1988.
5. Lutz, J.D., Allen, D.H., and Haisler, W.E., "A Finite Element Model for the Thermoelastic Analysis of Large Composite Space Structures," Journal of Spacecraft and Rockets, Vol. 24, No. 5, pp. 430-436, 1987.
6. Moshaiov, A. and Vorus, W.S., "Elastic-Plastic Plate Bending Analysis by a Boundary Element Method with Initial Plastic Moments," Int. J. Solids Structures, Vol. 22, pp. 1213-1229, 1986.
7. Timoshenko, S.P. and S. Woinowsky-Krieger, Theory of Plates and Shells, McGraw-Hill, New York, 1959.
8. Ashton, J.E. and Whitney, J.M., Theory of Laminated Plates, Technomic, Connecticut, 1970.
9. Bathe, K.J., Finite Element Procedures in Engineering Analysis, Prentice-Hall, Englewood Cliffs, 1982.
10. Chan, K.S., Lindholm, U.S., Bodner, S.R., and Walker, K.P., "A Survey of Unified Constitutive Theories," Non-Linear Constitutive Relations for High Temperature App. ~ 1984, NASA CP 2369, pp. 1-24, 1985.
11. James, G.H., Imbrie, P.K., Hill, P.S., Allen, D.H., and Haisler, W.E., "An Experimental Comparison of Current Viscoplastic Models at Elevated Temperature," J. Engr. Mat. Tech., Vol. 109, pp. 130-139, 1987.
12. Imbrie, P.K., James, G.H., Hill, P.S., Allen, D.H., and Haisler, W.E., "An Automated Procedure for Material Parameter Evolution and Uncertainty Analysis for Viscoplastic Constitutive Models," to appear in J. Engr. Mat. Tech., 1988.
13. Haisler, W.E. and Imbrie, P.K., "Numerical Considerations in the Development and Implementation of Constitutive Models," NASA CP 2369, NASA Lewis Research Center, pp. 169-186, 1985.
14. Tony, M., NASA Lewis Research Center, personal correspondence.

Table 1. Laser Parameters for the Specified Tests

Test	Shot Number	Incident Energy (KW)	Beam Area (cm ²)	Heat Flux (KW/cm ²)	Shot Duration (sec)
1	49540	1.4	1.4	1	5.0
2	49541	2.8	1.4	2	3.0
3	49546	4.2	1.4	3	1.0
4	49550	7.0	1.4	5	1.2-1.6

Table 2. Bodner-Partom Model Material Constants for Hastelloy X

Constant		Temperature			
		Room Temp	1200°F	1600°F	
n	1.0	1.0	1.0	0.75	
D ₀	10E4	10E4	10E4	10E4	
m ₁	- MPa ⁻¹ (KSI ⁻¹)	0.02 (1.38E-4)	0.1 (6.89E-4)	0.1 (6.89E-4)	
m ₂	- MPa ⁻¹ (KSI ⁻¹)	1.8 (1.24E-2)	2.4 (1.65E-2)	2.4 (1.65E-2)	
m ₃	- MPa ⁻¹ (KSI ⁻¹)	0.001 (6.89E-6)	0.01 (6.89E-5)	0.01 (6.89E-5)	
z ₀	- MPa (KSI)	1200 (1.74E5)	1550 (2.248E5)	600 (8.7E4)	
z ₁	- MPa (KSI)	2000 (2.9E5)	2000 (2.9E5)	2000 (2.9E5)	
z ₂	- MPa (KSI)	1200 (1.74E5)	1550 (2.248E5)	600 (8.7E4)	
z ₃	- MPa (KSI)	1200 (1.74E5)	800 (1.16E5)	500 (7.25E4)	
A ₁	- sec ⁻¹	0	6.5E-7	6.5E-7	
A ₂	- sec ⁻¹	0	6.5E-7	6.5E-7	
r ₁	0.98	0.98	0.98	0.98	
r ₂	0.98	0.98	0.98	0.98	
E	- MPa (KSI)	2.07E6 (3.002E7)	1.61E6 (2.335E7)	1.37E6 (1.987E7)	

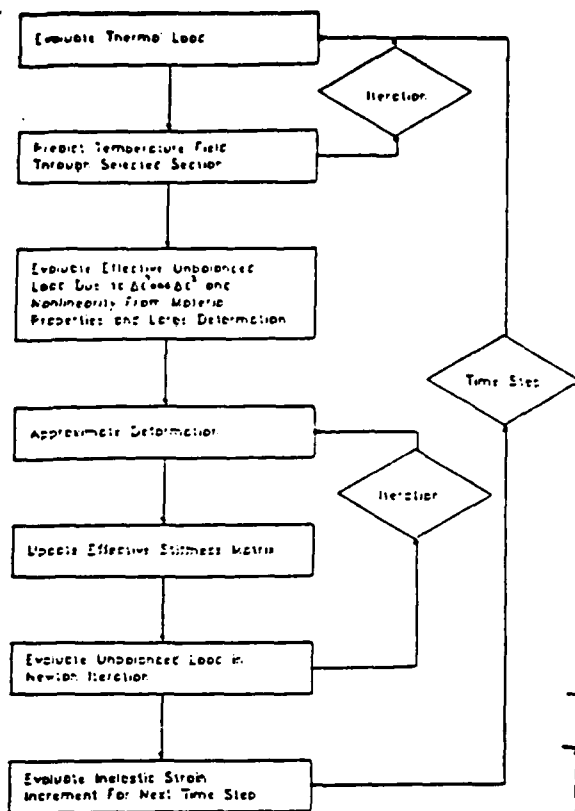


Fig. 1 Flowchart of Solution Algorithm

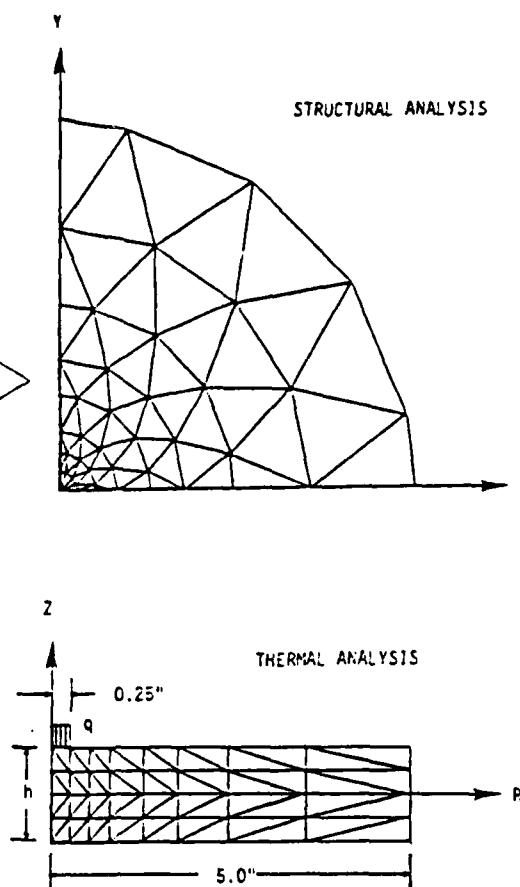
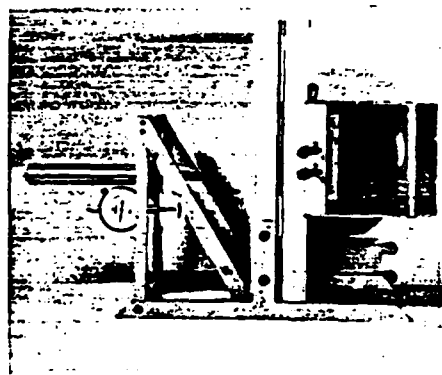


Fig. 2 Mesh Diagram of the Thermal and Structural Analysis

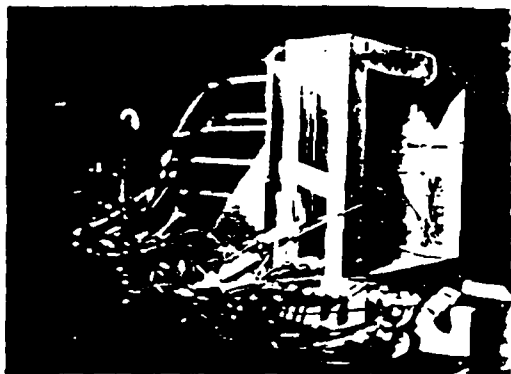


a) Test Frame - Assembly View



b) Test Frame - Side View

Fig. 3 Low Input Heat Energy Test Frame

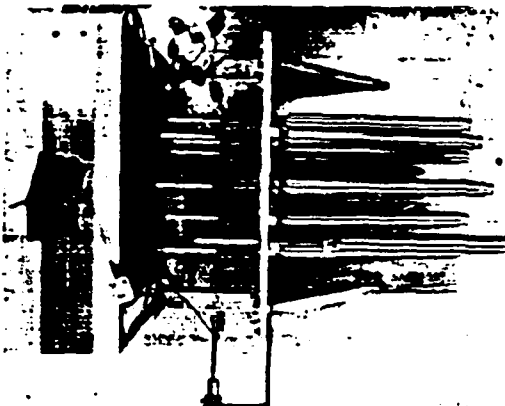


a) Support Structure - Side View

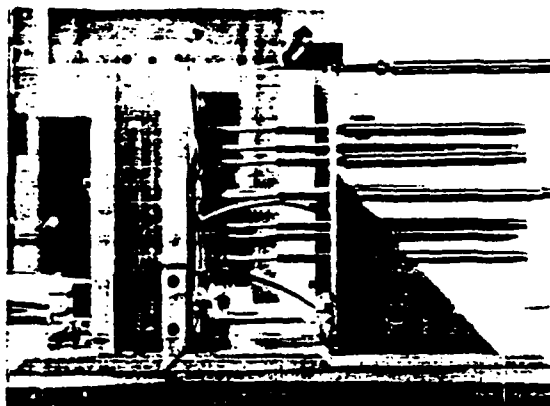


b) Support Structure - Front View

Fig. 4 Plate Specimen Support Fixture



a) LVDT Support Stand - Top View

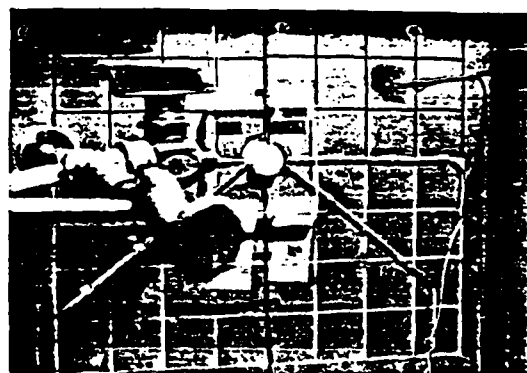


b) LVDT Support Stand - Side View

Fig. 5 LVDT Support Stand Positioned Behind the Specimen



a) Before Ablation



b) After Ablation

Fig. 6 Plexiglass Samples Used to Measure the Laser Beam Width and Density

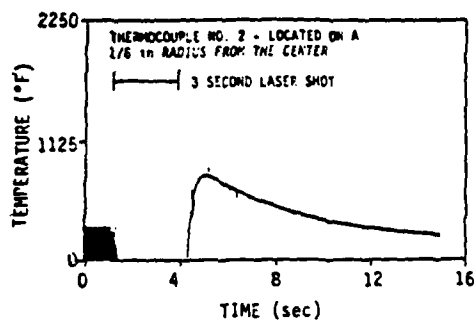


Fig. 7 Typical Thermocouple Output for a 2 KW/cm² 3 Second Duration Test

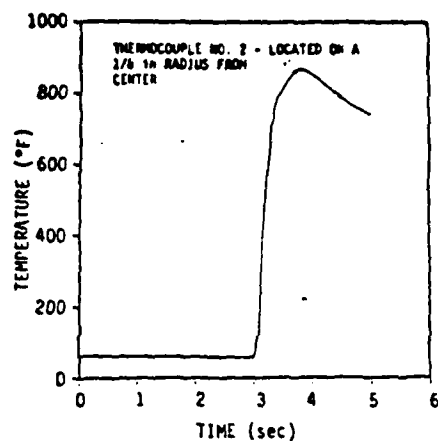


Fig. 8 Time Averaged Thermocouple Output for a 2 KW/cm² 3 Second Duration Test

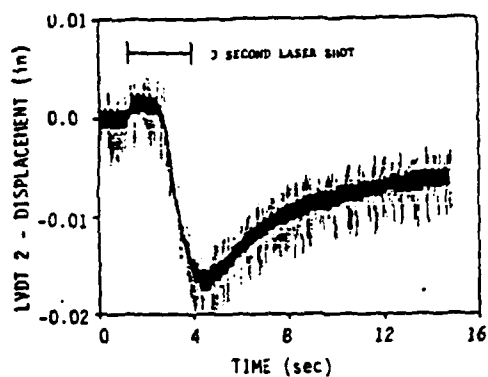


Fig. 9 Typical LVDT Output for a 2 KW/cm² 3 Second Duration Test

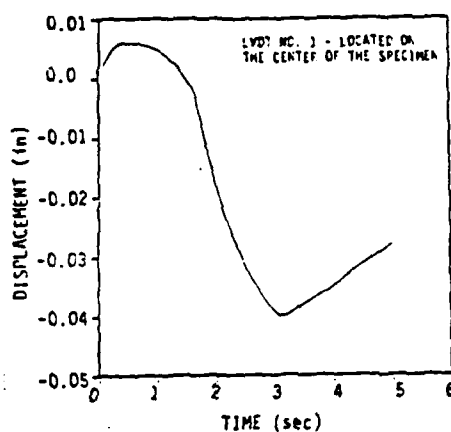


Fig. 10 Time Averaged LVDT Output for a 2 KW/cm² 3 Second Duration Test

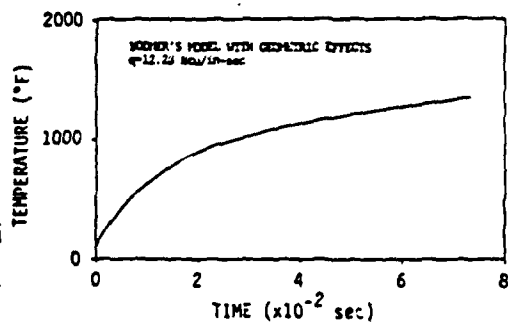


Fig. 11 Predicted Temperature at the Front Surface and Center of the Plate

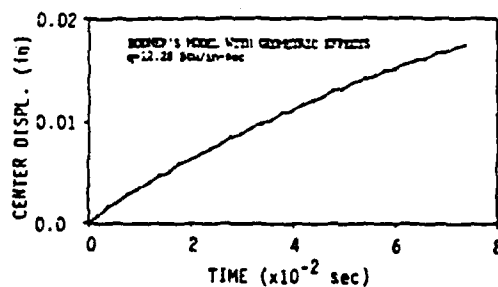


Fig. 12 Predicted Displacement at the Center of the Plate

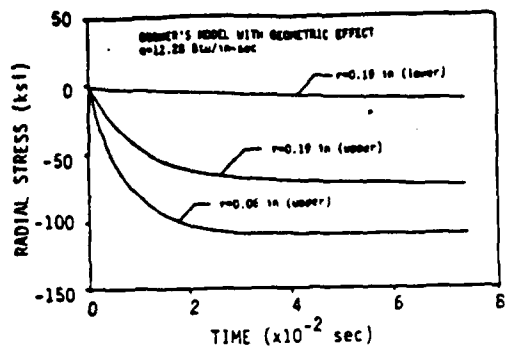


Fig. 13 Radial Stress At Various Locations

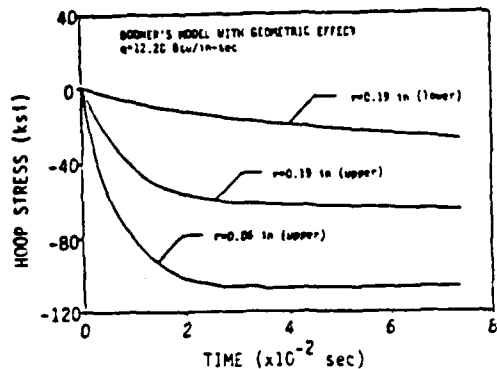


Fig. 14 Hoop Stress at Various Locations

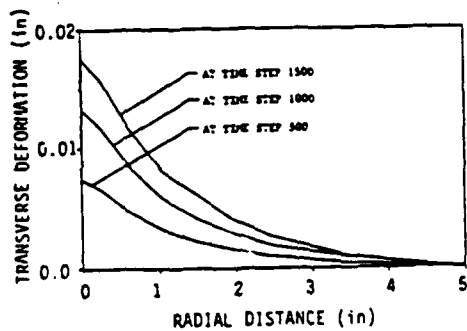


Fig. 15 Transverse Deformation at Various Times